


Title	Au nanorods-semiconductor nanowire hybrid nanostructures : nanofabrication techniques and optoelectronic properties
Author(s)	Pescaglini, Andrea
Publication date	2014
Original citation	Pescaglini, A. 2014. Au nanorods-semiconductor nanowire hybrid nanostructures : nanofabrication techniques and optoelectronic properties. PhD Thesis, University College Cork.
Type of publication	Doctoral thesis
Rights	© 2014, Andrea Pescaglini. http://creativecommons.org/licenses/by-nc-nd/3.0/ 
Embargo information	No embargo required
Item downloaded from	http://hdl.handle.net/10468/2024

Downloaded on 2017-02-12T14:00:16Z



UCC

University College Cork, Ireland
Coláiste na hOllscoile Corcaigh

Ollscoil na hÉireann
NATIONAL UNIVERSITY OF IRELAND

University College Cork
Tyndall National Institute
Chemistry Department



Au Nanorods-Semiconductor Nanowire Hybrid Nanostructures : Nanofabrication Techniques and Optoelectronic Properties

A Thesis Presented to
The National University of Ireland
for the degree of
Doctor of Philosophy
by
Andrea Pescaglini



October 2014

Head of Department
Prof. Martyn Pemble

Supervisor
Dr. Daniela Iacopino

Contents

1. Introduction	1
1.1. The promise of Plasmonics	1
1.2. Colloidal metal nanostructures for plasmonic devices	9
1.3. Integration of plasmonic nanoparticles in 1D semiconductor nanowires	16
1.4. Classical theory of plasmonic	23
1.4.1. Quasi-free electron gas approximation	23
1.4.2. Volume and surface plasmons	27
1.4.3. Localized surface plasmons	30
1.5. Scope of the thesis	34
2. Synthesis and optical properties of Au nanorods	37
2.1. Introduction	37
2.2. Synthesis and characterization of Au nanorods	41
2.2.1. Au nanorods with sub-20nm diameter	41
2.2.2. Au nanorods with diameter above 20nm	44
2.2.3. Purification of colloidal solution for dielectrophoresis	46
2.3. Modeling the optical properties of Au nanorods	48
2.3.1. Optical properties of Au nanorods in inhomogeneous environ- ment and effective refractive index approximation	49
2.3.2. Scattering and absorption properties of single nanorods	54
2.3.3. Scattering and absorption properties in closely-spaced nanorod arrays	57
2.4. Conclusion	62

3. Controlled assembly of Au nanorods into 1D architectures	65
3.1. Introduction	66
3.2. Dynamics of metal nanorods in oscillating electric field	67
3.3. Experimental section	72
3.4. Electric field assisted deposition of Au nanorods	74
3.5. Core-shell model for colloidal nanorods	77
3.6. Influence of the substrate on the nanorod assembly	86
3.7. Electrical Properties of Au nanorod networks	88
3.8. Conclusion	91
4. Enhanced Raman scattering in single ZnO nanowire by Au nanorods	93
4.1. Introduction	94
4.2. Experimental section	96
4.3. Classical Raman scattering theory	97
4.4. Fabrication of Au nanorod-ZnO nanowire hybrid nanostructure	100
4.5. Raman scattering in single Au nanorods decorated ZnO nanowire	107
4.6. Conclusion	116
5. Nanofabrication and electronic transport in ZnO nanowire field-effect devices	117
5.1. Introduction	117
5.2. Experimental Section	120
5.3. Fabrication of ZnO nanowire field-effect devices	120
5.3.1. Nanowire deposition and sample preparation	120
5.3.2. Nanofabrication of electrical contacts on single ZnO nanowire	121
5.4. Electrical properties of ZnO nanowire FET device	123
5.5. Joule Heating in ZnO NW-FET device	129
5.6. Nanowire-FET device for selective decoration of single ZnO nanowire	135
5.7. Conclusion	138
6. Au nanorod-ZnO nanowire hybrid device	139
6.1. Introduction	139
6.2. Experimental section	142

6.3. Photoconductivity in ZnO nanowire	144
6.3.1. Photoresponse above-bandgap radiation	144
6.3.2. Photoresponse below-bandgap radiation	149
6.3.3. Decoration of ZnO nanowire FET devices with Au nanorods .	152
6.4. Photoconductivity spectroscopy on hybrid devices	153
6.5. Hot-electron generation in hybrid device	156
6.6. Hot-electron injection process at nanorod-nanowire interface	159
6.7. Conclusions	163
7. Conclusion	165
7.1. Summary	165
7.2. Future work	168
A. Fabrication protocols	171
A.1.	
Mask-selective droplet deposition method : Process A	171
A.2.	
Mask-selective droplet deposition method : Process B	172
A.3.	
Fabrication of metal pads by optical lithography	173
B. Publications	175

Declaration

The work presented in this thesis is Andrea Pescaglini's own work unless otherwise stated and has not been submitted for another degree, either at University College Cork or elsewhere.

The synthesis of Au nanorods with diameter larger than 20 nm in section 2.2.2 was done by Alfonso Martin and the dark-field spectra in section 2.3.2 were measured by Carola Schopf. The ZnO nanowire were growth by Davide Cammi in Prof. Carsten Ronning's laboratory in Institute of Solid State Physics, University of Jena, Germany (Chapter 4,5 and 6). The Raman spectroscopy measurements in Chapter 4 were performed in Prof. A. Cantatero's laboratory in the Institute of Material Science, University of Valencia and were done in part by Eleonora Secco.

The present thesis is submitted for the degree of Doctor in Philosophy at University College Cork

Head of UCC Chemistry Department

External examiner

Internal examiner

Supervisor

Prof. Martyn Pemble

Prof. Gareth Redmond

Prof. Justin Holmes

Dr. Daniela Iacopino

Andrea Pescaglini

Abstract

The objective of this thesis is the exploration and characterization of novel Au nanorod-semiconductor nanowire hybrid nanostructures. I provide a comprehensive *bottom-up* approach in which, starting from the synthesis and theoretical investigation of the optical properties of Au nanorods, I design, nanofabricate and characterize Au nanorods-semiconductor nanowire hybrid nanodevices with novel optoelectronic capabilities compared to the non-hybrid counterpart.

In this regards, I first discuss the seed-mediated protocols to synthesize Au nanorods with different sizes and the influence of nanorod geometries and non-homogeneous surrounding medium on the optical properties investigated by theoretical simulation. Novel methodologies for assembling Au nanorods on (i) a Si/SiO₂ substrate with highly-ordered architecture and (ii) on semiconductor nanowires with spatial precision are developed and optimized.

By exploiting these approaches, I demonstrate that Raman active modes of an individual ZnO nanowire can be detected in non-resonant conditions by exploring the longitudinal plasmonic resonance mediation of chemical-synthesized Au nanorods deposited on the nanowire surface otherwise not observable on bare ZnO nanowire.

Finally, nanofabrication and detailed electrical characterization of ZnO nanowire field-effect transistor (FET) and optoelectronic properties of Au nanorods - ZnO nanowire FET tunable near-infrared photodetector are investigated. In particular we demonstrated orders of magnitude enhancement in the photocurrent intensity in the explored range of wavelengths and 40 times faster time response compared to the bare ZnO FET detector. The improved performance, attributed to the plasmonic-mediated hot-electron generation and injection mechanism underlying the photoreponse is investigated both experimentally and theoretically.

The miniaturized, tunable and integrated capabilities offered by metal nanorods-semiconductor nanowire device architectures presented in this thesis work could have an important impact in many application fields such as opto-electronic sensors, photodetectors and photovoltaic devices and open new avenues for designing of novel nanoscale optoelectronic devices.

Acknowledgments

Firstly, I would like to thank Dr. Daniela Iacopino for giving me the opportunity to read my Ph.D. in Nanotechnology Group at Tyndall National Institute. Her direction, advice, support and the confidence she put on me during these years have been invaluable.

I am grateful to the Head of the group Dr. Aidan Quinn for giving insightful advice during this work and to Dr. Alan O’Riordan, Dr. Karen Dawson, Dr. Mary Manning, Dr. Hugh Doyle for fruitful suggestions at different stage of my Phd. A special thanks to Dr. Michael Burke, Dr. Pierre Lovera and Dr. Nicolas Sassiati for scientific and non-scientific discussions and for their help in the lab. I also wish to thank Dan O’Connell for his help and suggestions in the lithography work, Noreen Nudds for sharing her experience on the wire-bonder and Krimo Khalfi for providing exceptional assistance and maintenance to the equipment in the Training Fab. I am very thankful to Dr. Emanuele Pelucchi for many interesting and helpful discussions that truly improved my research and for his advice and support to this work and also to Dr. Gediminas Juska for his assistance in the lab.

I wish to thank all PIs in the Marie-Curie *Nanowiring* ITN. In particular, Dr. Angela Rizzi, project coordinator, Dr. Carsten Ronning for his smart insights and his sense of humour during the *Nanowiring* meetings, Dr. Nuria Garro for her co-supervision during my secondment in the University of Valencia and also Dr. Giancarlo Cicero and Dr. Davide Calestani for interesting discussions. I would like to thank Dr. Val Zwiller and Dr. Michael Reimer for their co-supervision during the secondment at TU/delft and Dr. Erick Bakkers for his supervision during the secondment at TU/e.

I would like to devote a special tribute to all *Nanowiring* fellows. Among all, a special thanks to Eleonora Secco for the fantastic time spent in Valencia (and in Cork) sharing both personal and work-related troubles and successes. Obviously I cannot forget the other two *fuffoli*: Carla Oppo and Davide Cammi. I have had wonderful moments with you, we faced together the difficulties of doing a Phd and we had a lot of fun together, making every *nanowiring* meeting a really special event.

Because science covers only one part of the Phd life I would like to thank all friends who work hard to keep me busy during the remaining free time. In particular, former and current students in Nanotechnology group : Micki Mitchell (known as *entropy*), Ethel Noonan (who also was my *beloved* flatmate), Keith Linehan (*the busy man*), Umberto Emanuele (*the.....donkey*), Alfonso Martin (*Alfonsino*), Carola Schopf (the *Spanish* girl although she is German) and also Darragh Carolan, Amelie Wall (sorry, now I should say Dr. Amelie Wall), Marcus Russell, Niamh Creedon, Roxane Puicevert, Katarzyna Maj, Sean berry, Colm Barret, Daniel Jones, John MacHale. Also, a special thanks to my flatmate Mafalda Goncalves and to Farzan Gity, Pietro Pampili, Daniel Lordan (the other *beloved* flatmate) and Liza Vereshchagina for challenging me at squash.

A huge, massive thanks to all Italian friends. A special thanks to Marco Belcastro, we started together our adventure in Tyndall four years ago and we have shared many memorable *experiences* during this period. I had also great and unforgettable time with Domenico Pepe, Francesco Brandonisio, Nicola Brandonisio and Giuseppe Talli. Our *brainstorming* coffee-break sessions, brunch sessions, nights out and their *great minds* (especially Dr. Pepe) have been priceless moments and companionship in these years. I would like to mention other very good friends Walter Messina, Anna Paschero, Fabrizio Fortino, Roberto Mincione, Lorenzo Mereni, Marina Manganaro and Salvatore Tedesco.

Last but not least, I would like to thank my parents for their essential support and encouragement during these years away from home. They have always represented a solid, although sometimes invisible, *reference point* in my life; and thanks to Melissa, for her constant, enduring and immovable love during all these years despite the distance, she is an essential presence in my life.

Andrea Pescaglino

*To my parents
and Melissa*

'You have to learn the rules of the game. And then you have to play better than anyone else.'

Albert Einstein

Chapter 1.

Introduction

1.1. The promise of Plasmonics

In the last decades we have assisted to a progressive miniaturization of electrical components, driven by the semiconductor industry, towards the fabrication of more compact, low-power consumption and faster portable electronic devices. From a technological point of view, the miniaturization process needs to be supported by progresses in CMOS-compatible fabrication techniques, in order to reach higher resolutions (that actually is around ~ 15 nm for state-of-the-art transistors). Additionally, a deep understanding of the electronic properties of semiconductor materials and low-dimensional systems with a size-regime approaching the border line between classical and quantum mechanics is also an essential requirement.

The nano-sizing evolution in the semiconductor electronic field, described by the well-known Moore's law, is actually able to realize truly nanoscale elements fully capable to compute, transmit and store data. As discussed, further improvement in performance are linked with the ability to increase the density of the operational units, achievable by reducing the size of transistors, as well as the speed at which data are computed and transmitted (figure 1.1a). Regarding the former aspect, the present technology is still capable of further improvement in terms of resolution and device densities, although accessing quantum regime paradigm will require completely novel technologies and architectures for computing data, as assessed by the emerging research field of quantum information and computation [1]. On the other hand, processor performances in semiconductor technology show limitations. Heat

generation and signal delay issues associated with electronic interconnection limit the speed rate to a range of ~ 10 GHz [2]. Consequently, further improvement directed to exceed such range will require the development of radically new chip-scale technology able to operate beyond the limits imposed by semiconductor technology and to reach optical frequencies that, to date, are only achievable in dielectric photonics [3]. Unfortunately, photonics circuitry cannot be easily scaled below the diffraction limit of the light (about $\sim \lambda/2$ that is one of two order of magnitude larger than the electronic counterparts), therefore the large mismatch between electronic and photonics components hampered up to now the on-chip integration and miniaturization.

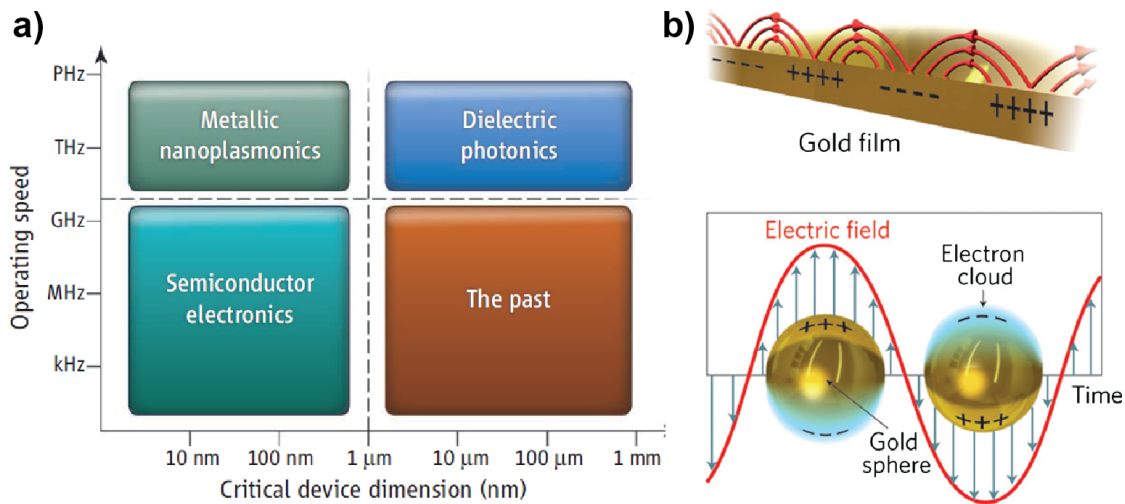


Figure 1.1.: a) The characteristic domains in terms of operating speed and device sizes for semiconductor (electronics), dielectrics (photonics) and metals (plasmonics) [2]. b) Schematic representation of propagating surface plasmon at a metal-dielectric interface (top) and localized surface plasmon in metal nanoparticle (bottom) [4].

The new flourishing field of technology called *Plasmonics*, has recently emerged as a potential route towards miniaturization of optical components beyond the limit of traditional optics [5, 6, 7]. This capability is made possible by exploiting coherent electron excitations in the electronic gas of metal nanostructures and their ability to manipulate, propagate and enhance light in nanoscale volumes [8]. When metallic atoms form a crystal structure, valence electrons are shared in orbitals delocalized on the entire crystal and acquire a quasi-free nature [9]. Application of Maxwell's

equations at the metal-dielectric interface result in propagating wave-like solutions (figure 1.1b), also called *surface plasmon polariton* (SPP). The distinctive characteristic of surface plasmons compared to photons is that they have much smaller wavelength at a given frequency [6]. Therefore, using SPP enable the fabrication of nanoscale optical integrated circuit in which light can be guided, split, filtered, focused and also amplified in plasmonic nanodevices smaller than the optical wavelength [10]. For metallic nanostructures significantly smaller than the free-space wavelength, geometrical boundary conditions determine the frequency at which the electron oscillation are driven resonantly (in this context called *localized surface plasmon*) producing a very strong charge displacement and high field intensity in close proximity to the nanostructure (typically within 15 nm [11]). From this fundamental mechanism derive the unique optical properties and an extraordinary ability to concentrate light into sub-wavelength volumes and mediate, enhance the interaction between the propagating radiation and nanoscale objects.

Application of these exciting and unusual properties have been explored theoretically and experimentally in many fields, showing remarkable contributions in widespread technological areas such as imaging techniques [12], photodetectors [13], solar cells [14], catalytic and thermal processes [15, 16], non-linear optics [17] and molecular detection [18].

For instance, in optical microscopy, subwavelength optical imaging was one of the first practical applications with a tremendous impact on the technological development. In conventional microscopy the spatial resolution is limited by the light wavelength. Instead, in near-field scanning optical microscopy subwavelength metal-coated probe generates an evanescent near field with spatial resolution defined by the tip dimensions. With this approach, Huber *et al.* reached spatial resolution of 40 nm with terahertz radiation frequency having wavelength of 118 μm by means of a millimeter-long tapered metal wire tip (figure 1.2a) [19]. This approach was also used to image nanoscale objects such as carbon nanotubes [21] and DNA [22].

Integration of plasmonic nanostructures with semiconductor devices is one of the most exciting field of research offering great promises for advancing present technology. For instance, plasmonic-enhanced photodetectors and solar cells are among the most promising fields of application. Reduction in size of these devices would allow

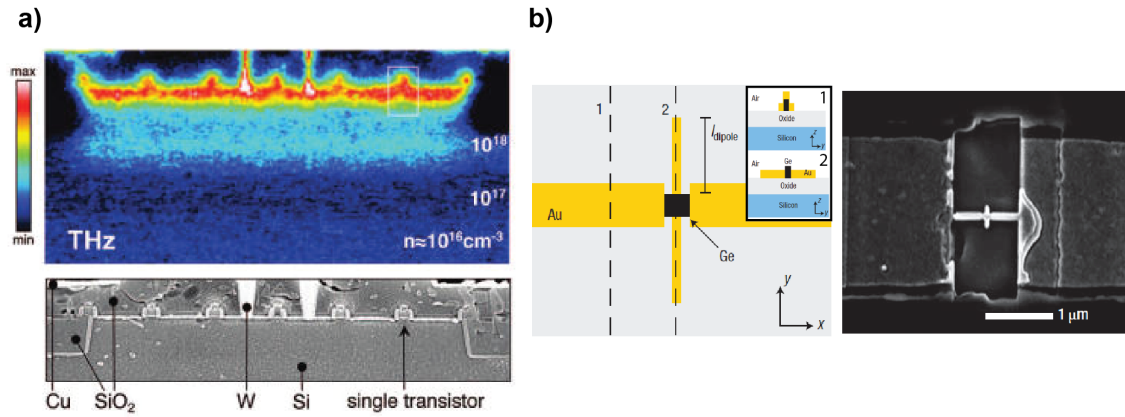


Figure 1.2.: a) An aNSOM image of a multiple transistor structure cross-section. Terahertz illumination ($\lambda=118$ nm) can distinguish between regions of different dopant density and can resolve the structure with a resolution of 40 nm [19]. b) Top view of a dipole antenna enhanced germanium photodetector (left). The two insets show the cross section along the line 1 and 2 respectively. On the right side the SEM image of the fabricated device [20].

more efficient charge collection thus increasing device efficiency, speed and reducing power consumption.

In traditional semiconductor device, typically, the minimum lateral size is determined by the diffraction-limited spot size of light and the thicknesses by the characteristic absorption depth of the material. Thin-film technology would allow faster carrier collection due to the decrease in the transit path before collection, but the reduced thickness below the characteristic absorption depth prevents efficient light trapping, thus provoking a drop in the overall efficiency. Indeed, integration of engineered metallic nanostructures with large scattering cross sections to efficiently trap light into the active semiconductor layer and to enhance light-matter interaction by means of the intensified local field represents a viable pathway to reduce device sizes without affecting performance [23]. An interesting example of this concept applied for photodetection was described by Tang *et al.* [20]. They exploited a dipole antenna to concentrate near-infrared radiation (~ 1.3 μm) in metal-semiconductor-metal germanium photodetectors with sub-wavelength volume of the order of $10^{-4}\lambda^3$, demonstrating a plasmonic enhancement factor of 20 in the detected photocurrent (figure 1.2b). Knight *et al.* showed first evidence of an alternative mechanism to exploit plasmonic resonances for photodetection [24]. They showed that surface

plasmon excited by incident radiation can decay non-radiatively by transferring energy to single electrons generating a non-equilibrium distribution of *hot electrons* above the Fermi energy. If the metal nanostructure is in direct contact with a semiconductor, hot electrons can be injected through the Schottky barrier formed at the interface into the semiconductor conduction band and collected by an applied bias. The proposed device, composed by an array of gold nanoantennas fabricated on *n*-type Si, showed a wavelength-resonant and polarization-sensitive photocurrent, demonstrating a spectral response at energies below the semiconductor bandgap (figure 1.3a). Furthermore, other examples of enhanced capability in semiconductor devices integrated with plasmonic nanostructures can be found applied to solar cell technology. For instance, enhanced light coupling in thin-film solar cell hybridized with metal nanoparticle were demonstrated with different materials such as crystalline and amorphous Si [25, 26], TiO₂ [27], perovskite [28], quantum well solar cells [29], and organic solar cells [30, 31].

The large field enhancements obtained in the proximity of metal nanostructures or in the interspace between coupled structures, has attracted a natural interest for boosting weak optical interaction such as non-linear processes. A striking result was demonstrated by Kim *et al.* who showed high-harmonic generation by focusing femtosecond laser onto an Argon gas mediated by arrays of resonant nanostructures [32]. The local electric field enhancement induced by interacting bowtie gold nanostructure arrays has been proposed and verified to be an effective pathway to generate extreme ultraviolet radiation (EUV) directly from a modest femtosecond laser with no extra cavities, allowing a possibly convenient reduction in size of coherent EUV light sources (figure 1.3b).

Also, other weak optical processes could take advantage from the plasmonic-mediated field enhancement. Plasmonic nanostructures have been investigated as a promising tool for single molecule detectors. Kinkhabwala *et al.* [18] found a large enhancement of a single molecule's fluorescence up to a factor of 1340 induced by metal nanoantenna (figure 1.3c) and Liu *et al.* demonstrated successfully antenna-enhanced hydrogen sensing at the single-particle level [33].

Similarly, Raman scattering signal of single or few molecules adsorbed at or in proximity of metal structures has been observed due to the many orders of magni-

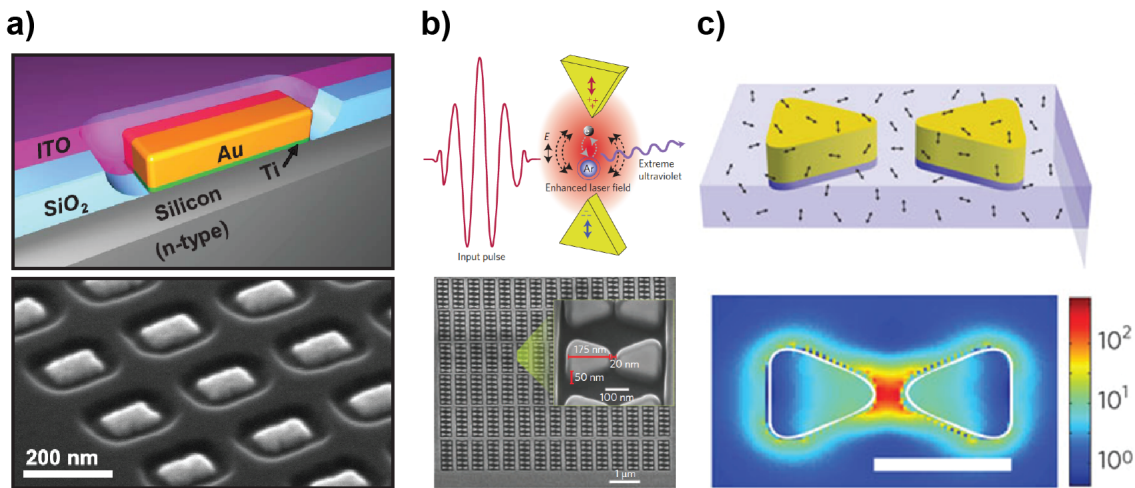


Figure 1.3.: a) (top) Representation of a single Au resonant antenna on n-type Si substrate and (bottom) SEM of a representative device [24]. b) (top) Scheme of work for high-harmonic generation mediated by plasmonic field enhanced. Ultraviolet radiation can be generated by focusing a femtosecond laser to an array of bowtie metal nanostructures in presence of argon gas. SEM image of the device (bottom) [32]. c) (top) Schematic of bowtie nanoantenna coated with TPQDI molecules (black arrows) in PMMA on a transparent substrate and (bottom) FDTD calculation of local intensity enhancement. Scale-bar 100 nm [18].

tude plasmonic-mediated signal enhancement [34]. This approach for expanding the capability of Raman spectroscopy, also called surface-enhanced Raman spectroscopy (SERS), has become a widely explored technique to study molecular structures and to detect ultra-low concentration of molecules in sensing devices [35, 36, 37].

Finally I mention that nanostructured materials composed by sub-wavelength metallic elements with regular arrangement form an entirely new class of optical materials called *metamaterials*. When the dimensions of the single component is much smaller than the light wavelength, the structure inhomogeneity cannot be resolved and the optical properties can be described by macroscopic parameters such as permittivity and permeability like in a homogeneous medium [38]. The ability to control and engineer the single component in ordered arrays allowed to create artificial materials with exotic optical characteristics such as negative refractive index [39], terahertz-active devices [40], superlens [41] and electromagnetic cloaks [42].

This brief snapshot on some of the most remarkable achievements obtained in the past decades in the field of Plasmonic supports the high expectations and promises

from future development to solve key weaknesses of present technology in many fields. Nevertheless, despite the great potential already vastly demonstrated, application of plasmonic-mediated processes are not exempt from limitations and challenges to be addressed. One of the main limitation arise from the ohmic losses due to intraband and interband electronic transitions, described by a non-vanishing imaginary part of the permittivity ϵ'' in metals. The intraband transition is an unavoidable process related to electron-electron scattering, electron-phonon scattering and scattering with crystal impurities that are often dominant at longer wavelength (near-infrared). The interband transition arises from the excitation of a valence electron to an unoccupied level in the conduction band. Interband transition require larger energies than the intraband counterpart and typically are dominant for radiation energies above ~ 2 eV [43]. Although the ideal case of $\epsilon''=0$ is not possible, every metal has a optimum optical region where the imaginary part reaches the minimum. For instance gold shows a minimum losses for wavelength in the range 600-800 nm (figure 1.4).

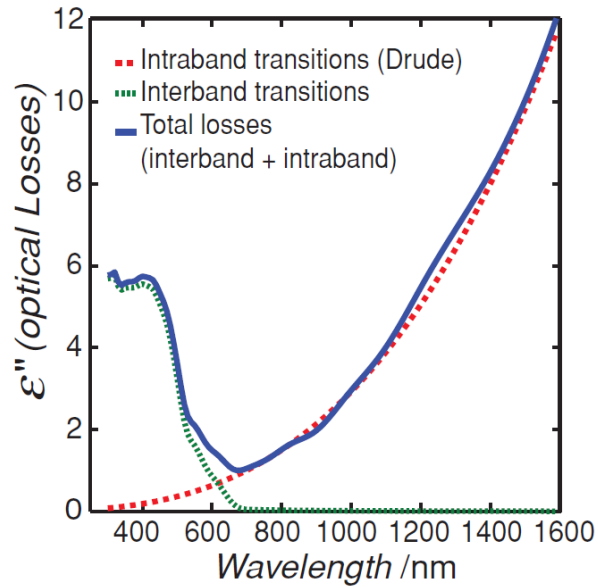


Figure 1.4.: *Individual contribution of intraband and interband transitions in the imaginary part of the permittivity of gold [43].*

At present, gold and silver are the most used metals in plasmonic devices and they have also the lowest ohmic losses. However the large cost, especially of gold, has encouraged research of alternative low-cost materials [44]. Copper and aluminum are

good candidates. Copper has the advantage that it can be compatible with the silicon manufacturing processes but its properties degrade significantly after oxidation in air, thus requiring additional protective layers [45, 46]. Aluminum outperforms both gold and silver in the blue and UV region therefore, although it experiences similar oxidation issues as copper, offers the best performance for application involving ultraviolet radiation [47]. Other alternative materials have been also considered for plasmonic applications. Alkali metals have been investigated theoretically [48] showing lower losses than silver in the visible range. However the strong reactivity constitutes the major limitation for practical applications.

Overall, large effort has been recently devoted to production of materials with engineered properties suitable for plasmonic application. For instance, metallic compounds have been explored to obtain materials with reduced carrier concentration and consequently lower ohmic losses [49]. However, the introduction of non-metallic elements in the metal lattice affects also the band structures and introduces impurities that increase Drude-damping losses, therefore an accurate optimization is needed. Alternatively, highly doped semiconductors can show metallic-like behavior [43]. In this case limitations arise from the extremely high level of dopant atoms required to reach the desired electronic density that could overcome the solubility limit of the dopants in the host material. Moreover the incorporation process increases the density of scattering centers respect to the pure semiconductor and could also affect the band structure, in particular the band-gap energy, thus increasing both the intraband and interband transitions. However, despite the challenges discussed, the feasibility of these two approaches to realize optimized plasmonic materials has been demonstrated highly promising.

The fabrication of metal nanostructures remains one of the major bottlenecks for mass production of plasmonic devices. Even though resolution of silicon manufacturing processes is actually capable to fabricate structures with nanometer dimension on the order of ~ 10 nm, realization of metal nanostructures require alternative processes and expensive nanofabrication instruments [44]. From this perspective the use of highly doped semiconductors would facilitate the integration of plasmonic nanostructures in the present semiconductor-device technology by exploiting CMOS-compatible strategies. An alternative approach, that is recently gaining at-

tention in the field, is the exploration of chemical routes for the chemical synthesis of metal nanostructures [50]. This approach offers a low-cost, high yield throughput that could potentially match the requirements imposed by industrial manufacturing.

Overall, the field of plasmonic can be appointed as one of the most promising fields of research with a potential large impact on future technological developments. The promising results obtained in the past decades are strongly driving an increasing scientific efforts in further design, development and optimization of plasmonic devices and integration with present electronic components, towards a new chip-scale technology integrating plasmonic and electronic devices to take advantage of the strengths of both.

1.2. Colloidal metal nanostructures for plasmonic devices

Colloidal Au nanoparticles have received much attention in the field of plasmonic since the recent development of reliable and reproducible synthetic protocols by El-Sayed *et al.* to growth size-controlled Au nanoparticles with high yield and tunable aspect ration from 1 (spherical particles) to more than 10 (nanorods) [51, 52]. This method provides an effective and low-cost process to realize metallic nanostructures that affords a promising alternative not only to top-down lithographic approaches [53] but also to other bottom-up techniques such as electrochemical methods [54], template methods [55] or photochemical reduction [56]. Moreover, compared to top-down fabricated structures the single-crystal nature of chemically synthesized particles offers better electronic properties minimizing ohmic losses [43] and resolution in the sub-10 nm regime in the nanoparticle size.

In colloidal Au nanoparticles, the surface curvature exerts restoring forces on the oscillating electrons so that resonances arise naturally from the scattering problem of sub-wavelength conductive nanoparticles under electromagnetic radiation. Therefore, the optical properties are highly tunable throughout the visible and near infrared region of the spectrum as a function of nanostructure size, shape, aggregation state and local environment. Moreover, the curved surface allows a direct

excitation of plasmonic resonances by incident radiation without mediation of any additional phase-matching techniques such as grating or prism to address the k -vector mismatch needed in the excitation of surface plasmon polaritons (see section 1.4) [57].

Usually, synthesized nanoparticle are highly symmetric with at least two of the three axes approximately equal. Consequently, they accommodate up to two plasmonic resonances: the longitudinal plasmon band corresponding to light absorption and scattering along the long axis, and the transverse plasmon band, corresponding to light absorption and scattering along the short axis (figure 1.5). For the special case of spherical nanoparticle these two modes degenerate to a single mode due to the higher degree of symmetry that appears around 520 nm and is almost insensitive to the nanoparticle radius [50].

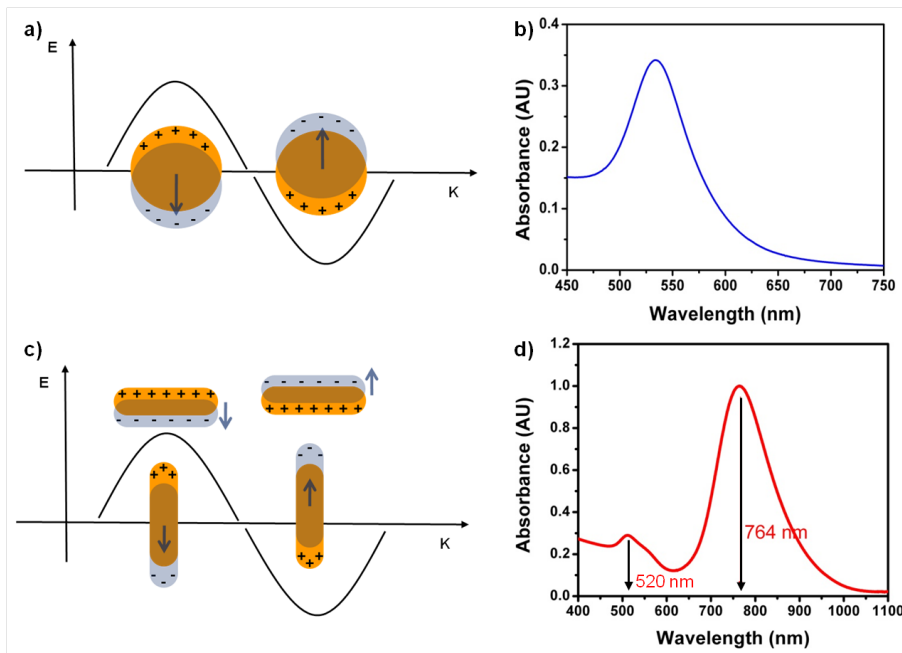


Figure 1.5.: a) Schematic of the coherent electron oscillations (plasmon) in spherical nanoparticle induced by electromagnetic radiation b) Absorption spectrum showing the plasmonic resonance in spherical nanoparticles c) Schematic of the two plasmon modes in rod-shape nanoparticle induced by electromagnetic radiation d) Absorption spectrum showing the transversal (520 nm) and longitudinal (764 nm) plasmonic resonances in rod-shape nanoparticles

The longitudinal surface plasmon resonance can be more finely tuned compared to the transversal one. For example a slight change in nanorod aspect ratio from 2.4 to

3 can lead to a 50 nm red-shift in the longitudinal plasmon mode, which is equivalent to the maximum tunability achievable with spherical nanoparticles ranging from 10 to 100 nm diameter [58].

Optical properties of Au nanorods have been investigated both experimentally and theoretically by many authors, demonstrating the key role played by the nanoparticle diameter on the scattering, absorption and extinction cross sections [59, 60]. In particular, the extinction intensity was found increase in a non-linear fashion with the radius and the absorption was found larger than the scattering cross section for nanoparticles with diameter below ~ 30 nm [61]. Moreover, detailed theoretical investigations of the light scattering in Au nanorods showed that plasmon resonances depends linearly on the rod length and the linear dependence is a function of the nanorod radius [62].

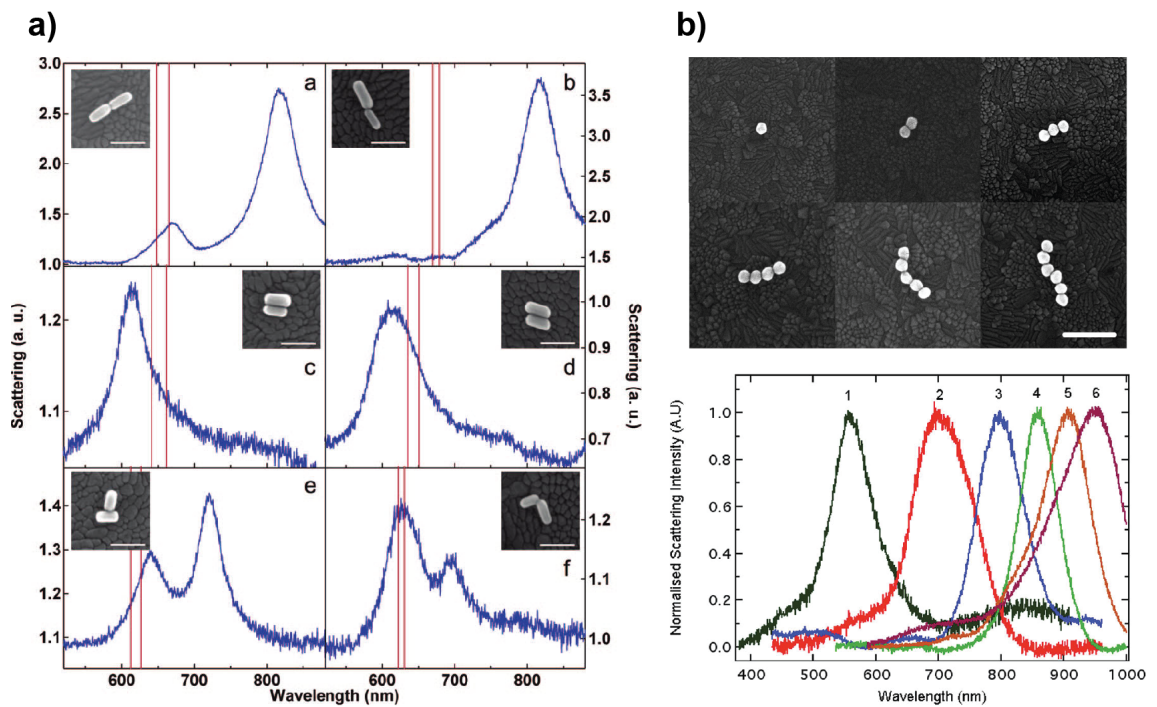


Figure 1.6.: a) Scattering spectrum for two Au nanorods in different configuration deposited on ITO substrate and in air. Insets show the SEM images of the particles giving rise to each scattering spectrum. Scale bar is 100 nm [63]. b) (top) SEM image of self-assembled nanoparticle chains on ITO (scale bar is 250 nm) and (bottom) normalized spectra labeled with numbers according the chain length [64].

More detailed investigation of the surface plasmon nature revealed that surface

plasmons featuring dipole-like charge distribution can be directly excited by incident radiation therefore are also referred as *bright modes*. In addition to that, *dark modes* such as quadrupole and high-orders multipoles coexist with the bright modes, but they couple marginally with the light due to their weaker nature and cannot be optically resolved. However, direct imaging of bright and dark modes in Au nanorods have been achieved by two-photon-induced photoluminescence and electron-energy-loss spectroscopy [65, 66, 67]. Interference between dark and bright modes can also give rise to additional optical features. In fact, the interaction between a broad resonance and a narrow discrete resonance could result in an newly asymmetric sharp resonance called Fano resonance [68]. Despite theory predicts that single spherical nanoparticles can exhibit Fano resonance due to interference between dipolar and quadrupolar modes, the damping in typical metals is too large to allow a direct observation, so most of the demonstrations were found in ordered array of metal nanostructures [68, 69, 70]. In larger nanorods however, where multipole modes and retardation effects are non-negligible, the interaction between the quadrupolar and octupolar resonances mediated by a substrate with large dielectric constant resulted in a Fano resonance of great interest for chemical and biological sensing due to a narrower bandwidth [71].

Ordered arrays of metal nanostructures

Exciting new properties emerge when individual colloidal metal nanostructures are organized into ordered arrays. In assemblies where the nanostructures are separated by a few nanometres, near-field coupling alters the plasmonic resonances and introduces new interesting properties [72]. Funston *et al.* [63] reported a shift in the resonances of Au nanorod dimers arranged in various configurations (i.e. side-to-side, end-to-end and at right angles) as shown in figure 1.6a. Also, experimental results were understood in terms of the plasmon hybridization model proposed by Prodan *et al.*, that explains the plasmonic coupling in analogy with molecular orbital theory [73, 74]. Furthermore, this theory opened up the intriguing perspective of using metal nanostructures as building block for *artificial molecules and solids*, that is a new exciting interdisciplinary area of research across plasmonic, chemistry, biology and material science [75, 76].

In larger assemblies of interacting nanoparticles the shift of plasmonic resonances is further increased. A clear demonstration of this trend was provided by Barrow *et al.* who observed a progressive red-shift in the plasmonic resonance in strongly-coupled Au nanoparticle chains with increasing number of element from 1 to 6 (figure 1.6b) [64, 77]. Interestingly, the red-shift of the longitudinal plasmon showed evidence of saturation for higher numbers of nanoparticles in the chain (around 10-12) that defines an effective interaction length for plasmonic coupling in accordance with theoretical models (see also Chapter 2) [78]. Near-field coupling between two adjacent nanoparticles also results in a strongly localized and intensified electric field in the inter-particle gap [79] that has been extensively explored for enhancing optical properties of molecular species such as light absorption [80], fluorescence [81, 82] and Raman scattering [83].

Kristen *et al.* provided a systematic study on the strong dependence of the field enhancement factor from the inter-particle distance (figure 1.7a) [84]. In particular, an enhancement factor on the order of 10^5 requires gap distance below 20 nm and the exponential decay of the plasmon coupling strength [86] suggests that further reduction below 10 nm would be highly desirable.

Following this route, 2D and 3D arrays of metal nanoparticles fabricated with various self-assembled techniques have shown great potential for surface-enhanced Raman scattering (SERS) reaching detection limit down to few molecules level [85]. For instance, Pollard *et al.* exploited the formation of electromagnetic hot spots in gold nanorods vertically aligned for SERS applications (figure 1.7b). Alvarez-Puebla *et al.* used Au nanorods organized in 3D supercrystals fabricated by simple droplet evaporation for detection of scrambled prions, demonstrating detection limit as low as 10^{-10} M [87]. Nikoobakht *et al.* [88] reported enhancement factor of 10^4 - 10^5 in the Raman spectra of pyridine and 2-aminothiophenol molecules adsorbed on Au nanorods deposited on silica film and a similar enhancement factors were also demonstrated by Martin *et al.* [89] in the Raman scattering of 4-aminobenzenethiol with arrays of Au nanorods assembled parallel and vertically respect to the substrate. Similar superstructures were also used for femtomolar detection of food contaminants [90] and bioanalytes [91].

In conclusion, colloidal metal nanoparticles afford the promise to miniaturize plas-

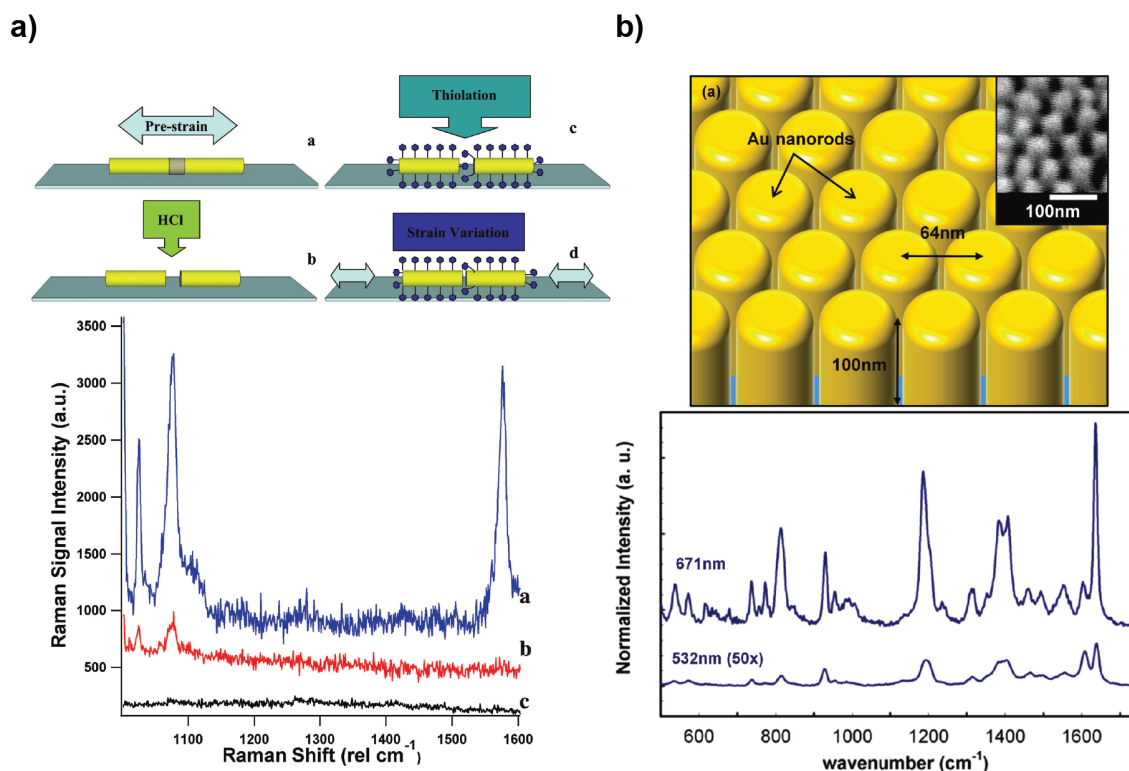


Figure 1.7.: a) (top) Schematic illustration of the dimer fabrication on elastomer substrate. (bottom) Raman spectrum of a nanorod pair functionalized with benzenethiol taken with (a) light polarized along the dimer long axis and 10 nm separation (b) light polarized perpendicular to the dimer long axis and 10 nm separation (c) light polarized along the dimer long axis separation of 300 nm [84]. b) (top) Schematic of Au nanorod array. Inset shows a SEM image of the fabricated surface. (bottom) Raman spectra of crystal violet molecules adsorbed on the nanorod array with excitation wavelength 532 and 671 nm [85].

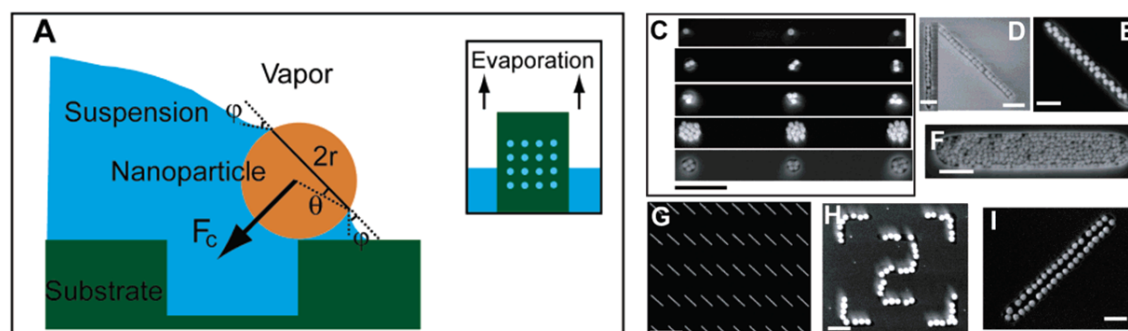


Figure 1.8.: a) Schematic illustrating the capillary force (F_c) assembly mechanism at the vapor-suspension-substrate three-phase contact line. c) Collection of SEM images of 50-nm particles in holes with different diameters. d-i) SEM images of 50-nm Au nanoparticles in lithographically-patterned trenches with different widths or orientations [92].

monic devices while keeping fabrication costs low. Nevertheless, other challenges need to be addressed. Most of the proof-of-concept devices in plasmonic have been demonstrated on structures fabricated by lithographic techniques (in particular e-beam lithography) due to the advantageous control on shape and location at the single nanostructure level. In fact, although synthetic routes have been demonstrated capable to produce monodisperse metal nanostructure with different geometries including spheres [93], cubes [94], rods [95], bipyramids [96], triangular prism [97], octahedrons and unsymmetrical nanocrystals [98] with finely tunable sizes, the major challenge regards the limited availability of tools for the precise placement and assembly of these nanostructures on a desire substrate.

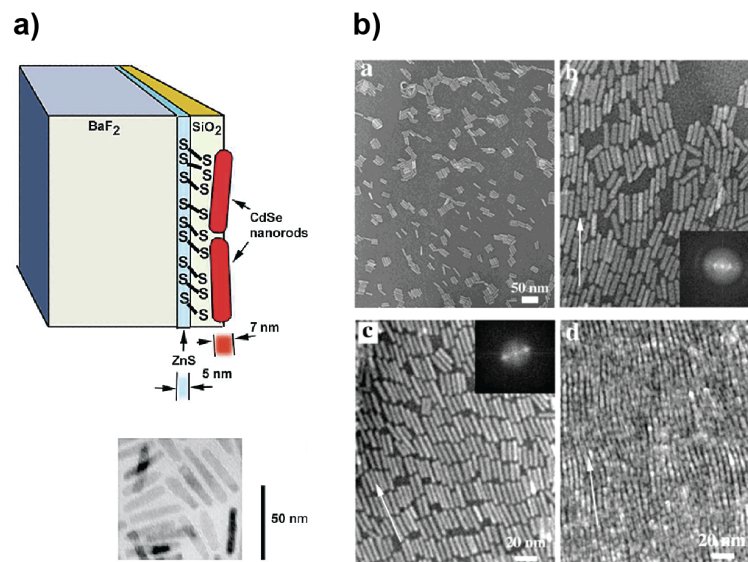


Figure 1.9.: a) (top) Sketch of sample consisting of single 5 nm wide ZnS nanolayer sandwiched between BaF_2 substrate and 100 nm SiO_2 film. The sample was cleaved in order to expose a 5 nm wide ZnS stripe to which CdSe nanorods (nanodots) are attached via hexanedithiol self-assembled monolayer and (bottom) TEM image of CdSe nanorods used to attach to the ZnS nanotemplate [99]. b) TEM images of nanorod assemblies at the water/air interface at different stages of compression : (a) isotropic distribution at low pressure; (b) monolayer with partial nematic arrangement; (c) monolayer with smectic arrangement; and (d) nanorod multilayer with nematic configuration. Insets in panels b and c are the Fourier transform of the corresponding image [100].

Mixed top down-bottom up approaches have been proposed as viable route. For instance, the capillary interaction at a solution interface has been demonstrated

able to drive particles arrangements on pre-patterned substrate with high degree of freedom in pattern geometry (figure 1.8) [92]. Artemyev *et al.* proposed to use a nanolayered substrated selectively functionalized as an intrinsic template for linear arrangement of anisotropic semiconductor nanorods (figure 1.9a) [99]. Alternatively, drying-mediated and Langmuir-Blodgett assembling (figure 1.9b) were found to induce monolayer formation of anisotropic colloids with a reasonable alignment on the micro scale but with poor control on positioning and directionality [100]. Also, droplet-evaporation [101], capillary flow [102], dielectrophoresis [103], templates [104, 105], lithographically fabricated trenches [106, 92], or chemically linked nanoparticles in solution [107, 108, 109] have been successfully used.

Despite all these efforts, development of novel and optimized assembly techniques remains a key challenge for the realization of plasmonic devices based on colloidal metal nanostructures. However, addressing this challenge together with an engineered design of the plasmonic properties of single and ordered arrays would open up a bright future for on-chip optical circuitry and hybrid plasmonic-enhanced semiconductor devices.

1.3. Integration of plasmonic nanoparticles in 1D semiconductor nanowires

Semiconductor nanowires

Semiconductor nanowires have been shown capable to address fundamental physical phenomena as well as to depict a potential step-forward in many technological sectors. Growth techniques, based on vapour-liquid-solid (VLS) mechanism, have allowed fabrication of a broad range of inorganic nanowire compositions such as Si, Ge, ZnO, CdS, GaN, GaAs, InP, InAs and also traditional inaccessible compositions like InGaN [110, 111, 112, 113]. Moreover, the nanosize diameter allows to accommodate large lattice mismatch at the interface between two materials, not achievable in 2D epitaxial growth. Therefore, axial and radial heterostructured nanowires have been attracted extensive interest due to the unprecedented level of flexibility in material engineering.

1.3. Integration of plasmonic nanoparticles in 1D semiconductor nanowires

The one dimensional (1D) nature together with dislocation-free structure and the ability to accommodate large lattice mismatch are associated with a number of properties which have interesting nanoelectronic and photonic applications [114, 115, 116, 117].

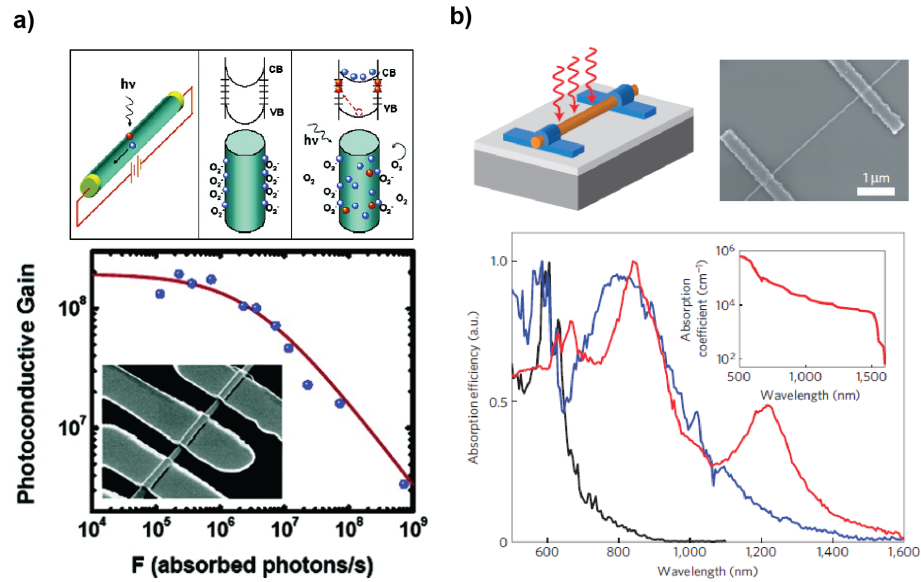


Figure 1.10.: a) Photoconduction in Zn nanowire photodetectors. Upon illumination with photon energy larger than the bandgap, electron-hole pairs are generated and holes are readily trapped at the surface. Under an applied electric field, the unpaired electrons are collected at the anode, which leads to a photoconductive gain up to 10^8 [118]. b) Schematic illustration of the germanium nanowire device used for photocurrent measurements (top left) and scanning electron microscopy image of a 25-nm-radius germanium nanowire device (top right). Measured spectra of absorption efficiency Q_{abs} for unpolarized light taken from individual germanium nanowires with radii of 10nm (black), 25nm (blue) and 110nm (red) (bottom).

In photodetection, semiconductor nanowires have showed great potential compared to the 2D counterpart due to (i) the prolonged lifetime of photogenerated carriers mediated by the in-built radial potential promoted by surface states and (ii) the reduced carrier transit time due to the high mobility achievable in high-quality single-crystal material combined with the micrometer or nanometer inter-electrodes distance. One of the first report on photodetection from single InP nanowire was presented in 2001 by Lieber's group, exhibiting highly polarized photoluminescence and polarized-sensitive photoconductivity with responsivities of 3000 A/W [119].

Following this pioneering work many other materials were explored such as GaN, Si, Ge, Se, CdS, ZnO and many others [120]. For instance, Soci *et al.* realized an UV photodetector based on single-crystal ZnO nanowire with photoconductive gain up to 10^8 (figure 1.10a) [118].

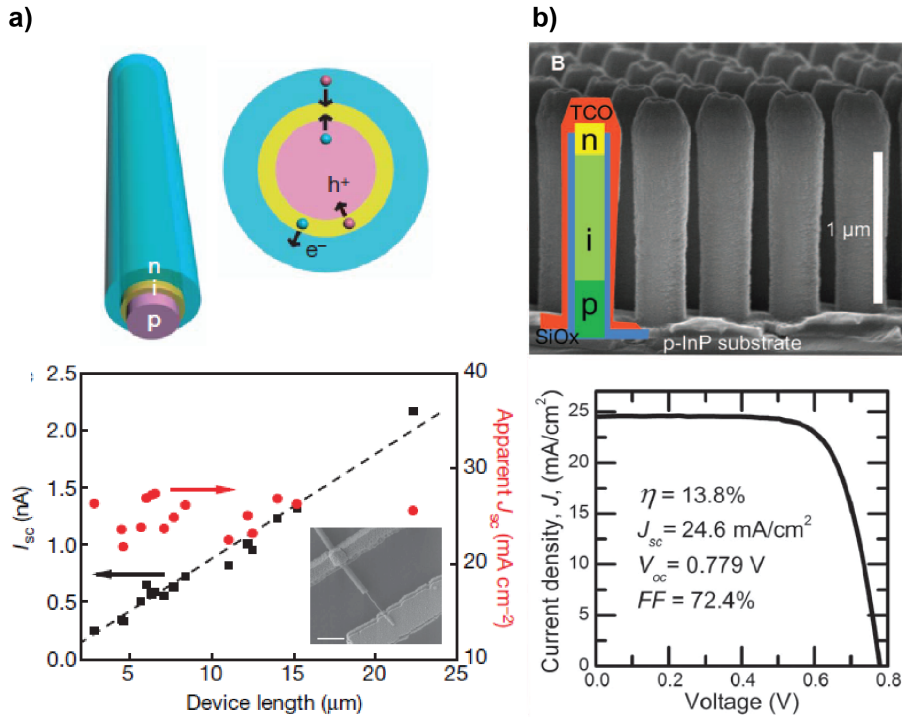


Figure 1.11.: a) Single core-shell Si nanowire solar cell. (top) Schematic of the device and (bottom) corresponding SEM image. (c) Device-length-dependent short-circuit current I_{sc} and current density J_{sc} measured under AM 1.5G illumination. Inset shows a representative device [121]. b) SEM image of the InP nanowire array solar cell with superimposed the p-i-n doping levels (top). Current density characteristic under AM 1.5G illumination [122].

Moreover, design engineering of the nanowire geometry was found capable to boost device performances. Brongersma *et al.* showed that light absorption in nanowire can be engineered by exploiting internal leaky modes resonances in optimized geometries (figure 1.10b). In this rational design the authors demonstrated a 25-fold enhancement in the absorption and wavelength selectivity in germanium nanowire [123]. This approach was applied to other semiconductor nanowires and allowed to boost the optical absorption beyond the intrinsic properties of the material [115].

Nanowire properties explored for photodetection are equally relevant for design-

1.3. Integration of plasmonic nanoparticles in 1D semiconductor nanowires

ing nanowire-based solar cells. To this aim both radial and axial heterostructured nanowires have been proposed [124]. For instance, Tian *et al.* realized single p-type/intrinsic/n-type (p-i-n) coaxial silicon nanowire solar cell. In this geometry the electron-hole pairs generated under radiation in the intrinsic part were readily collected at the p-type core and n-type shell thanks to a carrier collection distance smaller than the minority carrier diffusion length (figure 1.11a). This efficient carrier collection scheme allowed to reach an overall apparent efficiency of 3.4% [121]. Using a similar radial structure, higher efficiency up to 4.5% was demonstrated in GaAs nanowires under comparable illumination conditions (1.5 AM) [125]. Substantial improvement in light absorption was obtained in arrays of axial p-i-n InP nanowire with optimized diameter size and length of the top n-segment, demonstrating a record efficiency of 13.8 %, comparable with planar InP cells [122].

However, despite the variety of alternative materials [126, 127] and geometry explored [120, 124], the limited efficiency observed in semiconductor nanowire solar cells and photodetectors is mostly attributed to the limited light absorption caused by the sub-wavelength dimensions [14].

Nanoparticle-decorated semiconductor nanowires

Recently, decoration of semiconductor nanowires with metal nanostructures has been demonstrated to be a promising route to expand and improve a widespread range of nanowire functionalities such as allowing unconventional growth of semiconductor heterostructures, enhancing photocatalytic properties and molecular sensing and manipulate nanowire optoelectronic properties [128, 129, 130, 131]. Therefore, integration of metal nanostructures and their ability to localize, manipulate and enhance light into a nanoscale volume with the engineered electronic and optical properties of semiconductor nanowires open interesting perspectives in many applications involving light-matter interaction [8, 132, 33].

For instance, Hyun *et al.* used scanning photocurrent microscopy to resolve a local photocurrent enhancement by 20% along a Si nanowire decorated with Au nanoparticles under transverse polarization. The increment was attributed to a near-field plasmonic enhancement of light absorption in the nanowire (figure 1.12a) [133]. Galvanic displacement technique was proposed to decorate Si nanowires with

a variety of Au nanoparticles including single spherical nanoparticle with different sizes, dimers, nanorods and prisms [134]. The sub-nanometer gap separation with nanowire surface affords a larger coupling with the plasmonic resonances in the metal nanostructures resulting in a 24-fold enhancement in the Raman signal recorded where two nanoparticles were aggregated on both size of the nanowire. Also, enhanced photocurrent by a factor 2 was observed in Si nanowires decorated with Au nanoparticles compared with the bare nanowires (figure 1.12b). Similar plasmonic-related photoresponse was observed in silica nanowire with embedded Au clusters, suggesting application as wavelength-controlled nanoswitchers [135]. Enhancement of the optical absorption due to near-field plasmonic coupling with metal nanostructures were also demonstrated in other nanowire materials such as InAs nanowires [136] and GaAs nanowires [130, 137, 138].

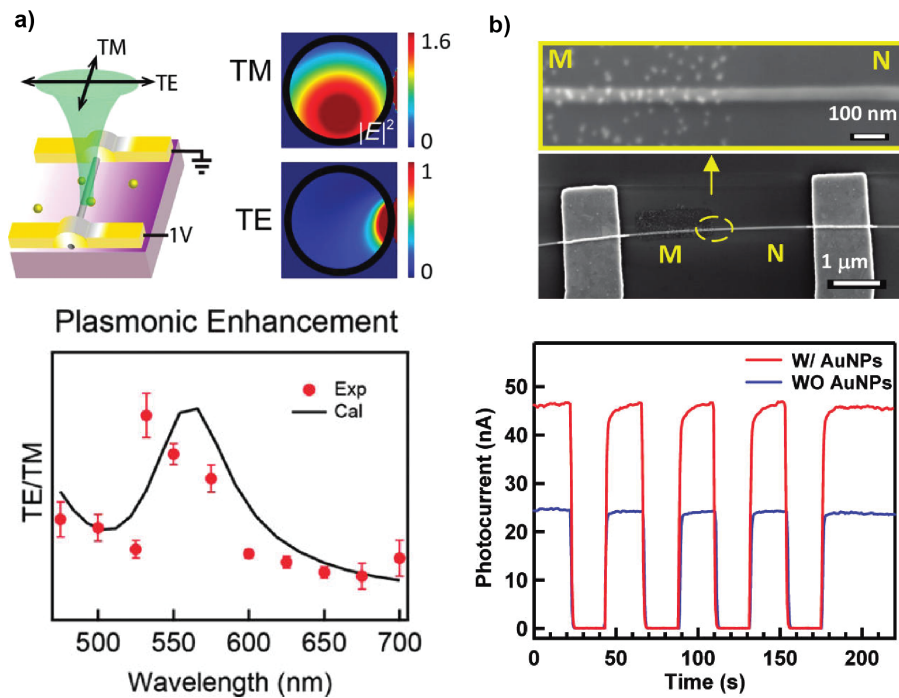


Figure 1.12.: a) Schematic of the device investigated by Hyun et al. and FDTD simulation of the field enhancement at the metal nanoparticle-nanowire interface (top). Enhancement of the ratio between photocurrent intensity under transversal and longitudinal polarization (bottom) [133]. b) SEM image of a Si nanowire half decorated with metal nanoparticles by galvanic displacement (top). The graph in the bottom show the comparison between the photocurrent measured in the left part (decorated nanowire) and right part (bare nanowire) [134].

1.3. Integration of plasmonic nanoparticles in 1D semiconductor nanowires

Decoration of ZnO nanostructures with metal nanoparticles has been also explored to change photoluminescence properties [139]. Cheng *et al.* showed increasing of band-edge emission of ZnO nanowire arrays by coating with Au metal nanoparticles [128].

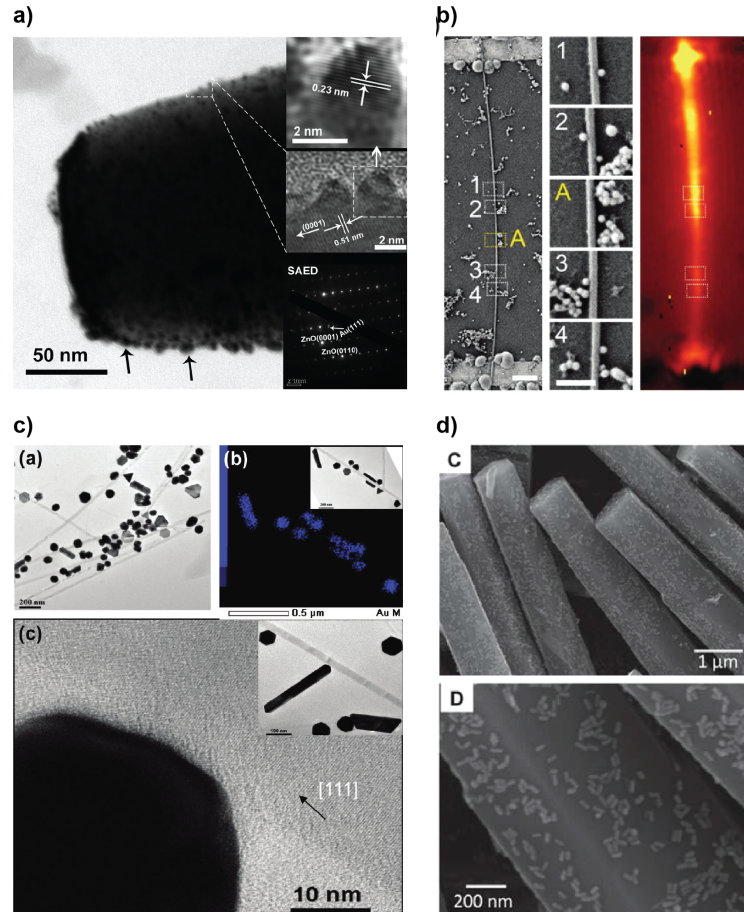


Figure 1.13.: Examples of semiconductor nanowires decorated with metal nanostructures by a) sputtering technique [140] b) droplet deposition [133] c) galvanic displacement [134] and d) chemical functionalization [141].

Dhara *et al.* explained the mechanism behind the enhancement on the basis of energetic electrons created by interband transitions (under UV light) or surface plasmon excitations (around 500 nm) in the metal islands capable of moving to the conduction band of ZnO thus contributing to increase the exciton recombination and photocurrent [140].

Another interesting field of application for hybrid nanostructures is molecular detection. While semiconductor and metal nanowires have been shown an ideal candidates as active elements for gas and biological sensors due to the high surface-

to-volume ratio that provides outstanding sensitivity, selectivity still remain the major challenge to be addressed. Zou *et al.* showed that a metal nanoparticles decorated nanowire hybrid field-effect transistor device can be used as a high selective gas sensor. In this prototype the engineered electronic properties of an In_2O_3 nanowire by Mg-doping, assisted by the catalytic properties of various metal particles, resulted in high sensitivity and selectivity in detecting CO , O_2 , H_2 and $\text{C}_2\text{H}_5\text{OH}$ [142]. A similar architecture was also proposed as an ion-sensitive metal-semiconductor field-effect transistor for chemical sensing [143]. Despite the promising route, the field of semiconductor nanowire based devices hybridized with metal nanostructures remains vastly unexplored, mainly due to limited availability of reliable fabrication techniques as well as limited support from theoretical studies. A number of different approaches have been proposed for decorating semiconductor nanowires with metal nanostructures. A well-known approach to form metal nanoislands with dimensions in the range of 3-6 nm is by sputtering of thin metal films directly onto the nanowires (see figure 1.13a) [140, 139, 128]. Alternatively, simply drop-casting of colloidal solutions of chemically synthesized metal nanoparticles have been used (figure 1.13b) [133, 144]. For large enough nanowires e-beam lithography also becomes a possible technique to fabricate geometry-customizable metal nanostructures within the resolution of the lithographic process [130]. Other than the above mentioned techniques, Chen *et al.* proposed galvanic displacement to decorate Si nanowires with Au nanoparticles with different morphologies [134]. In this process silicon nanowires provide electrons for reducing the metal ions in solution and at the same time serve as templates for the particles. Typical nanostructures resulting from the process are shown in figure 1.13c. Different particle shapes were synthesized (spherical, triangular, rodlike) with diameters between 20-100 nm attached to the nanowire body with less than 1 nm distance to the nanowire surface. Attachment of colloidal nanorods onto ZnO nanowires was also demonstrated by chemical functionalization with poly(2-vinyl pyridine) (figure 1.13d) [141]. However, a key challenge in the field still remains the availability of approaches leading to a simultaneous control on particle shape, size and density along the semiconductor nanowire.

1.4. Classical theory of plasmonic

The interaction of a propagating electromagnetic wave with metals can be reasonably described within the framework of classical electrodynamics based on the Maxwell's equations. Interestingly, also in the case of metal structures with nano-sized dimensions, a quantum mechanic formulation is usually not required. The high density of free electrons in metals (on the order of 10^{22} - 10^{23} cm^{-3} [145]) and the consequent small spacing between the energy levels compared to room temperature thermal energy $k_B T$ confers a *classical* nature to the metal behavior and quantum effects become observable only in highly-confined systems such as metal nanocrystals below 10 nm [146]. In this section the *quasi-free electron gas approximation* or *Drude approximation* will be presented to describe the electronic system in metals and coherent oscillations in the Drude electron gas called *plasmons* will naturally arise from the solutions of the Maxwell's equations with the appropriate boundary conditions.

1.4.1. Quasi-free electron gas approximation

We thus take as a starting point the general formulation of the Maxwell's equations relating the dielectric displacements field \mathbf{D} , the electric field \mathbf{E} , the magnetic field \mathbf{H} and the magnetic induction \mathbf{B} in the following form

$$\left\{ \begin{array}{l} \nabla \cdot \mathbf{D} = 0 \\ \nabla \cdot \mathbf{B} = 0 \\ \nabla \times \mathbf{E} = -\frac{\partial \mathbf{B}}{\partial t} \\ \nabla \times \mathbf{H} = \frac{\partial \mathbf{D}}{\partial t} \end{array} \right. \quad (1.1)$$

where we restrict to the case of absence of any external charge and currents. In linear, isotropic and nonmagnetic media the displacement field and magnetic field are further linked to the electric and magnetic induction fields via

$$\begin{aligned} \mathbf{D} &= \epsilon_0 \mathbf{E} + \mathbf{P} = \epsilon_0 \epsilon(\omega) \mathbf{E} \\ \mathbf{H} &= \mu_0 \mu \mathbf{B} \end{aligned} \quad (1.2)$$

with \mathbf{P} the polarization vector, describing the electrical dipole per unit of volume inside the material. The last important constitutive equation is the one between the internal current \mathbf{J} and the electric field \mathbf{E} defined by

$$\mathbf{J} = \sigma \mathbf{E} \quad (1.3)$$

where σ is the conductivity. Combining the expression for the charge conservation ($\mathbf{J} = \partial \mathbf{P} / \partial t$) with eq.(1.2) and taking the Fourier transform in time we derive the fundamental relationship between the dielectric function and the conductivity

$$\epsilon(\omega) = 1 + \frac{i\sigma(\omega)}{\epsilon_0\omega} \quad (1.4)$$

At low frequencies ϵ describes the electrical polarization arising from the response of bound charges to the driving field, while σ describes the contribution of free charges to the current flow.

In general, the properties of metals are described by a complex dielectric function $\epsilon(\omega) = \epsilon' + i\epsilon''$ and a complex conductivity $\sigma(\omega) = \sigma' + i\sigma''$ linked via eq.(1.4). An analytical expression for $\epsilon(\omega)$ can be formulated within the approximation of a quasi-free electron gas. Over a wide range of frequencies, the optical properties of a metal can be explained by assuming a gas of electrons of number density n moving against a fixed background of positive ion cores. The electron collisions with other electrons, phonons and crystal defects that dampen oscillations under an applied electromagnetic field are included in a characteristic collision frequency $\Gamma = 1/\tau$ with τ (relaxation time) typically on the order of 10^{14} s. The equation of motion for an electron in a plasma subjected to an external electric field \mathbf{E} is [57]

$$m_e \ddot{\mathbf{x}} + m_e \Gamma \dot{\mathbf{x}} = -e \mathbf{E} \quad (1.5)$$

with m_e the effective mass of the electrons. The solution $\mathbf{x}(t)$ of eq.(1.5) with an applied oscillating field $\mathbf{E}(t) = \mathbf{E}_0 e^{-i\omega t}$ induces a macroscopic polarization due to the electron displacement $\mathbf{P} = -ne\mathbf{x}$ explicitly given by

$$\mathbf{P} = -\frac{ne^2}{m_e(\omega^2 + i\Gamma\omega)} \mathbf{E} \quad (1.6)$$

and the associated dielectric displacement

$$\mathbf{D} = \epsilon_0 \left(1 - \frac{\omega_p^2}{\omega^2 + i\Gamma\omega} \right) \mathbf{E} \quad (1.7)$$

where $\omega_p^2 = ne^2/\epsilon_0 m_e$ is the *plasma frequency* of the free electron gas. Therefore, by comparison of eq.(1.7) with eq.(1.2) we derive the dielectric function for the free electron gas :

$$\epsilon(\omega) = 1 - \frac{\omega_p^2}{\omega^2 + i\Gamma\omega} \quad (1.8)$$

that can be conveniently written in the standard form $\epsilon(\omega) = \epsilon' + i\epsilon''$ with

$$\begin{aligned} \epsilon' &= 1 - \frac{\omega_p^2}{\omega^2 + \Gamma^2} \\ \epsilon'' &= \frac{\omega_p^2 \Gamma}{\omega(\omega^2 + \Gamma^2)} \end{aligned} \quad (1.9)$$

Since in the typical experimental conditions $\Gamma \ll \omega_p$, three frequency regions with well-defined optical properties can be distinguished [147].

In the *non-relaxation region* ($\omega \ll \Gamma \ll \omega_p$) the dielectric function becomes

$$\epsilon(\omega) \approx -\frac{\omega_p^2}{\Gamma^2} + i\frac{\omega_p^2}{\omega\Gamma} \quad (1.10)$$

We observed that at low frequency ($\omega \rightarrow 0$) ϵ' remains negative and constant and $|\epsilon''| \gg |\epsilon'|$. Therefore in this region metals are mainly absorbing with a penetration dept $\delta(\omega) \approx \frac{c}{\omega_p} \sqrt{2\Gamma/\omega}$ on the order of 100 nm [147].

For gold $\Gamma \sim 50$ THz [148], therefore visible wavelengths (frequencies in the range 430-750 THz) belong to the second region called *relaxation region* where $\Gamma \ll \omega \ll \omega_p$ and the dielectric function can be approximated as

$$\epsilon(\omega) \approx 1 - \frac{\omega_p^2}{\omega^2} + i\frac{\omega_p^2 \Gamma}{\omega^3} \quad (1.11)$$

In this region ϵ' is still negative and $|\epsilon'| \gg |\epsilon''|$ thus suggesting a substantial reduction of the absorption. However interband optical transitions not included in this simple model can modify the metal response by increasing the absorption already in the visible range of the spectrum.

Finally, for $\omega \gtrsim \omega_p$ we have

$$\begin{aligned}\epsilon' &\approx 1 - \frac{\omega_p^2}{\omega^2} \geq 0 \\ \epsilon'' &\approx \frac{\omega_p^2 \gamma}{\omega^3} \approx 0\end{aligned}\tag{1.12}$$

At frequency larger than the plasma frequency metal acquires a dielectric behavior showing a positive real part of the dielectric function. The imaginary part tends to zero, meaning an increasing in transparency of the material, although the intraband transition not considered here provide a important deviation from this ideal response.

As previously stated, the quasi-free electron gas approximation describes satisfactorily the behavior of real metal in the low frequency regime. At visible frequency the free electron model breaks down due to the occurrence of intraband transition, leading to an increase of ϵ'' (figure 1.14).

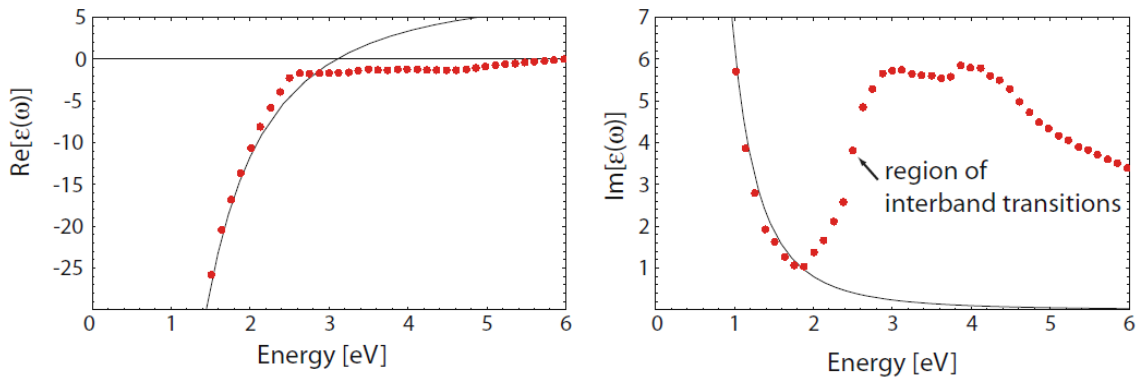


Figure 1.14.: Dielectric function of the free electron gas (solid line) fitted to the literature values of the dielectric data for gold [149] (dots). Interband transitions limit the validity of this model at visible and higher frequencies [57]

However, the inadequacy in describing the optical properties of noble metal at visible frequency can be theoretically overcome by including the contribution of bound electrons resonating at the frequency ω_0 , each per transition, in the equation of motion that leads to a Lorentz oscillator terms in addition to the free electron results [57].

1.4.2. Volume and surface plasmons

In the previous section I showed that the dielectric function of metals has the peculiarity to assume negative values for frequencies below the plasma frequency. This central result affords the possibility to fulfill particular conditions that give rise to resonance oscillations for the free electron gas. We now turn to a description of how the electron oscillations naturally arise from the application of Maxwell's equations to a system described by the dielectric function in eq.(1.8).

Combining the curl Maxwell's equations eq.(1.1) and taking the Fourier transform in space and time, we can obtain the following equation relating the wavevector \mathbf{k} and the frequency ω of the propagating wave with the electric field. The dielectric function assumes the form

$$\mathbf{k}(\mathbf{k} \cdot \mathbf{E}) - k^2 \mathbf{E} = -\epsilon(\omega) \frac{\omega^2}{c^2} \mathbf{E} \quad (1.13)$$

According to eq.(1.13) two type of waves are allowed to occur. For transverse wave ($\mathbf{k} \perp \mathbf{E}$) the general dispersion relation

$$k^2 = \epsilon(\omega) \frac{\omega^2}{c^2} \quad (1.14)$$

and using the metal dielectric function in the form of eq.(1.8) in the approximation of negligible damping we arrive to the dispersion law for the undamped free electron gas

$$\omega^2 = c^2 k^2 + \omega_p^2 \quad (1.15)$$

implying propagation of transverse electromagnetic waves only with frequency $\omega > \omega_p$, as expected from the dielectric nature of the free electron gas in this frequency region. When $\epsilon(\omega) = 0$, longitudinal wave ($\mathbf{k} \parallel \mathbf{E}$) is allowed to occur. In a ideal free electron gas this condition is satisfied at $\omega = \omega_p$. However also in a free electron gas with small damping the dielectric function tends to zero at the plasma frequency. Due to the vanishing dielectric function, from eq.(1.2) we obtain the relation between \mathbf{P} and \mathbf{E} for a longitudinal mode

$$\frac{\mathbf{P}}{\epsilon_0} = -\mathbf{E} \quad (1.16)$$

which means that a longitudinal wave occurs by means of a pure depolarization field in the plasma. In this case all the electrons oscillate in phase at the frequency ω_p . The quantum of this oscillation is called *volume plasmon*. An important observation is that because of the longitudinal character of these oscillations, volume plasmons cannot be directly excited by standard optical excitation, since the longitudinal wave does not couple with a transverse one.

There is another type of wave which is important in metal optics. This is a transverse magnetic wave confined at the metal-dielectric interface also called *surface plasmon polariton* (SPP). It is important to notice that the existence of this mode strictly requires a negative dielectric function in one of the two material involved.

I assume for simplicity the geometry schematically sketched in figure 1.15a. Two slabs of different materials characterized by a dielectric function $\epsilon_1(\omega)$ and $\epsilon_2(\omega)$ respectively, are superimposed along the z -direction forming an interface at $z=0$. Specifically, for a wave propagating along the x -direction showing no spatial variation along the y -direction ($\frac{\partial}{\partial y} = 0$) described by an electric field varying only in the z -direction in the form $\mathbf{E}(x, y, z) = \mathbf{E}(z)e^{-ik_x x}$, the solution of the curl Maxwell's equations should satisfy the following conditions that define a transverse magnetic mode with only E_x, E_z and H_y components non-zero

$$\begin{cases} E_x = -i \frac{1}{\omega \epsilon_0 \epsilon} \frac{\partial H_y}{\partial z} \\ E_z = -\frac{k_x}{\omega \epsilon_0 \epsilon} H_y \\ \frac{\partial^2 H_y}{\partial z^2} + (k_0^2 \epsilon(z) - k_x^2) H_y = 0 \end{cases} \quad (1.17)$$

with $k_0 = \omega/c$. The third equation in the system 1.17, known as *Helmholtz equation*, admits an explicit solution in the form

$$H_{y,j}(z) = A_j e^{ik_x x} e^{(-1)^j k_z z} \quad (1.18)$$

with j labeling the non-absorbing half-space for $z > 0$ ($j = 1$) and the adjacent conductive half space for $z < 0$ ($j = 2$). From the continuity of the tangential

component of the electric field at the interface we arrive to the condition

$$\frac{k_{z2}}{k_{z1}} = -\frac{\epsilon_2}{\epsilon_1} \quad (1.19)$$

that can be satisfy only if one of the two dielectric constant is negative, therefore the interface between a metal an a dielectric in the range of frequencies $\omega < \omega_p$ supports this type of evanescent wave. From the Helmholtz equation we also obtain

$$\begin{aligned} k_{z1}^2 &= k_x^2 - k_0^2 \epsilon_1 \\ k_{z2}^2 &= k_x^2 - k_0^2 \epsilon_2 \end{aligned} \quad (1.20)$$

and combined with eq.(1.19) we arrive to the dispersion relation of SPP

$$k_x = k_0 \sqrt{\frac{\epsilon_1 \epsilon_2}{\epsilon_1 + \epsilon_2}} \quad (1.21)$$

According to the eq.(1.21), propagating polaritons have the wavevector real and positive only if

$$\epsilon_2(\omega) < -\epsilon_1(\omega) \quad (1.22)$$

For a metal/air interface and within the approximation of free electron gas with a small damping, the dispersion relation becomes

$$k_x = k_0 \sqrt{\frac{1 - \frac{\omega_p^2}{\omega^2}}{2 - \frac{\omega_p^2}{\omega^2}}} \quad (1.23)$$

and the condition 1.22 is fulfill for $\omega < \frac{\omega_p}{\sqrt{2}} \equiv \omega_{sp}$.

Figure 1.15b shows the overall dispersion function. For $\omega > \omega_p$ metal support normal transversal wave with dispersion law $\omega^2 = ck^2 + \omega_p^2$. In the range $\omega_p > \omega > \omega_{sp}$ the k_x wavevector is imaginary, prohibiting propagation to exist. For $\omega < \omega_{sp}$ surface plasmon polaritons are allowed to occur. Notably, the SPP dispersion curve lies under the light line therefore excitation by standard light beam is not allowed unless special phase-matching techniques are used. In the limit of low frequency $(\omega_p/\omega)^2 \gg 1$ (mid-infrared or lower) the SPP dispersion tends to the light dispersion and the waves extend over many wavelengths into the dielectric space. On the other

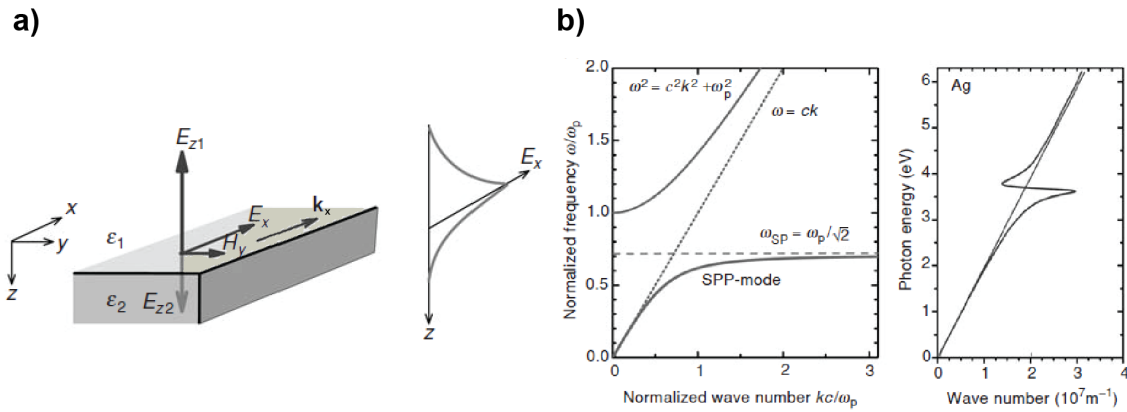


Figure 1.15.: a) Representation of a metal-dielectric interface and the evanescent electric field along z -direction. b) Surface plasmon polariton dispersion curve for an ideal free electron gas (left) and a realistic silver/air interface (right). [145].

hand, for frequencies approaching ω_{sp} the group velocity tends to zero and the wavevector $k_x \rightarrow \infty$. Because the SPP field decays as $e^{-|k_z||z|}$ in the dielectric with k_z given by eq.(1.24), a propagating wave can be confined below the diffraction limit of half of the wavelength in the dielectric for ω approaching ω_{sp} . It should be noticed that if we include the damping in the free electron gas model, k_x is in general complex, so the traveling SPP are damped with a propagation length $L \sim \text{Im}[k_x]^{-1}$, typically between 10-100 μm in the visible range. Finally we observed that for $k_x \rightarrow \infty$ the surface polariton acquire an electrostatic character, known as *surface plasmon*. Thus, surface plasmon can be also obtained from the solution of Laplace equation at the specific *resonant* frequency $\omega = \omega_{sp}$ [57]. This particular behavior, that represent an ideal limiting case for SPP, becomes the dominant effect when the metal volume considered is much smaller than λ^3 . We will discuss this interesting case in the following section.

1.4.3. Localized surface plasmons

Surface plasmon polaritons are propagating dispersive electromagnetic wave confined at the metal/dielectric interface in systems with dimensions larger than the wavelength. When the electron gas is confined in volumes $V \ll \lambda^3$ the plasma experiences a nearly space-independent external field (*quasi-static approximation*)

and modes arises naturally from the solution of Laplace equation $\nabla^2\Phi = 0$ with Φ the electrical potential. Due to the non-propagating nature of these modes they are known as *localized surface plasmons*. The effective restoring force exerted on the oscillating electronic system by the curved surface leads to resonances that amplify the field both inside and in the near-field zone outside the metal nanostructure. Moreover, another interesting consequence of the curvature is the possibility to excite directly the surface plasmons without phase-matching techniques [57].

For the highly-symmetric geometry of an homogeneous sphere in the quasi-static approximation, the spatial electric field distribution can be easily calculated analytically solving the Laplace equation in spherical coordinates and assuming the particle in an electrostatic field. In this approximation, once the spatial distribution of the field is known, the time-harmonic dependence can be added by including the term $e^{i\omega t}$ in the solution of Laplace equation.

We now consider a spherical particle with radius a ($2a \ll \lambda$) and dielectric function $\epsilon(\omega)$ immersed in a homogeneous, non-absorbing medium with dielectric function ϵ_m and an applied static electric field $\mathbf{E} = E_0\mathbf{z}$. By solving Laplace equation with appropriate continuity conditions of electric and displacement fields at the sphere surface, the electric fields inside \mathbf{E}_{in} and outside \mathbf{E}_{out} the sphere are [57]

$$\begin{aligned}\mathbf{E}_{in} &= \frac{3\epsilon_m(\omega)}{\epsilon(\omega) + 2\epsilon_m(\omega)}\mathbf{E}_0 \\ \mathbf{E}_{out} &= \mathbf{E}_0 + \frac{3\mathbf{n}(\mathbf{n} \cdot \mathbf{p}) - \mathbf{p}}{4\pi\epsilon_0\epsilon_m r^3}\end{aligned}\tag{1.24}$$

where \mathbf{n} the unit vector in the direction of the the observation point and $\mathbf{p} = \epsilon_0\epsilon_m\alpha\mathbf{E}_0$ the dipole moment with the polarizability α given by

$$\alpha = 4\pi a^3 \frac{\epsilon(\omega) - \epsilon_m}{\epsilon(\omega) + 2\epsilon_m}\tag{1.25}$$

We notice that \mathbf{E}_{out} has two terms, one is the external applied field and the second has the symmetry of a dipole field located in the center of the particle with a magnitude proportional to $|\mathbf{E}_0|$ and a frequency dependence given by $\epsilon(\omega)$ (we neglect the frequency dependence of the dielectric medium). In particular it is apparent that the polarizability experiences a resonant enhancement in correspondence of the minimum of $|\epsilon(\omega) + 2\epsilon_m|$ that leads to

$$\text{Re}[\epsilon(\omega)] = -2\epsilon_m \quad (1.26)$$

that is called *Fröhlich condition* and the associated mode the *dipole surface plasmon*. Using the dielectric function for a free electron plasma, the resonance frequency that verifies eq.(1.26) is

$$\omega_{lsp} = \frac{\omega_p}{\sqrt{1 + 2\epsilon_m}} \quad (1.27)$$

From this relation it is also evident that the resonance red-shifts as ϵ_m increases. This properties has been vastly explored for detecting changes in the refractive index of the surrounding medium for sensing applications.

Because in the quasi static approximation the spatial retardation effects are neglected, the oscillating dipole induced by an incident plane-wave $\mathbf{E}(\mathbf{r}, t) = \mathbf{E}_0 e^{i\omega t}$ can be written as $\mathbf{p}(t) = \epsilon_0 \epsilon_m \alpha \mathbf{E}_0 e^{i\omega t}$ leading to a scattering of the incident wave. The total field associated with the oscillating dipole has the form $\mathbf{H}(t) = \mathbf{H}_p e^{i\omega t}$ and $\mathbf{E}(t) = \mathbf{E}_p e^{i\omega t}$ and in the near-field zone ($kr \gg 1$) can be approximated as [150]

$$\begin{cases} \mathbf{E}_p = \frac{3\mathbf{n}(\mathbf{n} \cdot \mathbf{p}) - \mathbf{p}}{4\pi\epsilon_0\epsilon_m} \frac{1}{r^3} \\ \mathbf{H}_p = \frac{i\omega}{4\pi} (\mathbf{n} \times \mathbf{p}) \frac{1}{r^2} \end{cases} \quad (1.28)$$

The electric field shows a fast spatial decay $\sim r^{-3}$ with the distance from the metal surface. On the other hand, in the radiation zone for $kr \ll 1$ the dipole radiation is well approximated by a spherical wave

$$\begin{cases} \mathbf{H}_p = \frac{ck^2}{4\pi} (\mathbf{n} \times \mathbf{p}) \frac{e^{ikr}}{r} \\ \mathbf{E}_p = \sqrt{\frac{\mu_0}{\epsilon_0\epsilon_m}} \mathbf{H} \times \mathbf{n} \end{cases} \quad (1.29)$$

The scattering and absorption cross sections can be obtained by dividing the scattering and absorption energy rate by the incident light intensity, leading to [150]

$$\begin{aligned}
 C_{sca} &= \frac{k^4}{6\pi} |\alpha|^2 \\
 C_{abs} &= k \text{Im}[\alpha]
 \end{aligned}
 \tag{1.30}$$

and extinction cross section $C_{ext} = C_{abs} + C_{sca}$. Because $\alpha \sim a^3$, the scattering cross section scales with a^6 while the absorption cross section with a^3 . Therefore, small nanoparticles have the absorption cross section larger than the scattering cross section. Typically the crossover takes place for nanoparticles with diameter of 40-50 nm.

For a metal nanostructure with the more general ellipsoidal geometry with semi-axes $a_1 \leq a_2 \leq a_3$, Gans formulation [151] of the analytical solution for the Laplace equation in the quasi-static approximation leads to the following expression for the polarization [152]

$$\alpha_\nu = 4\pi a_1 a_2 a_3 \frac{\epsilon(\omega) - \epsilon_m}{3\epsilon_m + 3L_\nu(\epsilon(\omega) - \epsilon_m)}
 \tag{1.31}$$

with

$$L_\nu = \frac{a_1 a_2 a_3}{2} \int_0^\infty \frac{ds}{(a_\nu^2 + s)\xi(s)}
 \tag{1.32}$$

where $\xi(s) = \sqrt{(s + a_1^2)(s + a_2^2)(s + a_3^2)}$ and $\sum_i L_i = 1$. Therefore, an ellipsoidal metal structure experiences multiple resonances when

$$\text{Re}[3\epsilon_m + 3L_i(\epsilon(\omega) - \epsilon_m)] = 0
 \tag{1.33}$$

and substituting the dielectric function for an ideal free electron gas we arrive to the expression of the localized surface plasmon resonance frequencies

$$\omega_{lsp,\nu} = \omega_p \sqrt{\frac{1}{1 + \epsilon_m \frac{1-L_\nu}{L_\nu}}}
 \tag{1.34}$$

Within the class of ellipsoids, spheroids with $a_1 = a_2 < a_3$ are particularly interesting because represent a reasonable approximation to the real geometry of chemically prepared rod-shaped metal nanoparticles. For these non-spherical nanoparticles the polarizability exhibits two spectrally separated plasmon resonances, corresponding

to the oscillation of the electron plasma along the long (\parallel) and short (\perp) axes with frequencies

$$\begin{aligned}\omega_{lsp}^{\parallel} &= \omega_p \sqrt{\frac{1}{1 + \epsilon_m \frac{L_{\parallel}}{L_{\perp}}}} \\ \omega_{lsp}^{\perp} &= \omega_p \sqrt{\frac{1}{1 + \epsilon_m \frac{L_{\parallel} + 1}{2L_{\perp}}}}\end{aligned}\tag{1.35}$$

therefore, because $L_{\parallel} < L_{\perp} < 1$, he have $\omega_{lsp}^{\parallel} \leq \omega_{lsp}^{\perp}$. Numerical solution of the Maxwell's equation of the scattering problem for Au nanorods with more realistic geometry and dielectric function will be presented and discussed in Chapter 2.

1.5. Scope of the thesis

In the framework provided by the field of Plasmonics, colloidal Au rod-shaped nanoparticles (nanorods) have attracted an increasing interest mainly related to the nanosized dimensions, tunable optical properties in the visible and near-infrared region of the spectrum and the easy manufacturing. Although the optical properties arising from plasmonic resonances in these sub-wavelength objects have been extensively investigated in both isolated structures and ensemble of interacting elements, their integration in low dimensional semiconductor-based devices is still hampered by a number of challenges including the reliability and control on particle assembly and lack of theoretical and experimental investigation of physical phenomena in hybrid nanostructures. Therefore, the assembling of Au nanorods into functional optoelectronic devices and their integration in metal nanoparticles-semiconductor hybrid nanodevices, with rational design and engineered properties, is still a vastly unexplored field .

In this thesis we provide a comprehensive *bottom-up* approach in which, starting from a theoretical investigation of optical properties of single and arrays of Au nanorods, we designed and nanofabricated, via novel methodologies, Au nanorods-semiconductor nanowire hybrid nanodevices with expanded optoelectronic capabilities compared to the non-hybrid counterpart.

In particular, in **Chapter 2** the synthesis of Au nanorods by wet chemistry and

modeling of their optical properties by simulation tools will be discussed. The seed-mediated method used to growth Au nanorod and the morphological and optical characterization of the synthesized nanorods are described in details. The second part of the Chapter will be devoted to modeling the optical properties of the available nanorod geometries, including investigations of scattering and absorption cross sections dependence from nanorod size and the influence of a non-homogeneous surrounding medium. Finally, the optical properties of closely-spaced nanorod array in various configurations will be compared.

In **Chapter 3** the assembly of Au nanorods into 1D arrays by E-field assisted deposition will be demonstrated. A systematic investigation of the deposition process of Au nanorods (14×42 nm) capped with hexadecyltrimethylammonium bromide (CTAB) under E-field intensity ranging between 0.12 - 2.22×10^6 V/m and frequency between 100 kHz-55 MHz is presented. Evidence of a frequency dependence of the dielectrophoretic process will be discussed and elucidated by means of a core-shell model. On the basis of the proposed model, a detailed description of the particle dynamics under E-field is presented. Specifically, the contour-plot representation of the calculated dielectrophoretic force allowed the identification of experimental conditions where the assembly process is driven by localized field enhanced hot spots at the nanorods tip thus promoting an head-to-tail assembly. By exploring this scheme of work, reproducible assembly of Au nanorods in 1D arrays with length of 2-5 μm was obtained on Si/SiO₂ and quartz substrates.

In **Chapter 4** we report enhanced detection of ZnO surface optical Raman mode by exploitation of plasmonic resonances of Au nanorods deposited on ZnO nanowire surface. In particular, we present a novel mask-selective droplet deposition method for reproducible fabrication of hybrid structures constituted by Au nanorods deposited on ZnO nanowire surfaces. Detection of surface optical mode was observed under excitation of the Au nanorod longitudinal plasmon resonance while no detectable signal was found mediated by the transversal plasmon resonance. Moreover, the excitation wavelength corresponding to the maximum enhancement of the Raman mode was intentionally shifted by tuning the optical properties of Au nanorods, thus proving the plasmonic nature of the Raman enhancement observed. Finally, theoretical simulations were performed to support experimental findings. The

presented study provides evidence of the capabilities offered by longitudinal plasmonic resonance of Au nanorods for Raman spectroscopy investigation of individual semiconductor nanowires and corroborates the increasing interest of metal nanostructures - semiconductor nanowire hybrid structures for optoelectronic and sensing applications.

In **Chapter 5** the nanofabrication and a detailed electrical characterization of ZnO nanowire field-effect transistors (ZnO NW-FET) is presented. Optimization of the electrode geometry and the optical lithographic process allowed to fabricate large number (>30) of ZnO NW-FETs per substrate. Metal-ZnO nanowire ohmic contacts with contact resistivity of $10^{-11} - 10^{-10} \Omega \cdot \text{m}^2$ were realized using Ti/Al electrodes thus allowing to assess the intrinsic electronic properties of the ZnO nanowires. The devices resistance was investigated in different atmosphere (air and high vacuum) including the effect of rapid thermal annealing and estimation of nanowire resistivity, contact resistance, electron mobility and electron density was also provided. Finally, we explored the three-terminals ZnO NW-FET architecture for two applications. Firstly, we demonstrated that ZnO NW-FET can be successfully used as nano-heater up to more than 300°C and secondly, we propose a novel method to selectively decorate a target nanowire with colloidal nanorods by an engineered electric field configuration using three gates electrodes available in the FET architecture.

Finally in **Chapter 6** we characterized the photoconductivity behavior in ZnO nanowire under radiation with energy larger ($\lambda=265 \text{ nm}$) and smaller ($\lambda=650\text{-}850 \text{ nm}$) than the semiconductor band-gap in air and vacuum conditions. From time-resolved measurement under UV radiation, we demonstrated that the photocarrier generation and recombination response is the result of three processes characterized by different time-scale sensitive to the environment conditions. Detailed analysis of photoresponse to $\lambda=650\text{-}850 \text{ nm}$ radiation in Au nanorod-ZnO nanowire hybrid FET devices will be presented. In particular we demonstrated orders of magnitude enhancement in the photocurrent intensity in the explored range of wavelengths and 40 times faster time response. The improved performance were attributed to the plasmonic-mediated hot-electron generation and injection mechanism underlying the photoresponse. The proposed mechanism responsible for the improved performance demonstrated in hybrid devices is investigated both experimentally and theoretically.

Chapter 2.

Synthesis and optical properties of Au nanorods

In this Chapter the synthesis of Au nanorods by wet chemistry and modeling of their optical properties by simulation tools will be discussed. In section 2.2 seed-mediated method used to growth Au nanorod and the morphological and optical characterization of the synthesized nanorods are described in details. Section 2.3 will be devoted to modeling the optical properties of the available nanorod geometries, including investigation of scattering and absorption cross sections dependence from nanorod size and influence of non-homogeneous surrounding medium. Finally, optical properties of closely-spaced nanorod array in various configurations will be compared.¹

2.1. Introduction

Metal nanostructures have been successfully fabricated by both top-down and bottom-up approaches. Among top-down approaches, electron beam lithography is the most utilized fabrication technique [53]. It allows high degrees of freedom in geometries and control on the nanostructure positioning. These capabilities have been exploited to realize different geometries such as spherical particles, bowtie and rectangular antennas arrays used for demonstrating single molecular detection, non-linear optical phenomena and surface-enhanced Raman spectroscopy [14, 32, 18, 153]. Moreover,

¹Simulations presented in section 2.3 were published in *J. Phys. Chem. C*, 118(24),13260-13267, (2014); *J. Mater. Chem. C*, 2, 3536-3541, (2014); *Langmuir*, 30(34), 10206-10212, (2014)

in metal nanostructure arrays, this technique allows studies on maximization of field enhancement and collective phenomena through appropriate geometrical design. For instance, Dal Negro and co-workers demonstrated two orders of magnitude improvement in surface-enhanced Raman scattering measurements reachable by optimization of array geometries [154] and Liu *et al.* showed evidence of magnetic plasmon resonances in gold nanoparticles organized in heptamer-like structures (also called *artificial aromatic molecules*) [75]. However, top-down approach is not exempt from limitations. The resolution of the lithography process (~ 20 nm) prevents investigation of metal nanostructure behavior in the quantum regime (sub-10 nm sized structures) [146] and studies of enhancing phenomena in arrays with inter-particle distance below 10 nm (strongly-coupled regime) that would offer interesting opportunities for catalysis, quantum optics and sensing [155]. Other drawbacks of this technique includes the polycrystallinity of the nanostructures, the presence of an additional layer required to ensure the adhesion to the substrate (usually titanium or chromium) and prohibitive costs that prevents any integration into commercial devices.

The bottom-up synthetic approach constitutes a valid alternative as it addresses most of the limitations of the top-down approach. In particular, particle size can be scaled-down to few nanometers, self-assembling techniques allow inter-particle distance below 10 nm and cost production is greatly reduced. Despite different processes proposed such as electrochemical method [54], photochemical reduction [56], template method [55], the most popular method for the synthesis of colloidal nanorods is the seed-mediated growth. The success of this method derives from the simplicity of the procedure, high yield of reasonable monodispersity structures and fine tunability of nanorod size. Jana *et al.* in 2001 first reported anisotropic growth of citrated-capped gold seeds in HAuCl_4 solution containing hexadecyltrimethylammonium bromide (CTAB) and silver ions by addition of ascorbic acid reducing agent [52]. However the yield of this process was poor and the large fraction of gold nanospheres formed as reaction by-products impose time-consuming centrifugation steps to separate out nanorods. Later in 2003, El-Sayed *et al.* substantially improved the seed-mediated synthesis reaching a yield of almost 99% by replacing the sodium citrate with CTAB stabilizer in the seed solution [51]. Moreover, they showed tun-

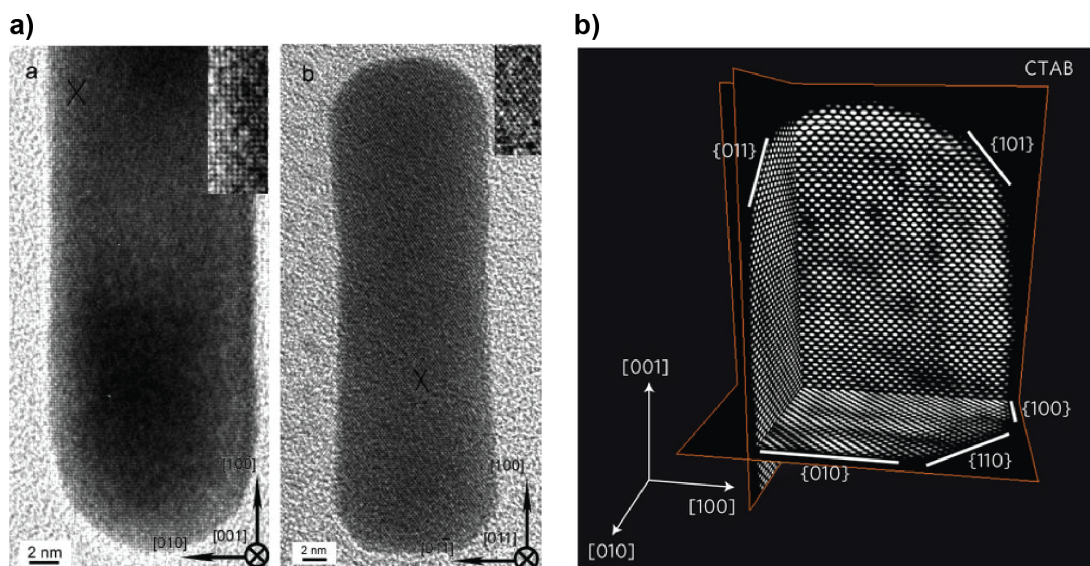


Figure 2.1.: a) High-resolution TEM image of gold nanorods synthesized by seed-mediated method showing nanorod aligned in $[001]$ (a) and $[011]$ (b) directions [156]. b) 3D reconstruction of Au nanorod showing individual atom position. It can be seen that $\{110\}$ and $\{100\}$ facets compose the morphology of the rod [157].

ing of the nanorod aspect ratio between 1.5 and 4.5 by control on the concentration of silver ions in solution. The nanorods obtained were single-crystalline elongated along the $[100]$ direction and having sidewall facets $\{100\}$ and $\{110\}$ as showed in the high-resolution TEM images and the related 3D reconstruction by Goris and co-workers in figure 2.1 [156, 157]. Liu *et al.* observed that, when the growth reaction was terminated prematurely (by adding *n*-dodecanethiol to the solution) most of these nanorods were found showing the $[110]$ side facet [156]. This observation suggests that during the growth, the sidewalls are dominated by $\{110\}$ facets that have higher surface energy respect to the others. Therefore the $\{100\}$ sidewall facets found in the fully grown nanorods were attribute to a later reorganization promoted by the minimization of the surface energy.

Following this observation, the mechanism proposed to explain the anisotropic growth of the original single-crystal seed relied on the key role played by CTAB and Ag^+ on the $\{110\}$ facets. In the proposed mechanism CTA^+ molecules bond preferentially to the sidewall facets due to their higher reactivity thus slowing down the crystal lateral growth respect to the $\{100\}$ end facets (see figure 2.2). Moreover

in the presence of silver ions, underpotential deposition of Ag(0) on the $\{110\}$ facets further reduced the lateral growth offering the possibility to finely tune the nanorod aspect ratio by changing the silver ions concentration [156].

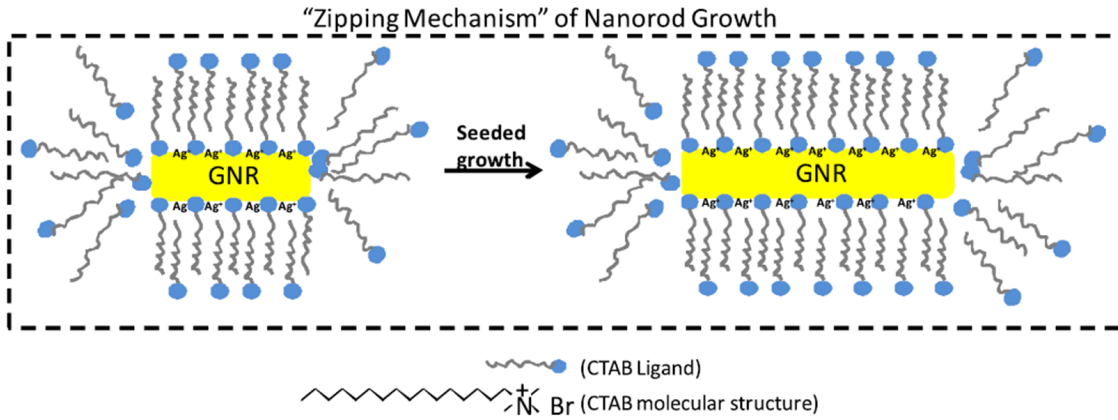


Figure 2.2.: Mechanism of nanorod growth. CTA^+ molecules bind preferentially to the sidewall facets due to the higher reactivity and slow down the crystal lateral growth respect to the $\{100\}$ end facets. Silver ions Ag^+ on the $\{110\}$ facets further reduce the lateral growth [158].

Chemical synthesized spherical and anisotropic metal nanoparticles have been successfully used for molecular detection [153], photodetection [159], molecular electronics [160, 161, 162] and quantum plasmonics [146]. Also, colloidal solution can be integrated in polymer-based matrix thus making them suitable for polymer solar cells [163] and biological applications such as biosensing [164], bioimaging [165] and photothermal therapy [166, 53]. However, the main limitation of this approach derives from the lack of control in the position and organization of colloids when deposited on a substrate. In the last decade self-assembly approaches have been developed to allow organization of nanoparticles in 1D, 2D and 3D arrays (see Chapter 3), but their limitation in particle manipulation and assembling reliability impose further developments of these methodologies for future integration in functional devices. Other additional drawbacks are the broadening of the plasmonic resonances observed in the colloidal solution due to Gaussian distribution in particle size (see section 2.3.2) and the presence of surfactant (CTAB) in solution that has been demonstrated affecting self-assembly processes and damaging other materials in multicomponents devices (see Chapter 3-4).

In this section, we present the synthesis of Au nanorods 14×42 nm with reasonable

monodispersity and reproducibility as well as tunability of the aspect ratio between 1 (spherical particle) and 5.8 (corresponding to a tuning of the longitudinal peak from 520 to 850 nm) by a seed-mediated method. Furthermore, synthesis of Au nanorods 22×54 nm up to 30×70 nm was achieved by adding an overgrowth process to the previous synthesis. The optical properties of the synthesized particles were investigated by UV-vis spectrometer. A systematic method for indirect estimation of the CTAB concentration from the optical spectrum was developed in order to accomplish a reproducible and controlled purification of the synthesized colloidal solution.

2.2. Synthesis and characterization of Au nanorods

2.2.1. Au nanorods with sub-20nm diameter

Au nanorods were synthesized by a standard seed-mediated method described by El Sayed *et al.* [51]. For the seed solution, 5 mL of an aqueous CTAB solution (0.2 M) were mixed with 5 mL of an aqueous HAuCl_4 solution (0.5 mM). To the stirred solution 0.60 mL of ice-cold NaBH_4 (0.010 M) was added, which resulted in the formation of a pale brown solution. Vigorous stirring of the seed solution was continued for 2 min after which the solution was kept at 27 °C. For the growth of nanorods, 140 μl of seed solution was added to an aqueous solution containing CTAB (50 mL, 0.20 M), AgNO_3 (2 mL, 4 mM), HAuCl_4 (50 mL, 1 mM) and ascorbic acid (0.7 mL of 0.0788 M), kept a 27 °C. Upon addition of seeds the color of the solution gradually changed from colorless to dark red (90 -120 min). Excess CTAB was removed by successive steps of centrifugation and re-dispersion in water.

Morphological and optical properties of synthesised Au nanorods were investigated by electron microscopy and UV-vis spectroscopy. Scanning electron microscopy (SEM) images of individual Au nanorods were acquired using a field emission SEM (JSM-7500F, JEOL UK Ltd.) operating at beam voltages of 2-5 kV. Transmission electron microscopy (TEM) images were acquired using a high resolution TEM (2100, JEOL UK Ltd.) operating at beam voltages of 200 kV.

Figure 2.3a-b show a typical SEM and TEM images of Au nanorods obtained from

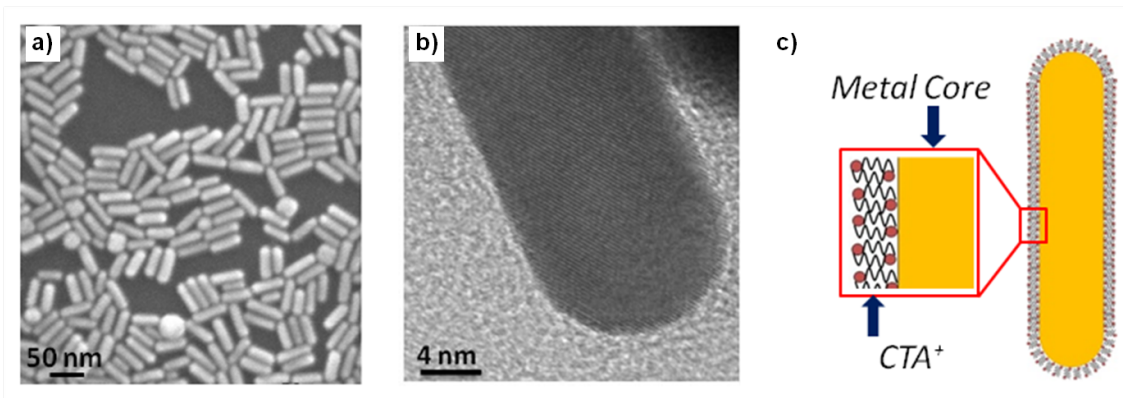


Figure 2.3.: a) SEM image of chemical-synthesized gold nanorods b) TEM image of single nanorod. c) Schematic of the metal rods structures. The Au nanorod has a metal core surrounded by a double layer of organic material (CTA^+) with total thickness of 2-4 nm.

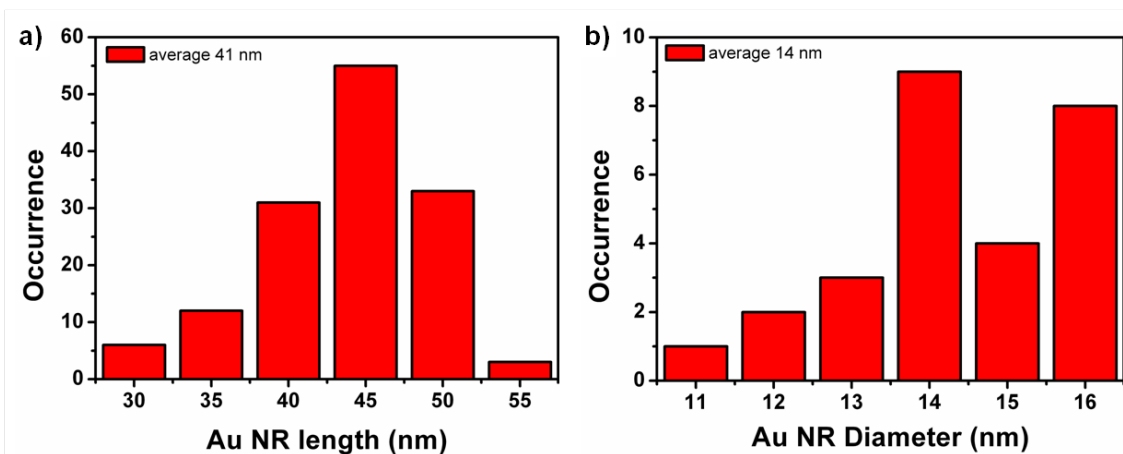


Figure 2.4.: Statistical distribution of a) length and b) diameter of 100 nanorods obtained from TEM images.

water dispersions. It should be noticed that CTAB molecules form an organic double layer around the Au nanorod metallic core, thus stabilizing the nanorods in solution (see schematic of figure 2.3c). The CTAB double layer has been estimated to be around 2-4 nm in thickness [167, 168]. From statistical analysis of 100 nanorods (figure 2.4) the mean nanorod radius and length were calculated to be respectively 14.0 ± 3 nm and 42 ± 5 nm and aspect ratio of 3.0 ± 0.2 , with a reasonably monodispersity; nanorod radius and length distribution are shown in histograms of figure 2.4a,b. Table 2.1 resumes the mean dimensions and aspect ratio obtained for 6 different synthesis. This data confirms that a reasonable reproducibility in dimensions and aspect ratio of AuNRs was achieved by the seed-mediated chemical synthesis approach.

Sample	Mean length (nm)	mean diameter (nm)	aspect ratio
A1	46	12	3.8
A2	48	14	3.4
A3	45	16	2.8
A4	55	21	2.6
A5	33	9	3.7
A6	41	13	3.2

Table 2.1.: Mean length, diameter and aspect ratio for 6 colloidal solution synthesized as described in the section 2.2.1.

Optical properties of as-prepared Au nanorods were investigated using UV-vis Agilent 8453 spectrophotometer. The absorbance spectrum of figure 2.5 was characterized by a transversal plasmon peak at 520 nm and a longitudinal plasmon peak at 764 nm. It is well known that the transversal mode is weakly dependent from the nanorod geometry whereas the longitudinal peak is extremely sensitive to the nanorod aspect ratio R . Literature data report that the aspect ratio of Au nanorods can be controlled by the amount of AgNO_3 added to the growth solution during the nanorods growth synthetic step [51]. In particular we have found experimentally that at low concentration ($65 \mu\text{l}/100$ ml) the anisotropic growth of the seed is totally suppressed and only particles were found in the final solution. At higher concentration (2.5 ml/100 ml) instead an increase of the aspect ratio was observed. I have performed three synthesis using respectively 0.016, 2 and 2.5 ml

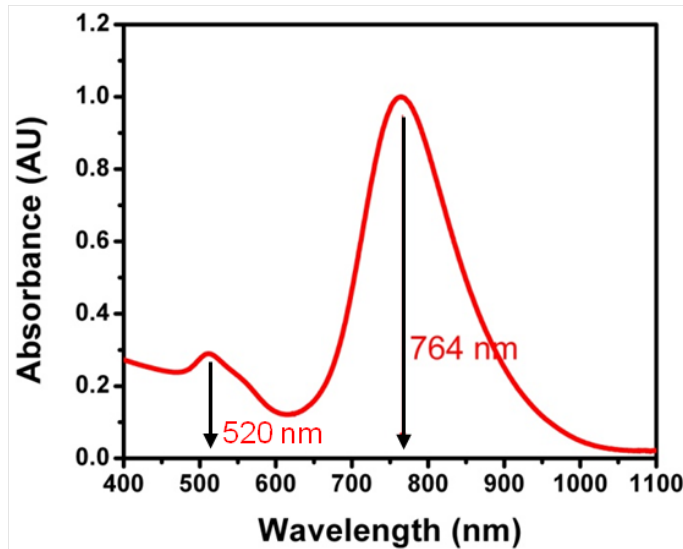


Figure 2.5.: Typical absorbance spectrum of chemical-synthesized gold nanorods with aspect ratio ~ 3 .

of a solution 4 mM AgNO_3 . The experimental results are summarized in the table 2.2. The nanorod aspect ratio was modulated from 1 (spherical particle) up to 5.8, corresponding to a tuning of the longitudinal peak from 520 to 850 nm. The Ag^+ ions prevent the radial growth of the seeds (~ 4 nm in diameter) during the growth, as demonstrated in the table 2.2. Consequently the R values reachable with this approach cannot exceed 7-8. Higher control in nanorod dimension and aspect ratio require more complex synthesis with multi-overgrowth steps [52].

Sample	AgNO_3 (ml)	Mean length (nm)	mean diameter (nm)	aspect ratio
A8	0.016	–	15	1
A1	2	46	12	3.8
A12	2.5	35	6	5.8

Table 2.2.: Mean length, diameter and aspect ratio for 3 colloidal solution synthesized as described in the section 2.2.1 with different AgNO_3 concentration.

2.2.2. Au nanorods with diameter above 20nm

Au nanorods with diameter above 20 nm were synthesized by a standard seed-mediated method described by Alvarez-Puebla *et al.* [169]. For the seed solution,

2.2. Synthesis and characterization of Au nanorods

3.75 ml of an aqueous CTAB solution (0.2 M) were mixed with 1.25 ml of an aqueous HAuCl_4 solution (1 mM). To the stirred solution 0.3 ml of ice-cold NaBH_4 (0.01 M) was added, which resulted in the formation of a pale brown solution. Mild stirring of the seed solution was continued for 40 min after which the solution was kept at 30 °C. For the growth of nanorods, 35 μl of seed solution was added to an aqueous solution containing CTAB (12.5 ml, 0.20 M), AgNO_3 (0.5 ml, 4 mM), HAuCl_4 (25 ml, 1 mM) and ascorbic acid (0.35 ml of 0.0788 M), kept a 30°C. Upon addition of seeds the color of the solution gradually changed from colorless to dark red (10-40 min). After 1 hour, overgrowth of standard nanorods was carried out by addition of ascorbic Acid 0.0788 M in drops of 5 μl every 5 minutes. The ascorbic acid was added until the intensity of the longitudinal peak reached the saturation. This condition was usually verified with addition of 80-120 μl of ascorbic acid.

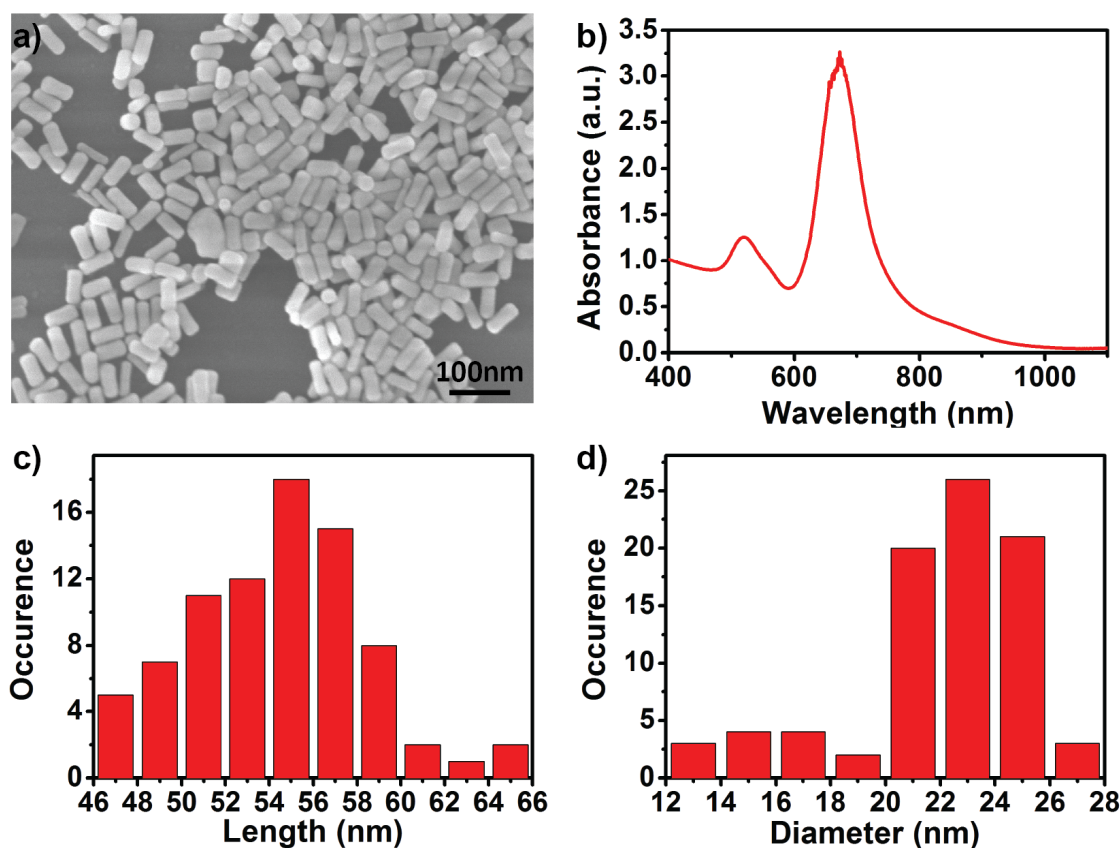


Figure 2.6.: a) Scanning electron microscopy of the synthesized metal nanorods with diameter above 20 nm used in Chapter 4 and 6 b) Absorption spectrum of the colloidal solution. Statistical distribution of a) length and b) diameter.

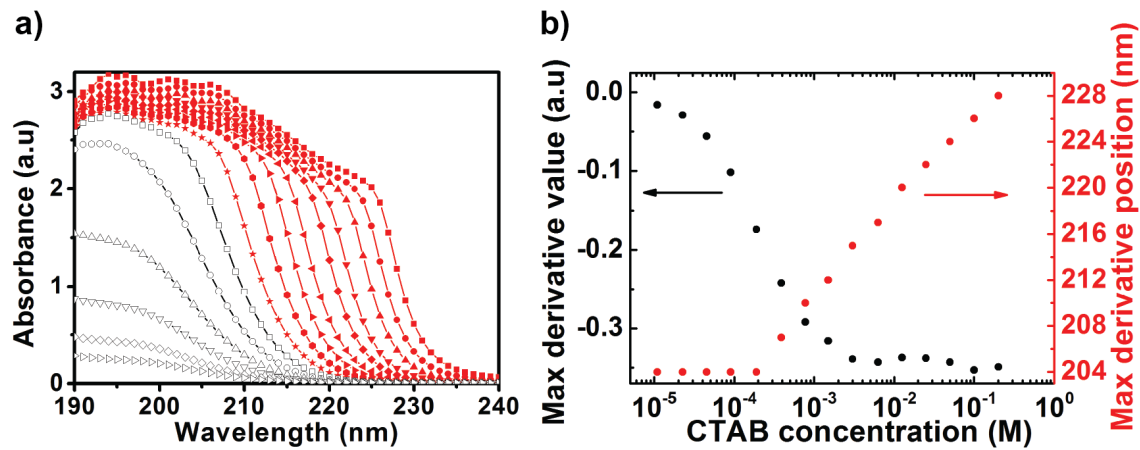


Figure 2.7.: a) Absorbance spectra of solutions with different concentration of CTAB
 b) Dependence of the maximum value of the absorbance derivative and its peak position as a function of the CTAB concentration.

Excess CTAB was removed by successive steps of centrifugation and re-dispersion in water (see section 2.2.3).

Figure 2.6a show a typical SEM of Au nanorods obtained from water dispersions. From statistical analysis of 100 nanorods the mean nanorod radius and length were calculated to be respectively 22 ± 3 nm and 54 ± 3 nm and aspect ratio of 2.4 ± 0.4 . Absorbance spectrum of figure 2.6b was characterized by a transversal plasmon peak at 520 nm and a broad longitudinal plasmon peak at 655 nm. It should be noticed that also the mean nanorod dimension varied from batch to batch within the range 20-30 nm in diameter and 50-70 nm in length with a longitudinal resonance peak in the range 650-700 nm.

2.2.3. Purification of colloidal solution for dielectrophoresis

The stability of the colloidal dispersion in solution is a fundamental requirement for any applications involving chemical-synthesized metal particles. Since the CTAB concentration in the growth solution (see section 2.2.1) was much higher than the critical concentration required to avoid cluster formation or precipitation of the final suspension, the excess of the surfactant was removed by means of centrifugation and re-dispersion in ultra-pure water ($18 \text{ M}\Omega\cdot\text{cm}$). In addition, the electric field-mediated assembly discussed in Chapter 3 and the fabrication process of hy-

brid devices in 4 were quite sensitive to ions and molecules in solution, therefore a method to estimate the concentration of CTAB in the colloidal solution was highly desirable to obtain reproducible results.

Absorption spectra of the as-prepared Au nanorods showed a CTAB peak at 200-230 nm whose intensity was related to the CTAB concentration in the nanorod dispersion. Although Au nanorods did not have any resonances at that wavelengths, they added a constant contribution to the absorption resulting in a vertical translation of the spectrum. Therefore, the absolute intensity of the CTAB peak could not be used for estimating the concentration. However, because a vertical translation of the spectrum does not change the peak shape, the derivative of the curve has a magnitude independent from any background contribution.

Following this observation, a calibration curve was realized by measuring the magnitude of the CTAB absorption peak derivative calculated between 190 nm and 300 nm for a series of CTAB solutions of known concentration, as shown in figure 2.7a. CTAB solution with concentration between 0.01 mM and 0.2 M were used. In the test solutions, the peak intensity increased with the CTAB concentration until ~ 3 mM (black symbols in figure 2.7a) than the peak become larger with an intensity almost constant (red symbols in figure 2.7a).

The Critical Micelle Concentration for CTAB was measured to be around 1 mM at 25°C [170], therefore this behavior was attributed to the formation of CTAB micelles after ~ 3 mM that prevent further increase of the free molecules concentration in solution although formation of micelles increase the absorption at longer wavelength. Figure 2.7b shows the module and the wavelength at which the maximum value of the derivative (D_{max}) occurs. The D_{max} increased monotonically until ~ 3 mM and then shifted linearly to longer wavelength. Therefore, it was possible to define a range of CTAB concentration within which D_{max} module and peak position were dependent from CTAB concentration in solution. A polynomial fit was used to find an analytical expression of the CTAB concentration.

A number of tests in different conditions demonstrated that a CTAB concentration larger than ~ 0.02 mM is required to maintain Au nanorods suspended in solution.

2.3. Modeling the optical properties of Au nanorods

Scattering and absorption cross sections of a metal particle with arbitrary shape can be computed by solving the Maxwell's equations with the appropriate boundary conditions. Analytical solutions exist only for highly symmetric spherical [171] and ellipsoidal [172] particles, therefore numerical approximation methods are generally required for non-spherical geometries [173]. Finite-Difference Time Domain (FDTD) method is one of the most powerful and popular method to model light-matter interaction. In this approach Maxwell's equations are discretized in finite-difference equations in space and time and solved self-consistently [174]. This method allows to simulate general inhomogeneous dielectric environment and to obtain, with a single simulation, the response of the system over a wide range of frequencies when a broadband pulse is used as a source. The main drawback of this method is that the discretization of the entire simulation volume with a sufficiently fine grid often requires large computation capabilities and time.

An alternative approach to solve the Maxwell equations was developed by Garcia de Abajo *et al.* in 2002 [175]. The so called Boundary Element Method (BEM) only discretized the boundaries between different dielectric materials, thus reducing substantially the computational requirements. For a given excitation, Maxwell's equations are solved by computing surface charges and currents at the particle boundaries and then calculating the electromagnetic fields and potentials at both the particle boundary and elsewhere. This approach is less general than FDTD in that it assumes dielectric bodies with homogeneous and isotropic dielectric functions separated by abrupt interfaces.

Nevertheless, the absorption spectra of Au nanorods showed in sections 2.2.1 and 2.2.2 referred to optical properties of colloidal solutions that deviated substantially from the properties of isolated or clustered nanorods on Si/SiO₂ substrate considered in this work. Therefore, simulation tools able to predict the optical response in different environment are important for understanding the results presented in Chapter 4 and 6. For this reason FDTD simulations using FDTD Lumerical software were undertaken to elucidate the contribution of both the CTAB layer surrounding the single nanorod and the substrate to the red shift of the plasmonic resonances.

Scattering and absorption cross section of single nanorods with different sizes were analyzed. Also, optical properties in ordered nanorods arrays were investigated by using BEM simulation (MNPBEM Matlab toolbox) [176].

2.3.1. Optical properties of Au nanorods in inhomogeneous environment and effective refractive index approximation

The longitudinal plasmonic resonance in Au nanorods has been demonstrated very sensitive to the geometrical aspect ratio as well as to the refractive index of the surrounding medium. Many authors explored this interesting capability for biological and chemical sensing applications [173]. The plasmonic-based devices discussed in Chapter 4 and 6 require to engineer the optical properties of the nanorods (scattering versus absorption ratio and wavelength at which plasmonic resonances appear) in order to maximize the system efficiency under specific conditions. Despite the fact that nanorods are often modeled as a metal body surrounded by an homogeneous medium with a well defined dielectric constant, inhomogeneities of the surrounding medium can shift the plasmonic resonances with non-negligible contributions [61].

Figure 2.8a-b shows a SEM image of a single Au nanorod with diameter 26 ± 2 nm and length 68 ± 2 nm on ITO substrate and the related dark-field spectra in air. The Au nanorod, synthesized as described in section 2.2.2, were measured in an inverted IX-71 Olympus microscope with an oil immersion dark-field condenser (Olympus U-DCW) and 100X objective. The plasmon resonance was found peaked at 685 nm with a FWHM of 39 nm (transversal plasmonic peak was not detected due to the low scattering cross section of this mode).

Figure 2.9a reports the simulated scattering and absorption cross sections (normalized to the geometrical cross section of the nanorod) for a nanorod having a cylindrical body ended with two hemispherical caps with diameter 26 nm and total length of 68 nm in air (refractive index $n = 1$) with light incident along x-axis and polarized along z-axis. In the simulated spectrum the longitudinal plasmonic resonance was found at 590 nm, more than 100 nm blue-shifted respect to the value measured with the experimental spectrum. It should be noticed that the error on the nanorod dimension generates an error of ~ 20 nm on the peak position.

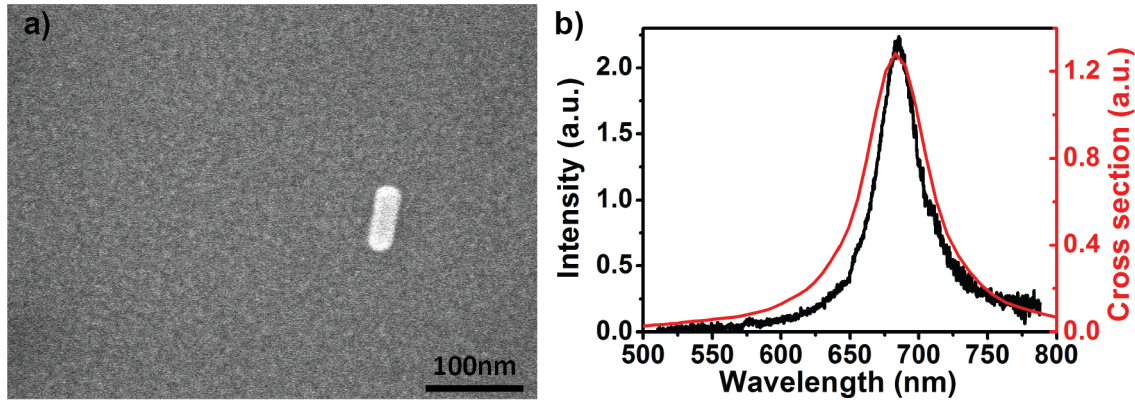


Figure 2.8.: a) SEM image and b) dark-field scattering spectrum of a single Au nanorod having diameter of 26 ± 2 and length 68 ± 2 nm on ITO substrate and the scattering cross section calculated by FDTD simulation (from figure 2.9d).

The red-shift of ~ 100 nm can be attributed to the non-homogeneity of the environment, in particular to the presence of a CTAB double layer on the metal surface and the ITO substrate. In order to address this discrepancy, we first consider the contribution of a dielectric shell around the nanorod. CTAB double layer is expected to form a 2-4 nm shell around the nanorod with a refractive index $n = 1.4$ [167, 177]. Figure 2.9b shows that the longitudinal plasmon resonance red-shifts to 624 nm by adding a 3 nm shell around the nanorod surface.

A variation of 1 nm in the shell thickness shift the peak position of ± 6 nm and a change of 0.14 in the shell refractive index (10% of the nominal value) causes a shift of ± 8 nm in the plasmonic resonance. Secondly, we considered that for a nanorod deposited on ITO substrate ($n = 1.85$ at $\lambda = 650$ nm) a further red-shift is observed. Figure 2.9c reports the longitudinal surface plasmon (LSP) peak at 671 nm, with a variation of ± 6 nm associated to an error of 0.18 in the refractive index of the substrate. It should be noticed that in the simulated geometry we assumed the nanorod in touch with a perfectly flat substrate. However, the roughness of the ITO surface (see SEM image in figure 2.8) does affect the plasmonic resonance, as also reported in the literature [178]. Figure 2.9d shows that embedding the nanorod into the substrate by 2 nm results in a LSP red-shift of 11 nm thus reaching the wavelength of 682 nm. This value is in excellent agreement with the measured spectrum within the error on the nanorod size (see figure 2.8b). A summary of the

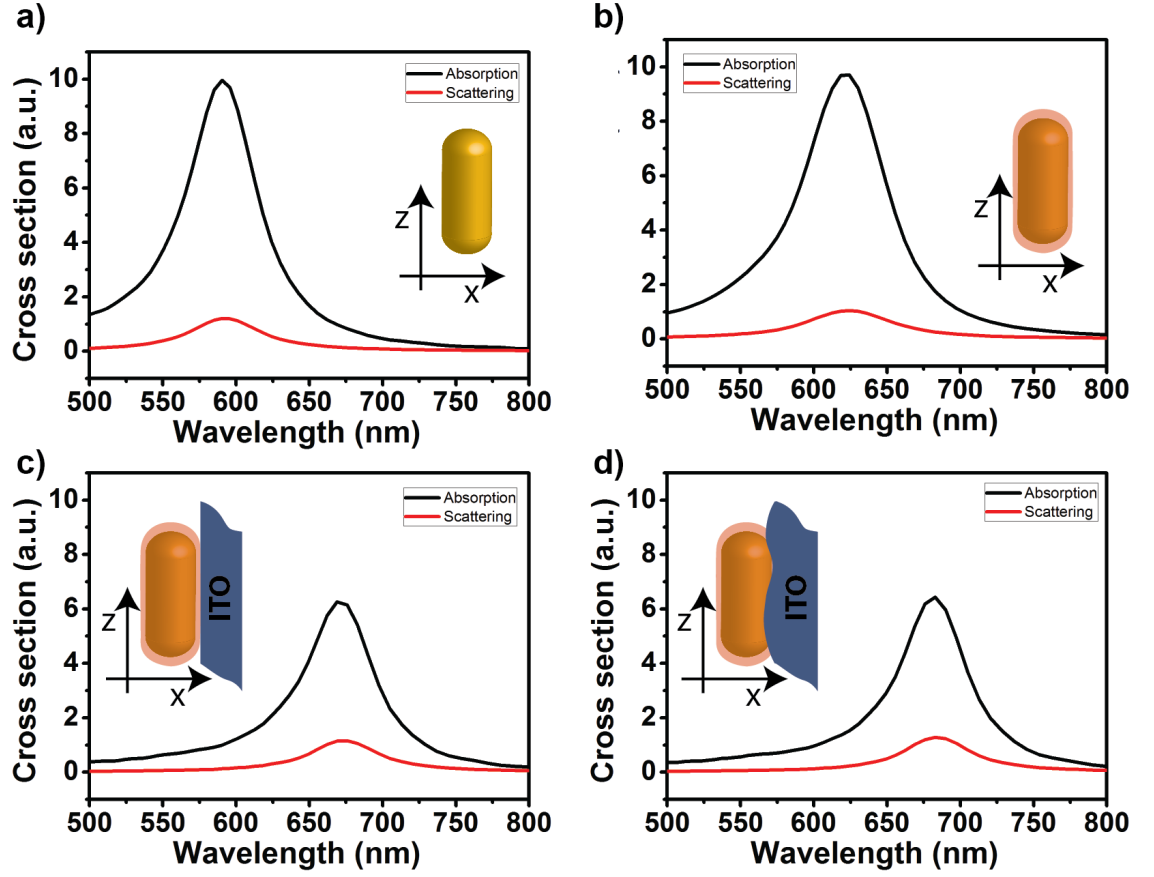


Figure 2.9.: *Finite-difference time domain simulation of the scattering cross section of a Au nanorod with diameter 26 ± 2 and length 68 ± 2 nm a) in air, b) covered by 3 nm of shell with a refractive index ($n = 1.4$), c) covered by 3 nm of shell on ITO substrate ($n_{eff} = 1.85$) and d) partially embedded into the substrate by 2 nm.*

red-shifts calculated related to contributions from the dielectric shell, substrate and substrate roughness together with the change in the longitudinal plasmon resonance associated with the 10% variation of the explored parameters is reported in table 2.3.

We observed that the presence of the substrate affects most the plasmon red-shift respect to the bare nanorod (47 nm shift) followed by the dielectric shell (34 nm shift). Therefore the original discrepancy between the measured and simulated spectrum of the nanorod in air was entirely ascribed to the inhomogeneity of the medium surrounding the particle. Interestingly, despite the number of parameters introduced in the simulation (shell thickness, shell refractive index, substrate refractive index, substrate roughness), the uncertainty of the nanorod dimensions (aspect

	Parameter	LSP position (nm)	Shift (nm)	Variation with 10% of the parameter (nm)
Bare NR		590	–	–
	aspect ratio	–	–	22
NR with shell		624	34	–
	shell thickness			6
	shell refractive index			8
NR with shell on ITO		671	47	
	substrate refractive index			6
	substrate roughness	682	11	2

Table 2.3.: Simulated longitudinal surface plasmon (LSP) resonance position for a bare nanorod (NR) 26×68 nm in air, NR with a 3 nm shell and on ITO substrate. The red-shift of the peak position respect to the bare NR in air is reported as well as the variation of the peak position when the simulation parameters are varied by 10% respect to the specified value.

ratio) due to the resolution of the SEM image, remained as major source of error limiting the accuracy of the simulation.

In order to asses the validity of this simulation tool we compared the scattering spectra of 5 single nanorods obtained by dark-field spectroscopy in figure 2.10 with the simulated scattering cross sections (see table 2.4). The nanorod dimensions, estimated from SEM images, were found in the range of 24-34 nm in diameter and 65-71 nm in length. The related optical scattering spectra showed the longitudinal plasmonic resonance within the interval 637-692 nm with a FWHM between 37-47 nm (calculated from the Lorentzian fit of the curves). For comparison, figure 2.10b reports the absorption spectrum of the entire colloidal solution that shows a longitudinal peak at 655 nm with an FWHM of 64 nm calculated from the Lorentzian fit of the data. We notice that the FWHM value is larger than the FWHM of single nanorods thus indicating that the absorption spectrum of the ensemble is broadened by the size distribution of the particles.

All simulations were performed by assuming the nanorod as a cylinder with two hemispherical caps having a 3 nm dielectric shell with refractive index $n = 1.4$, deposited on ITO substrate ($n = 1.85$) and partially embedded by 2 nm into the substrate as previously described. Dimensions and LSP resonances of the measured

Sample	Mean length ± 2 (nm)	mean diameter ± 2 (nm)	LSP (nm)	FWHM (nm)	Simulated LSP ± 20 (nm)
NR1	65	24	692	37	680
NR2	68	26	685	39	682
NR3	71	34	637	47	624
NR4	67	29	646	40	649
NR5	67	30	639	45	642

Table 2.4.: *Properties of single nanorods investigated by dark-field spectroscopy having scattering spectrum reported in figure 2.10a. The mean length and diameter were measured from the SEM images, longitudinal surface plasmon (LSP) resonance and full-width half maximum (FWHM) of the scattering dark-field spectrum were obtained from the Lorentzian fit of the curves. Simulated LSP resonances were performed with fdtd method.*

nanorods with the peak position of the simulated scattering cross sections were found in excellent agreement with the experimental data and are reported in table 2.4. It is relevant for the content of this thesis to notice that when a nanorod was deposited on a Si/SiO₂ substrate ($n_{sub} = 1.54$) a blue shift was expected due to the lower refractive index. For the representative nanorod discussed at the beginning of this section (26×68 nm) a shift of 16 nm was found (see next section for more details).

Novo *et al.* investigated experimentally the influence of the surrounding medium and substrate refractive indexes on the optical properties of single Au triangular prisms [97]. They explained the observed behavior on the basis of an effective refractive index n_{eff} given by a linear combination of the refractive index of the substrate (n_{sub}) and the surrounding medium (n_{med}) as

$$n_{eff} = \alpha \cdot n_{med} + (1 - \alpha) \cdot n_{sub} \quad (2.1)$$

with α varying between 0.1 and 0.65 depending on whether the particles are embedded in a polymer matrix or deposited onto the substrate. Following the same idea, we simplified the simulated system by assuming the nanorod with given dimensions embedded in a homogeneous medium having an effective refractive index. According to our simulations, the value of $n_{eff}=1.25$ had to be used to reproduce the experimental scattering spectra of figure 2.10a. It should be said that despite the position of the LSP was reproduced within the effective refractive index approximation, the

intensity of the scattering and absorption cross section were found overestimated of a factor ~ 2 respect to the simulation in figure 2.9d.

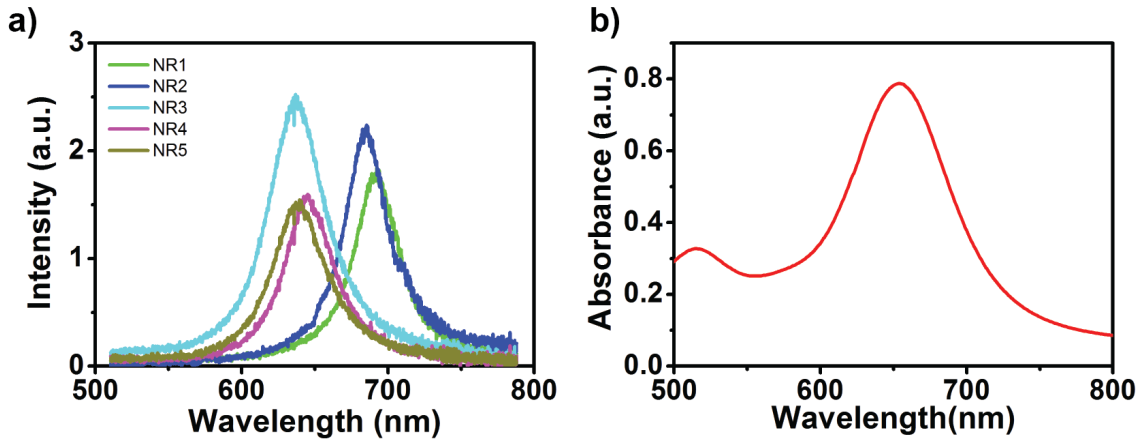


Figure 2.10.: a) *Dark-field scattering spectra of 5 single nanorods and b) the absorption spectrum of the colloidal solution.*

The effective refractive index approximation will be used in section 2.3.3 for studying the optical properties of nanorod arrays of different sizes and geometries by BEM method.

2.3.2. Scattering and absorption properties of single nanorods

The accuracy of FDTD simulations demonstrated in the previous section allows to predict the optical resonances of single nanorods with different sizes in the more realistic environments which will be encountered in Chapters 3, 4 and 6.

Simulated absorption, scattering and extinction spectra (normalized to the geometrical cross section) for longitudinal and transversal polarization of three particles, named (a),(b),(c) with dimensions 14×42 nm, 22×54 nm and 30×70 nm respectively deposited on SiO_2 substrate, are shown in figure 2.11a-f. For light polarization parallel to the long nanorod axis, the plasmonic resonance was found at 672 nm in nanorod (a), 635 nm in nanorod (b) and 621 nm in nanorod (c). The blue shift in the longitudinal resonance between these nanorods is related to the decreasing in the aspect ratio from 3 in particle (a), 2.5 in (b) and 2.3 in (c). The plasmonic resonance for transversal polarization is almost insensitive to the particle dimension and was peaked at 516 nm and 529 nm in the absorption and scattering cross sec-

tions respectively. The main differences between the three nanorod sizes were found in the absorption and scattering cross sections. Firstly, we observe that the cross sections of the transversal mode were more than an order of magnitude smaller than the longitudinal resonance, indicating a weaker nature of the former compared to the latter. Secondly, the scattering cross section increased by a factor 2 between the 14×42 nm rod and 22×54 nm rod and by a factor 3 between 22×54 and 30×70 rod. On the other hand the normalized absorption cross sections remained almost constant for the three particles despite the different geometry. This behavior suggests that the absorption cross section increased almost linearly with the geometrical cross section of the nanorod while the scattering cross section had showed a supralinear dependence. Therefore, the increasing particle size was expected to be more effective in enhancing the scattering than the absorption cross section. According to this, we observed experimentally that scattering spectra of single nanorods with diameter below 20 nm were not detectable in our dark-field microscope setup whereas spectra of 20×60 nm (or larger) nanorods were recorded as shown in figure 2.10a.

It is interesting to notice that for a given particle size, the longitudinal plasmonic resonance could be red shifted by embedding the particle in a polymer matrix with appropriate refractive index. For instance, nanorod (b) on SiO_2 substrate ($n_{sub} = 1.54$ at $\lambda=650\text{nm}$) surrounded by a polymer (resist S1813) ($n_{med} = 1.63$ at $\lambda=650$ nm) showed a red-shift of 5 nm in the transversal resonance (TSP at 534 nm) and 98 nm in the longitudinal resonance (LSP at 733 nm) as demonstrated in figure 2.12. From this results it is also evident that the longitudinal plasmon is more sensitive to the surrounding medium respect to the transversal one, as previously demonstrated [50]. The red-shift of plasmonic resonance by changing the refractive index of the surrounding medium will be exploited in Chapter 4.

The previous discussion suggests that a theoretical analysis of the optical properties of Au nanorods represent a powerful tool in order to find the optimized geometry matching the requirements of any designed experiment. For instance, nanorods with diameter below 20 nm have been shown having a strong absorption that makes them suitable for photothermal applications [179] and generation of hot-carriers (see Chapter 6). On the other hand larger particle with diameter above 30 nm have a larger scattering cross section that could be more favorable for applications where

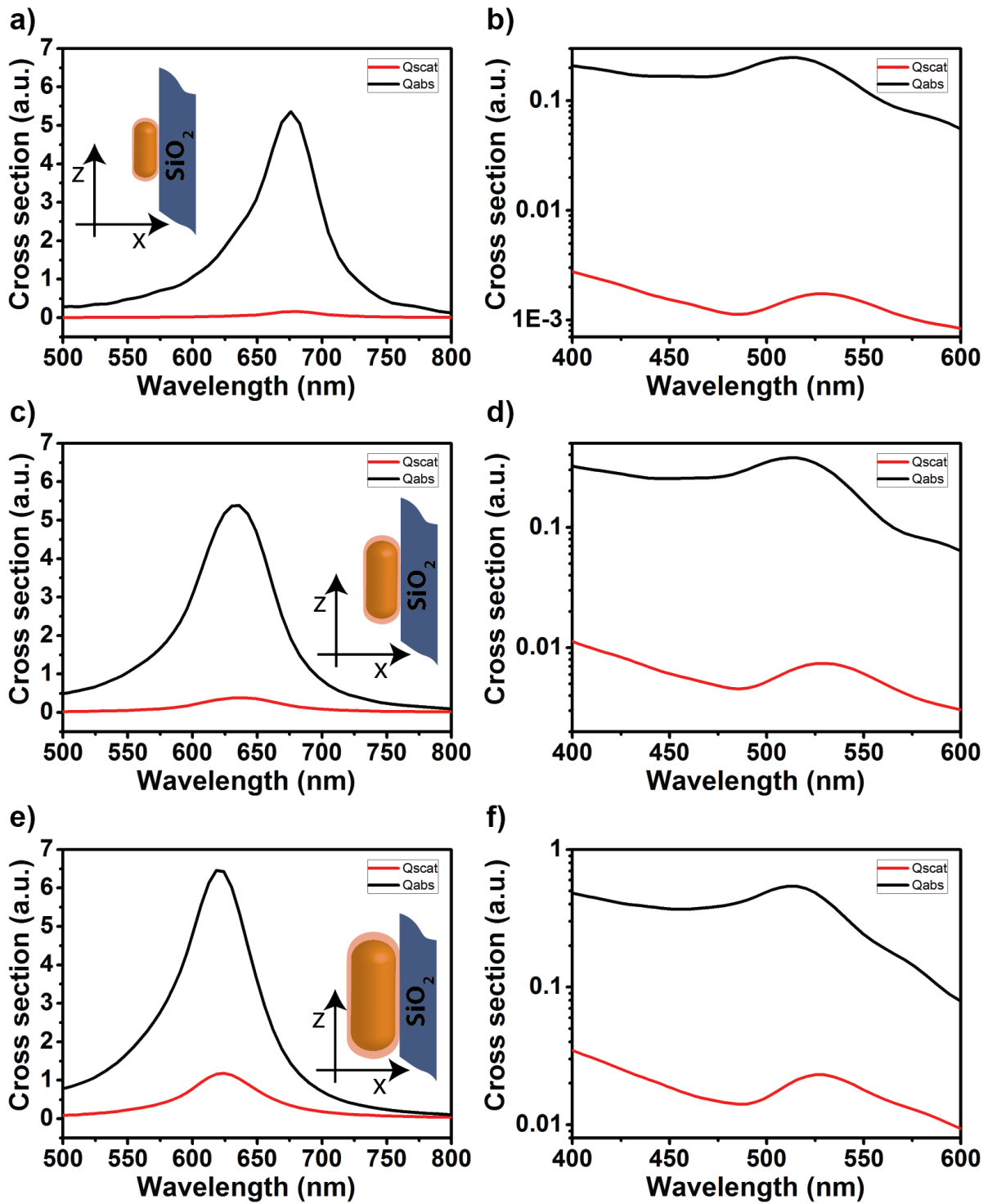


Figure 2.11.: FDTD simulations of scattering and absorption cross sections for light impinging along the x-axis and polarized along the z-axis (left) and y-axis (right) of a nanorod with dimensions a-b) 14×42 nm, c-d) 22×54 nm and e-f) 30×70 nm.

local re-radiation of incident light is required (SERS, photovoltaic) as discussed in Chapter 4. Moreover the longitudinal plasmonic resonance can be finely tuned between 520 nm to more than 1000 nm by designing nanorod with appropriate aspect ratio or changing the dielectric constant of the surrounding medium.

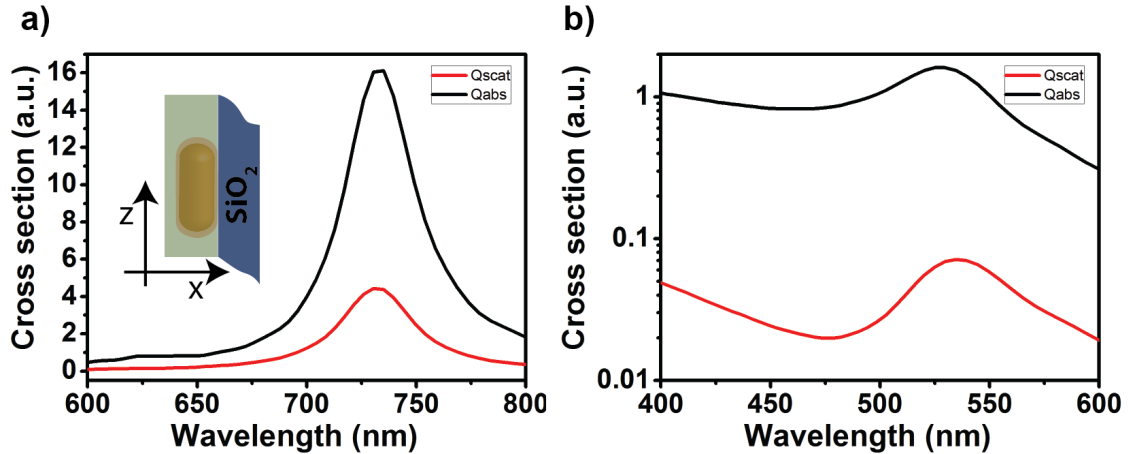


Figure 2.12.: *FDTD simulations of scattering and absorption cross sections for a nanorod 22×54 nm on SiO_2 substrate surrounded by a medium with refractive index of 1.63.*

2.3.3. Scattering and absorption properties in closely-spaced nanorod arrays

We also examined the properties of nanorods clustered in closely-spaced assemblies. In this condition near-field coupling shifts the plasmonic resonances compared to the resonances of isolated particles and generates new resonances. The rapid E-field decay outside the metal surface limits the maximum gap size between two nanorods to ~ 10 nm for an effective coupling to occur. This condition is usually well verified in self-assembled nanorods where the inter-nanorod distance is in the range of 3.4-9 nm due to the CTAB double layer [167]. For large arrays of particles, BEM approach represents a more effective method to solve Maxwell equations with a modest computational requirements. Herein we use this method to investigate the optical properties of closely-spaced nanorods in various configurations.

Simulations were performed using MNPBEM Matlab toolbox [176] where each nanorod was modeled as a cylinder ending with two hemispherical caps, the inter-

nanorod distance was 4 nm and the array was surrounded by an homogeneous medium with an effective refractive index $n_{eff} = 1.34$ (see section 2.3.1). The n_{eff} value was determined by a direct comparison between the simulated and measured spectra showed in figure 2.10.

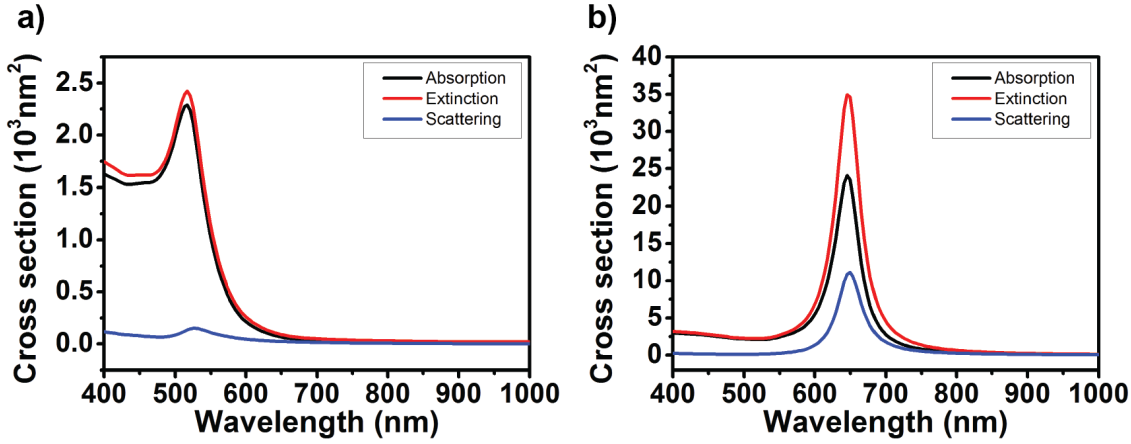


Figure 2.13.: Boundary element method simulations of extinction, scattering and absorption cross sections of a nanorod 30×67 nm under light polarized along (a) the short and (b) long axis of the nanorod. The LSP was found at 645 nm in reasonable agreement with the experimental data of table 2.4.

Figure 2.13a-b shows the extinction, scattering and absorption cross section for the transversal surface plasmon (TSP) and longitudinal surface plasmon (LSP) of a 30×67 nm nanorod. The TSP was found at 516 nm and the LSP at 645 nm, in reasonable agreement with the experimental value reported in table 2.4 within a variation ± 30 nm, due to the error on the nanorod size. Shape and position of the longitudinal and transversal plasmonic resonances changed dramatically when other particles are in close proximity due to near-field coupling among the surface plasmons of the particles [63]. A separation distance of 4 nm between adjacent nanorods will be used in the simulations whose discussion follows [167].

In figure 2.14 we simulated the extinction spectrum of 1D chain with 9 nanorods 30×67 nm aligned side-by-side. The plasmonic resonance for light polarized along the x-direction (TSP) was found at 589 nm thus showing a red-shift respect to the single nanorod of 73 nm and more than an order of magnitude enhancement in the extinction cross section. On the other hand, LSP blue-shifted from 645 nm in the

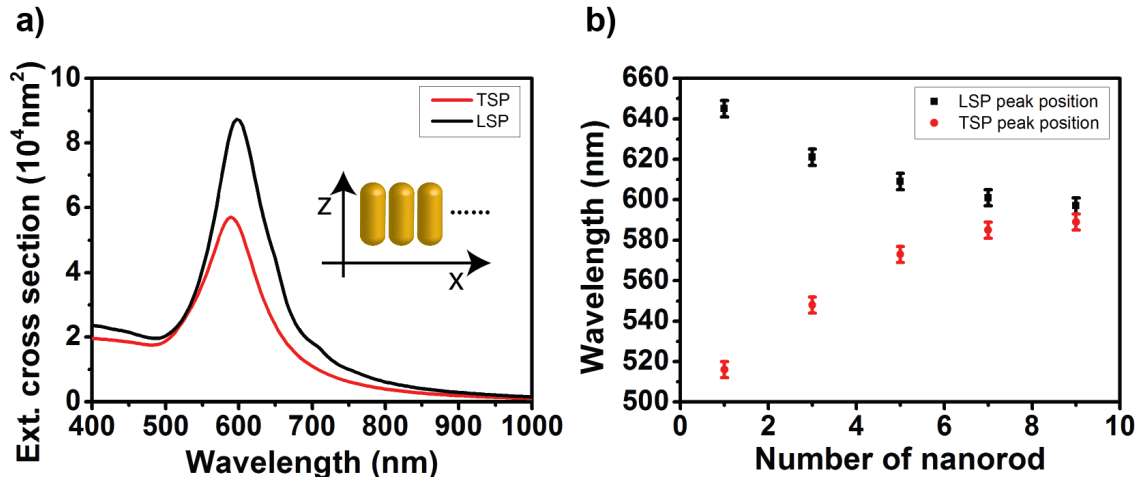


Figure 2.14.: a) Boundary element method simulations of extinction cross section for an array of 9 nanorods 30×67 nm aligned side-by-side with light propagating along y-axis and polarized along z-axis (black line) and x-axis (red line). b) Position of the transversal surface plasmon (TSP) and longitudinal surface plasmon (LSP) vs number of nanorods in the array.

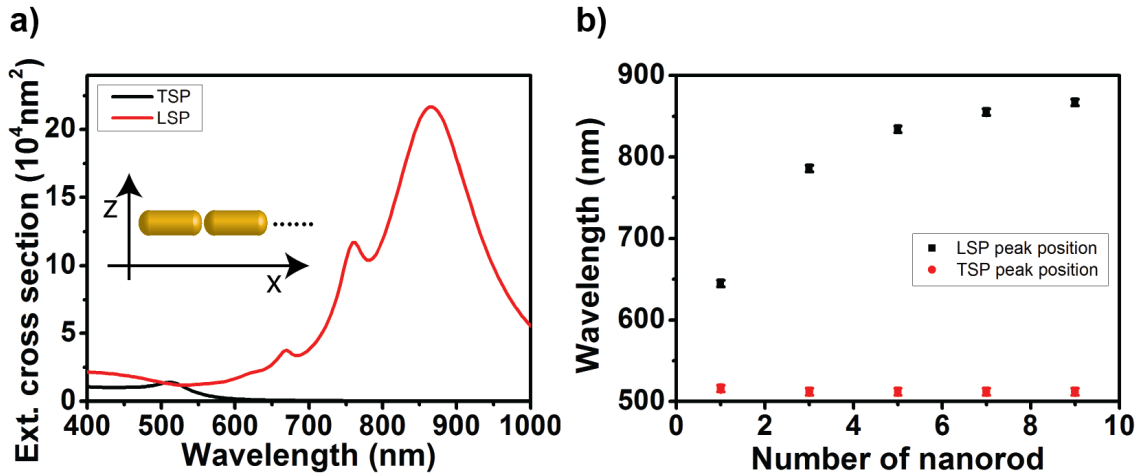


Figure 2.15.: Boundary element method simulations of the a) LSP and TSP extinction cross section for an array of 9 nanorods 30×67 nm aligned end-to-tail and b) the LSP and TSP peak position in assemblies with 1,3,5,7 and 9 nanorods.

isolated nanorod to 597 nm. Figure 2.14b shows the peak position in the simulated extinction cross section for the TSP and LSP at varying nanorod numbers. The LSP blue-shifted progressively with the increasing of the nanorod numbers while the TSP moved towards longer wavelengths. The shifting was not linear with the number of particles and showed a saturation for array length above 7 nanorods. Noticeably, the transversal and longitudinal resonance converge to the same wavelength thus resulting in a single and intense peak at ~ 600 nm.

Different optical properties arise if the nanorods are assembled end-to-end instead of side-by-side. Figure 2.15 shows 1D arrays of 9 rods 30×67 nm in end-to-tail configuration. The LSP peak was found at 867 nm with almost one order of magnitude larger and a broader shape than the single nanorod. Moreover weaker resonances appeared at 762 nm and 669 nm. The red shift of the LSP peak observed after adding one by one nanorod along the chain is plotted versus the number of nanorods in figure 2.15b. The largest shift was found between the configuration with one nanorods and three nanorods. For subsequent nanorods, the shift decreased down for further increasing in nanorods number and the resonance peak reached a saturation at 867 nm. According to simulations, the plasmonic coupling in 1D array of nanorods assembled end-to-tail allows an asymptotic maximum in the plasmonic resonance wavelength at chain length of 7-9 nanorods. Noticeably, this result is in excellent agreement with experimental demonstration in chain of spherical particles demonstrate by Barrow *et al* [64].

Following the observation of the asymptotic behavior that limits the number of nanorods effectively coupled, it is reasonable to approximate the behavior of large arrays of particles with an arrays 7×6 array for parallel aligned nanorods and 6×6 for vertical aligned nanorods. This approximation is not able to describe the entire complexity of the optical response of a large arrays but still provides some useful information accessible with modest computational requirements.

In the 7×6 array of parallel aligned nanorods simulated extinction spectra (figure 2.16a) showed a intense peak at 576 nm under x-polarized light with two smaller resonances at 675 nm and 831 nm. For light polarized along the z-axis the extinction spectra presented a broad shape reaching the maximum at 994 nm with two sharp resonances at 667 nm and 834 nm (figure 2.16b). Notably the scattering cross section

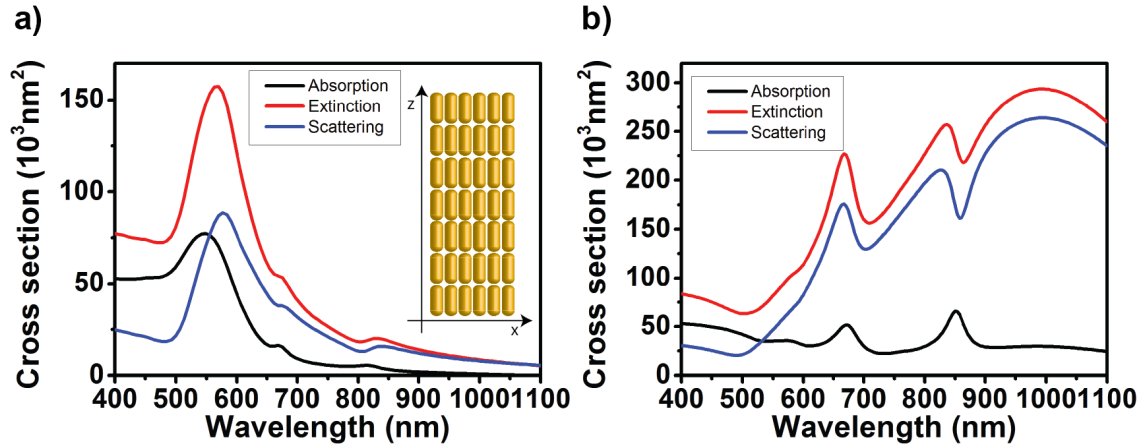


Figure 2.16.: *Boundary element method simulations of the optical extinction, scattering and absorption cross sections of an array 7×6 of nanorods 30×67 nm separated by 4 nm gap with light incident along the y-axis and polarized along a) x-axis and b) z-axis. Inset shows the simulated array of nanorods.*

was found more than 5 times larger than the absorption cross section. Optical cross sections of a 6×6 array of vertical aligned nanorods 30×67 nm under light impinging along the z-direction and polarization along the x-direction is shown in figure 2.17a. The scattering cross section was larger than the absorption (see for comparison figure 2.11) and the plasmon resonance was found having two peaks at 621 nm and 570 nm with a broad shape, thus resulting in a FWHM more than 5 times larger than the single nanorod (268 nm compared to 41 nm deduced from the Lorentzian fit). Finally for a random oriented array of nanorods (8 nanorods oriented along z and 8 nanorods oriented along x) as depicted in the inset of figure 2.17b the longitudinal and transversal plasmon resonances become of comparable magnitude and close in wavelength thus resulting in a large broad peak of around 700-800 nm. It should be pointed out that inter-nanorod distance and nanorod sizes have an important influence on the array optical cross sections. Simulations suggest that a decreasing of the inter-nanorod distance results in a larger red shift due to the stronger coupling. On the other hand above ~ 10 nm the coupling is almost negligible for nanorods with dimension 30×67 nm. Regarding particle size, although the coupling of the longitudinal plasmons was found also in arrays of 14×42 nm nanorod, the transversal plasmonic mode required larger diameter to be effective. Therefore arrays of nanorod

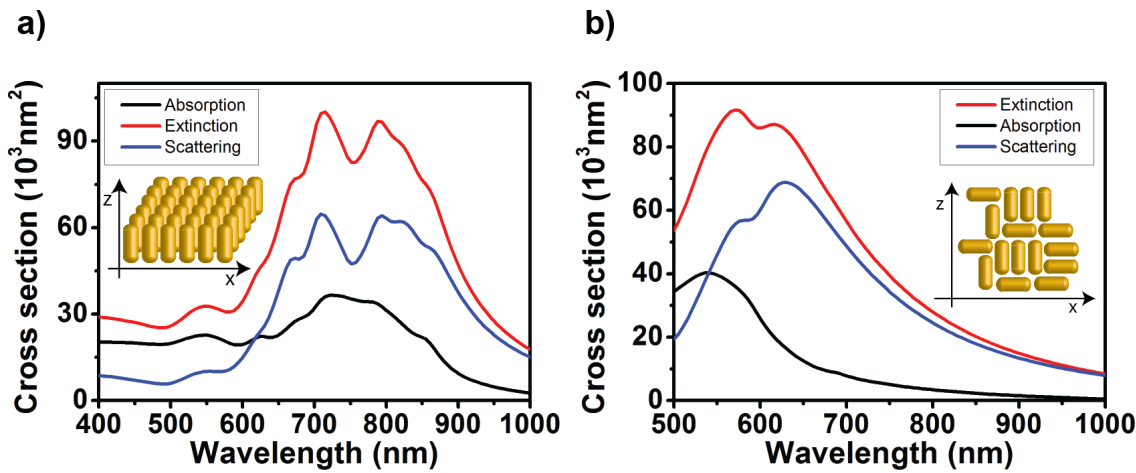


Figure 2.17.: Boundary element method simulations of the optical extinction, scattering and absorption cross sections of a) array 6×6 of nanorods 30×67 nm separated by 4 nm gap with light incident along the z-axis and polarized along the x-axis and b) array of 16 nanorods 30×67 nm separated by 4 nm gap oriented with light incident along the y-axis and polarized along the z-axis. Insets show the simulated array of nanorods.

with diameter smaller than ~ 20 nm showed a transversal plasmonic mode almost independent from the array size and similar to the resonance of an isolated nanorod.

2.4. Conclusion

In this Chapter the synthesis of Au nanorod of different sizes ranging between 14×42 nm up to 30×70 nm by seed-mediated method was presented and discussed. A systematic approach to purify the as-prepared solution of colloidal nanorods was developed and used to prepare the samples investigated in Chapters 3,4 and 6. The optical properties of colloidal solutions and single nanorods on ITO substrate were investigated experimentally by UV-Vis and dark-field spectroscopy, and theoretically by FDTD and BEM simulations. A detailed analysis of the influence of the CTAB layer surrounding the nanorod and the substrate on the plasmonic resonance was carried out and compared to the experimental dark-field spectra. Moreover the optical properties of nanoparticles with different sizes namely 14×42 nm, 22×54 nm and 30×70 nm were simulated and compared. Furthermore the influence of near field coupling in arrays of closely spaced metal nanorod were elucidated. These simulation

tools will be used in Chapter 4 and 6 to predict the optimum size of nanorods to be integrated in the hybrid devices and to explain the observed behaviors.

Chapter 3.

Controlled assembly of Au nanorods into 1D architectures

The assembly of Au nanorods of average size 14×42 nm was investigated by electric field assisted deposition. Nanorods displayed a rich assembly behavior with formation of one dimensional (1D) architectures under specific experimental conditions. The assembly process was found to be dependent on both the intensity of the applied electric field and the frequency, in contrast to what was expected for metallic particles. A theoretical model based on interpretation of nanorods as core-shell entities was proposed in order to explain the observed behavior. As a result, the overall deposition process was represented by a contour plot, where the force acting on nanorods was displayed as a function of both electric field and frequency. In particular, an area of the contour plot was identified where the deposition process was driven by the generation of localized hot spots of high E-field magnitude, leading to formation of well-aligned 1D nanorod architectures bridging the electrode gaps. Electrical characterization showed that 1D architectures displayed tunneling behavior across the inter-nanorod gap. The controlled organization of nanorods into 1D architectures presents opportunities for electronic, sensing and plasmonic applications.¹

¹This work was published as Pescaglioni *et al.*, Controlled Assembly of Au Nanorods into 1D Architectures by Electric Field-Assisted Deposition *J. Mater. Chem. C*, 2, 6810-6816, (2014)

3.1. Introduction

As already discussed, anisotropic Au nanostructures have been extensively investigated for their unique optical properties making them attractive for sensing and optoelectronics [180, 181, 182]. In particular, the enhanced optical and electrical phenomena arising from the assembly of Au nanorods into specific alignment configurations have been used in a number of sensing, photonic and electronic applications [59, 88, 183, 71, 184, 185, 186]. For example, the high density of plasmonic hot spots generated in close-packed three- and two- dimensional (3D, 2D) nanorod arrays has been used for demonstration of surface-enhanced Raman scattering (SERS) detection of biological and chemical species [91, 90, 169, 89]. 2D parallel arrays of Au nanorods recently fabricated by our group by droplet evaporation methods have been proposed as plasmonic tags for anti-counterfeiting applications [187]. Such 2D arrays also displayed strongly enhanced photoconductance, due to a bolometric enhancement of the arrays' conductance upon excitation of the longitudinal surface plasmon mode of the nanorods [188].

Controlled organization of Au nanorods into 1D architectures is a much more challenging task compared to 2D and 3D assemblies but it is motivated by the potential applications that such assemblies would have in microelectronics (ie. electrical ultra-small interconnections) and photonics (ie. plasmonic waveguides) [189, 190, 191, 192]. Despite the feasibility of complex geometries and scalability offered by top-down lithographic techniques, the advantage of bottom-up approaches relies on the ability to decrease the interparticle distance (i.e. ≤ 20 nm) within the array, which in turn leads to enhanced plasmonic coupling effects. Preparation strategies for 1D nanorod assemblies based on bottom-up techniques have been explored based on the use of (i) templates [104, 105, 193], (ii) lithographically fabricated trenches [106, 92] or (iii) chemically linked nanoparticles in solution [107, 108, 109].

However, these approaches were limited by high complexity in substrate preparation, lithographically-limited resolution and low yields, respectively [194]. Thus, the development of a unified fabrication approach compatible with scalable top-down fabrication technologies and yielding to controlled formation of 1D nanorod architectures still remains a key challenge.

3.2. Dynamics of metal nanorods in oscillating electric field

Electric field assisted deposition is a compatible approach that has emerged as promising technique for the manipulation of spherical metallic micro- [186, 195] and nano-particles [196] and 1D polymer structures [197]. Electric field assisted deposition of Au nanorods has resulted in fabrication of multi-nanorod wires bridging microscopic electrode gaps [198]. Poelsema *et al.* [199] quantitatively investigated the deposition and alignment of Au nanorods under applied E-fields. Although they reported high density deposition of nanorods, formed structures rarely bridged the electrode gaps and displayed limited alignment due to mutual nanorod dipole interactions.

In this Chapter I investigate the electric field assisted deposition of Au nanorods (14×42 nm) bearing a hexadecyltrimethylammonium bromide (CTAB) ligand shell into micron-spaced electrodes. The process was found dependent on both the intensity of the applied E-field and the frequency, leading to formation of well aligned 1D architectures under specific experimental conditions. A theoretical model based on Au nanorods surrounded by CTAB ligands as core-shell material was developed in order to explain the unusual frequency dependence of the deposition process. Under this model the deposition process was described by a contour-plot representation where the force acting on a nanorod was displayed as a function of both the electric field intensity and frequency. Furthermore, an area of the plot (ie. specific values of field intensities and frequencies) was identified where predictable and reproducible formation of 1D nanorod architectures occurred. Electrical characterization of 1D architectures showed tunneling transport across inter-nanorod gap and a hysteretic behavior associated with the co-deposition of charged CTAB ligands.

3.2. Dynamics of metal nanorods in oscillating electric field

The dynamic of an uncharged particle in an oscillating electric field is usually called dielectrophoresis. The interaction between an applied electric field \mathbf{E} and the induced dipole \mathbf{p} on the particle, arising from the dielectric constant and conductivity difference between the surrounding medium and the particle, gives rise to a transla-

tional and rotational motion that offers interesting possibilities for particle manipulation. Historically, this theory was developed for dielectric particles and biological cells, where the large range of possible dielectric constant and conductivity values results in a rich variety of responses under applied oscillating fields.

Homogeneous dielectric particles and medium with ohmic loss in oscillating electric field are conveniently described by a complex permittivity in the form [200]

$$\tilde{\epsilon}_{p/m}(\omega) = \epsilon_{p/m}(\omega) + i \frac{\sigma_{p/m}(\omega)}{\omega} \quad (3.1)$$

where $\epsilon_{p/m}(\omega)$ and $\sigma_{p/m}(\omega)$ are the frequency dependent permittivity and conductivity of the particle and medium respectively, i the imaginary number and ω the E-field frequency.

When a linearly polarized AC electric field $\mathbf{E}(t) = \text{Re}[\mathbf{E}_0 e^{i\omega t}]$ is applied, the particle acquires an effective dipole moment along the α axis ($\alpha = x, y, z$) defined by

$$\mathbf{p}_\alpha(t) = \text{Re} \left[3V \epsilon_m \tilde{K}_\alpha \mathbf{E}_{0,\alpha} e^{i\omega t} \right] \quad (3.2)$$

where V is the particle volume and \tilde{K}_α is the frequency dependent complex Clausius-Mossotti factor. In homogeneous ellipsoidal particles the Clausius-Mossotti factor is generally defined by

$$\tilde{K}_\alpha(\omega) = \frac{\tilde{\epsilon}_p(\omega) - \tilde{\epsilon}_m(\omega)}{3 [\tilde{\epsilon}_m(\omega) + (\tilde{\epsilon}_p(\omega) - \tilde{\epsilon}_m(\omega)) L_\alpha]} \quad (3.3)$$

with α labeling the x , y and z directions and L_α the depolarizing factor along the α -axis (see section 1.4.3). In the case of prolate ellipsoid with a and b the long and short semiaxis and eccentricity $e = \sqrt{1 - b^2/a^2}$ the depolarizing factor can be calculated as

$$\begin{cases} L_a = \frac{1 - e^2}{2e^3} \left[\ln \left(\frac{1 + e}{1 - e} \right) - 2e \right] \\ L_a + 2L_b = 1 \end{cases} \quad (3.4)$$

Depending from the permittivity and conductivity of particle and medium, the Clausius-Mossotti factor is modulated in frequency and can assume positive or nega-

3.2. Dynamics of metal nanorods in oscillating electric field

tive values corresponding to a induced dipole oriented parallel or anti parallel to the electric field. If the applied electric field is non-homogeneous in space, the induced dipole on the particle experiences a translational force, called dielectrophoretic force (\mathbf{F}_{DEP}), expressed by

$$\mathbf{F}_{DEP}(t) = \mathbf{p}(t) \cdot \nabla \mathbf{E}(t) \quad (3.5)$$

and substituting eq.(3.2) the expression for the time-averaged dielectrophoretic force becomes

$$\langle \mathbf{F}_{DEP} \rangle_{\alpha} = \frac{3}{2} \pi a b^2 \epsilon_m \text{Re}[\tilde{K}_{\alpha}] \nabla |\mathbf{E}_{\alpha, rms}|^2 \quad (3.6)$$

where E_{rms} is the root-mean-square value of the oscillating electric field. Depending on the Clausius-Mossotti factor sign, the dielectrophoretic force acts moving the particle towards the area with highest electric field (positive dielectrophoresis) or to the area with lower electric field (negative dielectrophoresis). Moreover, in a linearly polarized electric field, the torque force

$$\mathbf{T}_{ROT}(t) = \mathbf{p}(t) \times \mathbf{E}(t) \quad (3.7)$$

acquires the final form

$$\langle \mathbf{T}_{\alpha} \rangle = \frac{2}{3} a b^2 \pi \epsilon_m (L_{\gamma} - L_{\beta}) \text{Re}[\tilde{K}_{\beta} \tilde{K}_{\gamma}] E_{0\beta} E_{0\gamma} \quad (3.8)$$

with α , β and γ ordered following the right-handed convention for the coordinate system $x \rightarrow y \rightarrow z \rightarrow x$. Even if the alignment of the long axis along the field lines is often the favorable condition, the configuration with the short axes aligned respect to the electric field is also possible due to the frequency dependence of the Clausius-Mossotti factor.

Similar arguments hold also for pure metal particles immersed in dielectric surrounding medium, however some considerations regarding the expression of the complex permittivity and the Clausius-Mossotti factor need to be discussed.

In section 1.4.1 we showed that the dielectric function of metals has the form

$$\epsilon(\omega) = 1 + \frac{i\sigma(\omega)}{\epsilon_0\omega} \quad (3.9)$$

At ultra-low frequencies used in dielectrophoresis (MHz or below), far from the optical region, the complex conductivity of the metal is almost real, as expected for a perfect conductor. Therefore, if we neglect the contribution of bonded electron to the polarization, the complex permittivity of the Au nanoparticle can be approximated as

$$\epsilon_{Au}(\omega) \approx 1 + \frac{\sigma_{Au,0}}{\epsilon_0\omega} \quad (3.10)$$

where σ_0 is the DC conductivity. Due to orders of magnitude larger conductivity of the metal compare to the surrounding medium, the Clausius-Mossotti factor remains constant up to extremely high frequency ($>10^{12}$ Hz) well above the experimental accessible range. Consequently \mathbf{F}_{DEP} and \mathbf{T}_{ROT} can be considered independent from the applied E-field frequency and the dielectrophoretic force can only be used to induce a collective motion of particles in the region with highest electric field intensity (positive dielectrophoresis) and torque force aligns uniquely one axes to the electric field.

It is relevant for the work presented in this Chapter to notice that \mathbf{F}_{DEP} and \mathbf{T}_{ROT} in the form of eq.(3.6) and (3.8) remain valid for multi-shell nanorods by substituting the $\tilde{\epsilon}_p$ with an effective permittivity $\tilde{\epsilon}_{eff}$ that includes the effects of the internal structure of the particle on the permittivity. Details on $\tilde{\epsilon}_{eff}$ will be provided in section 3.5.

The dielectrophoretic force and the torque force have been successfully used in manipulation of dielectric and metal particles, semiconductor nanowire [201], carbon nanotube [202] and biological cell [203]. However, the previous forces are not the only forces governing the dynamics of colloidal particles in solution under electric field. Electrical forces such as electrothermal force, coulomb force and non-electrical forces like Buoyancy force and Brownian motion can be of the same magnitude of the dielectrophoretic forces, giving a non-negligible contribution to the particle dynamics [204]. Referring to the experiments described in section 3.4, no evidence of electrothermal flow and sedimentation due to gravitational force were observed.

3.2. Dynamics of metal nanorods in oscillating electric field

Therefore, in this work Brownian motion and dielectroforetic force can be considered the main forces acting on nanorods in solution under oscillating electric field.

Concerning diffusion, Brownian motion is a stochastic process arising from irregular motion of molecules in the liquid that imparts random forces to the particle in suspension. The average particle displacement $\langle x \rangle$ along the x direction after a time t (average over a large number of particles) due to the Brownian motion is calculated by means of a distribution probability $P(x, t)$ that satisfy the diffusion equation

$$\frac{\partial}{\partial t}P(x, t) = D\frac{\partial^2}{\partial x^2}P(x, t) \quad (3.11)$$

and the normalization condition

$$\int_{-\infty}^{+\infty} P(x, t)dx = 1 \quad (3.12)$$

where $D = kT/f$ is the diffusion coefficient and

$$f = \frac{8\pi a}{2\ln\left(\frac{2a}{b}\right) - 1} \quad (3.13)$$

is the friction coefficient for a ellipsoid with long axis a and short axis b . From these definitions follow that the average displacement $\langle x \rangle_B = 0$ and the quadratic displacement is

$$\langle x^2 \rangle_B = \int_{-\infty}^{+\infty} P(x, t)x^2dx = 2Dt \quad (3.14)$$

When the external force \mathbf{F}_{DEP} is applied, a deterministic motion of the particle is observed only if the displacement $\langle x^2 \rangle_F$ induced by the external force is larger than the displacement $\langle x^2 \rangle_B$ caused by brownian motion. From this condition follows that, in the steady state, a threshold intensity of the external force $|\mathbf{F}_t|$ expressed by

$$|\mathbf{F}_t| \sim \sqrt{\frac{2Df^2}{t}} \quad (3.15)$$

is required to have an observable motion of the colloidal particles in the direction

of the applied external force during the time t . Therefore for $|\mathbf{F}| \gg |\mathbf{F}_t|$ the motion of the colloidal system with particle density $n(x, t)$ in steady-state condition is described by

$$\begin{cases} \frac{\partial n}{\partial t} + \nabla \cdot (n \cdot \mathbf{v}) = -\nabla \cdot \left(-D\nabla n + \frac{n\mathbf{F}_{DEP}}{f} \right) \\ \left\langle \frac{\partial \mathbf{v}}{\partial t} \right\rangle_t + \langle (\mathbf{v} \cdot \nabla) \mathbf{v} \rangle_t = -\frac{f \langle \mathbf{v} \rangle_t}{m} + \frac{\langle \mathbf{F}_{DEP} \rangle_t}{m} \end{cases} \quad (3.16)$$

where in the second equation we considered time-average values of the quantities and we used $\langle \frac{F_B}{m} \rangle_t = 0$. Experimental evidence of a threshold value for \mathbf{F}_{DEP} required to initiate a nanorod motion as well as the effect of the dielectrophoretic force will be discussed in details in section 3.4.

3.3. Experimental section

Au nanorods were synthesized using a seed-mediated method described in section 2.2.1. The as prepared Au nanorod solution (1 ml) was centrifuged twice to remove CTAB excess and re-dispersed in 1 ml of deionized water, resistivity 18 M Ω -cm. The final CTAB concentration was estimated to be ~ 0.05 mM using the method described in section 2.2.3. Dimensional statistical analysis of 100 nanorods gave a mean nanorod diameter and length of respectively 14 ± 3 nm and 42 ± 5 nm (aspect ratio of 3.0 ± 0.2).

Electric field-based experiments were performed on lithographically patterned pairs of opposing electrodes (1 μ m width, 50 μ m length) separated by 2 μ m and 5 μ m gaps connected by means of interconnection tracks to the contact pads (figure 3.1a).

Electrodes, interconnection tracks and contact pads were fabricated by (i) thermal evaporation of 45 nm Au and 5 nm Ti on Si/SiO₂(300nm) substrates and (ii) thermal evaporation of 5 nm Ti and 30 nm Au on quartz substrates (the quartz substrate was coated by 25 nm of amorphous silicon adhesion layer). Metallization was patterned using standard photolithography and lift-off techniques. Nanorods self-assembly experiments were undertaken by applying a sinusoidal AC voltage using a function generator (HP8116A Hewlett Packard) with amplitude between 0.35 and 7 V_{rms}

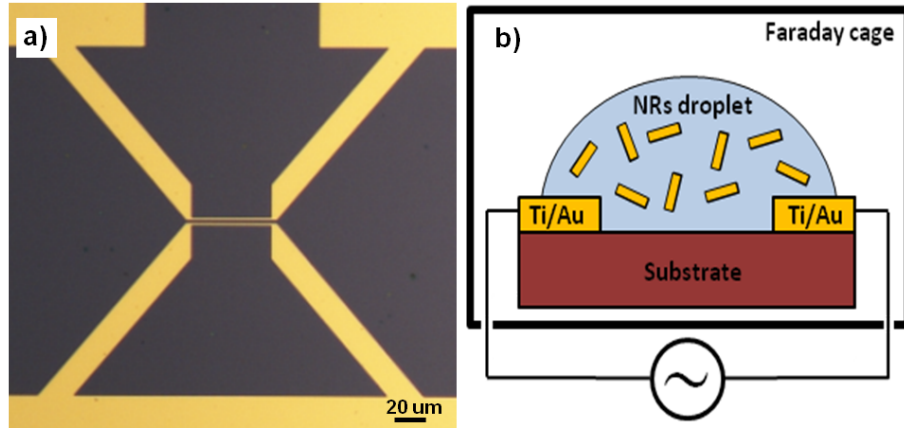


Figure 3.1.: a) Optical image of Ti/Au electrodes separated by $2\ \mu\text{m}$ gap on Si/SiO₂ substrate b) Schematic representation of the set-up used in dielectrophoretic process.

(1-20 V_{pp}) and frequency range between 500 kHz and 55 MHz on a given electrode chip via direct probing to contact pads as depicted in figure 3.1b. Measurements were conducted in a Faraday cage in dark conditions in order to avoid any external electromagnetic noise and to minimize electrothermal processes [205]. A $5\ \mu\text{l}$ drop of aqueous nanorod solution was placed on the chip surface in the presence of an applied electric field for ca. 5 min. Following nanorod assembly, the field was disconnected, the excess nanorod solution was flushed with water and the substrate dried under stream of nitrogen. We found that the application of the field for a time-scale much shorter than the drop evaporation time (roughly 30 min for $5\ \mu\text{l}$ drop) was effective in ensuring that (i) any fluidic shear forces active at the liquid-air boundary of the receding meniscus did not perturb the orientation of the assembled nanorods, (ii) no assembly due to uncontrolled drop-evaporation induced processes could occur. Scanning electron microscopy (SEM) characterization was performed using a Scanning Electron Microscope (JSM 7500F, JEOL UK) at operating voltages of 10 kV. Electrical measurements were performed in a micromanipulator probe station (TTPX Probe Station 61914) connected to a Parameter Analyser (Agilent 4157B) at room temperature under high vacuum conditions ($3 \cdot 10^{-6}$ mbar).

3.4. Electric field assisted deposition of Au nanorods

Figure 3.2a-f show representative SEM images of nanorod assemblies obtained at various experimental conditions. Nanorods exhibited a rich assembly behavior which was found dependent from both the intensity of the applied E-field and the frequency. For a constant frequency of 15 MHz a decrease in nanorod deposition density was observed in the electrode gap as the E-field intensity was varied between $E = 2.20 \times 10^6$ V/m and $E = 0.98 \times 10^6$ V/m (figure 3.2a-c).

Specifically, dense networks of nanorods oriented in the direction of the applied E-field were observed at high field intensity, according to the behavior expected for pure metallic particles (figure 3.2a) [103]. At slightly lower applied E-fields formation of well separated 1D nanorod architectures bridging the electrode gap was observed (figure 3.2b). 1D architectures were well aligned along the direction of the applied field and were constituted by individual nanorods aligned in head-to-tail configuration. Figure 3.2c shows that further decrease of applied E-field produced no nanorod deposition in the electrode gap. Remarkably, and in contrast to what expected for pure metallic entities, the deposition process was also found to be frequency dependent. Figure 3.2d-e shows SEM images of nanorod assemblies obtained at increasing applied frequency values. Specifically, at $E = 1.72 \times 10^6$ V/m and 1 MHz high density deposition resulted in aggregation of nanorods into dense networks (figure 3.2d). At higher frequency ($E = 1.72 \times 10^6$ V/m, 15 MHz) well aligned and spaced 1D architectures were observed (figure 1e), with individual Au nanorod chains bridging the electrode gaps. Finally, no nanorod deposition occurred at $E = 1.72 \times 10^6$ V/m when the frequency was increased to 50 MHz (figure 3.2f).

In order to better understand the dynamic of 1D architecture formation and the unusual frequency dependence, a more detailed investigation was performed where the surface density of nanorods deposited between micro-spaced electrodes was measured across a range of applied E-fields for frequency values of 1, 15 and 50 MHz. Results obtained are shown in figure 3.3a. At both 1 and 15 MHz no nanorod deposition was observed until a threshold electric field strength (E_T) of 0.8×10^6 V/m and 1.2×10^6 V/m was applied, respectively. E_T is the minimum electric field strength required to overcome the Brownian motion of particles in solution and to

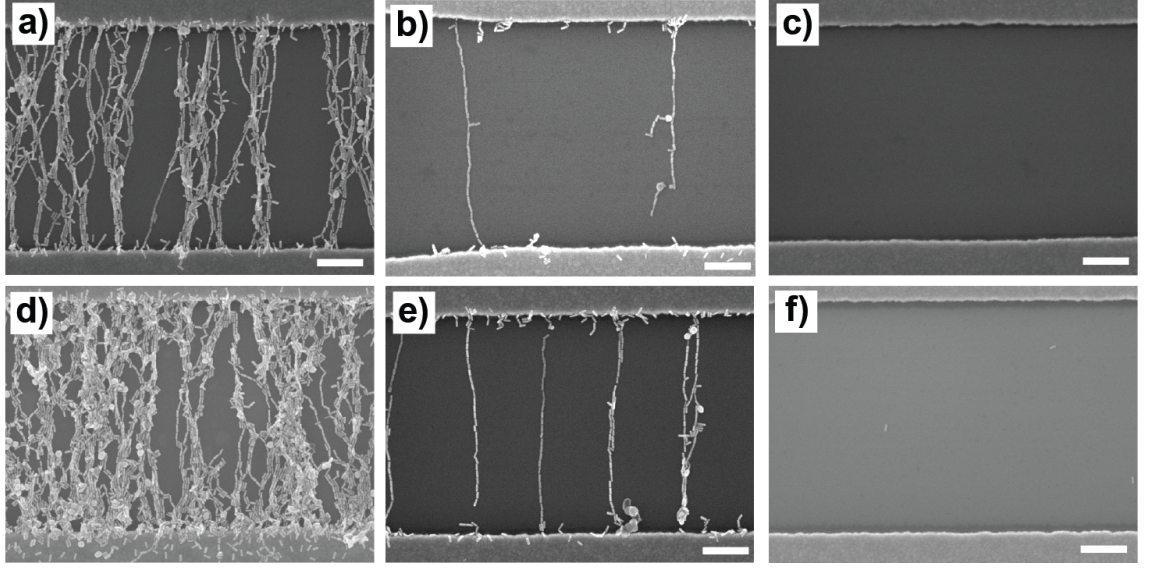


Figure 3.2.: SEM images showing electric field deposition of Au nanorods at increased (a-c) E -field values and (d-f) frequency values. Deposition conditions were: a) $E=2.20 \times 10^6$ V/m, 15 MHz; b) $E=1.48 \times 10^6$ V/m, 15 MHz; c) $E=0.98 \times 10^6$ V/m, 15 MHz d) $E=1.72 \times 10^6$ V/m, 1 MHz; e) $E=1.72 \times 10^6$ V/m, 15 MHz; f) $E=1.72 \times 10^6$ V/m, 50 MHz. Scale bars are 400 nm.

induce a deterministic motion in order for deposition to occur (see section 3.2). At applied voltages greater than E_T , an increase of deposited nanorod surface density with increasing of the E -field was observed, in agreement with the expression of the dielectrophoretic force (eq.3.6).

In the range of explored frequencies electrode polarization and AC electroosmosis are negligible, but electrothermal flow due to the Joule heating of the electrodes is an unavoidable process that generates a convective flow with a maximum velocity defined by [103]

$$v = M(\omega, T) \left(\frac{\epsilon_m \sigma_m V_{rms}^4}{2\pi^3 \lambda T \eta} \right) \frac{1}{r} \frac{\pi}{24} \quad (3.17)$$

where λ is the thermal conductivity, η the solution viscosity, r is the radial coordinate with its origin at the center of the electrode gap, and the frequency relaxation is contained in the dimensionless factor

$$M(\omega, T) = \frac{\frac{T}{\sigma_m} \frac{\partial \sigma_m}{\partial T} - \frac{T}{\epsilon_m} \frac{\partial \epsilon_m}{\partial T}}{1 + \omega \tau^2} + \frac{1}{2} \frac{T}{\epsilon_m} \frac{\partial \epsilon_m}{\partial T} \quad (3.18)$$

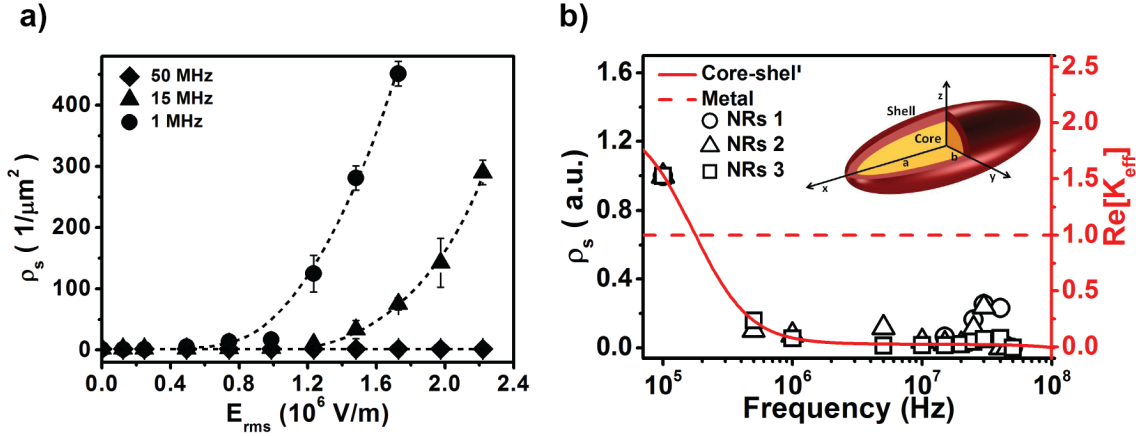


Figure 3.3.: (a) Surface density of Au nanorods deposited within a $2 \mu\text{m}$ electrode gap as a function of applied E-field at frequencies of 50, 15 and 1 MHz. The dotted lines are a guide to the eye; (b) (left axis) normalized surface density for three depositions of Au nanorods at $E = 1.8 \times 10^6$ V/m for applied frequencies between 100 kHz - 55 MHz; (right axis) real part of the Clausius-Mossotti factor ($Re[\tilde{K}_{eff}]$) for pure metal particles (dotted line) and for core shell particles (continuous line). Inset: core-shell nanorod representation used in the theoretical model.

where the relaxation time $\tau = \epsilon_m/\sigma_m$ is of the order of 10^{-7} s for a solution with $\epsilon_m = 80\epsilon_0$ and $\sigma_m = 4 \cdot 10^{-5}$ S/m. At low frequency, below the relaxation time, electrothermal flow would move down into the inter-electrodes and out across the electrodes, so an accumulation of particles in the area around the gap could occur from this process. However, in all performed experiments no particles were found neither outside or inside the electrode area for applied electric fields below the threshold. Moreover, above the threshold electric field, the density of particle was not found to follow the power law $\rho_s \sim V_{rms}^4$ as expected from eq.(3.17) at fixed frequency. Therefore the nanorod dynamics in solution is determined by the brownian motion and the dielectrophoretic force. The experimental data showed that the density of nanorods deposited within the electrode gap decreased when the applied frequency was increased from 1 MHz to 15 MHz. At 50 MHz no nanorods were deposited in the area between the electrode gaps in the range of applied E-fields. In figure 3.3b, we report the normalized surface density of nanorods found within the electrode gap when an electric field intensity of 1.8×10^6 V/m and frequencies in the range between 100 kHz and 55 MHz were applied. Different solutions displayed the same behavior: a sharp reduction of accumulated particle density between 100

kHz and 1 MHz, followed by a plateau between 5 MHz and 20 MHz and a rapid decreasing of particle density to negligible values above 35 MHz.

3.5. Core-shell model for colloidal nanorods

In order to explain the observed frequency dependence, we propose a model where CTAB-coated Au nanorods are treated as core-shell entities, as depicted in the inset of figure 3.3b. In section 3.2 we introduced the Clausius-Mossotti factor $\tilde{K}_\alpha(\omega)$, the depolarizing factor L_α and the dielectrophoretic force \mathbf{F}_{DEP} experienced by a prolate ellipsoidal metal particle in linearly polarized electric field. For pure metallic nanostructures, where conductivity and permittivity are much higher than that of the medium, the Clausius-Mossotti factor can be approximated to $\tilde{K}_\alpha(\omega) \approx L_\alpha^{-1}$. Therefore, the dielectrophoretic force driving nanoparticle deposition is only function of the applied E-field intensity and it is independent from the applied frequency, as represented by the dashed red line of figure 3.3b. The observed frequency dependence was explained by introducing a model where CTAB-coated Au nanorods were treated as core-shell entities. The complex permittivity of core-shell ellipsoidal particles $\tilde{\epsilon}_{p,\alpha}(\omega)$ was calculated from the values of the complex permittivity of the core $\tilde{\epsilon}_c(\omega)$ and the shell $\tilde{\epsilon}_s(\omega)$ by using [206]:

$$\tilde{\epsilon}_{p,\alpha}(\omega) = \tilde{\epsilon}_s(\omega) \frac{\tilde{\epsilon}_s(\omega) + (\tilde{\epsilon}_c(\omega) - \tilde{\epsilon}_s(\omega)) [L_{1,\alpha} + \nu_1(1 - L_{2,\alpha})]}{\tilde{\epsilon}_s(\omega) + (\tilde{\epsilon}_c(\omega) - \tilde{\epsilon}_s(\omega)) [L_{1,\alpha} + \nu_1 L_{2,\alpha}]} \quad (3.19)$$

where the particle was approximated to a shelled ellipsoid with an outer polar radius a_1 , inner equatorial $a_2 = 21nm$, an equatorial radius b_1 and an inner polar radius $b_2 = 7nm$ and $\nu_1 = a_1 b_1^2 / a_2 b_2^2$. For simplicity we restricted our analysis to the component along the main axis of the spheroid ($\alpha = a$) therefore we replaced $L_{1,\alpha}$ and $L_{2,\alpha}$ with the depolarizing factors $L_{1,a} = 0.109$ and $L_{2,a}$ referred to the inner and outer ellipsoid respectively and we assumed that the two spheroids share the same foci. The complex permittivity of water was taken in the form $\tilde{\epsilon}_m = \epsilon_m + \sigma_m / i\omega$ with $\epsilon_m = 80\epsilon_0$ and σ_m the permittivity and conductivity of the medium and we used the gold dielectric function $\epsilon_{Au} = 1 + i\sigma_{Au,0} / \epsilon_0\omega$ for the complex permittivity of the particle core as discussed in section 3.2.

Inserting eq.(3.19) into the Clausius-Mossotti factor, eq.(3.3), it was possible to calculate the magnitude of the dielectrophoretic force as a function of the frequency and intensity of the electric field. According to this model, the density of deposited particles is expected to be proportional to the dielectrophoretic force and to show a frequency-dependent modulation determined by an effective Clausius-Mossotti factor \tilde{K}_{eff} defined by

$$\rho_s(\epsilon_s, \sigma_s, \sigma_m, \sigma_0, b_1, \omega) = A \cdot Re[\tilde{K}_{eff}(\epsilon_s, \sigma_s, \sigma_m, \sigma_0, b_1, \omega)] \quad (3.20)$$

where $\epsilon_s, \sigma_s, \sigma_m, \sigma_0$ and b_1 are the free parameters of the model. The continuous red curve in figure 3.3b shows the calculated dependency of $Re[\tilde{K}_{eff}]$ respect to the frequency. The curve was calculated by fitting the experimental data of figure 3.3b by applying the least-square fitting procedure. Experimental data were very well fitted by the model, showing that for relatively small size metal nanorods the contribution from the surrounding CTAB ligands cannot be considered negligible. From the best fit we obtained the following estimation for the free parameters: $\epsilon_s = 11.3 \pm 0.7\epsilon_0$, $\sigma_s = 1.01 \pm 0.05 \cdot 10^{-4}$ S/m, $\sigma_m = 1.1 \pm 0.2 \cdot 10^{-5}$ S/m, $\sigma_0 = 0.28 \pm 0.05$ S/m, $b_1 = 11.5 \pm 0.4$ nm and $A = 1.64 \cdot 10^3$.

The conductivity of pure water ($\sim 5 \cdot 10^{-6}$ in this experiment) is expected to be increased by the presence of residual impurities from the chemical synthesis (see section 2.2.1) such as surfactant molecules and ions. In order to take into account the effect on the conductivity of the surrounding medium, we included this parameter in the fit and a value of $1.1 \pm 0.2 \cdot 10^{-5}$ S/m larger than the conductivity of pure water was obtained. Regarding the permittivity of the particle shell, we notice that although the permittivity for organic molecules is $\sim 5\epsilon_0$, dielectric constants of cell membranes can be as large as $10\epsilon_0$ or more [206]. CTAB molecules form a positively charged double layer around the metal surface that induces counterions adsorption on the layer surface. Due to the complexity of this structure the conductivity and dielectric constant could sensibly deviate from the value for the organic molecule towards a response more typical of a cell membrane. Also the conductivity value obtained for the shell layer σ_s was found in agreement with previous reports for cell membranes [206]. Notably, the DC conductivity of a single

nanorod chain bridging the electrodes in vacuum was found of the order of $10^{-3} - 10^{-4}$ S/m (see section 3.7) in reasonable agreement with the fit value obtained for shell conductivity that is expected dominating the DC conduction through the chain. On the other hand, the effective conductivity value for the metal core requires more careful considerations. If we use the DC conductivity of bulk gold ($4 \cdot 10^8$ S/m) the first sharp decreasing of particle density at 100 kHz-1 MHz can be well reproduced. However, the second dispersion at 50 MHz cannot be fitted. The frequency at which this second dispersion occurs is mainly determined by the conductivity magnitude of the metal core. Using the conductivity of bulk gold the dispersion appears at frequency of 10^{11} - 10^{12} Hz, outside the explored range. The change of sign of the real part of Clausius-Mossotti factor (indicating a transition from positive to negative dielectrophoresis) in correspondence of the second dispersion is critical to explain the reason for the absence of particle deposition observed above 50 MHz independently of the intensity of the electric field applied. The data fit including σ_0 as free parameter gave a value of 0.28 ± 0.05 S/m that is lower than the DC bulk gold conductivity but still four orders of magnitude larger than the conductivity of the surrounding medium.

The core-shell model proposed is a simplified picture of a very complex system that in general required an electrokinetic model for a more satisfactory description. The principal limitations of the core-shell structure are the oversimplification of the surrounding medium properties (due to the presence of molecules, ions and colloidal particles) and the internal structure of the shell (that include a double CTAB layer and counterions layer adsorbed on the surface). From the mathematical formulation of our model, the build-up of charge at each interface determines a dielectric dispersion [207]. Therefore in a core-shell structure only two dielectric dispersions can be obtained. The sharp variation of density at 30 MHz would require a second shell to be mathematically described. However, the intensity of that peak was found weak and largely variable in different colloidal batches thus it was considered negligible in first approximation. Moreover such variability as well as the observed electrical shorts obtained at 30 MHz suggests attributing the peak to the properties of the surrounding medium more than to the particle itself.

The simple core-shell model presented was able to describe the two dielectric

dispersions observed in the dielectrophoretic force and most importantly to prove that the largely used approximation of pure metal nanorod in aqueous medium is no longer valid for Au nanorods of size range 10×40 nm bearing CTAB on the surface.

Next I calculated the magnitude of the F_{DEP} acting on an Au nanorod ($a = 21$ nm, $b = 7$ nm) in aqueous medium ($\epsilon_m = 80\epsilon_0$) inserting in eq.(3.6) the values of \tilde{K}_{eff} and $\nabla |E_{rms}^2|$ calculated in the center of a $2 \mu\text{m}$ gap by finite element method simulations (see section 3.6). The calculated F_{DEP} values for an applied E-field intensity of 1.72×10^6 V/m were 2×10^{-17} N and 7×10^{-18} N at 1 MHz and 15 MHz, respectively. The threshold force required to overcome Brownian motion (F_B) for a single Au nanorod was estimated to be $F_B = 9 \times 10^{-18}$ N from the E_T experimentally observed in section 3.4. The large dielectrophoretic force acting on individual nanorods at 1 MHz compared to the threshold force justifies the high density of particles found experimentally in the electrode gaps (figure 3.2d). On the other hand, at 15 MHz the dielectrophoretic force acting on individual nanorods is comparable to the threshold force and no nanorod deposition should occur in the electrode gaps.

The observed formation of 1D architectures under these experimental conditions (figure 3.2e) was ascribed to the dis-homogeneity of the E-field intensity across the electrode gap. In order to quantify this effect, simulation of the E-field intensity for an applied E-field $E = 1.48 \times 10^6$ V/m across an electrode gap of $2 \mu\text{m}$ containing nanorods assembled in head-to-tail configuration was performed. Simulations were undertaken using commercial finite element software package Comsol Multiphysics 4.1 (COMSOL, SE). The 3D geometry consisted of two electrodes 200 nm width, $1 \mu\text{m}$ long and 50 nm thick separated by $2 \mu\text{m}$ on top of Si/SiO₂ (300 nm) substrate. The nanorod was modeled as a core with a cylindrical body (radius 7 nm and length 28 nm) and two hemispherical caps (radius 7 nm) covered by 2 nm shell. The dielectric constant and conductivity value for nanorod core, shell and surrounding medium extracted from the parametric fit were used in this simulation. The electrodes and particles were covered by $100 \mu\text{m}$ thick water layer ($\epsilon_m = 80\epsilon_0$) with an applied voltage of 4.2 V_{rms} ($E = 1.48 \times 10^6$ V/m in the center of the gap) across the electrodes. Floating condition were applied to the Si boundary and the Neumann condition on the other external boundary.

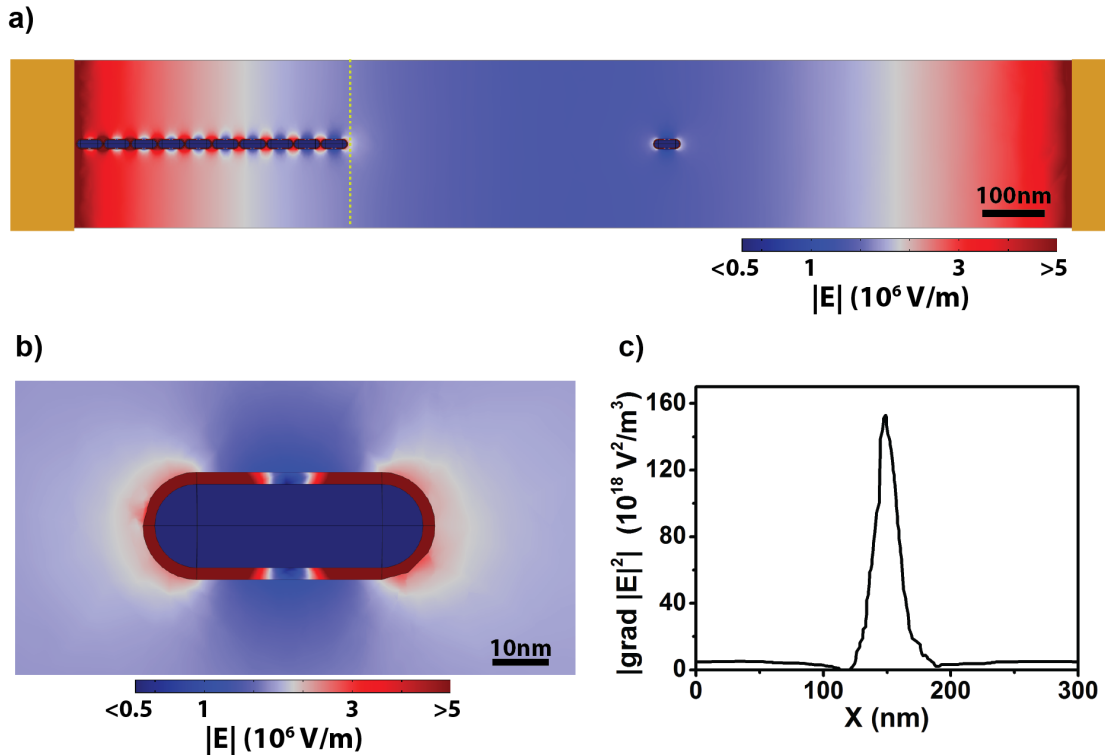


Figure 3.4.: *Finite element method simulation of electric field magnitude inside a $2\ \mu\text{m}$ gap on Si/SiO₂ substrate and around a chain of 10 aligned nanorods having core-shell structure with an applied voltage of $4.2\ V_{rms}$. Electrodes were colored in yellow for clarity. a) Electric field intensity on a plane $12\ \text{nm}$ above the substrate. b) Electric field intensity around an isolated nanorod in the center of the gap showed in a). c) Calculated magnitude of the $\nabla |E|^2$ along the dotted line in a) $10\ \text{nm}$ far from the chain.*

Figure 3.4a shows the E-field intensity simulated in a $2\ \mu\text{m}$ gap having 10 nanorods in head-to-tail configuration and an isolated nanorod in the center of the gap. The E-field intensity was found enhanced in proximity of the electrodes edges of more than one order of magnitude (see section 3.6 for more details), in the inter-nanorod gap along the chain and at the chain outer end. Figure 3.4b shows an enlargement of the E-field in proximity of the isolated nanorod in figure 3.4a. The electric field remained mainly confined within the shell due to the difference in refractive index respect to the surrounding medium. However a field enhancement around the nanorod tips due to the induced polarization was clearly observable. The interaction between the nanorod dipole and the spatial non-homogeneous E-field showed in figure 3.4a drove the migration towards the electrodes, promoting initial attachment of individual

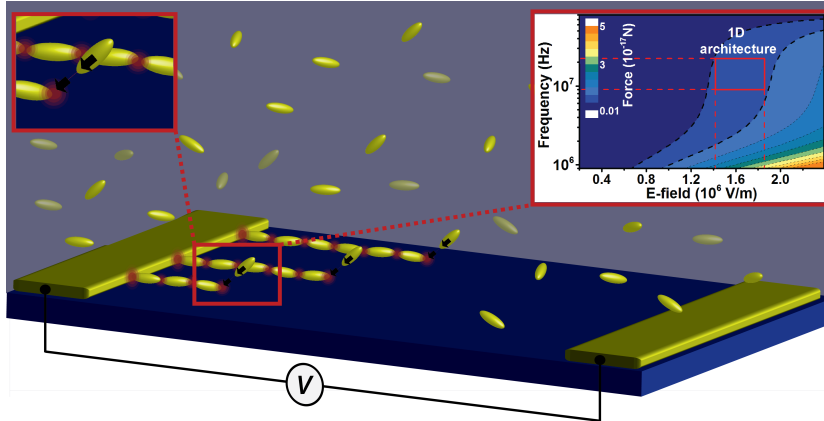


Figure 3.5.: Schematic representation of the assembly process mediated by localized E -field hot spot. After the first nanorod attachment at the electrode edge, an E -field enhanced hot spot is generated at the outer tip of the nanorod due to the nanorod polarization. Under the appropriate condition of E -field intensity and frequency, the following nanorod deposition is driven by the localized E -field hot spot thus allowing a selective assembly at the nanorod tip with high degree of alignment.

nanorods on the electrode edges; subsequently, generation of high magnitude electric field *hot spots* at the nanorod tips induced assembly of nanorods into head-to-tail configuration, as shown in figure 3.5. This process required that the F_{DEP} generated by the applied macroscopic E -field had intensity below the threshold value in order to avoid collective motion of suspended nanorods. Under this condition, in proximity of the nanorod-chain tip, where the enhanced electric field allows formation of a localized area with larger $\nabla |E_{rms}^2|$ (see profile in figure 3.4c), the dielectrophoretic force drove the deposition, resulting in highly selective and well oriented nanorod chain.

We should notice that the presented assembly mechanism relies on the condition that the torque force acting on the nanorod-dipole aligns the main axis of the particle to the external electric field. To prove this hypothesis we calculated the torque force using the expression 3.8 by means of the Clausius-Mossotti factor $\tilde{K}_{eff}(\omega)$ extracted from the core-shell model. In the explored range of frequencies (100 kHz-55 MHz) the torque force was found having a negative value indicating a stable configuration with the main axes aligned respect to the electric field (see figure 3.6a). From the simulated behavior the torque force was expected to change sign below 100-200

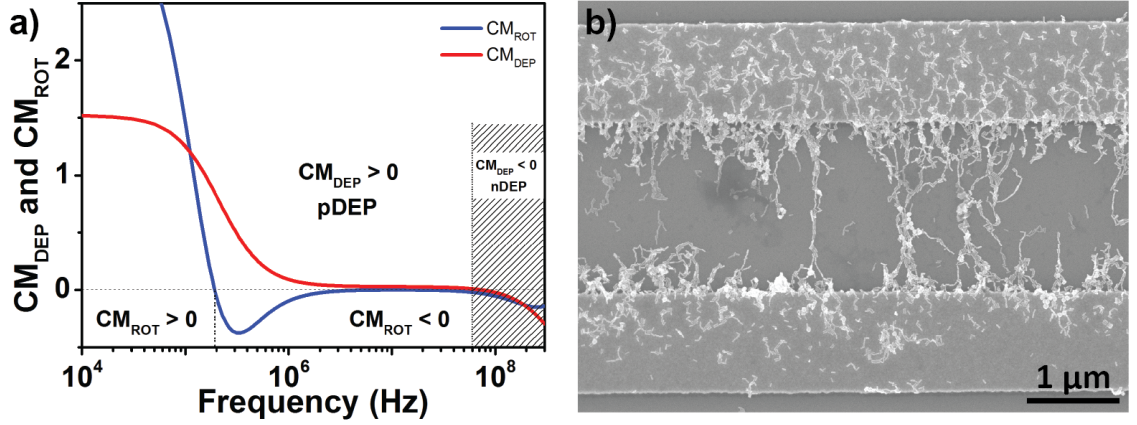


Figure 3.6.: a) Calculated real part of the Clausius-Mossotti factor (CM_{DEP}) and coefficient $CM_{ROT} = \text{Re}[\tilde{K}_\beta \tilde{K}_\gamma]$ showing the behavior of dielectrophoretic force and torque force respectively. Negative values of the CM_{DEP} indicates negative dielectrophoresis instead positive values indicates positive dielectrophoresis. Analogously, negative values of the torque force implicate a stable configuration with the main axes of the nanorod aligned along the electric field lines whereas positive values a preferred alignment of the short axes. b) SEM image of a nanorod deposition obtained at 100 kHz with 10 V_{pp} applied. At this frequency the model predicts a side-by-side alignment of nanorods but a clear evidence of this assembly was not observed.

kHz. However, the predicted change in orientation was not observed experimentally (figure 3.6b) and electrical shortcuts during the assembly process, often occurring at such low frequency range, prevented a satisfactory investigation.

According to the proposed core-shell model, the deposition process can be conveniently described by a contour-plot representation where the force acting on a particle in solution is displayed as a function of both electric field intensity and frequency. As shown in figure 3.7, three main areas can be identified in the plot, corresponding to the experimental conditions $F_{DEP} > F_B$, $F_{DEP} \lesssim F_B$ and $F_{DEP} < F_B$. The condition $F_{DEP} > F_B$ should promote dense network deposition of nanorods in the area between the electrodes; the condition $F_{DEP} \lesssim F_B$ should result in 1D architecture formation and the condition $F_{DEP} < F_B$ should result in no nanoparticle deposition between the electrodes. To show the validity of our model we marked as A-F areas of the plot corresponding to the experimental conditions of electric field deposition shown in figure 3.2a-f. As predicted, points A ($E = 2.2 \times 10^6$ V/m, 15 MHz) and D ($E = 1.72 \times 10^6$ V/m, 1 MHz) were located in the area where

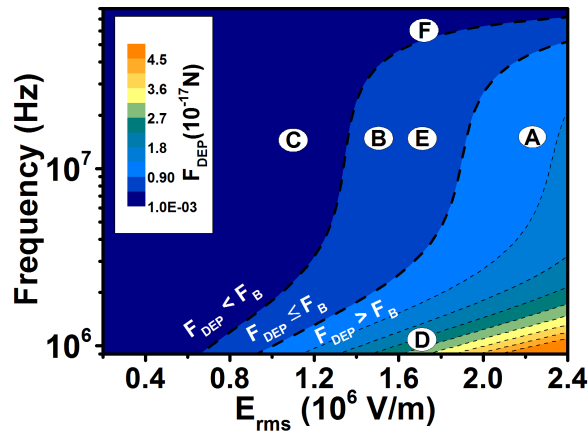


Figure 3.7.: Contour plot showing the magnitude of dielectrophoretic force acting on a single particle as function of frequency and applied electric field intensity.

the condition $F_{DEP} > F_B$ promoted deposition and assembly of nanorods into dense networks predominately oriented in the direction of the applied E-field. Points B ($E = 1.48 \times 10^6$ V/m, 15 MHz) and E ($E = 1.72 \times 10^6$ V/m, 15 MHz) were located in the $F_{DEP} \lesssim F_B$ area and showed reduction in nanorod deposition density and formation of well-ordered and separated 1D architectures. Finally, points C ($E = 0.98 \times 10^6$ V/m, 15 MHz) and F ($E = 1.72 \times 10^6$ V/m, 50 MHz) were located in the area $F_{DEP} < F_B$ and gave no nanorod deposition. The correspondence of deposition processes obtained at different applied E-field (points A, B, C) and at different frequencies (points D, E, F) support our speculation of a 1D architecture formation process driven by a dielectrophoretic process localized in hot spot areas.

Closer observation of 1D nanorod architectures shown in figure 3.2b revealed that individual nanorods constituting individual architectures were well aligned by respect each other. In order to quantify the remarkable degree of alignment we employed the order parameter S defined as $S = \langle 2 \cos^2 \theta - 1 \rangle$ [199], where θ represents the angle between the nanorod long axis and the electric field direction ($S = 0$ for random alignment, $S = 1$ for perfect alignment). For the calculations we used nanorods distributed over an area of $12 \mu\text{m}^2$ within the electrode gap. Histograms of angular distribution of Au nanorods along applied E-field direction are shown in figure 3.8.

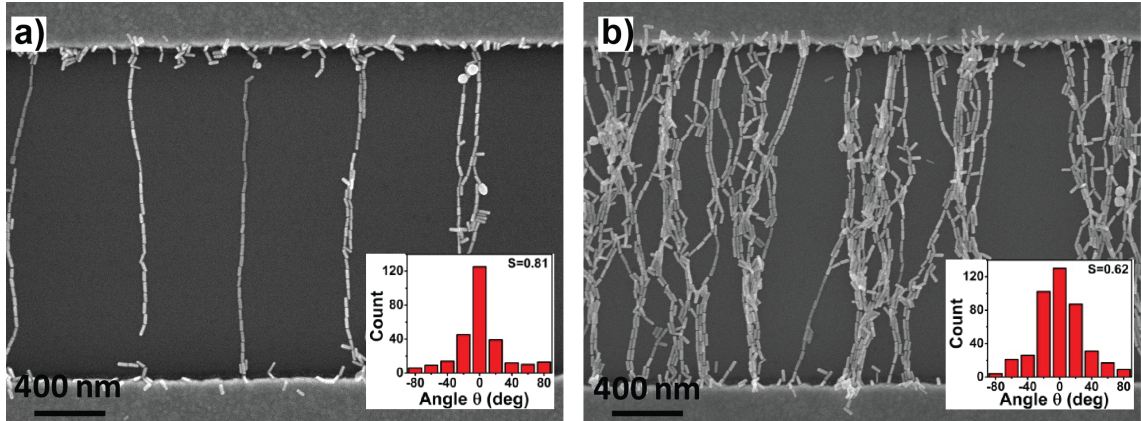


Figure 3.8.: SEM images showing electric field deposition of Au nanorods at the following deposition conditions: a) $E = 1.72 \times 10^6$ V/m, 15 MHz (figure 3.2e); b) $E = 2.20 \times 10^6$ V/m, 15 MHz (figure 3.2a); Insets: angular distribution of Au nanorods along the applied E -field direction.

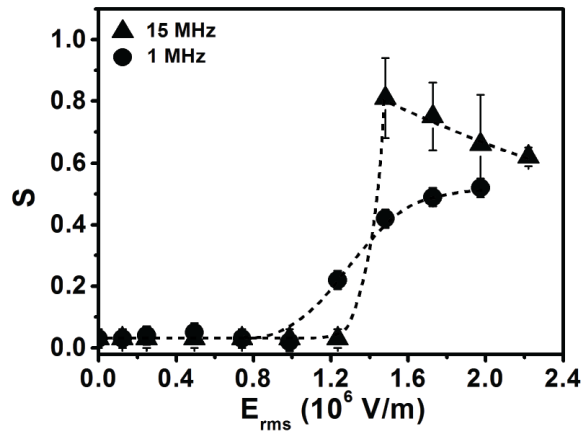


Figure 3.9.: Order parameter S as function of the applied electric field for nanorod 1D architectures assembled at both 1 MHz and 15 MHz. The dashed lines are a guide to the eye.

An $S = 0.81 \pm 0.13$ was obtained for the angular distributions of nanorods in figure 3.8a ($E = 1.72 \times 10^6$ V/m, 15 MHz). This value significantly exceeded order parameters previously reported in literature, where strong inter-nanorod dipoles resulted in randomization of the local electric field in densely accumulated electrode gaps [199]. As comparison an $S = 0.62 \pm 0.03$ was calculated for dense networks shown in figure 3.8b ($E = 2.20 \times 10^6$ V/m, 15 MHz), in agreement with values reported in literature for similar assemblies [199]. Figure 3.9 plots S as function of the applied electric field for nanorod chains assembled at both 1 MHz and 15 MHz, respectively. At 1 MHz, a gradual increase of the degree of alignment up to a saturation value of $S = 0.52 \pm 0.03$ was observed, consistent with the formation of dense networks. At 15 MHz the order parameter increased to 0.81 for experimental conditions corresponding to 1D nanorod architectures formation. At higher applied fields the order parameter decreased to 0.62, due to electric field randomization processes.

3.6. Influence of the substrate on the nanorod assembly

The parameter-space representation (figure 3.7) suggests the independence of the assembly process from the inter-electrodes distance and from the employed substrate. In order to investigate these two key properties we performed the experiments on 5 μm gap on Si/SiO₂ and quartz, setting the E-field intensity and frequency in accordance with the contour plot in figure 3.7. Figure 3.10a shows electric field induced alignment with an applied electric field of $E_{rms} = 1.6 \times 10^6$ V/m at 10 MHz between 5 μm spaced electrodes (8.8 V_{rms} applied between the electrodes) on Si/SiO₂ substrate. Nanorods were found accumulated near and over the metal electrodes with a low density of particle in the center of the gap and no evidence of head-to-tail assembly .

On the other hand, under similar experimental conditions, formation of 1D nanorod chains bridging the 5 μm gap-spaced electrodes were observed on quartz substrate as shown in figure 3.10b. In order to investigate the different behavior observed in

3.6. Influence of the substrate on the nanorod assembly

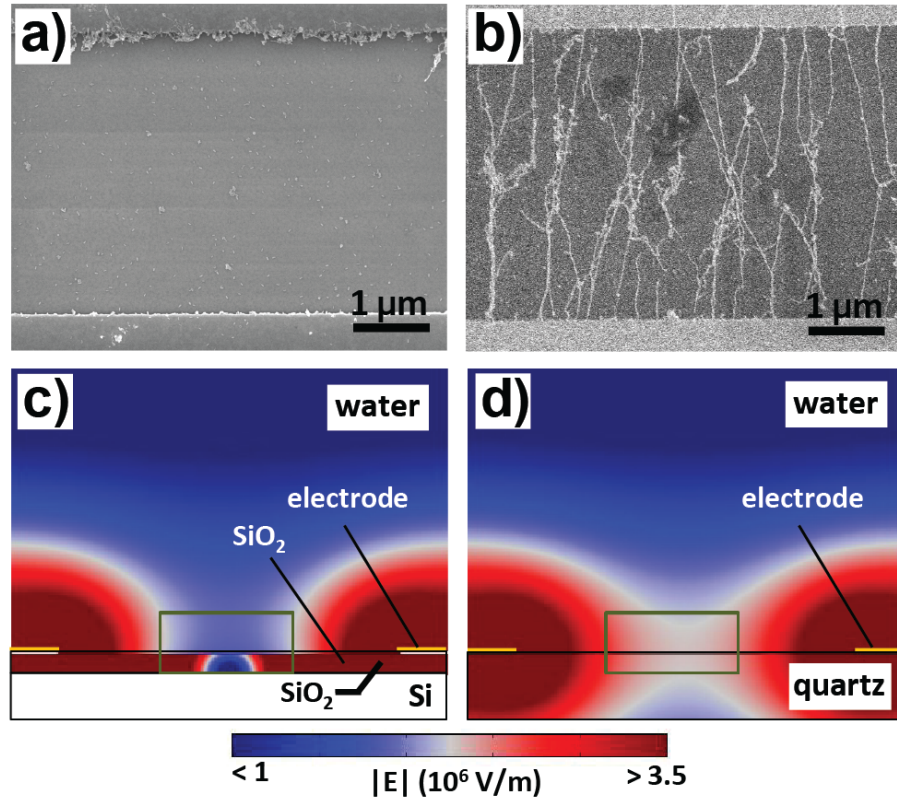


Figure 3.10.: Dielectrophoretic assembly with an applied electric field of $E_{rms} = 1.6 \times 10^6$ V/m at 10 MHz between $5 \mu\text{m}$ spaced electrodes ($8.8 V_{rms}$ applied between the electrodes) on a) Si/SiO₂ substrate and b) quartz substrate. Finite element method simulation of the static electric field in c) Si/SiO₂ and d) quartz substrate with $8.8 V_{rms}$ applied.

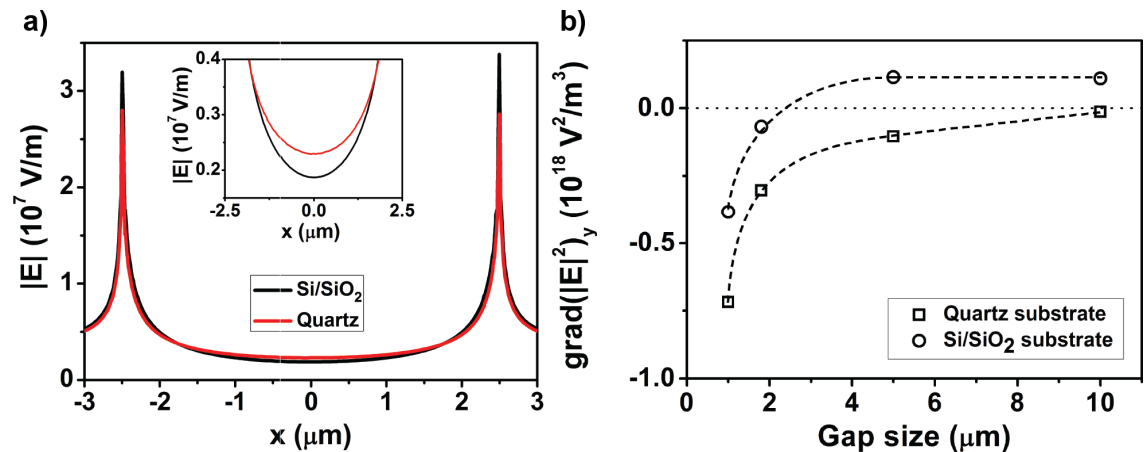


Figure 3.11.: Finite element method simulation of a) the electric field intensity across $5 \mu\text{m}$ gap in Si/SiO₂ and quartz substrate with $8.8 V_{rms}$ applied b) Intensity of the $\nabla |E_{rms}|^2$ in the center of the gap for $1 \mu\text{m}$, $2 \mu\text{m}$, $5 \mu\text{m}$ and $10 \mu\text{m}$ inter-electrodes distance.

Si/SiO₂ and quartz, electric field simulations were undertaken by using commercial software (COMSOL Multiphysic). As the length of the electrodes is much bigger than their width, thickness and mutual spacing, the dimension along the length was ignored, thus reducing this problem to 2D. The investigated geometry consisted of two electrodes 1 μm wide and 50 nm thick separated by 5 μm on a silicon substrate covered with a layer 300 nm thick of SiO₂. The electrodes were considered to be submerged under a 100 μm thick water ($\epsilon = 80\epsilon_0$) layer. Figure 3.10c-d shows a simulation of the electric field strength in proximity of electrodes spaced 5 μm apart in presence of an applied field of 8.8 V_{rms} . The field intensity profile across the gap (figure 3.11a) reached the maximum value in correspondence of the electrode edge. In the center of the gap the intensity profile was found to be of a factor ~ 2 larger on quartz substrate respect to Si/SiO₂.

In figure 3.11b we report the $\nabla |E_{rms}|^2$ values across the gap of 1 μm , 2 μm , 5 μm and 10 μm . Simulations indicate that in Si/SiO₂ substrates, the presence of a floating Si back-gate induced a sign crossover in the central region of the 5 μm electrode gap and a negative dielectrophoresis prevented the accumulation. The negative dielectrophoresis induced by the substrate coupling with the electrodes has been also found in gaps larger than 5 μm [199]. Our experimental data and simulations demonstrate that, depending on the silicon oxide thickness and the dielectric mismatch between silicon oxide and external medium, a critical gap length exists below which the back-gate effect is completely screened (roughly 2 μm in our experiment). We performed simulations also in 100 μm thick quartz substrate. The $\nabla |E_{rms}|^2$ was found positive in all simulated gaps, indicating that quartz substrate is a more suitable alternative to Si/SiO₂ for large area assembly using the described method. This is very relevant results for nanophotonic applications, where large area of ordered arrays of nanorods on transparent substrates might be required.

3.7. Electrical Properties of Au nanorod networks

Finally we measured the electrical properties of fabricated 1D architectures. Figure 3.12a describes the I-V characteristics of the 1D architecture shown in figure 3.2b (point B in figure 3.7). The entire electrode gap was constituted by three individual

3.7. Electrical Properties of Au nanorod networks

chains carrying ~ 50 nanorods in head-to-tail bridging the gap between electrodes, equivalent to a mean nanorod density of $\rho_s = 33 \pm 15 \mu\text{m}^{-2}$. The electrical response was found not linear and the current measured at 6 V was 2 pA, corresponding to an estimated resistance of $1.5 \times 10^{12} \Omega$ above the threshold voltage (4.4 V). The not linear behavior was typical of tunneling transport across multiple barriers whose characteristics were associated to the size distribution of the inter-nanorod gap, with the largest gap dominating the transport across the chain. A hysteretic behavior was also observed, which was ascribed to the presence of co-deposited charged CTAB molecules across the chain. As comparison the electrical characteristics of higher density networks were also measured. Inset of figure 3.12b shows the SEM image of a nanorod deposition obtained at 15 MHz and $1.97 \times 10^6 \text{ V/m}$. These experimental conditions corresponded to a point between A and B of figure 3.7 and lead to a medium density nanorod density deposition ($\rho_s = 135 \pm 10 \mu\text{m}^{-2}$). In contrast with 1D architectures where nanorod chains were well separated, medium nanorod density deposition caused formation and intersection of closely spaced chains resulting formation of small chain networks. Figure 3.12b shows a representative I-V characteristic related to the medium-density nanorod network. For this electrode gap a quasi-linear behavior with current of 30 nA at 1 V was measured, corresponding to a resistance of 40 M Ω that is 5 order of magnitude lower than the value measured in 1D architectures.

For such medium-density networks a small residual hysteresis was also noticeable around the maximum values of explored voltage. We also investigated the electrical behavior of high-density networks shown in figure 3.2a, which corresponded to a $\rho_s = 290 \pm 20 \mu\text{m}^{-2}$ (deposition condition represented by point A in figure 3.7). In this range of ρ_s , nanorods assembled both head-to-tail and side-by-side and formed dense three-dimensional networks within the electrode gap (see inset in figure 3.12c). The I-V curve of figure 3.12c showed a linear electrical response in the range of applied voltages. A current of about 80 A at 10 mV was measured and the calculated resistance was 111 Ω . Remarkably, the resistance was 5 and 10 orders of magnitude lower than resistance calculated for medium-density network and 1D architectures, respectively. Figure 3.12d shows resistance values measured for eight electrode gaps containing 1D architectures, medium and high density nanorod networks. Data

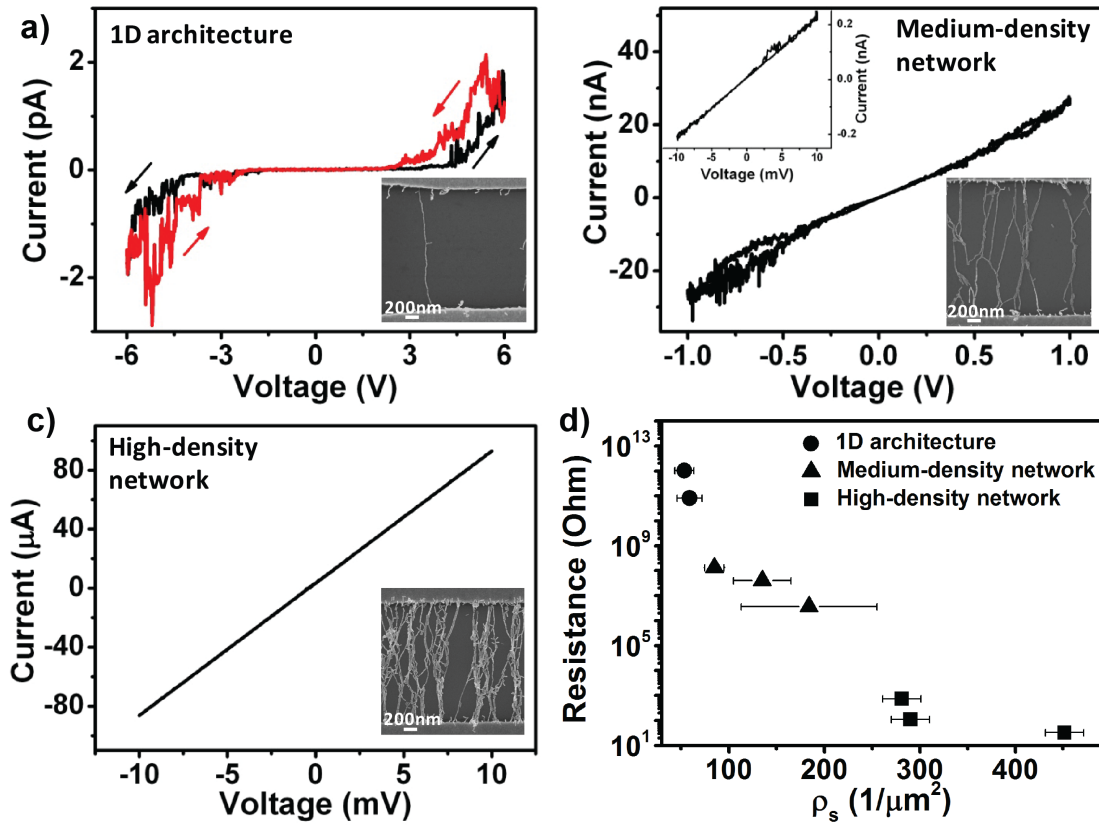


Figure 3.12.: Representative I - V characteristics obtained from a) 1D architecture b) medium-density network and c) high-density network; Insets: corresponding SEM images of measured nanorod architectures; d) Resistance values extracted for eight measured devices with variable Au nanorod densities.

shows a good reproducibility of the results and supports the identification of three different resistive regimes for 1D architecture, medium-density network and high-density network respectively, separated by 3-5 orders of magnitude. The observed variations in resistance were ascribed to the increased number of percolation paths as well as the dimensionality available in assembled nanorod networks of increasing density. Our findings are in agreement with previous studies on highly ordered nanoparticle arrays, where multilayer structures showed conductance several orders of magnitude larger than in monolayer structures [208, 209]. In particular Ressler *et al.* [210] reported 57Ω and $1.5 \text{ M}\Omega$ resistance values for 3D and 2D Au nanoparticle wires, respectively. They associated the observed 5-orders of magnitude difference in conductance to the number of percolation paths due to geometrical difference

between investigated wires.

3.8. Conclusion

In conclusion we demonstrated controlled and reliable formation of 1D Au nanorod architectures by electric field assisted deposition. The unexpected frequency dependency of the deposition process was explained with the introduction of a theoretical model based on the definition of Au nanorods like core shell material entities. A novel contour plot was derived from the theoretical model, which correlated obtained 1D nanorod assemblies with specific sets of experimental parameters. Theoretical and experimental investigation of the influence of the substrate on the electric field mediated assembly was also discussed. Electrical characterization showed that 1D architectures displayed tunneling behavior across the inter-nanorod gap with resistance values of the order of $G\Omega$ s. Denser nanorod networks displayed conductive behavior with resistances of the order of $M\Omega$ and $k\Omega$. The associated increased conductance was ascribed to the higher number of percolation paths in denser networks. The controlled fabrication of 1D architectures demonstrated in this paper is relevant for microelectronic, optoelectronic and molecular sensing applications. In particular, low density architectures with tunneling behavior could find applications as molecular diodes, molecular memory and logic devices.

Chapter 4.

Enhanced Raman scattering in single ZnO nanowire by Au nanorods

*In this Chapter I report enhanced detection of surface optical (SO) Raman mode in single ZnO nanowire by exploitation of plasmonic resonances of Au nanorods. In particular, I present a novel mask-selective droplet deposition method for reproducible fabrication of hybrid structures constituted by Au nanorods deposited on ZnO nanowire surfaces. Detection of SO mode was observed under excitation of the Au nanorod longitudinal plasmon resonance while no detectable signal was found mediated by the transversal plasmon resonance. The excitation wavelength corresponding to the maximum enhancement was intentionally shifted by tuning the optical properties of Au nanorods, thus proving the plasmonic nature of the Raman enhancement observed. Additionally theoretical simulations were performed to support experimental findings. The presented study provides evidence of the capabilities offered by longitudinal plasmonic resonance of Au nanorods for Raman spectroscopy investigation of individual semiconductor nanowires and corroborates the increasing interest of metal nanostructures - semiconductor nanowire hybrid structures for optoelectronic and sensing applications.*¹

¹This work will be published as *Enhanced Raman Scattering of Single ZnO Nanowire by Rod-shaped Au Nanoparticles*, Pescaglini *et al.*, in preparation

4.1. Introduction

In the past decades surface-enhanced Raman spectroscopy (SERS) has been demonstrated having extended capabilities compared to traditional Raman spectroscopy [211]. The intense electromagnetic field generated by plasmonic resonances in proximity to noble metal nanostructures has been largely exploited to compensate for the weak nature of the inelastic photon-phonon scattering, thus solving the low detection sensitivity generally affecting Raman spectroscopy. In fact, the role played by plasmonic resonances in SERS is double: simultaneous amplification of the incident electromagnetic radiation and enhancement of the radiation scattered off by the target object [212, 213]. As a result, 4-8 orders of magnitude enhancement in the Raman signal [37, 93] can be easily achieved with an electric field intensity enhanced by a factor 10^{2-4} (within the $|E|^4$ -approximation) [213], commonly found within 15-nanometer hot spots around a metal nanostructures [11]. The outstanding capabilities of SERS have been vastly used for non-destructive characterization and detection of chemical species down to single-molecule resolution [34, 214]. Despite molecules represent the ideal targets to demonstrate the enhanced abilities compared to standard Raman spectroscopy, also semiconductor nanostructures can benefit from this technique [215]. In fact, SERS analysis can potentially provide meaningful information on crystal defects, surface states, interface crystal quality in heterostructures in both resonant and non-resonant conditions. Among the most investigated semiconductor materials, ZnO nanostructures have attracted significant attention for a wide range of applications such as light emitting diode [216, 217], optical pumped laser [218], UV-photodetectors [219] and piezoelectric nanogenerators [220, 221, 222] applications at room temperature, among others. Various groups have reported enhancement of the Raman signals of ZnO - metal nanocomposites under resonant conditions [215, 223, 224, 225]. More recently, Rumyantseva *et al.* used Au and Ag nanoparticles to investigate ZnO quantum dots [226]. Raman scattering under non-resonant condition of ZnO nanocrystals deposited on a glass substrate were not detected due to the ultra-low scattering cross section in such small nanostructures. Instead, the ZnO $A_1(\text{LO})$ mode was detected from quantum dots deposited either on a substrate containing Au nanoparticles and Ag nanopar-

ticle leading to an enhancement factor of 10^{2-4} . For larger nanostructures such as semiconductor nanowires, generation of highly localized electric field hot-spot at a desire location has been achieved by tip-enhanced Raman spectroscopy (TERS), where the field enhancement is obtained between a laser-illuminated STM tip and the nanowire [227, 228]. Matsui *et al.* used this approach to resolve nanoscaled variation in crystalline properties of a GaN substrate with resolution below the diffraction limit of the light [229]. Moreover due to the different electric field configuration generated by the tip, forbidden Raman modes were also observed [230]. Alternatively, covering the nanowire surface with SERS-active elements would offer the possibility to combine the advantage of tip-enhanced Raman spectroscopy (TERS) with the simultaneous generation of multiple hot-spot, as in SERS, to benefit from the stronger signal collected [231]. For example, Peng *et al.* investigated the Raman scattering in Si nanowires decorated with Ag nanoparticles by galvanic displacement technique [232]. They obtained a 7-fold enhancement in the resonant Raman scattering from a Si nanowire with 30 nm diameter, including the enhancement of a new Raman band at 495 cm^{-1} due to HF etching in the galvanic process. Similar approach was successfully used by Chen *et al.* to decorate Si nanowires with gold nanostructures of different morphologies [134]. Resonant Raman spectroscopy revealed that the highest enhancement (by factor 24) of the Si TO mode was obtained with two spherical nanoparticles (70 nm diameter) attached on both side of the nanowire. However, despite the encouraging results obtained so far, decoration techniques such as surface functionalization [233], galvanic displacement [234] and sputtering [235] have shown limited availability of metal nanostructure geometries and semiconductor materials, thus constraining the materials suitable for decoration and plasmonic properties of the SERS-active elements (see also section 1.3). Consequently, the understanding of the real capabilities of this approach for characterizing semiconductor nanowires is still vastly unexplored. For instance, non-spherical nanostructures such as rod-shaped metal particles have been scarcely explored for this application despite demonstrations of larger enhancing capabilities compared to the spherical counterpart [89, 236].

In this Chapter I demonstrate that Raman scattering of surface optical (SO) modes an individual ZnO nanowire can be detected in non-resonant conditions by

exploring the longitudinal plasmonic resonance mediation of chemically synthesized Au nanorods deposited on the nanowire surface by a novel mask-selective droplet deposition. This approach provides a general method to decorate *in situ* semiconductor nanowires with colloidal metal nanostructures having engineered optical properties with high yield and reproducibility. By exploiting this method we demonstrated for the first time tunable Au nanorod-mediated SERS on large band-gap semiconductor nanowire in non-resonant conditions. In particular, we successfully measured SO modes of ZnO with laser wavelength of 647 nm, otherwise not detected in the absence of Au nanorods. Moreover, by engineering the optical properties of the metal nanostructures, enhancement of the phonon modes was achieved with different laser wavelengths on the same nanowire. The experimental results were supported by finite-difference time domain (FDTD) simulations used to investigate the central role played by plasmonic resonances in Au nanorods. The results show the powerful capabilities of the presented approach for the characterization of single semiconductor nanowires with a resolution below the traditional Raman spectroscopy and open up a promising scenario for integration of these hybrid nanostructures in optoelectronics and sensing devices.

4.2. Experimental section

ZnO nanostructures were grown by CVD using vapour-liquid-solid (VLS) mechanism in a high temperature tube furnace. Briefly, a p-Si chip sputtered with 5 nm Au was placed in the colder region downstream of a furnace tube. ZnO powder was heated at 1350°C and nanowires were grown under Argon gas flow at substrate temperatures between 1100-950°C. Dimensional statistical analysis on the obtained nanowires, gave lengths between 1 μm to 10 μm with a mean value of 5 μm and diameters between 40 nm and 500 nm (mean value around 200 nm). ZnO nanowire were transferred by dry-method onto a clean Si(n⁺⁺)/SiO₂ (300 nm) substrate.

Au nanorods were synthesized using a seed-mediated method described in section 2.2.2. The as prepared Au nanorod solution (1 ml) was centrifuged twice to remove CTAB excess and re-dispersed in 1 ml of deionized water, resistivity 18 M·cm. The final CTAB concentration was estimated to be 0.05 mM using the method

described in section 2.2.3. Dimensional statistical analysis of 100 nanorods gave a mean nanorod diameter and length of respectively 29 ± 5 nm and 68 ± 5 nm (aspect ratio of 2.4 ± 0.2). Scanning electron microscopy (SEM) characterization was performed using a Scanning Electron Microscope (JSM 7500F, JEOL UK) at operating voltages of 10 kV.

After dry transfer of ZnO nanowires on a clean Si(n⁺⁺)/SiO₂ (300nm) substrate, the substrate was covered by a layer of photoresist (S1813) by spin-coating. For the sample A, the photoresist was baked at 120°C for 2 min and exposed to O₂-Plasma using RIE system operating at 100 W with O₂ flow of 50 sccm and a process pressure of 45 mTorr for 7 min in order to reach a resist thickness of ~100 nm. Sample B was baked at 110°C and the photoresist etched by two steps of exposition to UV light and development in MF319 for few seconds in order to reach similar final resist thickness. Au nanorods solution were dropped on top of the substrate and dried at constant temperature of 110°C. Nanorods not attached on the nanowire surface together with the residual resist were removed by standard solvent cleaning.

Raman measurements were carried on in back-scattering configuration (where the wave vectors of the incident and the scattered light are collinear). A microscope objective (100 X) focused the laser on the sample with a spot size ~1 μm. The microscope is coupled to a T64000 triple spectrometer from Jobin-Yvon and a nitrogen-cooled charge-coupled device detector. The spectral resolution of the whole system was of 2 cm⁻¹ at 500 nm.

4.3. Classical Raman scattering theory

Raman spectroscopy is a non-invasive and versatile technique extremely useful for studying vibrational modes, interband electronic transition, exciton and electron-phonon interactions of homogeneous and heterostructured semiconductors [237].

Vibrational modes in crystalline semiconductor are quantized in phonons and the atomic displacement $\delta(\mathbf{r}, t)$ associated with a phonon can be expressed as plane waves [238] :

$$\delta(\mathbf{r}, t) = \delta(\mathbf{q}, \omega_0) \cos(\mathbf{q} \cdot \mathbf{r} - \omega_0 t) \quad (4.1)$$

with wavevector \mathbf{q} and frequency ω_0 . The electric susceptibility χ of the material will be affected by the fluctuation of density. Within the adiabatic approximation, χ can be taken to be a function of δ . At room temperature the atomic vibration are small compared to the lattice constant, so electric susceptibility can be expanded as a Taylor series in δ :

$$\chi(\delta) = \chi_0 + (\partial\chi/\partial\delta)_0\delta(\mathbf{r}, t) + \dots \quad (4.2)$$

where the χ_0 is the unperturbed susceptibility and the second term is the variation induced by the phonon $\delta(\mathbf{r}, t)$. When a plane wave described by

$$\mathbf{E}(\mathbf{r}, t) = \mathbf{E}_i(\mathbf{k}_i, \omega_i) \cos(\mathbf{k}_i \cdot \mathbf{r} - \omega_i t) \quad (4.3)$$

is incident on the material, an associate polarization $\mathbf{P}(\mathbf{r}, t)$

$$\mathbf{P}(\mathbf{r}, t, \delta) = \chi(\mathbf{k}_i, \omega_i, \delta)\mathbf{E}_i(\mathbf{k}_i, \omega_i) \cos(\mathbf{k}_i \cdot \mathbf{r} - \omega_i t) \quad (4.4)$$

with same wavevector and frequency of the radiation is induced in the material. Inserting eq.(4.1) and (4.2) in eq.(4.4) we can write the polarization as

$$\mathbf{P}(\mathbf{r}, t, \delta) = \mathbf{P}(\mathbf{r}, t, \delta)_0 + \mathbf{P}(\mathbf{r}, t, \delta)_S + \mathbf{P}(\mathbf{r}, t, \delta)_{AS} \quad (4.5)$$

where $\mathbf{P}(\mathbf{r}, t, \delta)_0$, $\mathbf{P}(\mathbf{r}, t, \delta)_S$ and $\mathbf{P}(\mathbf{r}, t, \delta)_{AS}$ are defined as

$$\mathbf{P}(\mathbf{r}, t, \delta)_0 = \chi_0(\mathbf{k}_i, \omega_i, \delta)\mathbf{E}_i(\mathbf{k}_i, \omega_i) \cos(\mathbf{k}_i \cdot \mathbf{r} - \omega_i t) \quad (4.6)$$

and

$$\mathbf{P}(\mathbf{r}, t, \delta)_S = \frac{1}{2}(\partial\chi/\partial\delta)_0\delta(\mathbf{q}, \omega_0)\mathbf{E}_i(\mathbf{k}_i, \omega_i) \cos[(\mathbf{k}_i + \mathbf{q}) \cdot \mathbf{r} - (\omega_i + \omega_0)t] \quad (4.7)$$

and

$$\mathbf{P}(\mathbf{r}, t, \delta)_{AS} = \frac{1}{2}(\partial\chi/\partial\delta)_0\delta(\mathbf{q}, \omega_0)\mathbf{E}_i(\mathbf{k}_i, \omega_i) \cos[(\mathbf{k}_i - \mathbf{q}) \cdot \mathbf{r} - (\omega_i - \omega_0)t] \quad (4.8)$$

The first term on the right hand side in eq.(4.5) is responsible for the elastic scattering of the light (Rayleigh scattering). The radiation produced by the second and third term in the polarization is called respectively Stokes scattered and anti-Stokes scattered light. In the Stokes process an incident phonon with frequency ω_i and momentum \mathbf{k}_i will be scattered with frequency $\omega'_i = (\omega_i - \omega_0)$ and momentum \mathbf{k}'_i and a phonon with frequency ω_0 and momentum $\mathbf{\Omega} = \mathbf{k}_i - \mathbf{k}'_i$ will be created. In the anti-Stokes process a phonon with frequency ω_0 and momentum $\mathbf{\Omega}$ will lose its energy to generate a photon with $\omega'_i = (\omega_i + \omega_0)$ and momentum $\mathbf{k}'_i = \mathbf{k}_i + \mathbf{\Omega}$. At room temperature most of the phonons are in the ground state so Stokes process are more likely than Anti-Stock process. The intensity of the scattered radiation can be calculated from the induced polarization and it is proportional to [237]

$$I \propto |\mathbf{e}_i \cdot \mathfrak{R} \cdot \mathbf{e}_s|^2 \quad (4.9)$$

where $\mathfrak{R} = (\partial\chi/\partial\delta)_0\delta(\omega_0)$ is the Raman tensor. The scattered intensity is dependent from the vibration amplitude δ , the third-rank tensor $(\partial\chi/\partial\delta)_0$ and the incident and scattered polarization unit vectors \mathbf{e}_i and \mathbf{e}_s . The consequence of the eq.4.9 is that the scattered radiation vanishes for certain polarization \mathbf{e}_i and \mathbf{e}_s and scattering geometries. The so called *selection rules* are very useful for determining the symmetry of Raman-active phonons. By measuring the scattered light intensity in different polarization it is possible to deduce the frequency and symmetry of the zone-centre phonon mode and two-photon Raman scattering allows to estimate the phonon density of state.

In semiconductor with wurtzite symmetry, such as ZnO, the zone-center optical phonon can be classified according to the irreducible representation $\Gamma = A_1 + E_1 + 2E_2 + 2B_1$. The B_1 modes are silent modes, the A_1 and E_1 are polar modes and E_2 are non-polar modes (figure 4.1). The Raman tensors for each of these modes are given by [239]

$$E_2^{(1)} = \begin{pmatrix} d & 0 & 0 \\ 0 & -d & 0 \\ 0 & 0 & 0 \end{pmatrix}, E_2^{(2)} = \begin{pmatrix} 0 & d & 0 \\ d & 0 & 0 \\ 0 & 0 & 0 \end{pmatrix}, E_1(x) = \begin{pmatrix} 0 & 0 & c \\ 0 & 0 & 0 \\ c & 0 & 0 \end{pmatrix}$$

$$E_1(y) = \begin{pmatrix} 0 & 0 & 0 \\ 0 & 0 & c \\ 0 & c & 0 \end{pmatrix}, A_1(z) = \begin{pmatrix} a & 0 & 0 \\ 0 & a & 0 \\ 0 & 0 & b \end{pmatrix}$$

For polar modes, the coordinate in parentheses denotes the direction of the phonon polarization. The Raman scattering experiments discussed in this Chapter are referred to the Stokes process in ZnO nanowire in backscattering geometry with light impinging perpendicular to the long axis of the nanowire. In this configuration the Raman tensors allow exclusively the detection of E_2 , $A_1(TO)$, $E_1(TO)$ and surface modes.

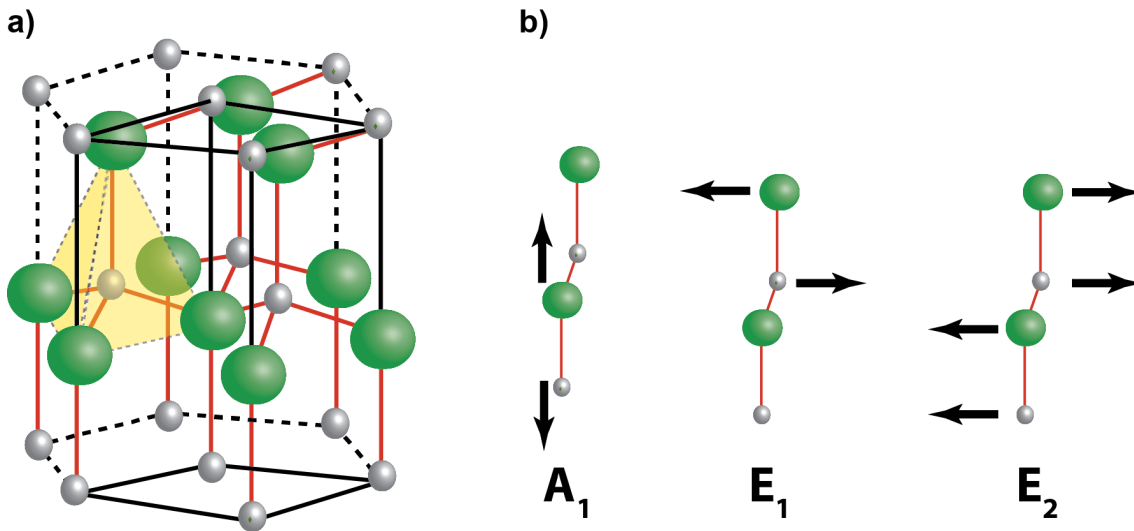


Figure 4.1.: a) Representation of the wurzite crystal structure b) Schematic of the ions displacement related to the two polar phonon modes A_1 and E_1 , and the non-polar mode E_2 .

4.4. Fabrication of Au nanorod-ZnO nanowire hybrid nanostructure

Herein we present a new approach that allow high-yield and reproducible fabrication of nanowires decorated with metal nanoparticle. In particular, the process was designed to maximize particle deposition on the nanowire surface and optimized for nanowire size and nanorods solution used in the experiments performed in this work.

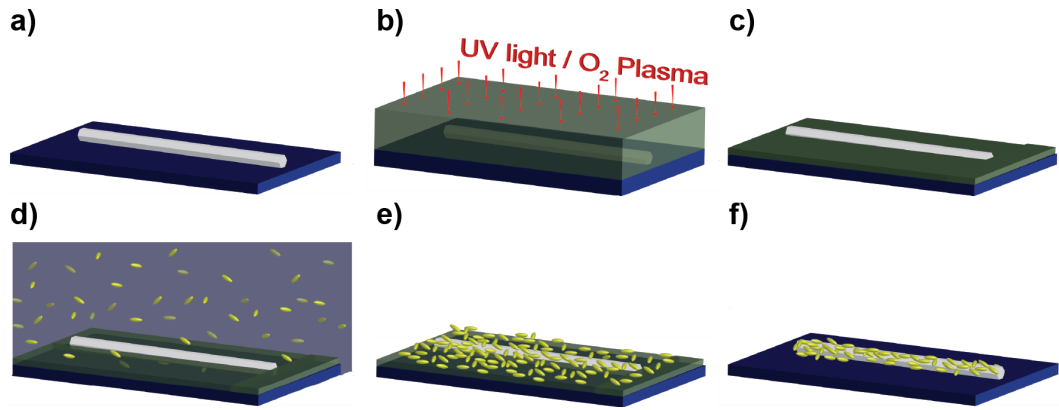


Figure 4.2.: Representation of the new process for particle deposition. a) ZnO nanowire deposited on Si/SiO₂ substrate b) Resist deposition by spin-coating and etching by O₂ plasma (process A) or UV light exposition (process B). c) After etching the layer thickness is smaller than the nanowire diameter d) drop and dry deposition of colloidal metal nanorods e) Au nanorods cover the entire surface and the nanowires f) after the lift-off the resist is completely removed and only nanorods attached on the nanowire are left.

An overview of the process is illustrated in figure 4.2. ZnO nanowires were dispersed on Si(n⁺⁺)/SiO₂ (300nm) substrate by mechanical transfer (Figure 4.2a). After the resist deposition, the resist layer was etched to reduce the thickness below the nanowire diameter as shown in figure 4.2b-c. After nanorods deposition (figure 4.2d-e) the substrate was cleaned to remove completely the residual resist and the excess of surfactant precipitated during the nanoparticles deposition (figure 4.2f). Details of the nanofabrication steps including resist deposition, etching, nanorod deposition and lift-off are described in the following paragraphs and fabrication protocols can be found in appendices.

Resist deposition

The Si/SiO₂ substrate with ZnO NWs was firstly covered by a spin-coated resist (S1813) and baked on a hot plate at 120°C. The resist thickness was measured with a TENCOR profilometer and was found having a reproducible value of 1.4 μm over the centre of the substrate and reaching higher values (up to 1.8-2 μm) near the sample edges. Only the homogeneous area covered by 1.4 μm of resist was further processed. The thickness of the resist was set to be much larger than the nanowire

diameter (200-300 nm) so the resist surface remained almost flat even above the NWs with a maximum variation below 30 nm.

Resist etching

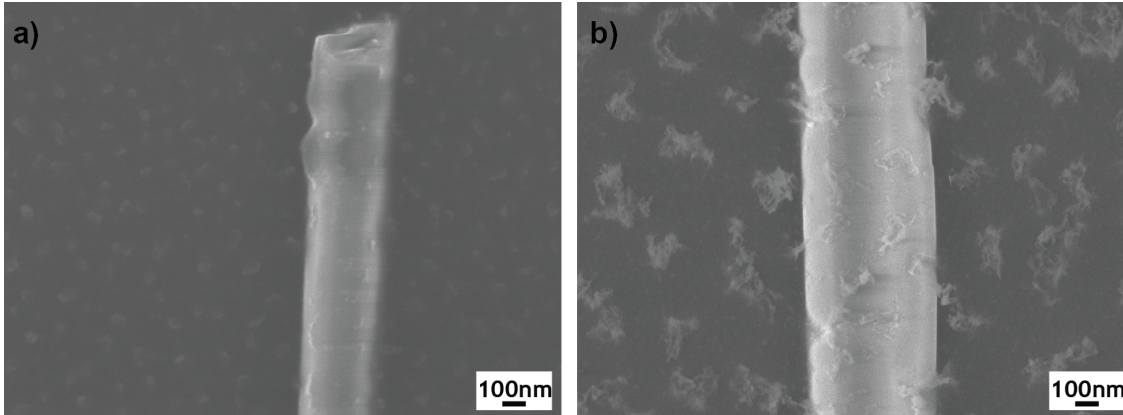


Figure 4.3.: Resist etching by oxygen plasma (process A). a) Scanning electron microscopy image of ZnO nanowire after plasma process with parameters oxygen flow: 50 sccm, forward power: 100 W, pressure: 100 mTorr, (etching rate ~ 170 nm/min) and b) Oxygen flow: 50 sccm, forward power: 100 W, pressure: 30 mTorr (etching rate ~ 250 nm/min)

In the following step the resist layer was etched to reduce the thickness to a value smaller than the NW diameter (statistical mean value calculated on a large number of NWs was used). Two processes, namely A and B, were used to etch the resist. In process A the sample was exposed to oxygen plasma while in process B a lithographic technique was employed to partially remove the resist.

In process A the substrate was exposed to oxygen plasma inside a Reactive-Ion Etching system (RIE). The system chamber was pumped down to $2 \cdot 10^{-6}$ mbar before a constant flow of oxygen gas (50 sccm) was activated. The mechanical and chemical etching of the resist was previously investigated by testing the process under different pressure conditions, ranging between 30 to 100 mTorr with an applied forward power of 100 W. Representative SEM images of two tests at (a) 100 mTorr, 100 W and (b) 30 mTorr, 100 W are shown in Figure 4.3a-b. At 100 mTorr the etching rate was ~ 170 nm/min, lower than the value found at 30 mTorr (~ 250 nm/min). The difference in the rate suggests that under 100 mTorr the etching is more isotropic

4.4. Fabrication of Au nanorod-ZnO nanowire hybrid nanostructure

compared to test (b) where lower pressure allows unistropic and mechanical etching directed perpendicularly to the substrate plan.

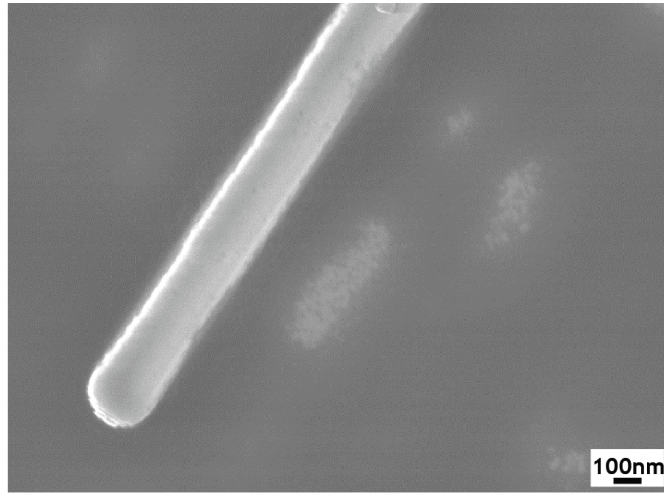


Figure 4.4.: Scanning electron microscopy image of a ZnO nanowire after resist etching by process B with ~ 100 nm of residual layer.

After oxygen plasma, the resist thickness was reduced below the nanowire diameter, however under condition (a) (figure 4.3a) the nanowire surface still has a residual layer that cannot be removed with a longer plasma time, possibly due to a chemical degradation of the resist during the process. The etching under condition (b) (figure 4.3b) performs better although random fluffy residuals were found over the entire substrate. The main advantage of this process consist in the reproducibility and consistency of etching rates therefore the results. However, even in the best conditions showed in figure 4.3b, a complete removal of resist from the upper part of nanowire was not obtained. Moreover, although SEM images did not evidence any surface damage on the nanowire, the plasma treatment could affect the properties of nanowires. In order to address this issue we developed an alternative process (B) to reduce the resist thickness. The spin-coated resist was baked at 110°C on a hot plate for 2 min than was loaded on a mask-aligner and exposed to UV light. Following the exposition, the resist was developed in MF-319 and the thickness reduced to 900-700 nm. A second step of UV exposition and development allowed to reduced the thickness in the range of 100-200 nm. A representative SEM image is reported in figure 4.4. Nanowires surface was found very clean without any visible residuals

(compared to the plasma treatment in figure 4.3). We should notice that despite the better result, this process is very sensitive to the baking temperature, exposure and development time thus the reproducibility of the resist thickness was within ~ 100 nm.

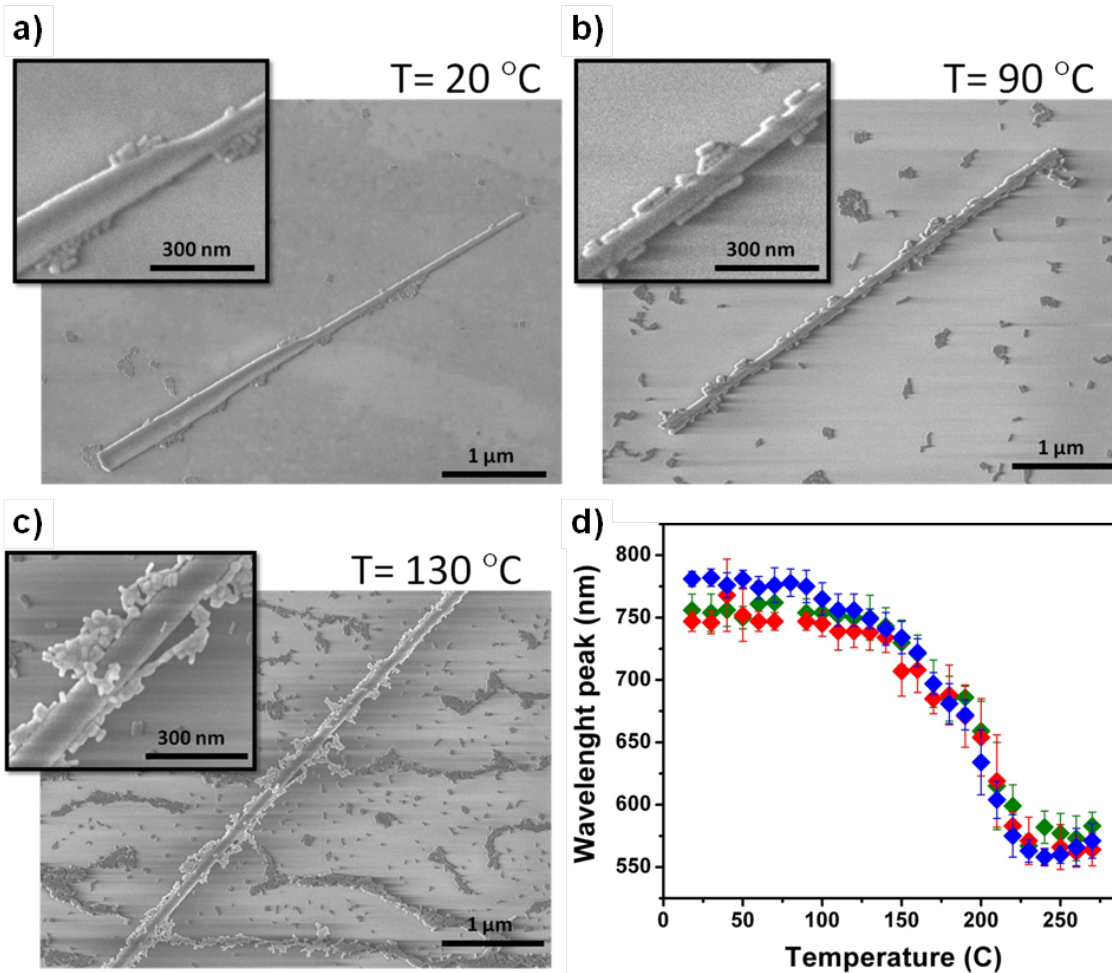


Figure 4.5.: *Droplet deposition of colloidal Au nanorods on ZnO nanowire deposited on Si/SiO₂ substrate at a) 20 °C b) 90 °C c) 130 °C. d) Longitudinal surface plasmon peak positions in Au nanorods deposited on glass slide after 5 min of heating at different temperatures.*

Nanorods deposition and lift-off

After resist etching, colloidal particles were deposited on the substrate by droplet evaporation. Despite the simplicity of the process, several particle configurations can be obtained with this method, depending on particle-solvent interaction, solvent-substrate interaction and evaporation condition.

4.4. Fabrication of Au nanorod-ZnO nanowire hybrid nanostructure

Systematic investigation of the nanorods deposition by droplet evaporation was carried out on Si/SiO₂ substrate. No significant differences were found when the process was repeated on Si/SiO₂ substrate covered by resist. For water-based colloidal solution where a large contact angle is formed between the drop and the SiO₂ substrate, the convective fluid motion inside the drop, induced by surface evaporation, results in particle accumulation at the drop edge (coffee-stain effect) [102]. At low evaporation rate, the coffee-stain effect prevents particle deposition over the entire surface covered by the drop, limiting the effectiveness of this process to decorate nanowires deposited on the substrate. In order to maximize the nanorod distribution, a systematic analysis of the droplet evaporation process was performed by heating the substrate at different temperatures (figure 4.5). At room temperature the evaporation rate was slow enough (5 μ l drop required 30 min to dry) that coffee stain effect took place, thus accumulating nanorods on the external edge of the drop over a ring of tens of microns. ZnO nanowires located within the ring were covered by a dense and continuous layer of packed nanorods. Outside the accumulation ring, low density of nanorod was found, resulting in a poor effectiveness in nanowire decoration (figure 4.5a).

At T=90 °C, the faster evaporation rate reduced the coffee-stain effect, the thickness of the accumulation ring was reduced down to few microns and single or small cluster of particles were found all over the surface covered by the drop. Most importantly, significant increasing of the number of particles attached on the nanowires is clearly visible in figure 4.5b. Particles were found attached on the nanowire side with a reasonable degree of alignment parallel to the main axis of the nanowire. This configuration can be ascribed to the formation of a thin film of solvent with the expected concave meniscus between the nanowire side and the substrate during the evaporation. The residing meniscus determines both particle accumulation on the nanowire side and alignment due to the nanorod anisotropy.

At higher temperatures the anisotropic nanorod shape could become no longer stable. Previous studies showed that, due to the thermodynamic tendency of lowering the surface energy, the rod-shape is unfavorable relative to the spherical-shape under exposure to light or heat [240, 241, 242]. Nanorods melted together or, if well separated, changed gradually shape into spherical particles. Figure 4.5c shows the

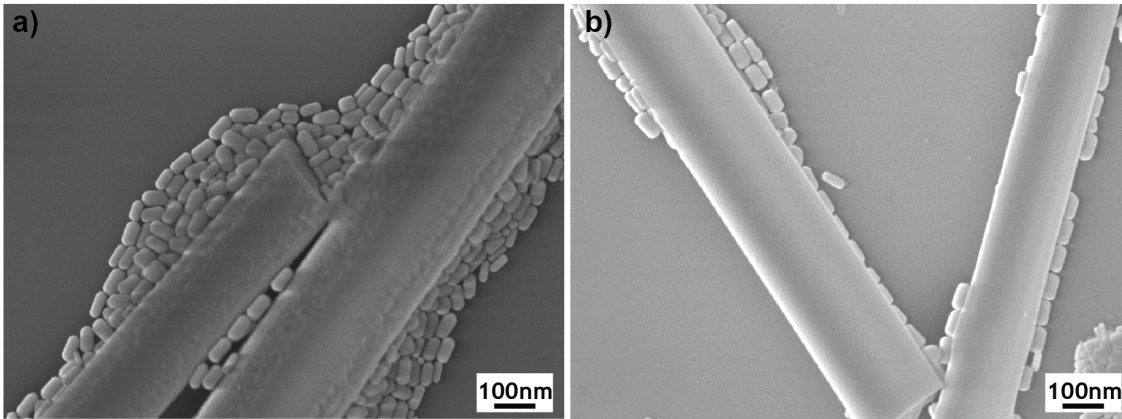


Figure 4.6.: Drop deposition of nanorods from solutions with different CTAB concentrations. Scanning electron microscopy image of ZnO nanowire after nanorod deposition from a solution with a) 0.2 mM and b) 0.06 mM of CTAB

nanorod deposition obtained when the evaporation temperature was set to 130 °C. Despite the higher nanorod density found on the substrate due to the faster evaporation rate, the inset in figure 4.5c clearly highlight cluster of nanorods partially fused. This reshaping/fusing process at temperature much below the melting point of the gold was investigated in more detailed in figure 4.5d. For this experiment, drops of nanorod solution were deposited on three glass slides and the longitudinal surface plasmon recorded by Uv-vis spectrophotometer after heating up the substrate for 5 min at progressively higher temperatures. The plasmon peak was found to be stable until $\sim 120^{\circ}\text{C}$. At higher temperature a blue-shift was observed which reached the value of ca. 550nm above 200°C , thus indicating a gradual reduction of the nanorods anisotropy to the spherical shape. Further investigation indicates that $T=110^{\circ}\text{C}$ is the highest reachable temperature that minimizes the coffee-stain effect without affecting the nanorod shape. During the drop evaporation, it was also observed that the concentration of the stabilizing surfactant CTAB in solution damaged the ZnO nanowire surface. Figure 4.6a shows a representative ZnO NW after exposition to a solution of 0.2 mM of CTAB. The surface roughness is evident after the drop and dry process. Further experimental data showed that the etching can be avoided by decreasing CTAB concentration below 0.1 mM in solution (4.6b).

It should be noticed that the direct droplet deposition on the substrate without

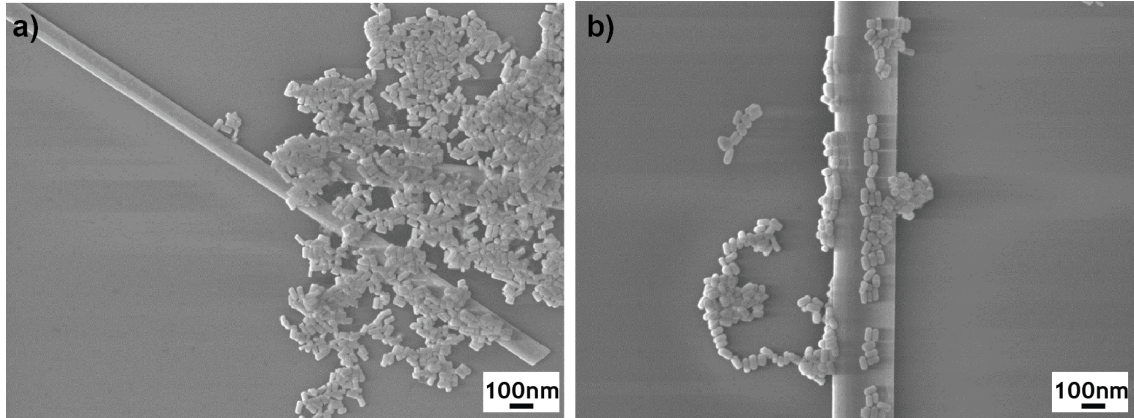


Figure 4.7.: Scanning electron microscopy image of Au nanorods-ZnO nanowire hybrid nanostructures obtained by mask-selective droplet deposition method involving a) process A and b) process B.

resist layer also results in decoration of the nanowires with the colloidal nanorods. However with this approach nanorods were found accumulating only on the side of the nanowires (as shown in figure 4.6), thus limiting the nanowire surface covered. Increasing the nanorod density in solution could potentially solve this drawback even though larger nanorod clusters would result nearby each nanowire. These closely-packed random assemblies of nanorods were found preventing Raman spectroscopy studies on the hybrid nanostructure and forming electric short-cuts in hybrid FET devices investigated in Chapter 6. Therefore the mask-selective deposition process is strictly required to fabricate the devices. Finally, the excess of surfactant (CTAB) and the residual resist were removed by standard lift-off technique. Figure 4.7 show a SEM image of the hybrid structures obtained after droplet deposition and resist removal. Nanorods were found attached to the entire nanowire surface available while the substrate was maintained almost cleaned from nanorods compared to the standard droplet deposition in figure 4.5.

4.5. Raman scattering in single Au nanorods decorated ZnO nanowire

The mask-selective droplet deposition method developed represents an effective way to decorate semiconductor nanowires with metal nanostructures having engineered

optical properties. The well-known seed-mediated protocol is able to synthesise nanostructures with sizes from few nanometers up to hundreds of nanometers and aspect ratio from 1 (spherical nanoparticles) to more than 20 [52].

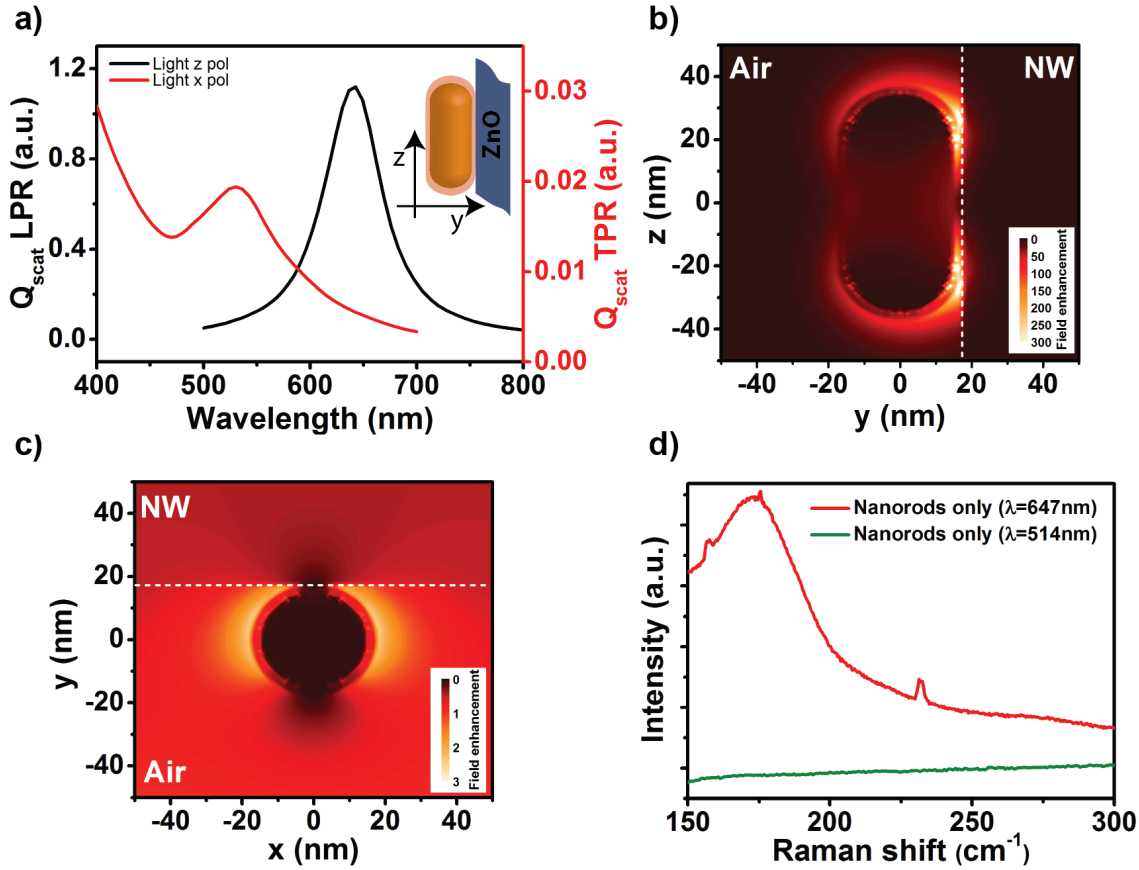


Figure 4.8.: a) *FDTD* simulation of scattering cross section normalized to the geometrical cross section of a Au nanorod 29×68 nm with 3 nm dielectric shell (refractive index $n=1.4$) on a ZnO nanowire (refractive index $n=1.98$) under light polarized along the z -axis (black curve) and x -axis (red curve). *FDTD* simulation of the electric field enhancement factor under light polarized along b) z -axis and c) x -axes. d) Raman spectra of CTAB molecules detected from Au nanorods deposited on SiSiO_2 substrate under laser radiation at 647 nm (red curve) and 514 nm (green curve).

Therefore, plasmonic resonance frequencies in Au nanorod-semiconductor nanowire hybrid nanostructures can be easily tuned by acting on the nanoparticle aspect ratio and surrounding medium, as discussed in Chapter 2. In particular, we observed in section 2.3 that longitudinal plasmonic resonance (LPR) shows a larger cross section and extreme sensitivity to both aspect ratio and surrounding medium [243]

4.5. Raman scattering in single Au nanorods decorated ZnO nanowire

compared to the transversal plasmonic resonance (TPR). Accordingly, a larger field enhancement factor is expected to result from excitation of LPR respect to TPR.

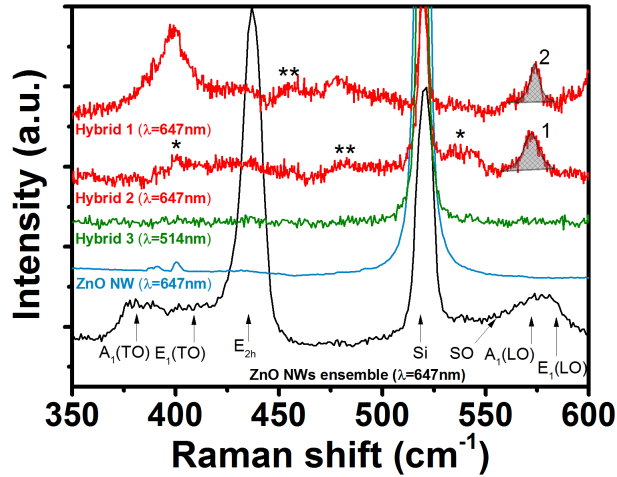


Figure 4.9.: Representative Raman spectrum of two single hybrid nanostructure under laser wavelength of 647 nm (red lines) showing variable peaks attributed to the CTAB (marked with asterisks) and a reproducible peak at 574 cm^{-1} ; Raman spectrum of an hybrid nanostructure with laser at 514 nm (green line); spectrum of a bare ZnO nanowire at 647 nm (blue line); Raman spectrum of a high-dense spaghetti-like ZnO naowires on Si/SiO₂ substrate obtained with laser wavelength of 647 nm. The $A_1(TO)$ peaked at 378 cm^{-1} , $E_1(TO)$ at 410 cm^{-1} , E_{2h} at 438 cm^{-1} , $A_1(LO)$ at 574 cm^{-1} and a shoulder peaking in 554 cm^{-1} attributed to surface optical SO mode were detected. The peak at 519 cm^{-1} was attributed to the Si substrate. Curves were shifted for clarity.

Figure 4.8a-c shows FDTD simulations performed to investigate the plasmonic resonances in an Au nanorod $29 \times 68\text{ nm}$ in contact with a ZnO surface under light impinging perpendicular to the surface (y-axis) and polarized along the z-axis and x-axis. A 3 nm organic shell around the particle (refractive index $n=1.4$) was also included (see section 2.2.1). The LPR was found at 642 nm (black curve in figure 4.8a) while the TPR at 529 nm (red curve in figure 4.8a). Under excitation of the LPR, a field enhancement factor larger than 300 times was found concentrated in the nanorod-nanowire interspace, although a smaller factor, mainly confined in proximity of the nanowire surface, was calculated inside the ZnO due to the refractive index mismatch (figure 4.8b). In fact, the enhancement factor of ~ 70 just below the nanowire surface was found decreasing to 1 within 20 nm. On the other hand

for transversal polarization (figure 4.8c) the generate field enhancement factor of ~ 3 in proximity of the metal surface barely penetrate inside the semiconductor surface (less than a factor 2), thus demonstrating the larger capabilities of the LPR respect to the TPR.

Experimental demonstration of the theoretical prediction was provided by probing the surface-enhanced Raman scattering of the CTAB molecule adsorbed on the nanorod surface. In fact, the Br-Au bond provides a strong Raman signature characterized by a peak at 174 cm^{-1} that was used as a reference for comparing the strength of the TPR and LPR under selective excitation [88]. Figure 4.8d shows that under laser wavelength of 514 nm, in resonance with the TPR, no signal was recorded from Au nanorods randomly deposited on Si/SiO₂ substrate while with 647 nm wavelength, in resonance with the LPR, the Br-Au peak was detected, thus corroborating the larger field-enhancement arising from the LPR respect to the TPR.

Following this analysis, LPR was used to enhance the Raman scattering of the ZnO surface optical (SO) phonon modes on a single nanostructure. Figure 4.9 shows the active Raman modes detected with 647 nm wavelength in a highly dense "spaghetti-like" substrate containing ZnO nanowires randomly oriented in the 3D-space where the A₁(TO) peaked at 378 cm^{-1} , E₁(TO) at 410 cm^{-1} , E_{2h} at 438 cm^{-1} , A₁(LO) at 574 cm^{-1} and a shoulder peaking in 554 cm^{-1} , that could be attributed to surface optical SO modes were observed. Nanowires considered in this work, with radius in the range of 100-150 nm, satisfied the condition $qr \gg 1$, where q is the SO mode wavevector typically on the order of 10^7 - 10^9 m^{-1} [244]. In this limit the frequency of the SO mode can be written as [245]

$$\omega_{SO}^2 = \omega_{TO}^2 \frac{\epsilon_0 + \epsilon_m}{\epsilon_\infty + \epsilon_m} \quad (4.10)$$

where ω_{TO} is the TO mode frequency at zone center, ϵ_0 and ϵ_∞ are the static and high-frequency dielectric constant of the bulk ZnO respectively and ϵ_m the dielectric constant of the surrounding medium. The backscattering geometry used in the experiment with light propagating perpendicular to the c-axis of the nanowire (long axis of the nanowire) with random polarization parallel to the substrate allowed excitation of both E₁ and A₁ bulk modes, therefore the observed SO mode could

4.5. Raman scattering in single Au nanorods decorated ZnO nanowire

be a mixing between the SO modes generated by the two bulk modes respectively. Using eq.(4.10) with $\omega_{TO}= 410 \text{ cm}^{-1}$ for A_1 mode and $\omega_{TO}= 380 \text{ cm}^{-1}$ for E_1 mode, $\epsilon_0= 10.29$, $\epsilon_\infty= 4.47$ and the single nanowire surrounded by an inhomogeneous surrounding medium of air and ZnO (due to the contact with other nanowires in the spaghetti-like substrate) described by an effective dielectric constant $\epsilon_m= 2.45$ obtained from eq.(2.1) with $\alpha \sim 0.5$, the wavenumber of the SO mode was calculated to be in the range $515\text{-}556 \text{ cm}^{-1}$, in agreement with the experimental value of 554 cm^{-1} measured.

For comparison, the spectrum collected from an individual ZnO nanowire under the same experimental conditions (blue line, excitation 647 nm) showed no evidence of any ZnO modes. In fact, the small cross-section of the non-resonant Raman scattering (laser wavelength below the semiconductor band-gap) hampers investigation of single nanostructures and requires large number of probed nanostructures in order to collect a detectable signal.

On the other hand, the red curves in figure 4.9 show two representative spectra of individual Au nanorods-decorated ZnO nanowires. The hybrid structure spectra recorded with 647 nm laser wavelength showed a reproducible peak centered at $572\text{-}574 \text{ cm}^{-1}$ that was attributed to the SO mode previously observed in the highly-dense spaghetti-like ZnO nanowire substrate. In fact, the medium surrounding the single hybrid nanostructure (Si/SiO₂ and air) had an effective dielectric constant of $\epsilon_m= 1.7$, lower than the ϵ_m calculated for the highly-dense ZnO nanowire substrate. The variation of the dielectric constant affects the wavenumber of the surface optical mode thus shifting the expected range for SO mode by $\sim 20 \text{ cm}^{-1}$ from $515\text{-}556$ to $532\text{-}574 \text{ cm}^{-1}$, in reasonable agreement with the new experimental value that increased from 554 to 574 cm^{-1} .

The enhancement of the SO mode mediated LPR of Au nanorods was estimated by at least a factor 10^3 in the hybrid structure compared to the single ZnO nanowire. The theoretical Raman enhancement within the $|E|^4$ -approximation [213] is proportional to the E_{EF}^2 , with E_{EF} the electric field enhancement factor, that was found on the order of 10^3 using $E_{EF} \sim 70$ extracted from the FDTD simulation showed in figure 4.8b, thus corroborating the electromagnetic origin of the observed enhanced. Moreover the localization of the electric field enhancement at the ZnO

surface demonstrated by the FDTD simulations further corroborate the assignment of the peak at 574 cm^{-1} to a SO mode rather than the bulk mode $A_1(\text{LO})$ also peaked in the range $572\text{-}576\text{ cm}^{-1}$ [239, 246].

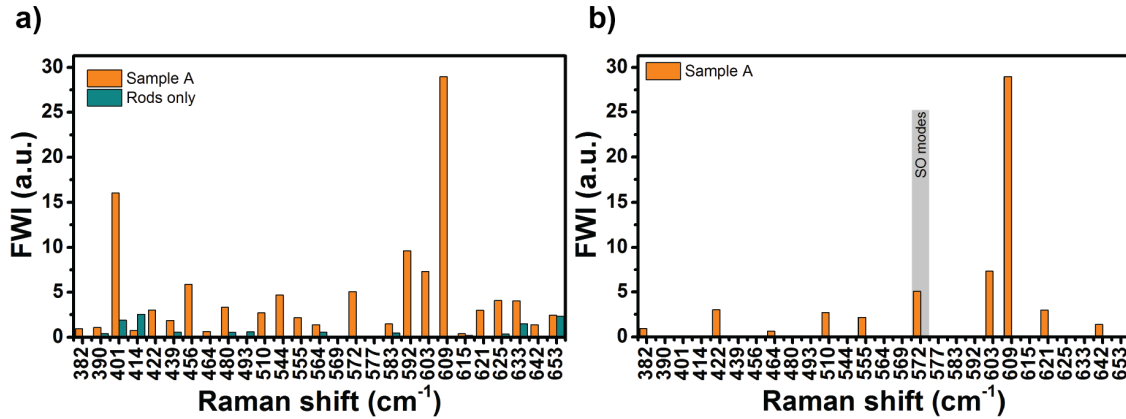


Figure 4.10.: Descriptive statistics of the Raman peak FWI detected on 9 measured hybrid nanostructures in sample A showing a) the entire set of detected peaks in the hybrid devices and the related substrate containing only Au nanorods and b) the Raman peaks not found in the nanorods. Gray columns indicate the peak attributed to the ZnO SO mode.

In figure 4.10a we show a descriptive statistics of the peaks found in 9 measured hybrid nanostructures (sample A) fabricated by mask-selective droplet deposition method using the process A (see section 4.4). The y-axis reports the frequency-weighted intensity (FWI) calculated by multiplying the average measured intensity of the Raman peak with the frequency encountered within the set of hybrid nanostructures measured. Each peak intensity was obtained from the Lorentzian fit of the peak by dividing the area under curve with the full-width-half-maximum (FWHM). Most of the peaks in figure 4.10a derive from the SERS effect on the CTAB bilayer, as expected from the large field enhancement within the layer (see figure 4.8b). The peaks centered at 390 cm^{-1} , 414 cm^{-1} , 456 cm^{-1} , 480 cm^{-1} , 493 cm^{-1} and 592 cm^{-1} were previously observed in CTAB crystalline [247, 248]. The peaks at 401 , 439 , 493 , 544 , 564 , 583 , 625 , 633 and 653 cm^{-1} , were found both in the spectra of hybrid nanostructures and in the Si/SiO₂ substrates containing Au nanorods only, therefore were attributed to the vibrational transitions of the CTAB. The detection of additional peaks compared to the CTAB crystalline is not surprising. In fact, it is well-known that molecules adsorbed on metal surfaces show Raman modes shifted

4.5. Raman scattering in single Au nanorods decorated ZnO nanowire

or new modes depending on the interaction between the molecule and the surface where it is adsorbed [231]. Moreover CTAB molecules on the Au nanorod surface forms a double layer that can introduce new vibrational resonances with respect to the isolated molecule [177]. Figure 4.10b shows the statistic after removal of all peaks attributed to the CTAB bilayer, highlighting how the SO mode, previously discussed, is one of the most relevant Raman peak within the collected statistic.

The remaining peaks at 422, 464, 510, 603, 609, 621 and 642 cm^{-1} were tentatively attributed to the CTAB, although no evidence of these resonances was found in the substrate with nanorods only. It should be noticed that chemical enhancement via charge transfer between the CTAB molecules and the ZnO surface could contribute to the SERS effects [249]. An evidence that corroborates this possible mechanism can be found in the statistic showed in figure 4.10a. The CTAB Raman peaks observed in the nanorods only have lower FWI compared to the same peaks found in the hybrid nanostructures, despite the statistic derived from spectra collected from spots with larger nanorod densities.

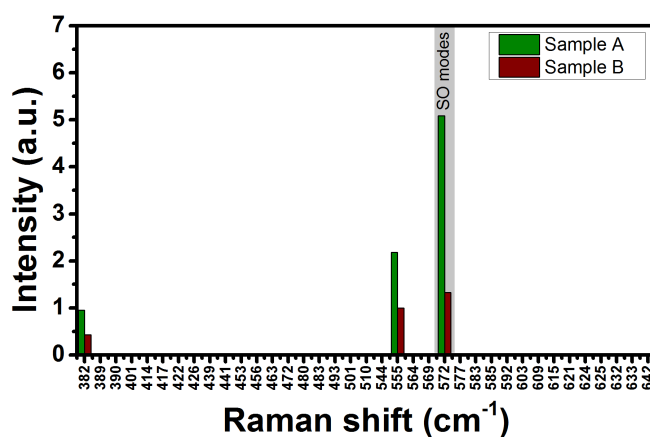


Figure 4.11.: *Statistical analysis of the ZnO Raman peaks found in Sample A and B.*

In order to demonstrate the reproducibility of the results, we repeated the statistical analysis on a second sample (sample B) fabricated by mask-selective deposition method following the alternative process B (see section 4.4). Figure 4.11 compares the statistics on the two samples referred to peaks not already associated to CTAB molecules. Only the peaks at 382 cm^{-1} and 555 cm^{-1} and 574 cm^{-1} were successfully

found in sample B, thus demonstrating the reliability and effectiveness in enhancing those peaks independently by the fabrication process.

To further prove if peaks at 382, 555 and 574 cm^{-1} were related to the ZnO and not to the CTAB, sample A was immersed in a methanol-based solution of 4-ABT (1 mM) in order to replace most of the CTAB on the nanorod surface with the 4-ABT molecule. The successful attachment of 4-ABT on the nanorods was firstly demonstrated by recording a SERS spectra on a hybrid structure and on a SiO_2 substrate containing nanorods only, showed in figure 4.12a. The representative spectra measured using laser wavelength at 647 nm denote the distinctive features of 4-ABT Raman transitions [89, 250] at 1004, 1073, 1139 and 1187 cm^{-1} with comparable intensity thus demonstrating the effective attachment on the gold nanorods.

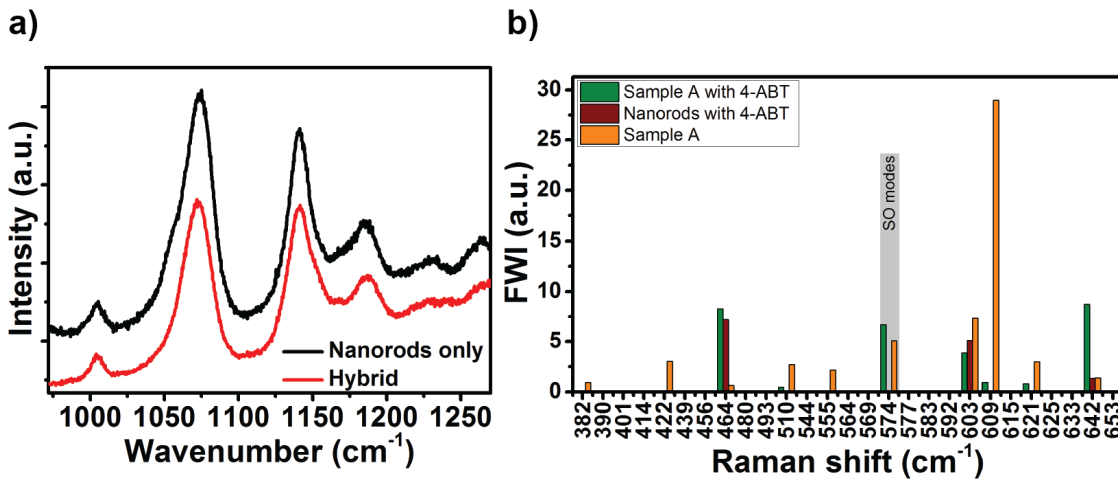


Figure 4.12.: a) Raman spectrum of 4-ABT detected from Au nanorods deposited on Si/SiO_2 substrate (black curve) and on a single hybrid nanostructure (red curve). b) Statistical analysis of Raman peaks found in Sample A after functionalization with 4-ABT molecule.

A direct comparison between the statistical analysis of the Raman peaks before and after the 4-ABT substitution on the same set of hybrid nanostructures is reported in figure 4.12b. The enhancement of the peaks at 464 and 642 cm^{-1} were associated to the characteristic vibrations of the benzene ring [250] and were also found in the sample with nanorods only. However, none of those peaks can be related to ZnO modes. The peaks at 422, 510, 603, 609 and 621 cm^{-1} showed an evident decrement in the FWHM that prove were related to CTAB molecules. Interestingly,

4.5. Raman scattering in single Au nanorods decorated ZnO nanowire

the peak at 574 cm^{-1} remained almost unchanged, corroborating our attribution to the ZnO. On the other hand, peaks at 382 and 555 cm^{-1} were not found after the functionalization therefore their attribution to the ZnO was not proved.

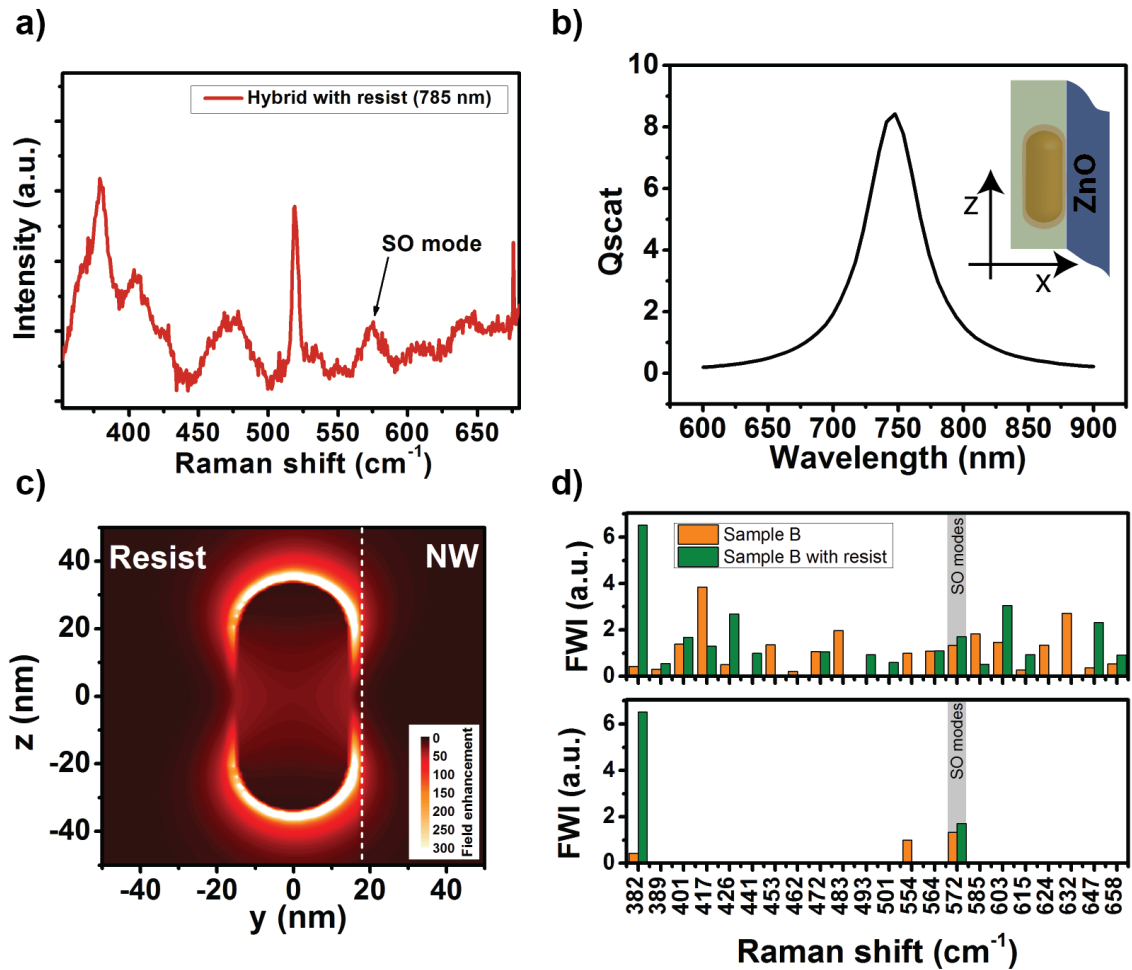


Figure 4.13.: a) Representative Raman spectrum of a single hybrid nanostructure immersed in polymer resist at laser wavelength of 785 nm. b) FDTD simulation of the scattering cross section normalized to the geometrical cross section of a $29 \times 68\text{ nm}$ Au nanorods under radiation polarized along the z-axis. Inset : schematic representation of the simulated geometry. c) FDTD simulation of the electric field enhancement factor under light polarized along the z-axis. d) Descriptive statistics of the Raman peaks and related FWI detected on 10 measured hybrid nanostructures on Sample B with and without resist.

Finally, in order to demonstrate the LPR origin of the ZnO modes enhancement and also to exploit the advantages offered by the LPR-mediated enhanced Raman scattering, we investigated the tunability of this process by manipulation of the optical properties of nanorods. Figure 4.13a reports a representative Raman spectrum

of an HbNW nanostructure embedded in a polymer resist (S1813) with refractive index $n=1.63$. In this sample the enhancement of the SO mode was found with the laser wavelength of 785 nm instead of 647 nm. FDTD simulation in figure 4.13b shows that the different surrounding medium shifted the LPR at 747 nm, therefore the laser at 785 nm was matching more efficiently the plasmonic resonances than the 647 nm resulting in a more effective enhancement. The electric field distribution (figure 4.13c) reveals a more symmetric field enhancement compared to the previous case with most of the field confined within the CTAB layer due to the lower refractive index respect to the surrounding medium although a comparable field enhancement was found inside the nanowire. According to this observation the spectrum showed in figure 4.13a shows more pronounced feature derived from the CTAB layer. The statistical comparison between Sample B with and without resist in figure 4.13d(top) shows a general enhancement of the Raman peaks. It should be noticed that despite the peak at 382 cm^{-1} showed a huge enhancement (4.13d, bottom), this was observed only one time (with very large amplitude) in the set of measured nanowires.

4.6. Conclusion

In conclusion, Raman enhancement of the ZnO SO mode was demonstrated in single hybrid structures formed by Au nanorods deposited on ZnO nanowires under excitation of longitudinal surface plasmon resonance of Au nanorods. FDTD simulations were used to investigate the spatial distribution and intensity of the enhanced electric field for different polarizations and to support the experimental findings. Intentional tuning of the optical properties of deposited nanorods resulted in shifting of the excitation wavelength at which the maximum of the SO mode enhancement was achieved. The probing of the structural vibrational properties of single large-bandgap semiconductor nanowire through deposition of metal nanorods open the way for novel sensing and opto-electronic applications. Moreover, our studies contribute to extend the capability of traditional Raman spectroscopy to the characterization of semiconductor materials thus providing new insights to the understanding of surface and interface properties of hybrid materials.

Chapter 5.

Nanofabrication and electronic transport in ZnO nanowire field-effect devices

In this Chapter, nanofabrication and detailed electrical characterization of ZnO nanowire field-effect transistor (ZnO NW-FET) is presented. Optimised electrode geometry and optical lithography method led to fabrication of large number (>30) of ZnO NW-FETs per substrate. Metal-ZnO nanowire ohmic contacts with contact resistivity of $10^{-11} - 10^{-10} \Omega \cdot m^2$ were realised using Ti/Al electrodes, thus allowing to assess the intrinsic electronic properties of the ZnO nanowire. The device resistance was investigated in different atmosphere (air and high vacuum). The estimation of nanowire resistivity, contact resistance, electron mobility and electron density was also provided. Finally, we used the aforesaid ZnO NW-FET architecture for two applications. Firstly, we demonstrated that ZnO NW-FET can be successfully used as nano-heater up to more than $300^\circ C$ and secondly, we propose a novel method to selectively decorate a target nanowire with colloidal nanorods by an engineered electric field configuration using the three gate electrodes available in the FET architecture.

5.1. Introduction

ZnO nanowires have been explored in the past decades as building-block for optical and electrically-injected ultraviolet nanolasers [251, 252, 253, 254, 218, 255], ultravi-

olet photodetectors [256, 257, 118], field-effect transistors [258, 259] and gas sensor [260, 261]. For these applications (and also the application discussed in Chapter 6) low-resistivity ohmic contacts to the ZnO nanowire are a crucial requirement for assessing the intrinsic electronic properties of the ZnO nanowire towards optimisation of the overall device performance. Au electrodes have been frequently used for contacting ZnO film [262], nanoribbons [263] and nanowires [264] despite the expected formation of a Schottky barrier at the Au-ZnO interface due to the work-function mismatch of ~ 0.7 eV [265]. For instance, Kim *et al.* reported low-resistance ohmic contact to *n*-type doped ZnO:Al layer with Ti/Au with contact resistance of 10^{-4} $\Omega\cdot\text{cm}^2$ after annealing at 300°C [266]. Goldberger *et al.* obtained ohmic devices using an O_2 plasma cleaning before the Au evaporation followed by annealing at $200\text{-}400^\circ\text{C}$ with contact resistance of $10^{-3}\text{-}10^{-2}$ $\Omega\cdot\text{cm}^2$ [258]. However, despite the ohmic behavior demonstrated with Au contacts, other metals with more suitable work-function offer the possibility to further lower the contact resistivity. In fact, few reports explored alternative metalization schemes achieving contact resistivity on the order of 10^{-5} $\Omega\cdot\text{cm}^2$ by FIB deposited Pt electrodes on ZnO nanowires [267] and 10^{-7} $\Omega\cdot\text{cm}^2$ with Ti/Al electrodes after annealing at 300°C [268].

Therefore, as crucial step in the fabrication of hybrid ZnO NW-FET devices discussed in Chapter 6, extensive attention was devoted to the optimization of the metal-ZnO nanowire interface during the nanofabrication process and the related electrical characterization of the NW-FET devices. In particular, we demonstrated that Al contacts form a low-resistivity ohmic contact with a contact resistivity on the order of $10^{-6}\text{-}10^{-7}$ $\Omega\cdot\text{cm}^2$ more than four order of magnitude less than Au contacts. These results corroborate the central role played by the metal contacts and support the use of Al contacts as a more suitable metal than Au. Moreover, device resistivity was also measured in different atmospheres (in air and high-vacuum) in order to investigate the influence of the environment on the device electrical performance as well as the effect of the thermal annealing process. Furthermore, three-terminals field-effects measurements allowed to estimate the nanowire resistivity of the order of $10^{-1}\text{-}10^{-2}$ $\Omega\cdot\text{m}$, field-effect mobility in the range of $40\text{-}100$ $\text{cm}^2/\text{V}\cdot\text{s}$ and electron density $\sim 10^{17}$ cm^{-3} .

The excellent optimization of the fabrication process achieved allowed to explore

applications in the field of micro and nano-heaters. The use of nanostructures as nanoscale heaters has been gaining increasing interest due to applications in many different fields. For instance, in biology and chemistry micro-heaters array devices have been used for manipulation of proteins [269], cell lysis [270] and protein synthesis [271]. Yan Jin *et al.* and Chen *et al.* used Silicon and metal nanowires respectively to control chemical reactions with nanoscale spatial resolution for selective growth of oxide nanowires [272, 273]. Park *et al.* proposed to use this approach to selectively functionalize the surface of silicon nanowires on a silicon-based substrate [274]. In particular, the localized Joule heating was used to ablate a protective polymer layer from a specific nanowire thus allowing a selective functionalization.

However, the small channel resistivity, on the order of $10^{-4}\Omega\cdot\text{m}$ or lower required to reach temperature larger than $300\text{ }^{\circ}\text{C}$ needed in most applications, limited the range of possible materials and most of the example in literature rely on heavily doped Si nanobelts or metal nanowires.

A possible route to overcome this limitation is exploring the three-terminals FET architecture where a doping of the nanowire and the related increasing in conductivity can be capacitatively induced by a third gate electrode. Following this approach, we explored for the first time the Joule heating process in ZnO NW-FET and we demonstrated the capabilities of a three terminals nanowire field-effect transistor to reach temperatures larger than $300\text{ }^{\circ}\text{C}$ by capacitatively-induced charge on the nanowire channel. The observed performance, supported by finite-element method (FEM) simulations, demonstrated that materials with resistivity in the range of $10^{-1}\text{-}10^{-2}\ \Omega\cdot\text{m}$ such as ZnO nanowires can be successfully used as micro-heaters. This approach sensibly expand the suitable materials for Joule-heating based processes in semiconductor nanowires thus opening to future application for radial doping, single core-shell heterostructuring and selective single nanowire functionalization. Finally, at the end of the Chapter, the NW-FET architecture will be also investigated for a selective decoration of single nanowire with colloidal nanoparticles. This novel approach, supported by FEM simulations, expands the dielectrophoretic process discussed in Chapter 3 by means of an engineered electric field configuration able to drive the colloidal nanoparticle towards a single target nanowire. The process designed for nanowire-based FET devices would allow selective decoration of space-

localized nanowire thus offering a fast and reliable method to decorate individual NW-FET device but also single nanowire in large arrays of nanowire-based devices. This process is interesting for development of plasmonic-enhanced photodetectors and multijunctions solar cell.

5.2. Experimental Section

ZnO nanostructures were grown by CVD using Vapour-liquid-solid (VLS) mechanism in a high temperature tube furnace (see section ??).

Scanning electron microscopy (SEM) images of nanostructures were acquired using a field emission SEM (JSM-7500F, JEOL UK Ltd.) operating at beam voltages of 5 kV.

Electrical contacts were fabricated by metal evaporation of Ti/Au 90nm/50nm and Ti/Al 10nm/190nm. Size of each electrical pad was $200 \times 200 \mu\text{m}$. Metalization was patterned using standard photolithography and lift-off techniques. I-V characteristics of ZnO nanowire field-effect transistor were performed with a parameter analyzer (E5270B) by direct probing using a Wentworth micromanipulator 6200 probe station. The measurements were carried out at room temperature in air under ambient light conditions. For the Joule heating experiments the entire sample were previously covered with a PMMA (ARP679.04) layer having thickness of ~ 200 nm by spin-coating (at 6000 rpm).

5.3. Fabrication of ZnO nanowire field-effect devices

5.3.1. Nanowire deposition and sample preparation

As-grown ZnO nanostructures were found having low monodispersity and presence of irregular nanostructures. Moreover CVD technique produced high density of highly intertwined structures (spaghetti-like configuration), see figure 5.1a. In order to purify the sample, ZnO nanostructures were mechanically transferred onto clean Si/SiO₂ substrates and larger structures were washed away by multiple injections of acetone (figure 5.1b). After the cleaning, residual random nanowires were found

well separated from each other and showed a reasonable degree of alignment along a preferential direction induced by the mechanical transfer. Statistical measurements of nanowire dimensions showed lengths in the range 1-10 μm with a mean value of 5 μm and diameters were found ranging between 40 nm and 500 nm (figure 5.1c-d).

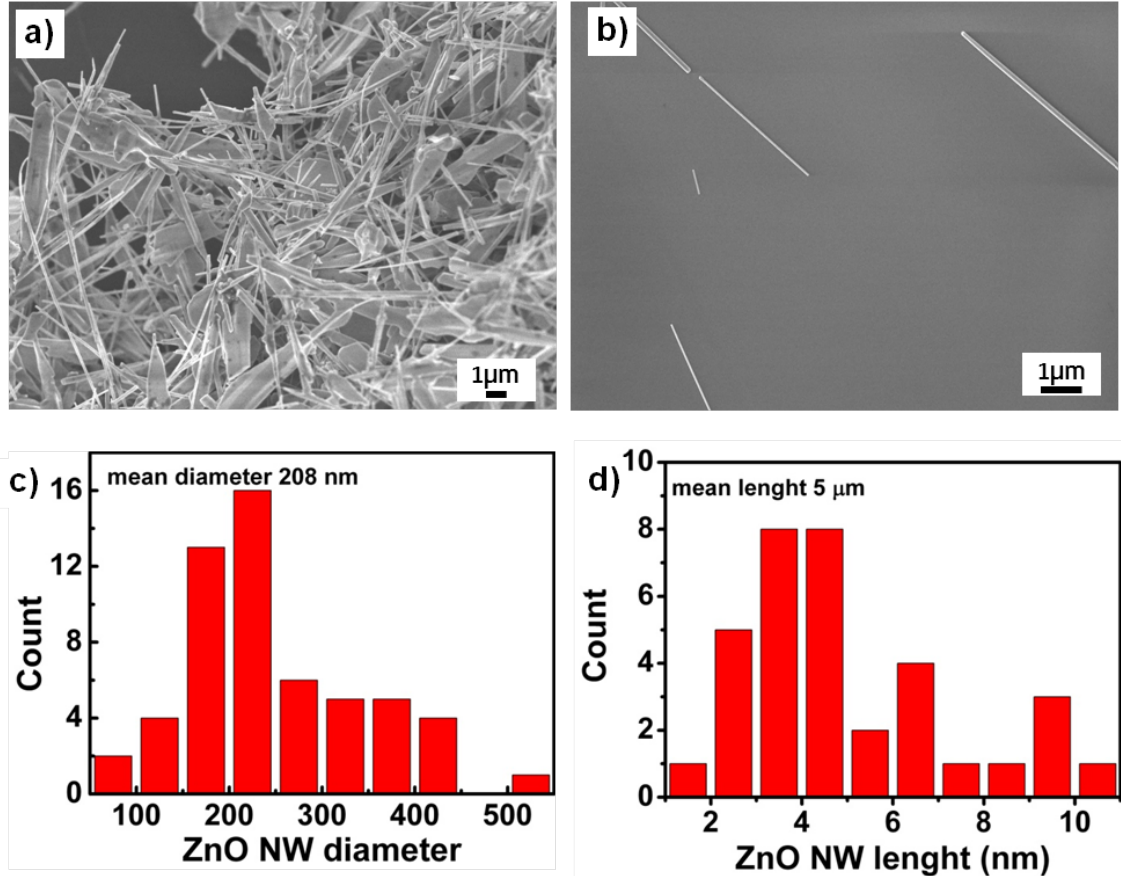


Figure 5.1.: Scanning electron microscope image of a) as-grown ZnO nanostructures b) deposition and cleaning of ZnO nanowire on Si/SiO₂ substrated by mechanical transfer. Statistical distribution of c) diameter and d) length of deposited nanowires.

5.3.2. Nanofabrication of electrical contacts on single ZnO nanowire

Fabrication of source-drain metal contacts on ZnO nanowires were realized by optical lithography. Electrode geometry was designed to maximize the number of random wires contacted. The unit box (figure 5.2), replicated 100 times on the optical mask, is an array of 20×20 pads. Each pad was a square 200×200 μm with castellated

edges, large enough to allow electrical measurement by direct probing. The $2\ \mu\text{m}$ (and $5\ \mu\text{m}$) gaps separating two consecutive pads was $10\ \mu\text{m}$ long and was repeated 10 times along each edge of the pad. Finally, in order to localize nanowires inside the array, each pad was labeled with alphabetic letters and each box with a number.

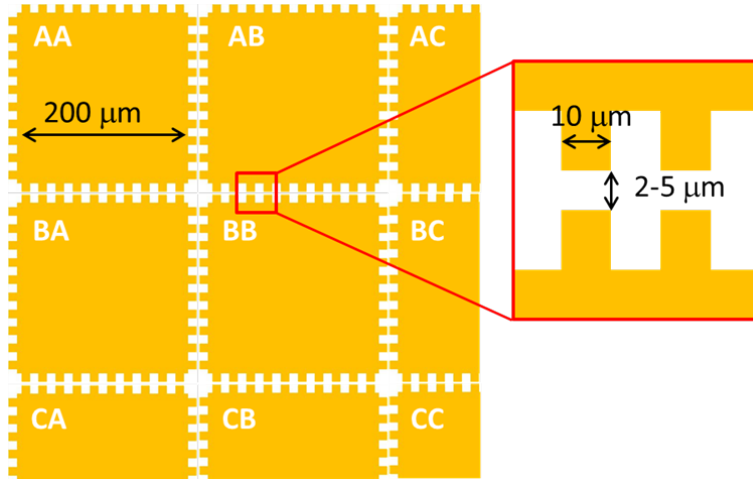


Figure 5.2.: Schematic of the pattern used to contact the nanowire. The array of 20×20 castellated pads defined the unit box. Each pad is $200\ \mu\text{m}$ large and the minimum distance between two consecutive pads is $2\ \mu\text{m}$ or $5\ \mu\text{m}$.

The lithographic process is described in figure 5.3 (see also appendix A.3). The clean sample was spin-coated with two layer of UV-sensitive resist (LOR3A and S1805). After cleaning the edges with acetone to remove the excess of resist, the sample was loaded in the Mask-Aligner. The standard optical mask used in lithography is a quartz slide with the negative design of the pattern in chrome. The mask was aligned respect to the nanowire direction and a physical contact with the sample was established. After an exposition to UV light, the sample was removed and immersed in the resist developer (MF319) to remove the resist from the exposed areas. An under-etch of the resist was carried out to improve the sharpness of the electrode edges. Following optical lithography, deposition of metal layers on the entire sample surface was performed in an e-beam evaporator. Au and Al metal contacts were explored as source-drain electrodes on ZnO nanowires and 10 nm layer of Ti was used to increase the adhesion of Al and Au on Si/SiO₂. After the metal evaporation, the lift-off was carried out in warm 1165 to remove the metal from the areas covered by resist. The alignment induced by mechanical transfer and the electrode

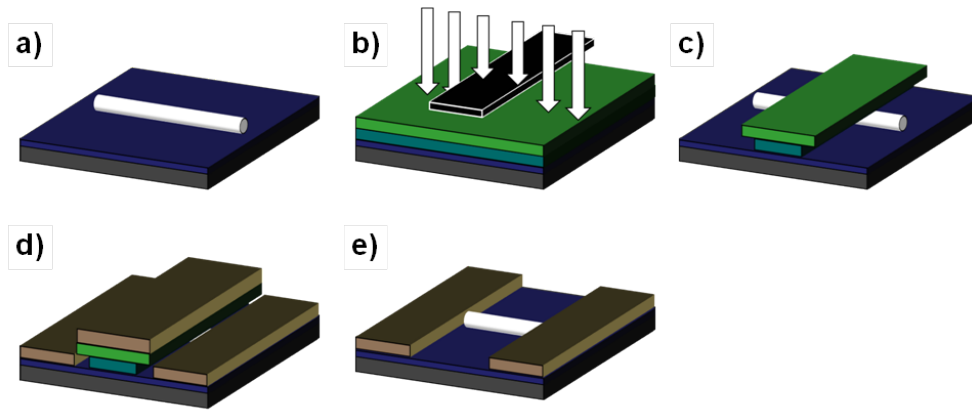


Figure 5.3.: Steps in the lithographic process. Nanowire on a clean Si/SiO₂ substrate (a) was covered with two resists layer by spin-coating and exposed to UV light through the optical mask (b). Exposed resist was removed and under-etch was performed (c) before metal deposition (d). After the lift-off the metal was left only on the exposed area (e).

geometry adopted were very effective in producing a large number (>30) of single contacted nanowires inside each patterned box. A typical device resulting from the nanofabrication is showed in figure 5.4. The electrode edges were found sharp, indicating an excellent optimization of the lithography process. Also the metal layer was observed to be continuous over the nanowire, ensuring that a good contact surface was fabricated.

5.4. Electrical properties of ZnO nanowire FET device

Investigation of the electronic properties of ZnO nanowires firstly requires a reliable method to form ohmic metal-ZnO contact. Addressing this aspect is not only crucial for studying the electronic properties of the nanowire but also for the performance of the hybrid FET device described in Chapter 6.

Figure 5.5a shows the two-points I-V characteristics of a representative device with 90 nm Ti and 50 nm Au (black line) and with 10 nm Ti and 90 nm Al (blue line). The resistance of the device with Ti/Au pads was larger than $10^9 \Omega$ and the non-linear I-V curve (see inset of figure 5.5a) was indication of a non-Ohmic contact between the metal and the nanowire. In order to demonstrate that the high resistance was related to the contact resistance we compared this result with the I-V

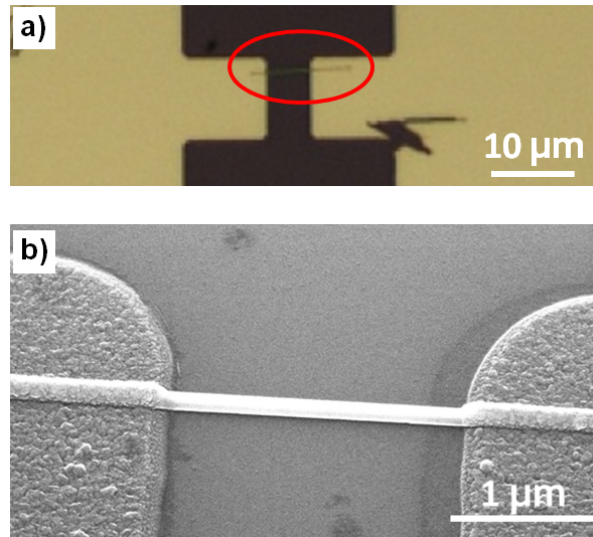


Figure 5.4.: a) Optical image and b) scanning electron microscope image of a ZnO nanowire contacted with Ti/Al 10nm/90nm metal electrodes.

curve measured in a device with Ti/Al contacts. For Al contacts the I-V response was clearly linear (ohmic contacts) and the resistance was of the order of 10^5 - 10^6 Ω , more than three orders of magnitude lower than the resistance observed in the previous device.

The observed behavior can be explained from the energy band structure alignment. The work-function of Au (5.47 eV) is sensibly higher than the work function of ZnO (4.65 eV) [140]. At the metal-nanowire interface the depletion of electrons in the ZnO results in upward band bending and formation of a Schottky barrier, giving rise to high contact resistance and non-ohmic behavior. On the other hand, the lower work-function of Al (4.33 eV) induces a downward band bending in the ZnO and consequently an ohmic response. These results show that despite Au electrodes have been often used in literature for contacting ZnO nanostructures, the contact resistance can be reduced by at least 3 orders of magnitude with Al electrodes, thus allowing a more efficient electron injection and collection in and from the nanowire. Effect of thermal annealing in forming gas on the contact resistance for the Ti/Al electrodes was also investigated. The device was heated up with a rate of 2 °C/s to 300 °C and annealed for 5 min. Figure 5.5b shows the I-V curves recorded before and after two annealing processes. A reproducible trend was observed in 5 devices: the resistivity was reduced by more than one order of

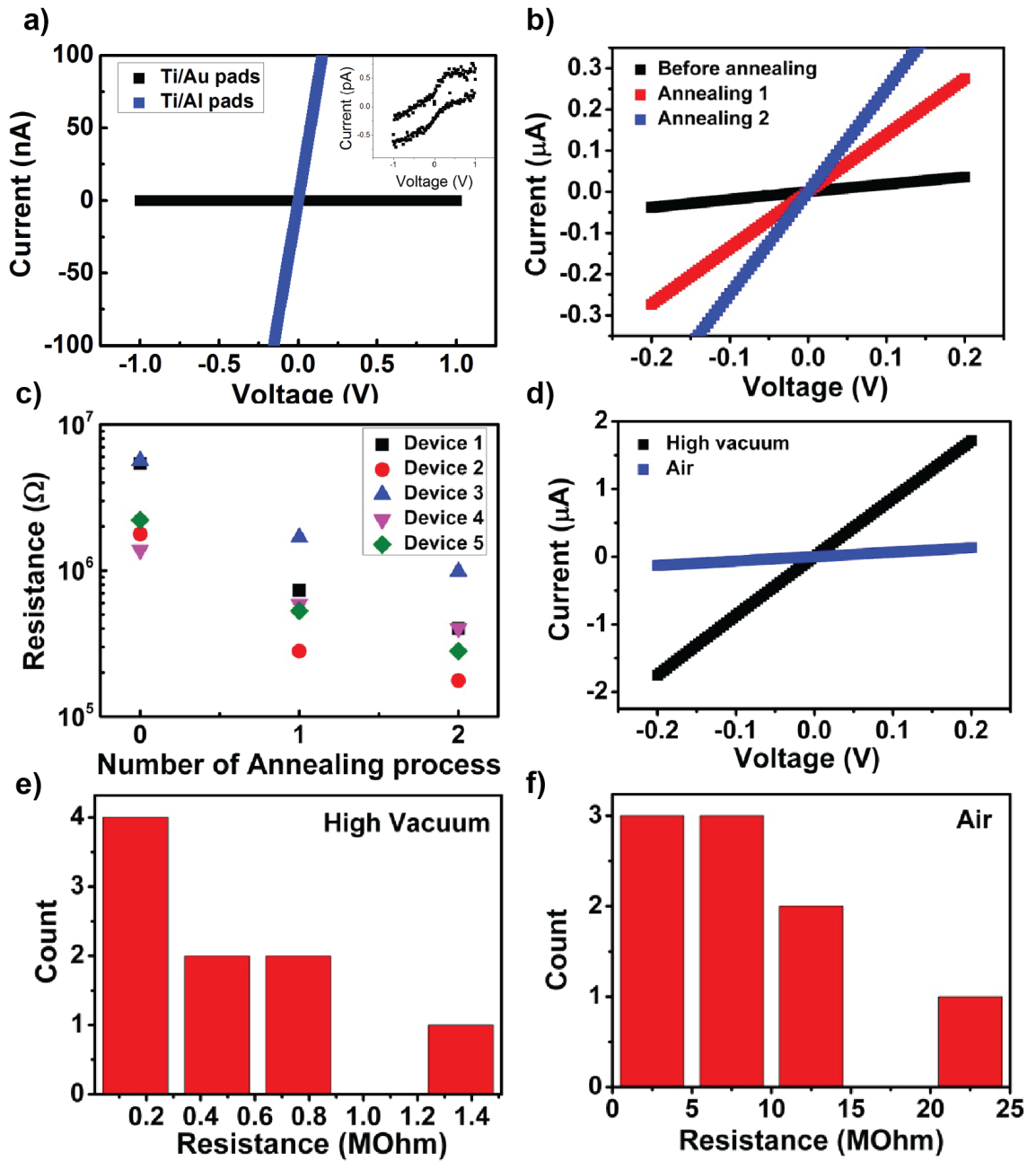


Figure 5.5.: a) I-V characteristic in air of ZnO nanowire contacted with Ti/Au (90 nm/50 nm) and Ti/Al (10 nm/90 nm) pads separated by $2 \mu\text{m}$ b) I-V characteristic of a ZnO nanowire contacted with Ti/Al/Ti (10 nm/150 nm/50 nm) electrodes before and after two annealing process c) Resistance in two-points configuration measured in 5 devices before and after two annealing process. d) I-V characteristic of ZnO nanowire with Ti/Al (10 nm/90 nm) pads separated by $2 \mu\text{m}$ in air and in vacuum. Statistical distribution of the resistance measured in 9 devices with Ti/Al (10 nm/90 nm) pads in e) high vacuum and f) in air.

magnitude (figure 5.5c). The lowering in the contact resistance after annealing at 300°C of Ti/Al electrodes was explained by Kim *et al.* with the formation of TiO species and the related oxygen vacancies V_O that form shallow donors near the the conduction band with consequent electron enrichment [275]. It should be noticed that in our experiments this trend was not confirmed over different batches of ZnO nanowires and an increasing of the device resistance of 1-2 orders of magnitude was also observed after the annealing process under comparable conditions. However, for those devices the two-points resistance without annealing was in the range of 10^5 - 10^6 Ω , comparable with the valued obtained in the devices showed in figure 5.5c after two consecutive annealing processes. ZnO NW-FETs studied in the rest of this Chapter and in Chapter 6 were fabricated with Ti/Al electrodes without any annealing process, unless otherwise specified. In figure 5.5d-f we studied the variability in resistance of the fabricated ZnO NW-FET in various atmospheres. The conductivity of ZnO nanowires was found larger in high vacuum compare to air as shown the I-V curve of figure 5.5d. Statistics performed on 9 devices (figure 5.5e-f) showed that the resistance of a ZnO nanowire electrically contacted with Ti/Al pads in high vacuum increase in air by more than one order of magnitude. This is due to the presence of electron traps created by oxygen species adsorbed on the nanowire surface forming a depletion region in proximity of the surface and reducing the free electrons available for conduction (see Chapter 6 for more details).

More detailed investigation on the electrical transport in ZnO nanowires was carried out using the FET architecture showed in the setup schematically depicted in the inset of figure 5.6a. In three-terminals configuration the lithographic patterned Ti/Al pads were contacted by direct probing and used as Source (S) and Drain (D) and the Si(n^{++}) layer separated from the ZnO nanowire by 300 nm SiO₂ as a third back-gate electrode capacitively coupled to the nanowire.

Figure 5.6a shows the I-V characteristics under different back-gate bias applied of a representative ZnO NW-FET device. The low-bias two points I-V showed an Ohmic behavior with device resistance of $7.007 \pm 0.002 \cdot 10^5$ Ω . This resistance includes the nanowire resistance and the contact resistance at the semiconductor-metal interface. From the previous discussion we expect an ohmic contact between Al and ZnO with negligible resistance respect to the nanowire channel. In order to

5.4. Electrical properties of ZnO nanowire FET device

provide an estimation of the contact resistance we measure the I - V_g curved of the device (Figure 5.6b). From the approximated current equation in the linear regime ($V_D \ll V_g$) [276]

$$\begin{cases} \frac{dI_{SD}}{dV_D} = \frac{\mu C_{NW-gate}}{L^2} (V_g - V_t) \\ \frac{dI_{SD}}{dV_g} = \frac{\mu C_{NW-gate}}{L^2} V_D \end{cases} \quad (5.1)$$

where I_{SD} is the source-drain current, V_D and V_g is the drain and back-gate voltage respectively, L the channel length and $C_{NW-gate}$ is the gate-capacitance expressed by

$$C_{NW-gate} = \frac{2\pi\epsilon_0\epsilon_r L}{\cosh^{-1}\left(\frac{r+h}{r}\right)} \quad (5.2)$$

where h is the SiO_2 thickness and r the nanowire radius and $\epsilon_r=3.9$. This expression holds for a cylindrical nanowire completely embedded in SiO_2 not for a nanowire landing on a SiO_2 layer and surrounded by air. However finite-element method simulations showed that the eq.(5.2) over-estimate the capacitance by a factor ~ 2 , thus still providing the correct order of magnitude [277]. The threshold voltage V_t can be calculated by direct extrapolation as showed in figure 5.6b, where the value on the V_g axes is the quantity $V_t + \frac{V_D}{2}$. For the measured device we obtained $V_t=-9.39\pm 0.08$ V. The negative V_t value suggests the presence of unintentional n -type doping due to structural defects. However the V_t values were found variable in the range of -10/10 V thus indicating a large variability of the unintentional doping among the ZnO nanowires. Using V_t and the transconductance (dI_{SD}/dV_g) calculated in the linear region (for $V_g > 5$ V) was possible to obtain the channel conductance by using

$$R_{FET} \equiv \frac{dI_{SD}}{dV_D} = \frac{dI_{SD}}{dV_g} \frac{V_g - V_t}{V_D} \quad (5.3)$$

We compare in table 5.1 the measured resistance R_m in two-points configuration and the resistance R_{FET} calculated from equation 5.3 for different applied gate voltages.

It can be seen that the calculated and measured values were reasonably close, in

V_g (V)	R_m (Ω)	R_{FET} (Ω)
0	$7.007 \pm 0.002 \cdot 10^5$	$8.29 \pm 0.09 \cdot 10^5$
5	$5.1607 \pm 0.0005 \cdot 10^5$	$5.41 \pm 0.05 \cdot 10^5$
10	$4.0242 \pm 0.0009 \cdot 10^5$	$4.01 \pm 0.03 \cdot 10^5$

Table 5.1.: Resistance R_m of the representative device measured in two-point configuration compared with the resistance R_{FET} calculated using eq.5.3 when a back-gate voltage of 0, 5 and 10 V was applied.

particularly the discrepancy decrease for larger back-gate voltage and at $V_g=10$ V the R_m and R_{FET} were coincident within the error. In fact, because the linear response region of the ZnO NW-FET was for $V_g \gtrsim 5$ V, eq.(5.1) does not approximate very well the behavior at $V_g=0$ V. Nevertheless, the excellent agreement between the channel resistance R_{FET} and the measured two-points resistance R_m demonstrates that the contact resistance is effectively negligible compared to the channel resistivity, and by direct comparison, can be estimated of the order of $R_c \sim 10^3 \Omega$ or lower. We emphasize that this is a rough estimation and a more precise analysis would require 4-points measurements on a single nanowire. However, from R_c we calculated the contact resistivity ρ_c by using the formula [278]

$$\rho_c = \frac{R_c^2 2\pi^2 r^3}{\rho_{NW}} \quad (5.4)$$

and a value of $10^{-11} - 10^{-10} \Omega \cdot \text{m}^2$ with $R_c \sim 10^3 - 10^4 \Omega$ was obtained. Notably this estimation is in reasonable agreement with the reported value in literature for ZnO-Al contacts reported by Kim *et al.*[275]. Equation 5.4 is valid in the limit of long contacts $L \gg L_T$ where the transfer length L_T

$$L_T = \frac{\pi r^2 R_c}{\rho_{NW}} \quad (5.5)$$

was found in the range of $\sim 10 - 100$ nm using $R_c \sim 10^3 - 10^4 \Omega$ and $\rho_{NW} \sim 5 \cdot 10^{-3} \Omega \cdot \text{m}$. This is much smaller than the contact length of the two metal electrodes in the measured device that was $4.7 \mu\text{m}$ and $8.5 \mu\text{m}$ respectively, thus justifying the use of eq.(5.4).

A number of physical parameters can be also extracted by further analysis. The electron mobility can be calculated by using

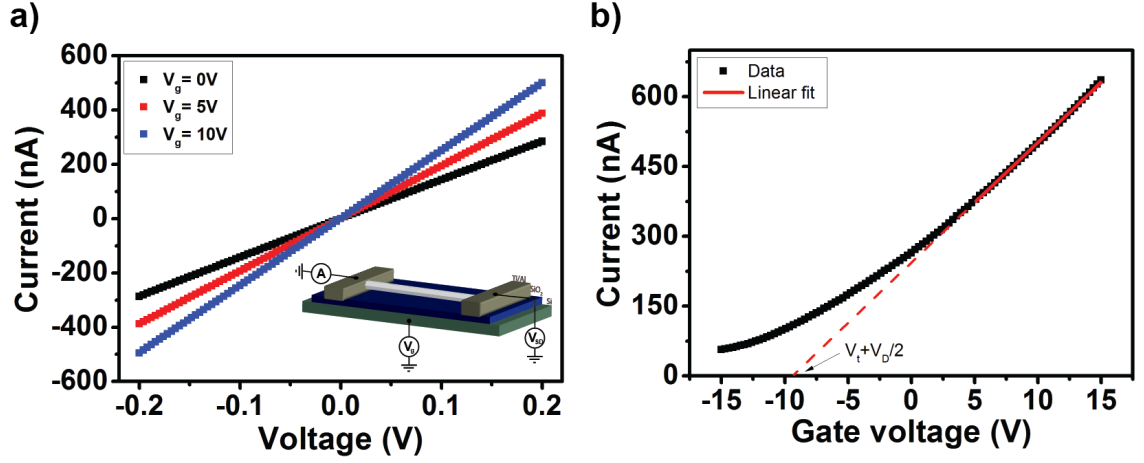


Figure 5.6.: a) Schematic of the ZnO nanowire field-effect device (NW-FET). Electrical characterization of a representative device comprise b) I - V characteristic of the NW-FET with applied back-gate voltage of 0, 5V and 10V and c) I - V_g characteristic with $V_{SD}=0.2V$. The red line is the linear fit used to calculate the transconductance.

$$\mu = \left. \frac{dI}{dV_g} \right|_{V_D} \cdot \frac{L^2}{C_{NW} \cdot V_D} \quad (5.6)$$

The calculated field-effect mobility was estimated to be $58 \text{ cm}^2/\text{V}\cdot\text{s}$ in agreement with previous reports [258]. Carrier concentration was calculated using the Drude approximation by

$$n = \frac{1}{\mu e \rho} \quad (5.7)$$

with e the elementary charge and ρ_{NW} the nanowire resistivity. The carrier concentration was estimated to be 10^{17} cm^{-3} .

5.5. Joule Heating in ZnO NW-FET device

In this section we explore the Joule heating process in ZnO nanowire when a source-drain current is forced in the NW-FET device. The capacitatively-induced charge in the nanowire channel, resulting from application of back-gate voltage, allowed to increase the nanowire conductivity by more than an order of magnitude. As result, temperature larger than $300 \text{ }^\circ\text{C}$ was generated in the NW.

Inset of figure 5.7a compares the I-V characteristic of a representative ZnO nanowire with the back-gate grounded ($V_g=0$ V) and $V_g=10$ V. The measured resistance of $5.76 \pm 0.07 \cdot 10^6 \Omega$ was decreased by a factor 4 to $1.39 \pm 0.02 \cdot 10^6 \Omega$ by applying 10 V to the back-gate. From the linear fit of the transfer characteristic I- V_g in air (figure 5.7b) we obtained the transconductance $dI_{SD}/dV_g=1.186 \pm 0.002 \cdot 10^{-8}$ S and the $V_t=-2.12 \pm 0.02$ V.

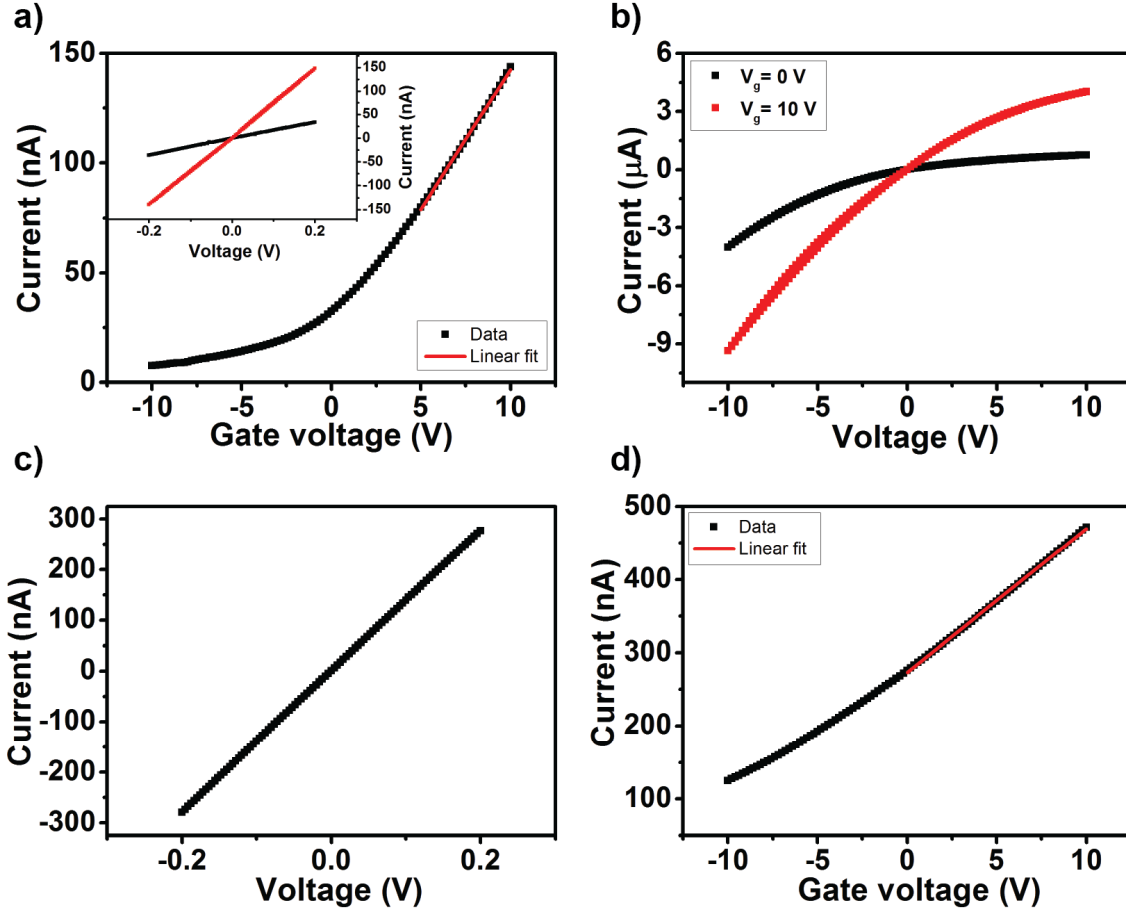


Figure 5.7.: Effect of the back-gate and PMMA on the electrical conductivity of the ZnO NW-FET. a) I- V_g characteristic and in the inset I-V characteristic and b) I-V at large V_{SD} of the device without PMMA. c) I-V characteristic and d) I- V_g characteristic of the device covered by PMMA.

Using eq.(5.1) it was possible to predict that the channel resistance could reach a value around $7.6 \cdot 10^5 \Omega$ at $V_g=20$ V, almost one order of magnitude less than the resistance at $V_g=0$. We should also consider that in the present device configuration, a capacitive coupling between the source/drain electrodes and the back-gate is unavoidable. Therefore for large source-drain voltages, as often required in

microheaters devices [279], the interaction with the back-gate induces asymmetric behavior between positive and negative bias applied. Figure 5.7b shows the I-V for source-drain bias of ± 10 V with the back-gate grounded (black curve) and at 10 V (red curve). Both curves are almost saturated at $V_g = 10$ V whereas at $V_g = -10$ V the source-drain current was more than double and no sign of saturation was found. This behavior was ascribed to the additional induced charges on the back-gate due to the coupling with the biased source electrodes (drain electrode was grounded during the measurements). In fact the charge accumulated on the back-gate are influenced by the ΔV between the source electrode and the back-gate. When the back-gate is grounded, large positive source bias determine accumulation of negative charge on the back-gate, thus affecting also the nanowire channel by reducing the conductivity. On the other hand, large negative source bias adds positive charge on the back-gate that results in an increased nanowire conductivity. We conclude that when a positive V_g is applied to the back-gate to increase the nanowire conductivity, large positive source-drain bias reduced the effect of the back-gate and a lower saturation current is reached compared to the case where large negative source-drain voltage was applied.

Furthermore, conductivity of ZnO nanowires is strongly affected by the presence of oxygen species in the surrounding atmosphere, that increase the depletion region at the ZnO surface and therefore the nanowire resistivity. In order to take into account also this aspect, we measured the electrical properties of the NW-FET covered by a polymer layer (PMMA), thus not exposed to air. The I-V curve in figure 5.7c at $V_g = 0$ V indicates a resistance of $7.187 \pm 0.001 \cdot 10^5 \Omega$, nearly one order of magnitude less than the resistance measured in air. It should be noticed that this variation in the nanowire resistance was found consistent with the variation observed in nanowires measured in air and in vacuum, as discussed in section 5.4, thus excluding presence of alternative process such as unintentional doping of the ZnO nanowire by the polymer or parallel electrical conductivity of the PMMA layer (resistance of an empty electrode gap with PMMA is on the order of $G\Omega$). Accordingly, from the I- V_g characteristic (figure 5.7d), the transconductance increased to $1.962 \pm 0.006 \cdot 10^{-8}$ S and the V_t shifted sensibly to a larger negative voltage (-13.8 ± 0.06 V). Using this values in the eq.(5.1), we expect to reach a resistance of $3 \cdot 10^5 \Omega$ with $V_g = 20$ V (we

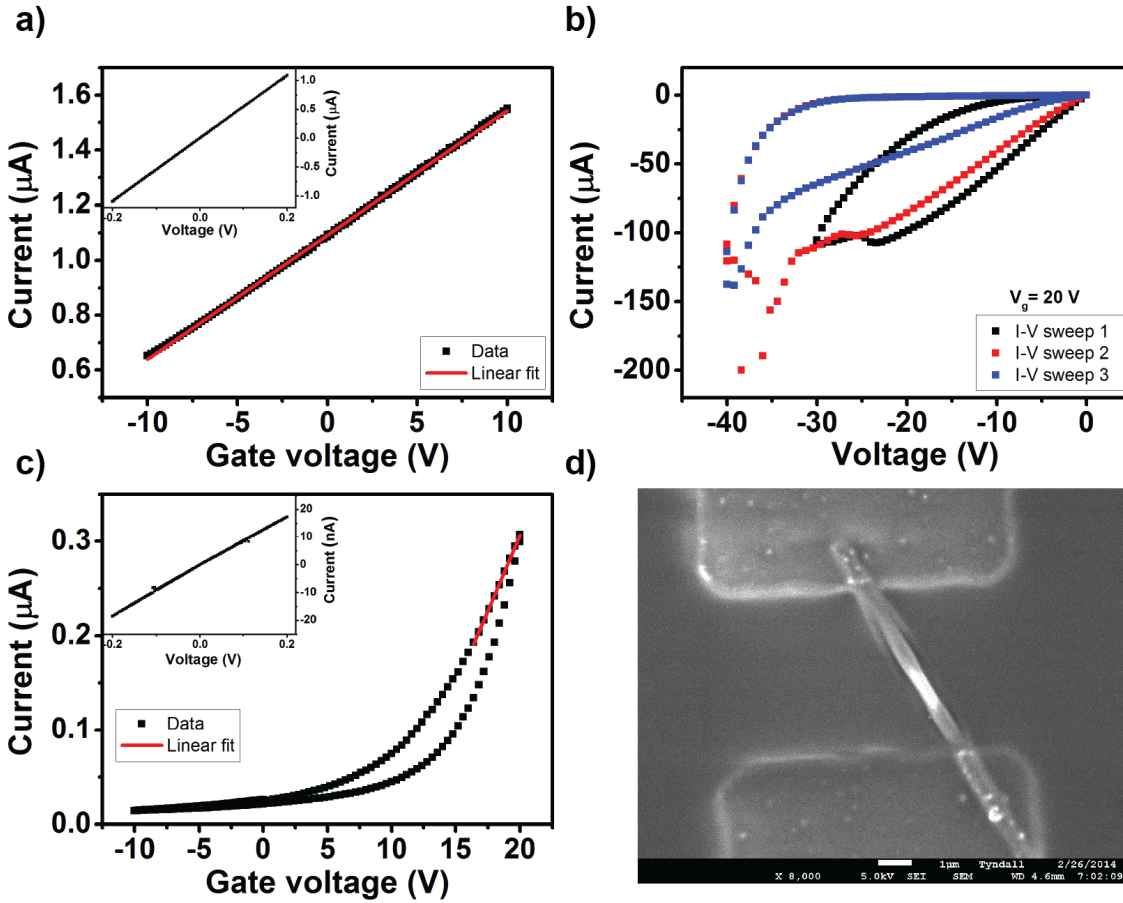


Figure 5.8.: Ablation of PMMA layer by Joule heating in ZnO nanowire FET device
 a) I - V and I - V_g characteristics of a representative device before the ablation. b) I - V sweeps from 0 V to -40 V with $V_g=20$ V were performed to force a current through the nanowire and heat it up via Joule heating. c) I - V and I - V_g characteristics after the ablation. d) SEM image of the device at the end of the process. A clear sign of PMMA ablation is visible.

assumed $V_D=0.2$ V), resulting in a factor ~ 20 in the conductivity improvement.

In this optimized conditions, we performed the Joule heating experiments on several nanowire-FET devices covered by a PMMA layer with thickness of ~ 200 nm in order to demonstrate the capabilities of this system to reach temperatures on the order of 300-400 $^\circ\text{C}$ required to abate the polymer [279]. In figure 5.8a-d we reported the entire set of measurements for a representative NW-FET before and after the Joule heating process. From the measured I - V and I - V_g characteristics of the device covered by PMMA we obtained a resistance of $1.8368 \pm 0.0003 \cdot 10^5 \Omega$, a transconductance $dI_{SD}/dV_g = 4.522 \pm 0.005 \cdot 10^{-8}$ S and a threshold voltage $V_t = -$

24.02±0.03 V. Using eq.(5.6) with the nanowire radius $r=254$ nm and length $L=5.96$ μm we obtained the electron mobility $\mu=88$ $\text{cm}^2/\text{V}\cdot\text{s}$ and nanowire resistivity at $V_g=20$ V of $4.52\cdot 10^{-3}\Omega\cdot\text{m}$. Following initial electrical characterization, three sweeps from 0 up to -40 V applied to the source-drain electrodes with a constant back-gate voltage of 20 V were performed as shown in figure 5.8b. The first sweep (black curve) from 0 to -30 V was not effective in producing any important changing, however a clear jump in resistivity was observed between the second and the third sweep with the extended range 0/-40 V (red and blue curves respectively). Thereafter, the new NW-FET resistivity, transconductance and threshold voltage calculated from the I-V and I- V_g characteristics in figure 5.8c were $3.8\cdot 10^{-1}\Omega\cdot\text{m}$ (at $V_g=0$), $3.21\pm 0.03\cdot 10^{-8}$ S and +10.36 V respectively. In particular, we observed an increase of the nanowire resistivity of almost two orders of magnitude and a large shift towards positive voltages of the V_t . The variation in the electrical properties of the device was associated with the PMMA ablation as demonstrated by the SEM image in figure 5.8d. In fact, we observed a complete ablation of the PMMA from the center and the side of the nanowire although a residual resist was found closer to the metal contacts.

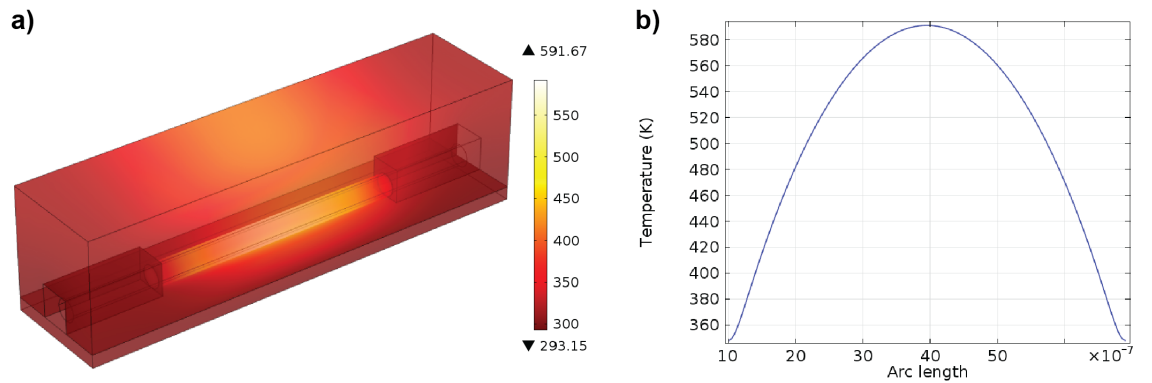


Figure 5.9.: *Finite-element method simulation of a) the temperature distribution generated by the Joule heating process. b) temperature profile inside the nanowire channel between the two electrodes.*

To further investigate the process, finite element method simulation using the commercial software COMSOL Multiphysics 4.3 were undertaken in order to simulate the temperature distribution along the nanowire. The simulated system (figure 5.9a) comprises a cylindrical nanowire with diameter 504 nm and length 9.9 μm with

two rectangular electrodes separated by 5 μm gap placed on 300 nm of SiO_2 substrate and covered by PMMA. The nanowire resistivity was assumed to be $4.52 \cdot 10^{-3} \Omega \cdot \text{m}$, the contact resistance between the metal and the nanowire $10^{-11} \Omega \cdot \text{m}^2$, the heat capacities C_p for ZnO, SiO_2 and PMMA were 40.3, 703 and 1466 J/kg·K and the thermal conductivity k was 110, 1.38, 0.2 W/m·K respectively. Thereafter the solution for the set of equations in the steady state

$$\begin{cases} \bar{E} = -\nabla V \\ \bar{J} = \sigma \bar{E} \\ \nabla \cdot \bar{J} = 0 \\ \nabla \cdot (k \nabla T) = -Q \end{cases} \quad (5.8)$$

with Q the heat flow generated by the joule heating process, were calculated in all the simulated volume. Note that the effect of the back-gate on the channel conductivity was considered in the resistivity value used for the channel conductivity therefore not included in the simulation. The simulated current density with 40 V applied between source and drain was found $1.4 \cdot 10^9 \text{ A/m}^2$, in agreement with the value measured at -40 V in the real device ($9.9 \cdot 10^8 \text{ A/m}^2$) thus supporting the validity of the simulations. Figure 5.9a-b show the temperature distribution in the simulated space volume and the temperature profile along the nanowire. Because of the contact resistance is much lower than the nanowire resistivity, the temperature along the nanowire reaches the maximum (320°C) in the center of the nanowire, as shown in the temperature profile in figure 5.9b. Accordingly, figure 5.8d shows a more effective PMMA ablation in the center of the nanowire while residual resist were found in the colder region near the electrodes. It is important to notice that, the resistivity value measured after the joule heating process with $V_g=0 \text{ V}$ would allow to reach only two degrees more than room temperature under comparable source-drain voltage applied.

These results corroborate the effectiveness of using the FET architecture to greatly improve the Joule heating capabilities of ZnO nanowire and provide an scheme of work to explore a larger variety of semiconductor materials for micro and nano-heaters.

5.6. Nanowire-FET device for selective decoration of single ZnO nanowire

The mask-selective droplet deposition method previously described allows to decorate nanowires distributed on a large substrate with high yield. In nanowire-based FET devices the nanowires are electrically contacted with at least two metal stripes, therefore an electric field-driven assembly of metal nanorods directly on the nanowire surface represents a valid alternative for selective deposition of nanorods on a target nanowire.

This approach relies on the dielectrophoretic force (see Chapter 3) imposed by an appropriate electric-field configuration that drives suspended nanorod in solution towards the selected nanowire. In the three terminals FET device, the nanowire is connected to the source and drain by metal pads and the Si(n⁺⁺) layer separated by 300 nm of SiO₂ from the nanowire was used as back-gate electrode. We firstly investigated the electric field in the simulated device by solving the appropriate equations (see previous section) using a finite element method simulation software (COMSOL Multiphysics 4.3). The simulated geometry consisted of a nanowire with a diameter of 300 nm and length of 5 μm in contact with two metal pad 450 nm thick on a Si substrate cover by 300 nm of SiO₂. Contact resistivity and nanowire resistivity were assumed to be 10⁻¹¹Ω·m² and 4.52·10⁻³Ω·m respectively. Two different configurations were investigated. In the first configuration the source electrode was set at potential of 5.7 V while the drain electrode and the back-gate were grounded. Similar conditions were previously used in Chapter 3 for assembling Au nanorods in 1D arrays. Figure 5.10a shows the electric field intensity calculated on a x-y plane at 150 nm from the SiO₂ surface. An intense electric field with magnitude of 10⁷ V/m was found at the electrode border edges and at the nanowire lateral sides due to the coupling with the back-gate.

At the contact point between the nanowire and the electrode the intensity dropped to very low values due to the equipotential condition. However the voltage potential dropped along the nanowire imposes a progressive reduction of the field intensity towards the grounded electrode. The E-field intensity along y-z plane in the center of the electrode gap is displayed in figure 5.10b. The dielectrophoretic force (directed

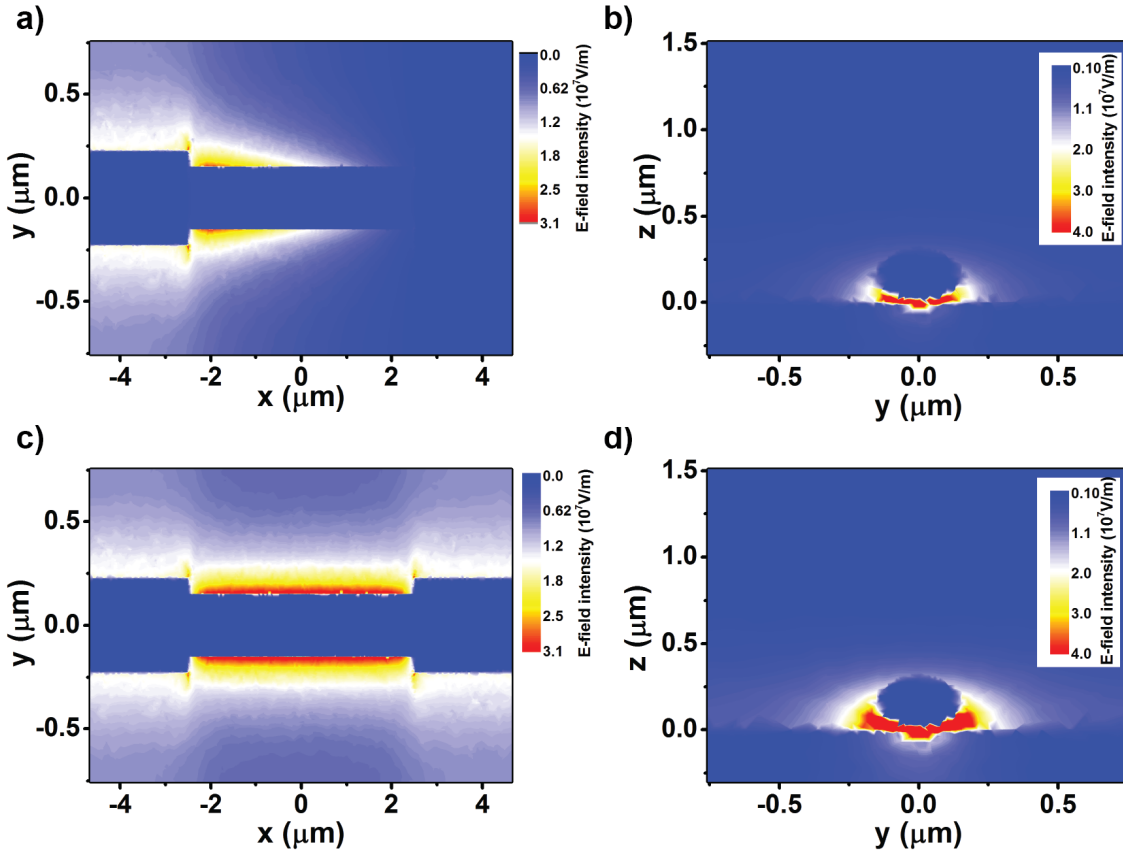


Figure 5.10.: Finite element method simulation of the electric field intensity in proximity to the ZnO nanowire FET device. Electric field magnitude was computed on a x - y plane at 150 nm above the SiO_2 surface and on a y - z plane in the center of the electrode gap for a-b) configuration with one electrode at 5.7 V_{rms} and the second electrode and the back-gate grounded and c-d) the back-gate at 5.7 V_{rms} and both electrodes grounded.

as the $\nabla |E|^2$) imposed by the electric field configuration induced a particle motion in solution towards the upper and side nanowire walls, although the spatial variation of the field magnitude along the nanowire would result in an inhomogeneous nanorod accumulation. In figure 5.10c-d we compare the second configuration where the back-gate was set at 5.7 V respect to the source and drain (grounded).

With these conditions the field intensity along the nanowire remained homogeneous (figure 5.10c) and the magnitude was enhanced by more than a factor 2 (figure 5.10c). Assembly experiments were undertaken by applying a sinusoidal AC voltage using a function generator (HP8116A Hewlett Packard) with amplitude between 4.2 and 6.4 V_{rms} (12-18 V_{pp}) and frequency 1 MHz on a given electrode chip via

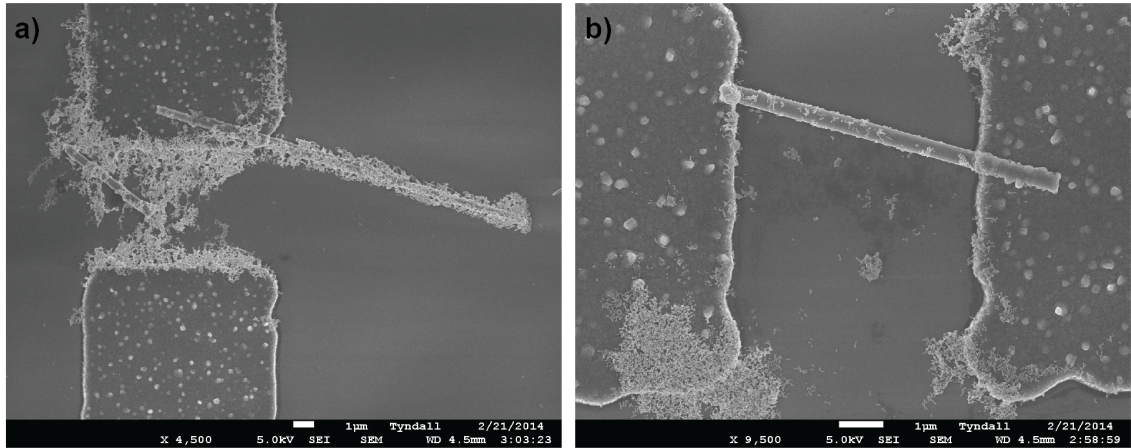


Figure 5.11.: SEM images of two representative ZnO nanowires decorated with Au nanorod by electric field mediated method obtained by applying a sinusoidal signal of a) 1MHz and $6.4 V_{rms}$ ($18 V_{pp}$) and b) 1 MHz and $5.7 V_{rms}$ ($16 V_{pp}$) to the back-gate with the source and drain electrodes grounded

gold wire bonds on the Al contact pads. A $5 \mu\text{l}$ drop of aqueous nanorod solution (CTAB concentration below mM) was placed on the chip surface in the presence of an applied electric field for ca. 5 min. Following nanorod assembly, the field was disconnected, the excess nanorod solution was flushed with water and the substrate dried under stream of nitrogen. Figure 5.11a-b show two representative ZnO nanowires contacted with one (5.11a) and two (5.11b) electrodes obtained by applying $6.4 V_{rms}$ and $5.7 V_{rms}$ respectively to the back-gate (both electrodes were grounded). Metal nanorods were found on the nanowire body and at the electrode edges as expected, with higher density for larger voltages applied. Because of the electric field configuration arise from the coupling between the nanowire and the substrate, also a single electrode contacting a nanowire permits the process to occur. Moreover, this configuration avoided electrical shorts between source and drain that could prevent nanorod deposition as discussed in Chapter 3. Compared to the mask-selective droplet deposition, this method afforded a selective nanorod deposition on a specific nanowire and a better control on the nanorod density deposited by acting on the electric field intensity and frequency. However, a more complex fabrication procedure limits the scalability of this decoration process.

5.7. Conclusion

Electrical characterization of ZnO nanowires devices with Ti/Au and Ti/Al metal contacts in air and high vacuum indicated that Al forms an Ohmic contact with the ZnO and, after RTA treatment, a device resistance below $10^6 \Omega$ in air was achieved. These resistance values are very promising for ZnO nanowire-based devices compared with the reported values in literature of the order of 10^8 - $10^9 \Omega$. Also, a detailed characterization of the nanowire resistivity, contact resistivity, field-effect mobility and electron density was provided. These data were used to model the Joule heating process in the NW-FET device by FEM simulation, showing that by exploiting the three-terminals configuration to increase by 1-2 folders the nanowire resistivity, temperature larger than 300°C can be reached in the center of the nanowire, otherwise not achievable in the traditional two terminal configuration. Furthermore, using a specific electric field configuration, only achievable in a NW-FET device, selective deposition of colloidal Au nanorods on a target nanowire was demonstrated. The optimization of the nanofabrication process developed in this Chapter and the investigation of the electronic properties of ZnO nanowires was a fundamental prerequisite for the development of the hybrid-FET devices discussed in Chapter 6.

Chapter 6.

Au nanorod-ZnO nanowire hybrid device

In this Chapter the photoconductivity behavior of ZnO nanowires under radiation with energy above band-gap ($\lambda=265$ nm) and below band-gap ($\lambda=650-850$ nm) both in air and high-vacuum conditions is presented. From time-resolved measurement under UV radiation, I demonstrated that the photocarrier generation and recombination response is the result of three processes characterized by different time-scale and sensitive to the environment conditions. In the second part of the Chapter I present a new class of near-infrared photodetectors comprising Au nanorods - ZnO nanowire hybrid systems. Fabricated hybrid FET devices showed a large photoresponse under radiation wavelengths between 650 nm and 850 nm, accompanied by an ultrafast transient with a time scale of 250 ms, more than one order of magnitude faster than the ZnO response under radiation above band-gap. A detailed investigation of the hot-electron generation and injection processes is discussed to explain the improved and extended performance of the hybrid device.¹

6.1. Introduction

Plasmonic nanostructures have been extensively studied for their unique ability to focus light into nanometer-scale volumes due to large localized electromagnetic

¹This work was published as *Hot-Electron Injection in Au Nanorod-ZnO Nanowire Hybrid Device for Near-Infrared Photodetection*, Pescaglini et al., *Nano Lett.*, 14(11), 6202-6209, (2014)

fields generated by surface plasmons [8]. Recently, potential applications have been widened by the observation that plasmonic nanostructures can also directly convert the collected light into electrical energy by generation of so called *hot electrons*, whereby surface plasmons excited by incident radiation can decay non-radiatively and generate an energetic electron instead of re-emitting a photon [280]. Such generated hot electrons usually relax to the ground state through electron-electron and electron-phonon interactions. However, when a hot electron with sufficient momentum is generated in a metallic nanostructure in direct contact with a semiconductor where an interface potential is formed (Schottky barrier like in the broad sense), the excited electron in the nanostructures might have sufficient energy to traverse the barrier. This effect can result in generation of enhanced photocurrent while exciting at photon energies below the band-gap of the semiconductor and confers widened optoelectronic features to the resulting metal-semiconductor hybrid device. The first evidence of hot electron generation and injection was reported by Zhao *et al.* [281], who investigated the photoelectrochemical response of TiO₂ film electrodes containing Au and Ag nanoparticles. They observed an anodic photocurrent peak at 560 nm, which they attributed to the surface plasmon resonance of metal nanoparticles. More recently, Tian *et al.* demonstrated a maximum incident photon to current conversion efficiency (IPCE) of almost 6% in Au nanoparticle sensitized solid-state heterojunction solar cells in correspondence of the absorption spectrum peak of the nanoparticles [282]. Enhanced photocatalytic activity mediated by surface plasmons was also demonstrated in TiO₂ nanotubes and nanospheres [283, 284]. The first example of hot electron generation for photodetection applications has been proposed by Knight *et al.* who fabricated Au resonant antennas on a n-type silicon substrate electrically connected through a top transparent electrode of indium tin oxide (ITO). The device generated photocurrent under radiation wavelengths 1250-1600 nm, displaying a maximum value in correspondence of the plasmonic resonance of the optical antenna [24]. The initial quantum efficiency of 0.01% was subsequently increased by about one order of magnitude by embedding the plasmonic structure within the semiconductor, thus creating a 3D Schottky barrier [285]. Overall, the field of plasmonic hot-electron generation in nanostructures is still at its infancy. Therefore, alternative plasmonic/semiconductor material combinations

together with alternative device geometries could be explored, potentially leading to the generation of detectors with higher efficiencies and extended tunable wavelength ranges [286]. For example, the transition from planar 3D architectures to 1D architectures based on semiconductor nanowires has been shown to support faster carrier collection [287] and to allow use of a wider range of semiconductor materials [114]. Plasmonic-enhanced photocurrent and optical absorption were observed in Si nanowires, induced by the enhanced electric field at the metal/semiconductor interface [133, 134, 135]. Enhanced optical absorption was also observed in hybrid InAs nanowires [136] and GaAs nanowires [137].

Among semiconductor nanowires, ZnO nanostructures have been extensively investigated for optoelectronic applications due to their large band-gap energy (3.3 eV) and ease and low cost of manufacturing [251, 256, 288, 289]. Several authors have investigated metal nanostructure-ZnO nanowire hybrid systems. For example band-edge emission photoluminescence and photocurrent enhancement, originating from metal to ZnO electron transfer, were detected in ZnO nanowires coated with metal nanoparticles [139, 128, 140]. However, plasmonic-mediated generation, injection and collection of energetic electrons in semiconductor nanowire-based hybrid devices for photodetection and photovoltaic applications remain a field vastly unexplored.

In this Chapter, I present intense near infrared photon-generated hot electrons in individual ZnO nanowire FETs (Field Effect Transistor) decorated with Au nanorods. The hybrid system displayed large photocurrents under irradiation between 650 nm and 850 nm, accompanied by an "ultrafast" response (for the system) with a time scale of 250 ms, more than one order of magnitude faster than the response of bare ZnO nanowires above band-gap radiation. Photoresponse arose by efficient hot-electrons generation and injection at the metal-semiconductor interface. Thus, in the proposed hybrid system Au nanorods acted as active elements, generating hot electrons that were injected into the wide band-gap ZnO nanowire, which functioned as a passive component for charge collection. A detailed investigation of the effect played by the Au nanorods on the process showed that the density of nanorods deposited on the nanowire affected photocurrent intensities and the height of the Schottky barrier. Theoretical predictions and simulations supported the experimen-

tal findings and showed that the selected nanorod anisotropic shape and size played a pivotal role in the hot-electron generation and injection processes. To the best of our knowledge this is the first report on hot-electron injection mediated by localized surface plasmons in hybrid metal nanorod-semiconductor nanowire FET devices.

The presented work is extremely promising for further development of novel miniaturized, tunable photodetectors and for highly efficient plasmonic energy conversion devices.

6.2. Experimental section

ZnO nanostructures were grown by CVD using vapour-liquid-solid mechanism in a high temperature tube furnace as reported elsewhere . Dimensional statistical analysis on obtained nanowires, gave lengths between 1 μm to 10 μm with a mean value of 5 μm and diameters between 40 nm and 500 nm.

Au nanorods were synthesized using a seed-mediated method described in section 2.2.2. The as prepared Au nanorod solution (1 ml) was centrifuged twice to remove CTAB excess and re-dispersed in 1 ml of deionized water, resistivity 18 $\text{M}\Omega\cdot\text{cm}$. The final CTAB concentration was estimated to be 0.05 mM. Dimensional statistical analysis of 100 nanorods gave a mean nanorod length and diameter of respectively 54 ± 3 nm and 22 ± 3 nm (aspect ratio of 2.4 ± 0.4). Scanning electron microscopy (SEM) characterization was performed using a Scanning Electron Microscope (JSM 7500F, JEOL UK) at operating voltages of 10 kV.

Photoconductivity measurements in high vacuum ($3 \cdot 10^{-6}$ bar) were performed in a Wentworth micromanipulator 6200 probe station. Characterization of the photocurrent was carried out by applying 50 mV DC bias via E5270B parameter analyzer by using the Setup 1 shown in figure 6.1b). The sample was investigated at room temperature and illuminated using an UV portable lamp with wavelength at 365 nm and nominal power of 4 W. The estimated power on the sample surface was 0.8 W/cm^2 .

Photoconductive measurements in air were carried out by mounting the sample on the home-made holder shown in figure 6.1a. Ten external pads of a T-shape PCB were connected to BNC terminations with a common ground to allow the electrical

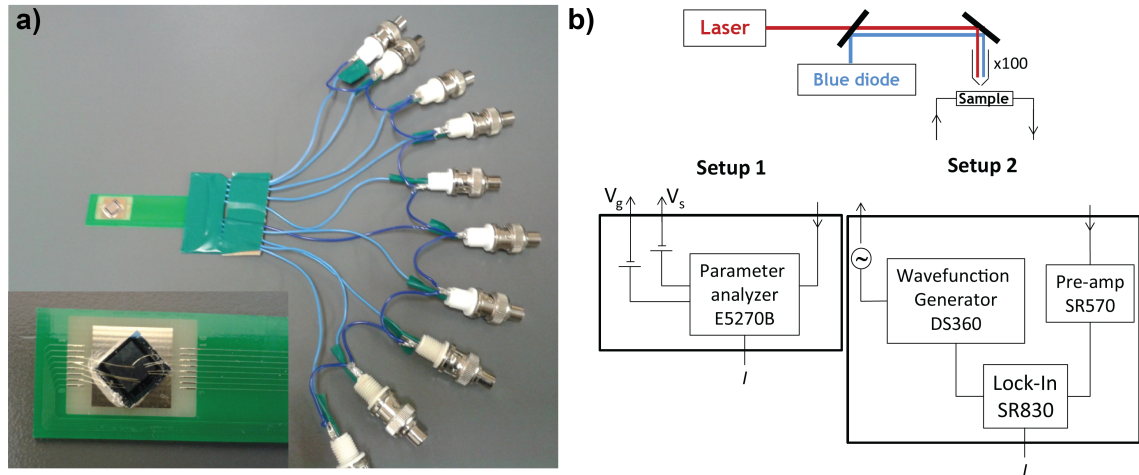


Figure 6.1.: a) Picture of the home-made holder used for the photoconductivity measurements in air. b) Schematic of the two setups used to perform the measurements. The optical setup consists of a tunable laser in the range 600-900 nm. The laser beam was focused on the sample through a beam splitter, a mirror and a 100 \times objective. Two electrical setups were used for the electrical measurements. Time-resolved measurement with exposition time of 200 s at variable back-gate voltages (time-resolution of 300 ms) were performed with setup 1. High resolution measurements with time resolution of 15 ms were realized with the setup 2.

readout. Silver paste was used to fix the sample to the holder and gold wire bonds connected the PCB pads to the device contacts and the backgate.

The sample was investigated at room temperature and illuminated using an UV portable lamp at 265 nm and nominal power of 4 W (the estimated power on the sample surface was 0.8 W/cm²) and a tunable supercontinuum source - a high-power Fianium fiber laser with an integrated acousto-optical filter operating in a pulsed-mode at 40 MHz with radiation wavelength tuning range of 600-1100 nm. The tunable laser was focused to a 2 μ m spot by using a 100 \times optical objective. A blue diode was used to illuminate the sample in order to place the laser spot on top of the device (see figure 6.1b).

Devices were kept in dark condition for at least a couple of hours until a steady dark-current value was reached. In order to investigate the fast photocurrent transient, photocurrent measurements were performed by illuminating the device for 15 s and recording the drain current for 90 s. Wave-function generator (SRS-DS360) was used to force a sinusoidal signal with amplitude 400 mV (frequency 19Hz) and

the output signal was sent to a pre-amplifier (SRS-SR570) and the current measured with a SRS-SR830 Lock-in amplified using an acquisition time of 15 ms and an integration time of 10 ms (see Setup 2 in figure 6.1b). Photocurrent measurements under longer illumination time (200 s) and different gate voltages were performed by three terminals configuration using HP-E5270B parameter analyzer with acquisition time of ~ 300 ms (6.1b).

6.3. Photoconductivity in ZnO nanowire

ZnO nanostructures have been extensively investigated for optoelectronic devices due to the large bandgap energy (3.3 eV), ease of manufacturing and low costs. Demonstration of functional devices such field effect transistors [258], UV photodetectors [257], UV light emitting diodes [290], nanolaser [251, 253] and gas sensors [260, 264] have been successfully achieved in the last decade thus suggesting ZnO as a potential low-cost alternative to GaN in optoelectronic applications. In particular, ZnO nanowire-based photodetectors have been shown capable of high sensitivity with photoconductive gain as large as 10^8 [120]. This high sensitivity can be ascribed to two main factors : (i) the presence of deep-level surface trap states that extend the photocarrier lifetime and (ii) the low dimensionality of nanowires that shortens the carrier transit time thus resulting in an efficient charge collection before recombination.

This section is dedicated to the investigation of the photoconductivity properties of ZnO nanowire under UV and near-infrared radiation. We show the evidence of three processes with well separated time-scales underlying the carrier generation and recombination. In particular we demonstrate a response dominated by deep level defects under both above and below bandgap excitation energies.

6.3.1. Photoresponse above-bandgap radiation

Representative photoresponse in air of a single ZnO nanowire irradiated by UV light for 200 s is shown in figure 6.2a.

The dark current value of 3.3 nA increased to 460 nA after 200 s of illumination

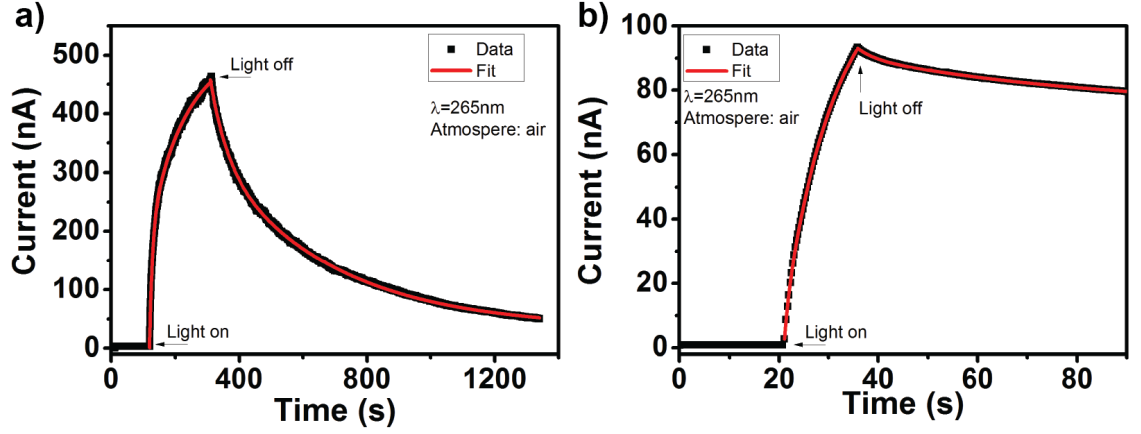


Figure 6.2.: Photoresponse of ZnO nanowire in air during exposition to UV light ($\lambda=265$ nm) for a) 200 s and b) 15 s. Red lines are the bi-exponential growth and decay fitting to the corresponding data.

without reaching the saturation. When the light was switched off the dark current values was recovered in more than one hour. The time-dependent photocurrent growth (I_{ph}) was fitted with the bi-exponential function [291]

$$I_{ph} = I_s + A_1(1 - \exp(-t/\tau_1)) - A_2 \exp(-t/\tau_2) \quad (6.1)$$

where I_s , A_1 , A_2 , τ_1 and τ_2 are fitting parameters. The experimental data were well reproduced by the expression 6.1 and the following values for the parameters were obtained : $I_s = 209 \pm 1$ nA , $A_1 = 306 \pm 1$ nA , $A_2 = 200 \pm 1$ nA , $\tau_1 = 118 \pm 2$ s and $\tau_2 = 9.7 \pm 0.1$ s. The time constants τ_1 and τ_2 extracted from the fit revealed a first component contributing to the photocurrent growth on the time scale of ~ 10 s and a second component more than ten times slower acting on the time scale of ~ 118 s. From the comparable magnitude of A_1 and A_2 we deduced that the two components have the same importance during the process.

The photocurrent decay was found having a similar exponential behavior. The data were fitted with the function

$$I_{ph} = I_\infty + B_1 \exp(-t/\gamma_1) + B_2 \exp(-t/\gamma_2) \quad (6.2)$$

where the values $I_\infty = 33.4 \pm 0.2$ nA, $B_1 = 297.7 \pm 0.4$ nA, $B_2 = 124.8 \pm 0.5$ nA, $\gamma_1 = 371 \pm 1$ s and $\gamma_2 = 50.1 \pm 0.3$ s represent the calculated set of fit parameters. The

relaxation time constants for the fast and slow component were found considerably longer than τ_1 and τ_2 previously calculated although having a comparable intensities. The values found for τ_1, τ_2, γ_1 and γ_2 are in agreement with previous reports [291]. However, we noticed that the fast component is the weight-averaged result of a superposition of two distinct components. In figure 6.2b we show a representative $I(t)$ obtained from a ZnO nanowire illuminated for 15 s with UV light and the related fits. For the photocurrent growth we found $I_s = 4.7 \pm 0.5$ nA , $A_1 = 116.6 \pm 0.4$ nA , $A_2 = 18.4 \pm 0.6$ nA , $\tau_1 = 10.9 \pm 0.1$ s and $\tau_2 = 0.98 \pm 0.06$ s and for the photodecay $I_\infty = 74.2 \pm 0.2$ nA, $B_1 = 15.6 \pm 0.1$ nA, $B_2 = 2.63 \pm 0.05$ nA, $\gamma_1 = 49 \pm 1$ s and $\gamma_2 = 3.6 \pm 0.1$ s. Therefore we deduced that the photocarrier generation under UV light was determined by at least three processes on different time-scales. A first fast process on a time scale below 1 s, a second process with time constant around 10 s and a third slow process on time-scale of ~ 100 s. We notice that although the second and third process can be well resolved with our setup (acquisition time ~ 300 ms) the fast process could be on the same scale or even much faster than the resolution time used.

Figure 6.3a shows a representative photoresponse of a ZnO nanowire during 300 s of exposition in vacuum. The photocurrent increased over time without reaching the saturation within the exposition time. The time-dependent bi-exponential growth parameters obtained from 6.1 were $I_s = 58 \pm 1$ nA, $A_1 = 0.7 \pm 0.2$ μ A, $A_2 = 56 \pm 1$ nA, $\tau_1 = 2432 \pm 964$ s and $\tau_2 = 39.7 \pm 0.7$ s.

We noticed that the slow component dominates the photoresponse ($A_1 \gg A_2$) and the related constant time τ_2 increased by almost a factor 4 in magnitude compared to the τ_2 measured in air. The decay process showed even more pronounced increasing in the time constants. The values obtained from the fit were $I_\infty = 16.7 \pm 0.5$ nA, $B_1 = 18.5 \pm 0.8$ nA, $B_2 = 330 \pm 29$ nA, $\gamma_1 = 3908 \pm 25$ s and $\gamma_2 = 101154 \pm 164$ s. In vacuum, the time constants related to the photocurrent relaxation were clearly longer than in air and several hours were required before the initial dark-current value was restored.

Evidence of three distinctive components in the photocurrent rise and decay were not previously reported in literature. We tentatively attributed these contribution to the free electron-hole pair generation and recombination, carrier trapping in the

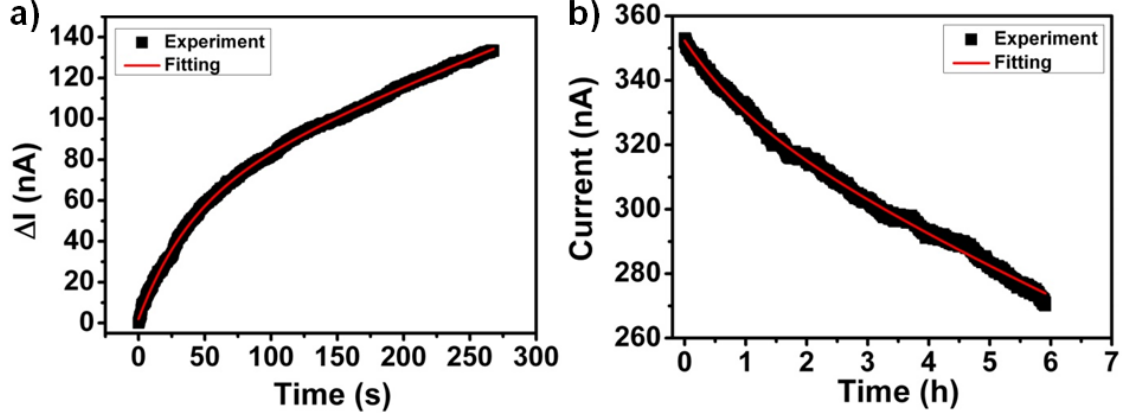


Figure 6.3.: a) Photoresponse of ZnO nanowire during exposition to UV light (365 nm) b) Photocurrent decay after exposition of 300 s. Red lines are the bi-exponential growth and decay fitting to the corresponding data.

deep defect levels and adsorption/desorption of oxygen species on the ZnO surface respectively.

The first process, free electron-hole pairs generation and recombination, is expected to occur on sub-nanoseconds time scale, as demonstrated by time-resolved photoluminescence studies [292]. The coefficients A_1 , B_1 for this process is one order of magnitude smaller than the coefficients related to the other two processes thus suggesting that only a small part of the generated electron-hole pairs contribute directly to the detected photocurrent. Photocurrent relaxation in ZnO with time constant on the order of hundreds ms or below is scarcely reported in literature. Studenikin *et al.* attributed the photocurrent transient in the range of 100 ns to the direct recombination of free electron-hole pairs [293] and Soci *et al.* found oxygen desorption on time scale of 20 ns in high-quality crystalline ZnO NW [287]. Our measurement cannot resolve such a fast processes due to a longer integration time (15-300 ms), however the detected fast transient could be related to similar processes. The second component is tentatively attributed to the carrier generation and recombination mediated by deep trap levels. We notice that, using the mobility value reported in section 5.4, the carrier transit time $T_t = L^2/\mu V$ (with L the channel length, μ the mobility and V the applied bias) in ZnO nanowire was calculated to be on the order of ns, comparable with the photoluminescence decay time for deep levels [294]. Therefore both carriers generated by defects ionizations

and free electron-hole pairs can undergo also multiple re-trapping before reaching the metal electrodes. Finally we assigned the third process (~ 100 s) to the adsorption/desorption of oxygen ions on the nanowire surface as suggested by the longer time-constant found in the measurements realized in vacuum compared to air.

The second and third components in the photocurrent response of ZnO nanostructures are well documented in literature. Dhara *et al.* reported a bi-exponential growth behavior of vertical aligned ZnO nanowire with a fast photocurrent growth characterized by a time constant in the range of 10-30 s followed by a slower growth with time constant of the order of hundreds seconds [291]. Similar behavior was found for the photocurrent decay. The first rapid component was attributed to the photogeneration and recombination of electron-hole pairs and the slow process to the adsorption and desorption of oxygen molecules. In particular, they proposed the following mechanism underlying the photoresponse: in dark conditions oxygen molecules are adsorbed on the nanowire surface and capture the free electrons, thus creating a depletion layer and band bending near the surface. During illumination with radiation energy larger than the bandgap, electron-hole pairs were generated. Following the built-in radial potential, photogenerated holes migrate towards the surface where they can recombine with adsorbed oxygen ions. Desorption and re-adsorption of oxygen species at the surface is a slower process respect to the electron-hole generation in agreement with the different time constants experimentally observed. Accordingly, the high vacuum conditions strongly affected the concentration of oxygen in the environment and compromised the photodesorption and adsorption of the O_2^-/O_2 species. Consequently, unpaired photogenerated electrons required a longer time to be re-trapped compared to the time required in air.

We noticed that the time-resolved photoluminescence studies on ZnO film reported a near-bandgap excitation emission (3.26 eV) with decay time in the range of hundreds of picoseconds that is much faster than the shortest time-scale photoconductive process in ZnO nanowire [292]. This time discrepancy between the generation-recombination of electron-hole pairs and photoconductivity response suggests that the latter is not dominated by the photocarrier lifetime but by the relaxation dynamics in the surface states [295]. Reemts *et al.* proposed to explain the

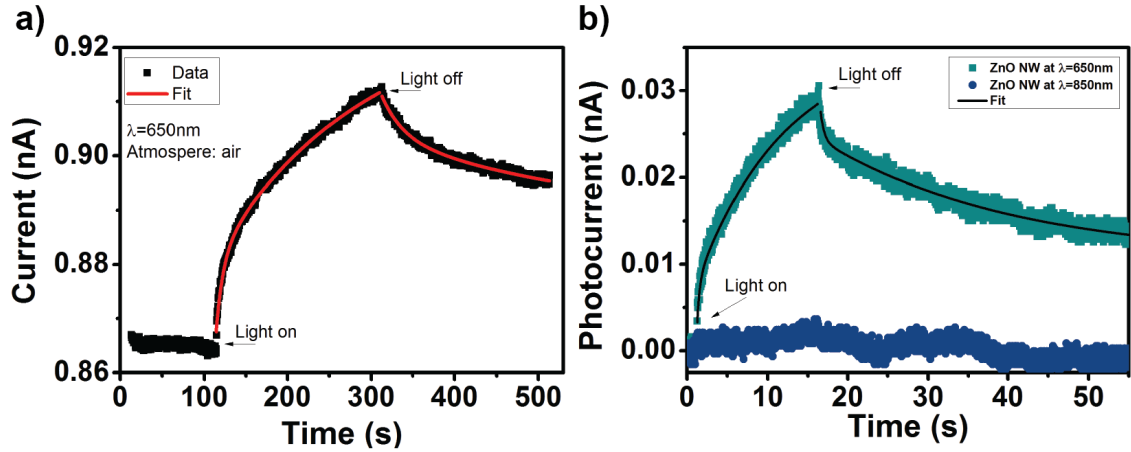


Figure 6.4.: a) Photoresponse of ZnO nanowire during 200 s exposition to light with $\lambda=650\text{ nm}$ b) Photoresponse of ZnO nanowire during 15 s exposition to light with $\lambda=650\text{ nm}$ and $\lambda=850\text{ nm}$. Red and black lines are the bi-exponential growth and decay fitting to the corresponding data.

mechanism of slow photocurrent rise and decay observed in highly porous ZnO films by assuming a finite probability for a lattice relaxation at the surface that traps photoexcited electrons in a metastable state with longer lifetime [296]. This theory was recently confirmed by theoretical calculation showing that the Zn-Zn distance decrease in presence of V_0^x oxygen vacancies and increase in case of V_0^{++} vacancies [297].

6.3.2. Photoresponse below-bandgap radiation

Photoconductive behavior of a representative ZnO NW FET was investigated under incident radiation with wavelengths at 650 nm and 850 nm (corresponding to photon energy of 1.9 and 1.45 eV respectively) and intensity of $\sim 20\text{ W/cm}^2$ in air. A photocurrent response at $\lambda=650\text{ nm}$ was found in the ZnO NW FET device although the excitation energy was below the ZnO band-gap energy (3.3 eV) (figure 6.4a).

Following 200 s exposition to laser radiation, the measured current increased from 864 pA to 913 pA although during the photodecay the same amount of time allowed to recovered only the 30% of the total photocurrent (48 pA). From the bi-exponential fit (red lines in figure 6.4a) we found for the photocurrent growth $I_s = 878.6 \pm 0.3\text{ pA}$, $A_1 = 48.1 \pm 0.7\text{ pA}$, $A_2 = 48 \pm 2\text{ pA}$, $\tau_1 = 178 \pm 7\text{ s}$ and $\tau_2 = 8.5 \pm 0.4\text{ s}$ and for the photodecay $I_\infty = 889 \pm 3\text{ pA}$, $B_1 = 11.9 \pm 0.9\text{ pA}$, $B_2 = 16 \pm$

2 pA, $\gamma_1 = 24 \pm 3$ s and $\gamma_2 = 237 \pm 99$ s. The values obtained for τ_{1-2} and γ_{1-2} are comparable to the values characterizing the ZnO photoconductivity under UV radiation while the intensity of the related coefficients changed considerably. The similarity in the time constants indicates the presence of identical processes for photocurrent generation under above-bandgap and below-bandgap radiations. However the variation in intensity between the photocurrent response under $\lambda=265$ nm and $\lambda=650$ nm can be attributed to the lower DOS of defects states in the range of explore energies. This observations corroborate the dominant role of the deep level defects in the photocarrier dynamics in ZnO nanowires.

To further characterized the short-time component we also performed high-speed measurements with time resolution of 15 ms (figure 6.4b). During 15 s of illumination the photocurrent increased progressively until a maximum value of 29 pA without reaching saturation. When the light was switched off, the photocurrent decreased by 60% within the next 55 s and the dark current value was completely restored only after few minutes. From the bi-exponential fit (black line in figure 6.4b). We individuated a fast component rising with time constant $\tau_1 = 0.33 \pm 0.04$ s and a slow component with time constant $\tau_2 = 10.9 \pm 0.4$ s. The relative importance of these two distinctive processes is given by the coefficient A_1 and A_2 . We found that the coefficient $A_1 = 8.7 \pm 0.6$ pA is one order of magnitude smaller than $A_2 = 67 \pm 1$ pA that indicates the slow process is dominating the photoresponse. Similar values were extracted from the decay process with $I_\infty = 3.940 \pm 0.003$ nA, $B_1 = 7.8 \pm 0.7$ pA, $B_2 = 33.9 \pm 0.2$ pA, $\gamma_1 = 0.47 \pm 0.08$ s and $\gamma_2 = 23.8 \pm 0.5$ s.

We also noticed that sub-bandgap photocurrent due to surface state excitation has been shown having a maximum in correspondence of the green-yellow photoluminescence band peaked at 2.48 eV [298] and a negligible contribution at lower energies. This is in agreement with our findings, as demonstrated by the absence of photocurrent detected at $\lambda=850$ nm in ZnO NW FET device (figure 6.4b).

Photocurrent response under visible radiation and photoluminescence in the green-yellow range of the spectrum in ZnO nanowires were also reported by different authors and related to structural defects such as antisite oxide O_{Zn} , Zn vacancy V_{Zn} and oxygen vacancy V_O [299, 294].

Liao *et al.* have studied the surface effects on photoluminescence in single ZnO

nanowires. At 10 K the visible emission was composed by blue- green peak centered at 2.48 eV and a weaker yellow luminescence peak at 2 eV [298]. The yellow peak remain stable with the increasing of the temperature whereas the green-blue peak decrease in intensity and at 300 K only a weak blue peak at 2.75 eV was observed. The authors attributed the visible emission to the three charge state of oxygen vacancies : double ionized oxygen vacancy V_0^{++} , singly ionized V_0^+ and neutral oxygen vacancy V_0^x . The V_0^{++} introduce an energy level inside the ZnO bandgap around 2 eV below the conduction band and the V_0^+ and V_0^x at 2.48 and 2.78 eV from the valence band respectively. Therefore the yellow emission was attributed to the recombination of V_0^{++} with conduction band electrons and the green and blue to the electron transition from V_0^+ and V_0^x to the valence band respectively. Moreover theoretical calculation [297] attributed the persistent photoconductivity to the ionization of V_0^x to V_0^{++} followed by lattice relaxation. The ionization of V_0^x to V_0^+ and V_0^+ to V_0^{++} have theoretical excitation energy of 2.83 eV and 2.4 eV thus are believed to be responsible for the observed photoconductivity under excitation energy below bandgap. Bera *et al.* [299] found a photocurrent response also by illuminating with energy radiation of 1.9 eV. They attributed the phenomenon to the ionization of Zn vacancies (V_{Zn}) and oxygen desorption on the ZnO surface [299, 300]. Moazzami *at al.* compared the decay times for the sub-bandgap photoconductivity and photoluminescence in ZnO epilayers. The broad peak centered at 2.35 eV (green emission) was attributed to deep recombination centers near the valence band. From time-resolved PL the near band recombination time constant was on the order of 100 ps whereas the decay time for deep levels was found around 20 ns, more than two order of magnitude longer. However the photocurrent decay response in the visible showed a longer decay time on the order of 80 min and was clearly reduce (also in intensity) after surface passivation with SiO_2 [294]. The photocurrent process under visible illumination was explained as follow : electron-hole pair are generated upon visible illumination by excitation of defects states (optical transition between defects state and band edge), than holes can be captured by deep trap levels that may have a long life time and after recombine with conduction band electrons. However a clear attribution of the different sub-bandgap transition experimentally observed has not been provided until date.

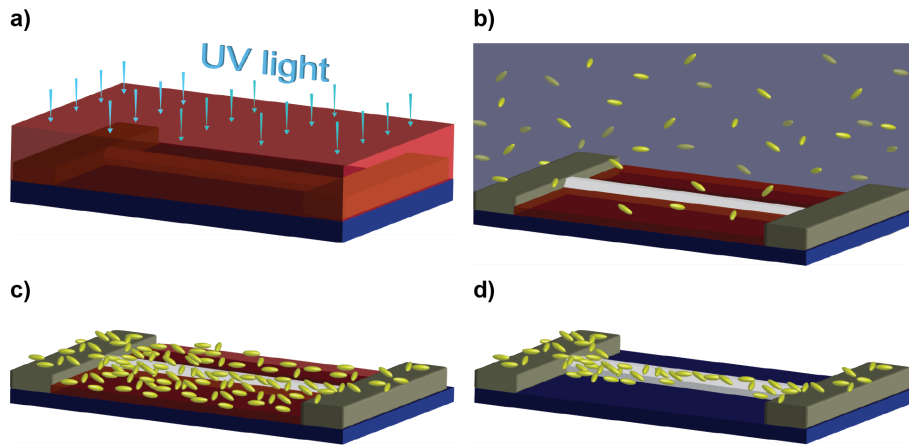


Figure 6.5.: Schematic representation of the process used to decorate with Au nanorods the ZnO nanowire FET device. a) Resist spinning and exposition to UV light b) resist removal and drop the colloidal solution c) nanorod deposition on the substrate d) lift-off.

6.3.3. Decoration of ZnO nanowire FET devices with Au nanorods

Au nanorod-ZnO NW hybrid FET devices (AuHbNW) were obtained by selective deposition of colloidal Au nanorods on fabricated ZnO nanowire FET devices. The process was adapted from the method presented in section 4.4 and schematically described in figure 6.5a-d (see appendix A.2 for more details). Specifically, a resist (S1813, $1.4 \mu\text{m}$) layer was deposited on substrates containing ZnO nanowire FETs by spin-coating. The resist was selectively etched by exposition to UV light followed by resist development so that complete removal was achieved on the metal pads and the nanowire top surface, while leaving a residual layer along the nanowire side and on the substrate surface (figure 6.5a). Au nanorods were deposited on the entire substrate surface by deposition of aqueous suspensions followed by evaporation at $110 \text{ }^\circ\text{C}$ (figure 6.5b-c). Finally, the residual resist layer was removed leaving Au nanorods selectively deposited on the ZnO surface (figure 6.5d).

A representative SEM image of the ZnO nanowire FET device decorated with Au nanorods is shown in figure 6.6a-b. A reproducible formation of hybrid devices with randomly oriented nanorods was achieved with the proposed method. Removal of resist in two different phases of the process allowed selective decoration of the ZnO nanowire surface while preventing Au nanorod deposition in the area between

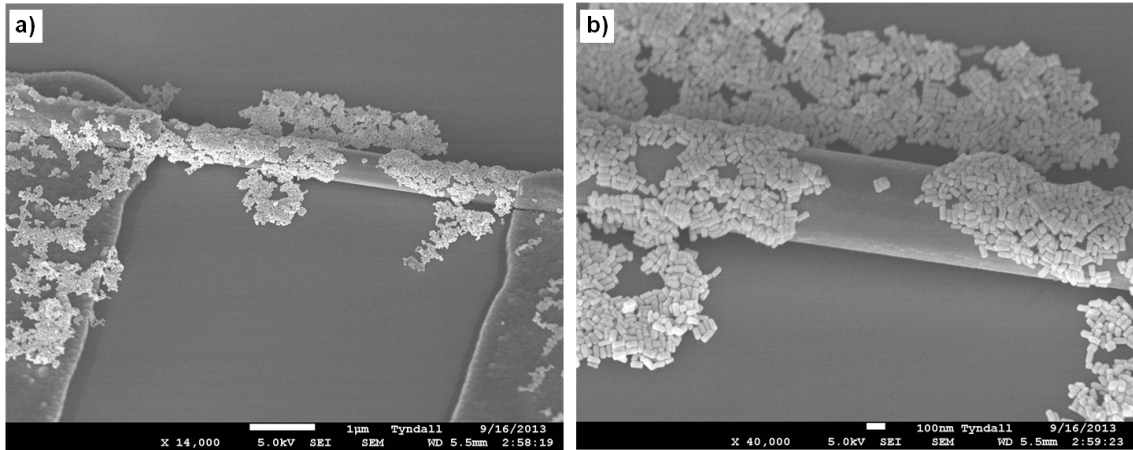


Figure 6.6.: a) Scanning electron microscopy of a AuHbNW-FET devices and b) details of the central part of the nanostructure showing the nanorods distribution along the nanowire.

contacting electrodes. This avoided the generation of electrical shorts arising from formation of nanorod networks in the area between the electrode gaps. Moreover, it should be emphasize that this process allows to realized hybrid devices without any limitation on materials and metal nanostructure size and geometry with high yield and reproducibility thus providing a step forward respect to the present techniques for fabrication hybrid FET devices and opening up to further advances in the field of hybrid metal nanostructure-semiconductor nanowire based devices.

6.4. Photoconductivity spectroscopy on hybrid devices

Photoconductive behavior of a representative hybrid device (AuHbNW FET) was investigated under incident radiation with wavelength between 650 nm and 850 nm (corresponding to photon energy of 1.9-1.45 eV) and intensity of $\sim 20 \text{ W/cm}^2$. Figure 6.7a reports the photoconductive behavior of a representative AuHbNW FET device. We clearly observed a strong enhancement in the response at 650 nm with a maximum photocurrent of 0.6 nA after 15 s of exposition. Also, a sharp transient was found in correspondence of the on/off state of the incident radiation with 70% variation in photocurrent within 400 ms. Notably a photocurrent of 0.26 nA was

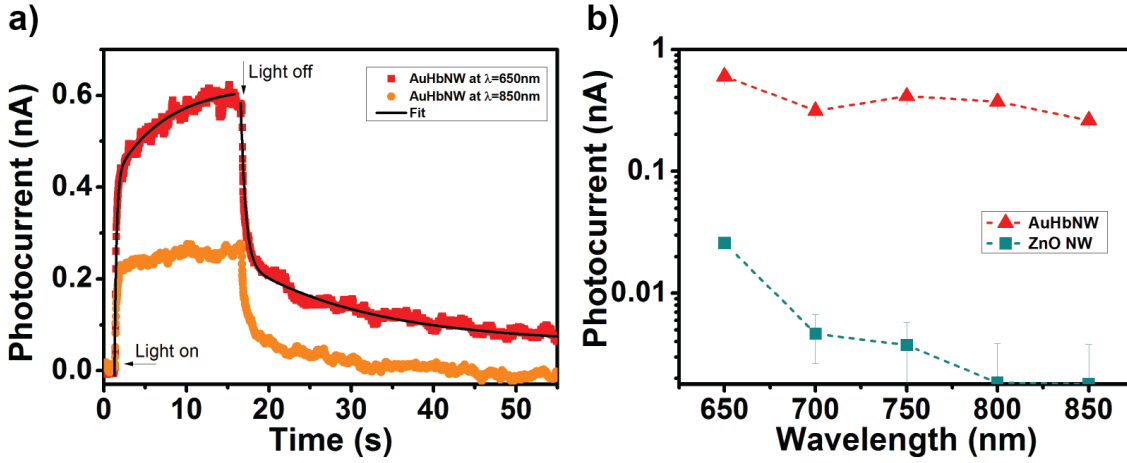


Figure 6.7.: a) Photoresponse of AuHbNW FET device nanowire during exposition to light with $\lambda=650\text{nm}$ and $\lambda=850\text{nm}$. Black lines are the bi-exponential growth and decay fitting to the corresponding data b) Photocurrent measured in AuHbNW and ZnO NW FET device for wavelengths in the range 650-850nm.

detected also for radiation with $\lambda=850\text{ nm}$. A comparison between the photocurrent values in ZnO NW FET and in hybrid device at different wavelengths is shown in figure 6.7b. In ZnO NW FET photocurrent detected with light at 650 nm was found showing a rapid decrement at longer wavelengths down to no-detectable values after $\sim 750\text{ nm}$. On the contrary, in the hybrid device the photocurrent was found orders of magnitude larger and having a slower decrement that allows light detection even outside the range explored.

To further characterized the devices response, we investigated the photogeneration and photodecay time scale using a bi-exponential fit described by eq.6.1 and eq.6.2 (black line in figure 6.7a).

Two components in the phototransient with time constants $\tau_1=6.3 \pm 0.4\text{ s}$ and $\tau_2=0.238 \pm 0.007\text{ s}$ and coefficients $I_s=19.55 \pm 0.02\text{ nA}$, $A_1=0.61 \pm 0.01\text{ nA}$ and $A_2=247 \pm 43\text{ nA}$ for the photoconductance rise and $\gamma_1=0.69 \pm 0.01\text{ s}$, $\gamma_2=16.5 \pm 0.3\text{ s}$, $I_\infty=18.761 \pm 0.002\text{ nA}$, $B_1=10 \pm 2\text{ }\mu\text{A}$, $B_2=0.637 \pm 0.002\text{ nA}$, for the decay were individuated in AuHbNW FET device. Most importantly, the coefficient A_2 was three orders of magnitude larger than A_1 . Therefore the overall weight-average time response in hybrid device $\tau_{hyb}=0.25\text{ s}$ was almost 40 times faster than ZnO NW device ($\tau_{ZnO}=9.7\text{ s}$).

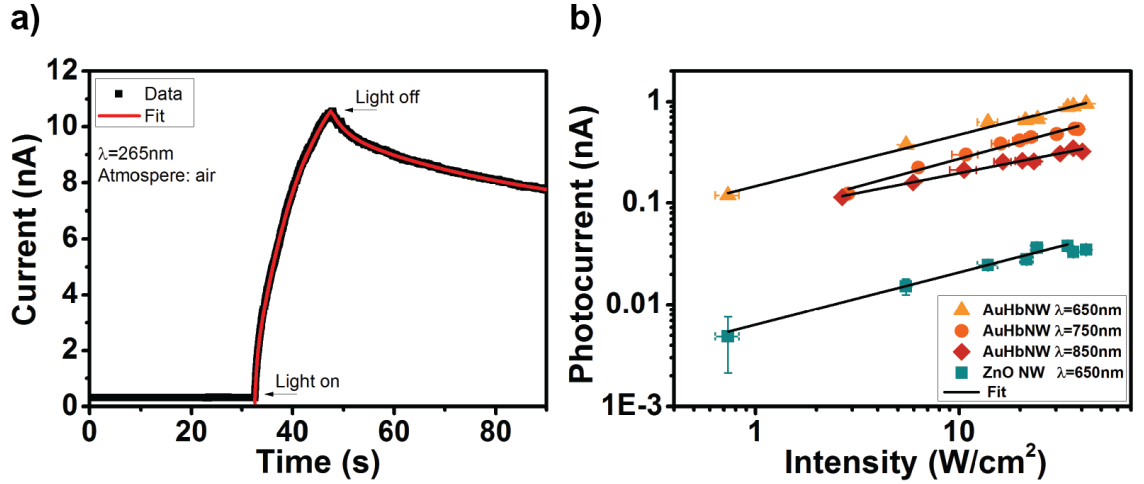


Figure 6.8.: a) Photoresponse of AuHbNW FET device during exposition to UV light (265 nm). Red lines are the bi-exponential growth and decay fitting to the corresponding data.

Interestingly, under UV radiation, although a larger photocurrent observed, both ZnO NW FET and AuHbNW FET devices showed a dominance of the slower process ($A_1 > A_2$) in the photoresponse. Figure 6.8 shows the measured $I(t)$ and related fit. Parameters values obtained were : $I_s = 0.82 \pm 0.2$ nA, $A_1 = 12.41 \pm 0.02$ nA, $A_2 = 5.85 \pm 2$ nA, $\tau_1 = 10.01 \pm 0.07$ s and $\tau_2 = 0.39 \pm 0.02$ s and $I_\infty = 6.53 \pm 0.03$ nA, $B_1 = 0.948 \pm 0.007$ nA, $B_2 = 3.29 \pm 0.02$ nA, $\gamma_1 = 2.74 \pm 0.05$ s and $\gamma_2 = 43.3 \pm 0.7$ s.

For photon energy above bandgap, direct generation of free electron-hole on sub-nanoseconds time scale is expected to be the main process in ZnO NWs. However the longer response time in our devices indicates a UV photoresponse dominated by electron-hole generation and recombination in defects trap states, as previously discussed in section 6.3.1-6.3.2. However the fast and enhanced response in AuHbNW FET device under near-infrared radiation requires an alternative explanation independent from the photocarrier dynamics in ZnO nanowire.

To quantitatively assess the photoresponse we investigated the power dependence of the photocurrent in AuHbNW and ZnO NW FET device (figure 6.10b). Under radiation with $\lambda = 650$ nm we observed that at laser intensity of 0.6 W/cm² the photoresponse of the ZnO NW was barely detectable whereas the photocurrent in AuHbNW FET was two order of magnitude larger. This extends the estimated detection limit for AuHbNW FET in the range of mW/cm². At higher power in-

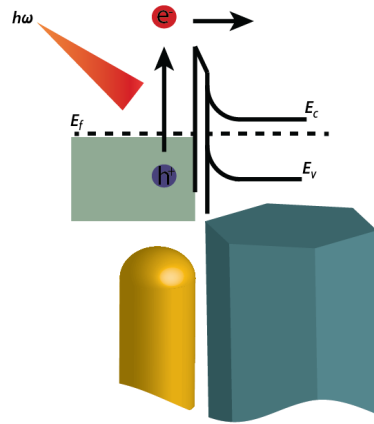


Figure 6.9.: Schematic representation of the hot-electron generation and injection process at the nanorod-nanowire interface.

stead, ZnO NW FET saturated above 20 W/cm^2 although no evidence of saturation was observed in AuHbNW FET device within the explored laser intensities. We also found a sub-linear dependence of photocurrent versus power following the power law $I_{ph} \sim P^\alpha$ with $\alpha = 0.51 \pm 0.08$ and 0.50 ± 0.02 for ZnO NW FET and AuHbFET respectively. In AuHbNW the α value remained smaller than the unit even at longer wavelength with $\alpha = 0.55 \pm 0.03$ at $\lambda = 750 \text{ nm}$ and $\alpha = 0.39 \pm 0.02$ at $\lambda = 850 \text{ nm}$. The comparable α values found in the measured devices suggests to attribute the observed behavior to the ZnO NW. Sub-linear dependence was previously reported in nanowires of different materials, including Si [301], ZnO [287], GaN [295] and ascribed to the saturation of hole-traps at high radiation power and consequent increasing of free electron-hole recombination leading to the saturation of the photoresponse [285, 294].

6.5. Hot-electron generation in hybrid device

Following this analysis we explain the photoconductivity behavior observed in the hybrid device in terms of plasmonic-mediated hot electron injection model. Figure 6.9 depicts schematically the process. Incident radiations excite localized surface plasmons (LSP) in Au nanorods. After excitation, LSP can decay radiatively by re-emitting a photon or non-radiatively by transferring energy to electrons thus creating a distribution of *hot electrons* above the Fermi energy of the metal. Electrons

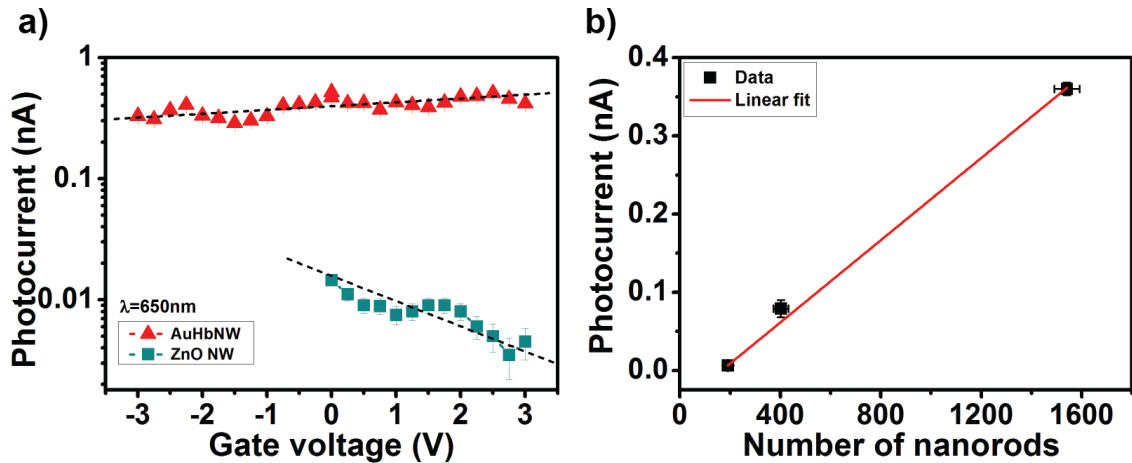


Figure 6.10.: a) Modulation of the photocurrent in ZnO NW and AuHbNW devices with the applied gate voltage. Dotted lines are guides for the eyes. b) Photocurrent intensity as a function of the number of nanorods in the AuHbNW device. Red line represent the linear fit.

with energy above the Schottky barrier at the Au nanorod-ZnO nanowire interface are directly injected in the conduction band of the ZnO whereas electrons with lower energy have an exponentially decreased probability to be injected. The hot-electron generation and injection process is estimated to take place on the order of subpicoseconds [302] thus contributing to enhance the fast component of photocurrent growth in agreement with the experimental observations.

It should be noticed that although the presence of an organic ligand shell on the Au nanorods and the Van der Waals bonds (or chemisorption chemical bonds) formed at the ZnO surface do not form a conventional Au-ZnO Schottky contact, the plasmonic-mediated hot-electron injection process previously described is still allowed to occur, in what is by all means an interface (admittedly complex) chemically bonded assembly. The excited hot-electrons in the Au nanorod have a probability to be excited either above whatever barrier is formed or tunnel through it, as previously reported in a number of other ligand-stabilized nanoparticle assembly systems [303, 304, 305, 306, 307], therefore not affecting the mechanism proposed but only the efficiency of the injection rate. When hot-electrons pass the Au nanorod-ZnO nanowire interface, the nanorod remains positively charged. At higher light intensities an increasing number of hot electrons are generated but the restoring electric field built up at the interface limits the injection rate resulting in a sub-linear pho-

to current increment with the illumination power. When the light is switched off, Au nanorod captures excess of electrons in the conduction band of the ZnO leading to a fast decreasing in conductance. To support this model we firstly investigate the photocurrent generation process in ZnO NW FET and AuHbNW FET devices we measured the photoresponse (radiation with energy 1.9 eV and intensity 20 W/cm²) at different backgate voltages (figure 6.10a). Due to the n-type nature of our ZnO NW, increasing of the electron density within the nanowire results from applying positive back-gate voltages therefore reducing the depletion region near the surface. In ZnO NW FET we observed a progressively decreasing of the photocurrent for positive applied voltages. This behavior confirms that sub-bandgap photocurrent is originated from surface defect states localized within the depletion region created by negative oxygen ions adsorbed [308], Zn vacancies [299] and oxygen vacancies [298, 297]. Surprisingly the photocurrent measured at different back-gate voltages in the hybrid device was found having a clearly different behavior. The values reported in figure 3b slightly decrease with changing the voltage from positive to negative values although the overall trend is fair less dependent by the backgate voltage compared to the behavior of the ZnO NW FET. This trend resembles the transfer characteristic in ZnO NW (see section 5.4) therefore we attributed the variation in photocurrent to the changes in the electron density in the conduction band due to electrostatic effects. We also investigated the influence of nanorod density on the device performance. Figure 6.10b reports the measured photocurrent at $\lambda=650$ nm in three AuHbNW devices having increasing number of Au nanorods on the surface. Number of nanorods were estimated by measuring the nanowire cross section area covered by particles divided by the geometrical cross section of a nanorod. The measured values of photocurrent in the three AuHbNW devices well satisfy the linear dependence respect to the number of particles, thus supporting the plasmonic origin of the photocurrent.

6.6. Hot-electron injection process at nanorod-nanowire interface

In this section we investigate in more details the hot-electron generation and injection process in the Au nanorod-nanowire system. In a perfect metal-semiconductor junction, the electron injection rate can be well approximated by the Fowler equation [309]

$$I_{ph} = I_0 \cdot (\hbar\omega - \Phi_b)^2 \quad (6.3)$$

where $\hbar\omega$ is the energy of the incident radiation and Φ_b the barrier height at the interface. Figure 6.11a show the measured photocurrent for different radiation energy in three AuHbNW devices with increasing number of nanorods. Displayed data were well fitted with eq.(6.3) and barrier height of 1.45 ± 0.03 , 1.26 ± 0.05 , and 0.56 ± 0.05 eV were obtained for the hybrid nanostructure with (i) lowest, (ii) medium and (iii) highest number of nanorods respectively. In a bare ZnO nanowire, the surface band bending was estimated to be between 1-1.7 eV above the Fermi energy depending on the surface passivation [310]. The Φ_b calculated for the hybrid structures (i) and (ii) matches perfectly the expected range indicating that for this range of particle density the barrier at the interface is mainly determined by the properties of the ZnO surface. However in the hybrid structure (iii), where the nanowire surface was almost completely covered by nanorods, the Φ_b value (0.56 eV) was found close to the expected barrier height at the Au-ZnO interface (0.65 eV) [311]. Therefore we deduced that at low nanorod densities the nanorod-semiconductor interface maintains the original properties of the semiconductor surface while for the limiting case of a nanowire fully covered by nanorods is determined by the difference in the work-function between the materials involved. The value of the interface energy barrier Φ_b plays a fundamental role in determining the rate of hot-electrons injection. Therefore these results provide important indications for optimizing the device by reducing the junction barrier Φ_b . Furthermore we investigated the role of nanorods-shaped particles in the hot-carriers generation. Govorov *et al.* [311, 312, 313] calculated the density of hot-carriers in metal nanocrystal using quantum linear response the-

ory. Efficient relaxation of surface plasmons into one-electron excitations appeared only in metal nanocrystals with dimension around 20 nm or below due to the non-conservation of the momentum of electrons in confined systems. Due to the small size of the nanorod used in this work (22×54 nm) we can compare the theoretical prediction with the experimental results.

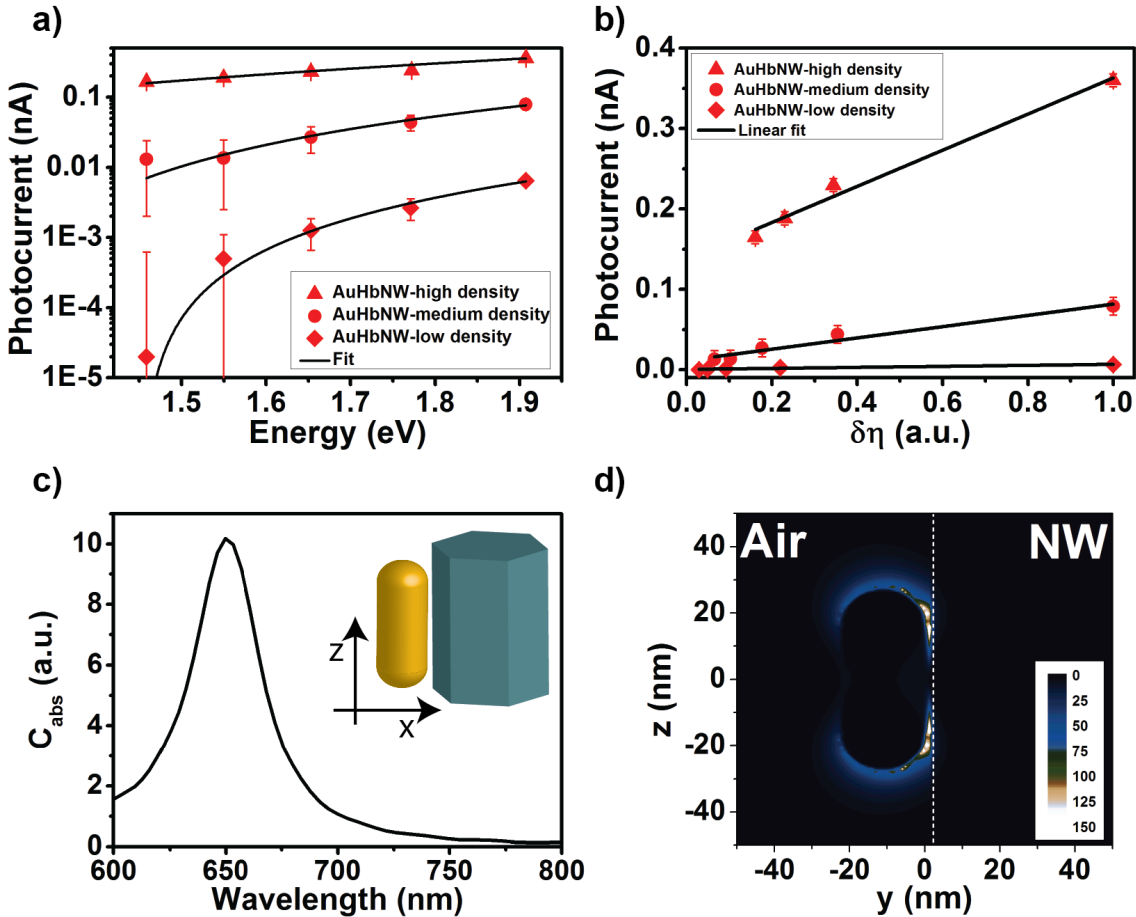


Figure 6.11.: a) Photocurrent dependence from the radiation intensity in AuHbNW with number of particle of 191 ± 20 (low density), 402 ± 30 (medium density), 1541 ± 50 (high density). Black line represent the linear fit. b) Photocurrent intensity vs hot-electron density calculated from eq.(6.4) and the relative linear fit (black line). FDTD simulation of a Au nanorod 22×54 nm on ZnO nanowire separated by $2 \mu\text{m}$ gap with light polarized along the z direction and incident along x of c) absorption cross section and d) the enhanced electric field factor.

The hot-carrier density was found dependent from the radiation energy $\hbar\omega$ as follow

$$\delta\nu \propto \frac{|\beta(\omega)|^2}{\omega^4} \quad (6.4)$$

with $\beta(\omega)$ the field-enhancement factor inside the metal nanostructure that for an ellipsoidal nanorod can be approximated as [200]

$$\beta(\omega) \approx \frac{\epsilon_m}{3(\epsilon_m + (\epsilon_{Au}(\omega) - \epsilon_m)L_a)} \quad (6.5)$$

with ϵ_m and ϵ_{Au} the dielectric constant of surrounding medium and gold respectively and L_a the depolarizing factor along the main axis defined in eq.(3.4).

Photocurrent values measured in the three devices at different radiation energies are plotted versus the hot-electron population $\delta\nu$ calculated from eq.(6.4) in figure 6.11b. A linear dependence were obtained by using $\epsilon_m=1$ and L_a as the only free parameter for the three samples, in excellent agreement with the theory. The extracted values for L_a were 0.095 ± 0.005 , 0.118 ± 0.008 and 0.28 ± 0.03 for the device (i), (ii) and (iii) respectively. From the statistical length and diameter we calculated using eq.3.4 a geometrical depolarizing factor (L_g) value of $L_g = 0.13 \pm 0.03$. We noticed that the L_a extracted from the device (i) and (ii) (low and medium nanorod density) perfectly match the expected L_g within the error. The increasing value of L_a with the nanorod density was attributed to the plasmonic near-field coupling between nanorods. We showed in section 2.3.3 that plasmonic resonances of isolated nanoparticles are heavily modified in closely spaced arrays. In particular for large arrays a blue shift of the main resonance is observed and new resonances at longer wavelength appear. The blue shift corresponds to a change in the aspect ratio of the effective scattering unit towards a more isotropic shape thus leading to an increasing of the L_a value. Figure 6.11c shows the calculated absorption cross section for a nanorod 22×54 nm in close proximity (separation of 2 nm) with the ZnO NW by finite-differential time domain simulations using Lumerical Solution software. A plasmonic resonance related to the longitudinal surface mode was found peaked around 650 nm. The number of hot carriers generated (i.e. the photocurrent) is expected to follow the absorption profile of the nanoparticle [314], thus reaching the maximum in proximity of the longitudinal surface plasmon and decrease at longer wavelengths. This is in agreement with the experimental results obtained from hy-

brid device. We should notice that the cross section of closely spaced nanorods can deviate from the curve showed in figure 6.11c due to inter-particle coupling. In particular, a broadening of the resonance peak might occur, so that a contribution at larger wavelengths are expected. Furthermore, FDTD simulations of the electric field enhancement occurring at the interface between closely spaced parallel Au nanorod-ZnO nanowire showed formation of an intense enhanced electromagnetic field in the area between adjacent structures (Figure 6.11d). It has been shown that only electrons with momentum perpendicular to the metal-semiconductor interface can be efficiently injected into the semiconductor [309]. This constitutes an important limitation to the carrier injection when an electromagnetic radiation propagating perpendicular to the metal-semiconductor junction is used [285]. However the localized enhance field at the interface generated by plasmons in nanorods allows to overcome this limitation and facilitate electrons injection inside the semiconductor.

The quantum efficiency of the hybrid device, defined as the number of electron collected per unit time divided by the number of absorbed photons was calculated to be $\sim 3\%$ at 650 nm, more than 30 times larger than the quantum efficiency in planar photodetectors based on hot-electron injection mechanism [24]. We should notice that this value was calculated by assuming an absorption coefficient equal to one for the nanorods that overestimates the number of absorbed photons. Moreover the device gain can also be increased by applying a bias voltage larger than the value used in these experiments (400 mV). We ascribed the higher efficiency to the use of reduced dimensions of the active metal nanostructure that provide a more efficient generation of hot-carriers, the electric field enhancement at the nanorod-nanowire interface that facilitate the electron injection and to the low dimensionality of the semiconductor nanowire that provide an efficient path for the charge collection.

A number of improvements can also be done to increase the performance by optimizing the single active elements, i.e. nanorods and nanowire, in this architecture. Reducing the gap size between nanorod and nanowire by passivating the nanorod surface with shorter molecules would reduce the barrier at the interface and a further size reduction should result in a more efficient hot-electron generation. Different semiconductor materials such as Si, GaN, GaAs, InP, InAs can be also used in place of ZnO for lowering the Schottky barrier, increasing the carrier collection efficiency

and also contribute directly to the photocurrent generation by direct optical transition.

6.7. Conclusions

In conclusion, I investigated the photoconductivity response of ZnO nanowire under radiation energy above-bandgap ($\lambda=365$ nm) and below-bandgap ($\lambda=650-850$ nm). Time-resolved measurements revealed three processes contributing to the photocurrent growth and decay. The first process characterized by a time-scale below 1 s was attributed to the fast free electron-hole generation, a second process with time constant of ~ 10 s attributed to the carrier generation and recombination at deep trap levels and a long process in ~ 100 s related to the adsorption/desorption of oxygen species on the ZnO surface.

I investigated the enhanced photoconductance of hybrid Au nanorods-ZnO nanowire hybrid FET devices fabricated by a novel combined lithography/droplet deposition method. Compared to the bare ZnO nanowire FET, hybrid devices showed more than two orders of magnitude enhanced photoconductivity and 40 times faster response for wavelengths in the range 650-850 nm. The improved performances were explained on the basis of plasmon-mediated hot-electron injection of photocarriers. The dependence of generated photocurrent from the metal nanostructure density and shape was investigated in details. The overall efficiency of $\sim 3\%$ was ascribed to a combined effect of the use of small dimension anisotropic active metal nanostructures and low dimensionality semiconductor nanowires. The hybrid device presented in this work opens new avenues for the designing of novel miniaturized tunable photodetectors across the visible-near infrared region. Most importantly, the proposed architecture allows to highly engineering the optoelectronic properties of the single hybrid device by finely tuning the plasmonic resonances of Au nanorods and using homogeneous or heterostructured semiconductor nanowire with optimized optical and electrical properties. We believe that the miniaturized, tunable and integrated capabilities offered by metal nanorod-semiconductor nanowire device architectures presented in this work could have an important impact in many application fields such as opto-electronic sensors, photodetectors and photovoltaic devices.

Chapter 7.

Conclusion

7.1. Summary

The objective of this thesis work was to develop new methodologies for integrating colloidal metal nanorods in semiconductor nanowire-based devices and to explore the additional functionalities that such hybrid nanostructures can afford compared to the bare nanowires.

In **Chapter 2** the synthesis of Au nanorods of different sizes ranging between 14×42 nm up to 30×70 nm by a seed-mediated method was presented and discussed. A systematic approach to purify the as-prepared solution of colloidal nanorods was developed and used to prepare the samples investigated in Chapters 3, 4 and 6. Optical properties of colloidal solutions and single nanorods on ITO substrates were investigated experimentally by UV-Vis and dark-field spectroscopy, and theoretically by FDTD and BEM simulations. A detailed analysis of the influence of the CTAB layer surrounding the nanorod and the substrate on the plasmonic resonance was carried out and compared to the experimental dark-field spectra. Moreover optical properties of nanoparticles with different sizes, namely 14×42 nm, 22×54 nm and 30×70 nm were simulated and compared. Furthermore the influence of near field coupling in arrays of closely spaced metal nanorod were elucidated.

In **Chapter 3** I demonstrated controlled and reliable formation of 1D Au nanorod architectures by electric field assisted deposition. The unexpected frequency dependency of the deposition process was explained with the introduction of a theoretical model based on the definition of Au nanorods as core-shell material entities. A novel contour plot was derived from the theoretical model, which correlated obtained 1D nanorod assemblies with specific sets of experimental parameters. Theoretical and experimental investigation of the influence of the substrate on the electric field medi-

ated assembly was also discussed. Electrical characterization showed that 1D architectures displayed tunneling behavior across the inter-nanorod gap with resistance values of the order of G Ω s. Denser nanorod networks displayed conductive behavior with resistances of the order of M Ω and k Ω . The associated increased conductance was ascribed to the higher number of percolation paths in denser networks. The controlled fabrication of 1D architectures is relevant for microelectronic, optoelectronic and molecular sensing applications. In particular, low density architectures with tunneling behavior could find applications as molecular diodes, molecular memory and logic devices.

In **Chapter 4** Raman enhancement of the ZnO surface optical mode was demonstrated in single hybrid nanostructures formed by Au nanorods deposited on ZnO nanowires under excitation of longitudinal surface plasmon resonance of Au nanorods. FDTD simulations were used to investigate the spatial distribution and intensity of the enhanced electric field for different polarizations and to support the experimental findings. Intentional tuning of the optical properties of deposited nanorods resulted in shifting of the excitation wavelength at which the maximum of the Raman mode enhancement was achieved. The probing of the structural vibrational properties of single large-bandgap semiconductor nanowire through deposition of metal nanorods opens the way for novel sensing and opto-electronic applications. Moreover, my studies contribute to extend the capability of traditional Raman spectroscopy to the characterization of semiconductor materials thus providing new insights to the understanding of surface and interface properties of hybrid materials.

In **Chapter 5** electrical characterization of ZnO nanowires devices with Ti/Au and Ti/Al metal contacts in air and high vacuum was presented demonstrating that Al forms a better Ohmic contact than Au with the ZnO and device resistance below $10^6 \Omega$ in air was achieved. These resistance values are very promising for ZnO nanowire-based devices compared with the reported values in literature of the order of 10^8 - $10^9 \Omega$. Also, a detailed characterization of the nanowire resistivity, contact resistivity, field-effect mobility and electron density was provided. These data were used to model the Joule heating process in the ZnO nanowire-FET device by FEM simulation, showing that by exploiting the three-terminals configuration to increase by 1-2 folders the nanowire resistivity, temperature larger than 300°C can be reached

in the center of the nanowire, otherwise not achievable in the traditional two terminal configuration. Furthermore, using a specific electric field configuration, only achievable in a nanowire-FET device, selective deposition of colloidal Au nanorods on a target nanowire was demonstrated.

Finally, in **Chapter 6** we investigated the photoconductivity response of ZnO nanowire under radiation energy above-bandgap ($\lambda=365$ nm) and below-bandgap ($\lambda=650-850$ nm). Time-resolved measurements revealed three processes contributing to the photocurrent growth and decay. The first process characterized by a time-scale below 1 s was attributed to the fast free electron-hole generation, a second process with time constant of ~ 10 s attributed to the carrier generation and recombination at deep trap levels and a long process in ~ 100 s related to the adsorption/desorption of oxygen species on the ZnO surface. I investigated the enhanced photoconductance of hybrid Au nanorods-ZnO nanowire hybrid FET devices fabricated by a novel combined lithography/droplet deposition method. Compared to the bare ZnO nanowire FET, hybrid devices showed more than two orders of magnitude enhanced photoconductivity and 40 times faster response for wavelengths in the range 650-850 nm. The improved performances were explained on the basis of plasmon-mediated hot-electron injection of photocarriers. The dependence of generated photocurrent from the metal nanostructure density and shape was investigated in details. The overall efficiency of $\sim 3\%$ was ascribed to a combined effect of the use of small dimension anisotropic active metal nanostructures and low dimensionality semiconductor nanowires.

Overall, this thesis work presented a systematic and comprehensive investigation of design, fabrication, modeling and characterization of Au nanorod-semiconductor nanowire hybrid nanostructures. The presented results open new avenues for designing novel miniaturized tunable devices across the visible-near infrared region. Most importantly, the proposed architecture allows to highly engineering the optoelectronic properties of the single hybrid device by finely tuning the plasmonic resonances of Au nanorods and using homogeneous or heterostructured semiconductor nanowire with optimized optical and electrical properties. I believe that the miniaturized, tunable and integrated capabilities offered by metal nanorod-semiconductor

nanowire device architectures could have an important impact in many application fields such as opto-electronic, sensors, photodetectors and photovoltaic devices.

7.2. Future work

The results presented in Chapters 2-6 afford a solid background for future development towards hybrid devices for nanoelectronics and nanophotonics. The assembling of 1D arrays of Au nanorods developed in Chapter 3 could be investigated as waveguide for transporting electromagnetic energy below the the diffraction limit of the light, that actually represent a fundamental limitation to scale-down optical devices [315]. One dimensional arrays of metal nanostructures have been explored both theoretically and experimentally for the guiding of radiation [316, 317]. Electromagnetic energy can be transported with propagation velocities of about 10% of the speed of the light and also guided around 90° corners in closely spaced metal nanoparticles via near-field coupling [132]. Compared to the present literature, 1D architecture presented in this work would offer a substantial reducing in the waveguide width below 10 nm and a reduction in losses due to a inter-nanorod gap in the range of 2-10 nm that allows a more efficient near field coupling. Moreover, the same assembly process could be exploited for facile formation of multiple junctions having size comparable with molecular lengths, thus presenting interesting possibilities as an ideal template for molecular electronics.

A number of exciting opportunities can be foreseen for hybrid Au nanorods-semiconductor nanowire hybrid devices. Firstly, further optimization of the hybrid nanostructures/nanodevices discussed in Chapter 4 and 6 could be addressed. The nanorod-mediated Raman spectroscopy discussed in Chapter 4 would require additional improvements devoted to minimize the influence of the organic surfactant adsorbed on the nanoparticle surface. In particular, it would be interesting to explore alternative synthetic protocols to grow a dielectric shell with controlled sub-10 nm thickness substituting the CTAB layer. This implementation would drastically reduce the background noise introduced by the molecules making more reliable the study of the vibrational properties of single semiconductor nanowires and also giving better insights into the processes involved in the Raman scattering enhancement.

A number of improvements could be also proposed to increase the performances of the hybrid photodetector presented in Chapter 6. For example, a reduction of the nanorod-nanowire distance by passivation of the nanorod surface would reduce the barrier at the interface and result in a more efficient hot-electron injection. Different semiconductor materials such as Si, GaN, GaAs, InP, InAs could in principle be used instead of ZnO to achieve a lower Schottky barrier, increasing carrier collection efficiency and also contributing directly to photocurrent generation by direct optical transition.

Secondly, exploring the versatility of the fabrication techniques developed to combine the strength of plasmonic metal nanoparticles properties for enhancing light-matter interaction or deliver a photon-to-electron energy conversion with the engineered optical and electrical properties of homogeneous and heterostructured semiconductor nanowires. The large variety of possible combination give rise to a new class of hybrid nanostructures with enhanced performance and widened capabilities. For instance, the results discussed in Chapter 6 could be applied to design a prototype of hybrid Au nanorods-semiconductor nanowire solar cell. Demonstration of single p-i-n core-shell nanowire solar cells have been already presented in literature, however the hybridization with metal nanorods could potentially boost the performance via increasing the light absorption at specific wavelengths or by direct contribution to charge generation. Similarly, a new scheme for optical pumped nanolaser could be also explored mediated by localized surface plasmon that could lower the threshold pump intensity for lasing to occur and open up to light up-conversion mechanism via plasmonic-mediated electron-hole injection. Finally, additional research directions could be gas and biological sensing, where the high sensitivity of semiconductor nanowire due to the high surface-to-volume ratio could be combined with catalytic effect induced by metal nanoparticles or specific functionalization of gold nanorods for selective detection of biological species.

Appendix A.

Fabrication protocols

A.1.

Mask-selective droplet deposition method : Process A

- Surface cleaning:
 - 2' Acetone
 - 2' Isopropanol
- Dry deposition of nanowires :
 - Mechanical deposition of nanowires
 - 2' Acetone (flushing with a syringe)
 - 2' Isopropanol (flushing with a syringe)
- Resist deposition:
 - Bake 2' at 130°C
 - HMDS (10" at 500 rpm + 1' at 4000 rpm)
 - Spin S1813 (10" at 500 rpm + 1' at 3000 rpm)
 - HMDS (10" at 500 rpm + 1' at 4000 rpm)
 - Spin S1813 (10" at 500 rpm + 1' at 4000 rpm)
 - Bake 2' at 120°C (temperature sharp and constant over 2 min)
- Resist etching by O₂ plasma RIE at 50 sccm, 45 mTorr, 100 W until the resist thickness is below the nanowire diameter
- Bake at 110°C
- Drop of the nanorod solutions on the substrate (drops of 2 μl each)
- Sample cleaning :
 - 15' 1165 (at room temperature and flushing 5 times with a pipette)
 - 15' Acetone
 - 15' Isopropanol

A.2.

Mask-selective droplet deposition method : Process B

- Surface cleaning:
 - 2' Acetone
 - 2' Isopropanol
 - Dry deposition of nanowires :
 - Mechanical deposition of nanowires
 - 2' Acetone (flushing with a syringe)
 - 2' Isopropanol (flushing with a syringe)
 - Resist deposition:
 - Bake 2' at 130°C
 - HMDS (10" at 500 rpm + 1' at 4000 rpm)
 - Spin S1813 (10" at 500 rpm + 1' at 3000 rpm)
 - HMDS (10" at 500 rpm + 1' at 4000 rpm)
 - Spin S1813 (10" at 500 rpm + 1' at 4000 rpm)
 - Bake 2' at 110°C (temperature sharp and constant over 2 min)
 - Exposition to UV light for 5 s
 - Development in MF319 for 8 s (moving the sample slowly during the immersion)
 - Exposition to UV light for 3 s
 - Development in MF319 for 5 s (moving the sample slowly during the immersion)
- Note : the development time can be slightly adjusted to reach the target thickness. However with these values a thickness of 100-200 nm is obtained with good reproducibility
- Drop of the nanorod solutions on the substrate (drops of 2 μ l each)
 - Sample cleaning :
 - 15' 1165 (at room temperature and flushing 5 times with a pipette)
 - 15' Acetone
 - 15' Isopropanol

A.3.**Fabrication of metal pads by optical lithography**

- Surface cleaning:
 - 2' Acetone
 - 2' Isopropanol
- Dry deposition of nanowires :
 - Mechanical deposition of nanowires
 - 2' Acetone (flushing with a syringe)
 - 2' Isopropanol (flushing with a syringe)
 - 2' bake at 125 °C
- Spin HMDS:
 - 10" a 500 rpm
 - 1' a 4000 rpm
- Spin resist LOR 3A:
 - 10" a 500 rpm
 - 1' a 4000 rpm
- Bake 5' at 170 °C
- Spin HMDS:
 - 10" a 500 rpm
 - 1' a 4000 rpm
- Spin resist S1805
 - 10" a 500 rpm
 - 1' a 4000 rpm
- Bake 2' at 115 °C
- Clean sample border (to improve mask contact)
- 4" exposition to UV light
- 25" development in MF319, stop in H_2O
- Bake 5' at 120 °C
- 20" Under-etch in MF319, stop in H_2O
- Metal evaporation by e-beam evaporator :
 - 10 nm Ti
 - 200 nm Al

Appendix A. Fabrication protocols

- Lift-off :
 - 10' in 1165 at 40° C
 - Flushing with a syringe in 1165
 - Rise in Acetone
 - Rise in Isopropanolo

Appendix B.

Publications

- **Dielectrophoretic Self-Assembly of Au Nanorods for Sensing Applications** *Andrea Pescaglino, Umberto Emanuele, Alan O’Riordan, Daniela Iacopino* *Journal of Physics:Conference Series*, 307, 012051, (2011)
- **Synthesis, Optical Properties and Self-Assembly of Gold Nanrods** *Alfonso Martin, Carola Schopf, Andrea Pescaglino, Alan O’Riordan, Daniela Iacopino,* *Journal of Experimental Nanoscience*, 7(6), 688-702, (2012)
- **Gold Nanowire Electrode Arrays: Investigations of Non-Faradaic Behavior** *Karen Dawson, Amelie Wahl, Andrea Pescaglino, Daniela Iacopino, Alan O’Riordan,* *Journal of The Electrochemical Society*, 161(2), B3049-B3054, (2014)
- **Surface-Enhanced Raman Scattering of 4-Aminobenzenethiol on Au Nanorod Ordered Arrays** *Alfonso Martin, Andrea Pescaglino, Carola Schopf, Vittorio Scardacci, Richard Coull, Lorraine Byrne, Daniela Iacopino* *The Journal of Physical Chemistry C*, 118(24),13260-13267 (2014)
- **Au nanorod plasmonic superstructures obtained by a combined droplet evaporation and stamping method** *Carola Schopf, Alfonso Martin, Micheal Burke, Daniel Jones, Andrea Pescaglino, Alan O’Riordan, Aidan J. Quinn and Daniela Iacopino* *Journal of Material Chemistry C*, 2, 3536-3541, (2014)
- **Facile formation of ordered vertical arrays by droplet evaporation of Au nanorod organic solutions** *Alfonso Martin, Carola Schopf, Andrea Pescaglino, Jin Jin Wang and Daniela Iacopino* *Langmuir*, 30(34), 10206-10212, (2014)
- **Controlled Assembly of Au Nanorods into 1D Architectures by Electric Field-Assisted Deposition** *Andrea Pescaglino, Alan O’Riordan, Aidan Quinn and Daniela Iacopino* *Journal of Material Chemistry C*, 2, 6810-6816, (2014)
- **Hot-Electron Injection in Au Nanorod-ZnO Nanowire Hybrid Device for Near-Infrared Photodetection** *Andrea Pescaglino, Alfonso Martin, Davide Cammi, Gediminas Juska, Carsten Ronning, Emanuele Pelucchi and Daniela Iacopino* *Nano Letters*, 14(11), 6202-6209, (2014)

- **Enhancing raman Scattering of single ZnO nanowire by Rod-shaped Au Nanoparticles** *Andrea Pescaglioni, Eleonora Secco, Alfonso Martin, Davide Cammi, Carsten Ronning, Andres Cantarero, Nuria Garro and Daniela Iacopino*, in preparation

Conferences/workshops

- IOP Conference *Sensors & their Application XVI*, Cork, September 2011
- *ICONO-ICOPE 2011*, Dublin, September 2011
- *Nanowiring Workshop*, Cambridge (UK), 2-6 October 2011
- *Postgraduate symposium on nanotechnology*, University of Birmingham (UK), December 2011
- *Nanowiring Workshop*, Turin (IT), 7-9 May 2012
- *Nanowiring Mid-term Review*, Valencia (Sp), 20-23 July 2012
- *ICON 2013*, Annecy (FR), September 2013
- *Advance school in semiconductor nanowires*, Alghero (IT), 7-15 October 2013

Secondments

- *InP nanowire growth by metallorganic vapour-phase epitaxy*
TU/e, Eindhoven, Netherlands, 27/02/2012-03/03/2012
- *Raman Spectroscopy on nanorods-decorated ZnO nanowire hybrid nanostructures*
University of Valencia, Valencia, Spain, 20/07/2012-04/08/2012
- *Raman Spectroscopy on nanorods-decorated ZnO nanowire hybrid nanostructures*
University of Valencia, Valencia, Spain, 26/11/2012-06/12/2012
- *Optical and electrical characterization of InP nanowire heterostructures*
TUE, Delft, The Netherland, 21/10/2012-31/11/2012

Poster

- **Nanorods-decorated nanowire superstructures for optoelectronics and sensing**
Andrea Pescaglioni, Aidan Quinn, Daniela Iacopino
Tyndall Postgraduate Poster Competition, July 2012

- **Electric Field Assisted Alignment of Au Nanorods on Nanoscale Devices**
Andrea Pescaglino, Alan O’Riordan, Daniela Iacopino
Tyndall Postgraduate Poster Competition, July 2011
- **Dark field optical microscopy of single nanoparticles and ordered nanoparticle arrays** *Carola Schopf, Andrea Pescaglino, Alan O’Riordan, Daniela Iacopino,* IOP Conference *Sensors & their Application XVI*, Cork, September 2011
- **Dark field optical microscopy of single nanoparticles and ordered nanoparticle arrays** *Carola Schopf, Andrea Pescaglino, Alan O’Riordan, Daniela Iacopino* ICONO-ICOPE 2011, Dublin, September 2011
- **Tunable Raman Scattering in Au Nanorods Decorated ZnO Nanowires Hybrid Structures** *Andrea Pescaglino, Eleonora Secco, Davide Cammi, Carsten Ronning, Nuria Garro , Daniela Iacopino* ICON 2013, Annecy, September 2013
- **Tunable Raman Scattering in Au Nanorods Decorated ZnO Nanowires Hybrid Structures** *Andrea Pescaglino, Eleonora Secco, Davide Cammi, Carsten Ronning, Nuria Garro , Daniela Iacopino* Advance school in semiconductor nanowires, Alghero, September 2013

Talk

- **Synthesis and Self-Assembly of Gold Nanorods**
A. Pescaglino, A. Martin, A. O’Riordan, D. Iacopino
Postgraduate symposium on nanotechnology, University of Birmingham (UK), December 2011

Bibliography

- [1] Thaddeus D Ladd, Fedor Jelezko, Raymond Laflamme, Yasunobu Nakamura, Christopher Monroe, and Jeremy L O'Brien. Quantum computers. *Nature*, 464(7285):45–53, 2010.
- [2] Mark L. Brongersma and Vladimir M. Shalaev. The case for plasmonics. *Science*, 328(5977):440–441, 2010.
- [3] Rashid Zia, Jon A Schuller, Anu Chandran, and Mark L Brongersma. Plasmonics: the next chip-scale technology. *Materials today*, 9(7):20–27, 2006.
- [4] Zhiqiang Liang, Jun Sun, Yueyue Jiang, Lin Jiang, and Xiaodong Chen. Plasmonic enhanced optoelectronic devices. *Plasmonics*, 9(4):859–866, 2014.
- [5] Dmitri K Gramotnev and Sergey I Bozhevolnyi. Plasmonics beyond the diffraction limit. *Nature Photonics*, 4(2):83–91, 2010.
- [6] Albert Polman and Harry A Atwater. Plasmonics: optics at the nanoscale. *Materials today*, 8(1):56, 2005.
- [7] Nathan C Lindquist, Prashant Nagpal, Kevin M McPeak, David J Norris, and Sang-Hyun Oh. Engineering metallic nanostructures for plasmonics and nanophotonics. *Reports on progress in physics. Physical Society (Great Britain)*, 75(3):036501, 2012.
- [8] J.A. Schuller, E.S. Barnard, W. Cai, Y.C. Jun, J.S. White, and M.L. Brongersma. Plasmonics for extreme light concentration and manipulation. *Nature materials*, 9(3):193–204, 2010.
- [9] Paolo Silvestroni. *Fondamenti di chimica*. Editoriale Veschi, 1989.
- [10] William L Barnes, Alain Dereux, and Thomas W Ebbesen. Surface plasmon subwavelength optics. *Nature*, 424(6950):824–830, 2003.
- [11] Hu Cang, Anna Labno, Changgui Lu, Xiaobo Yin, Ming Liu, Christopher Gladden, Yongmin Liu, and Xiang Zhang. Probing the electromagnetic field of a 15-nanometre hotspot by single molecule imaging. *Nature*, 469(7330):385–388, 2011.
- [12] Xiaolei Shi and Lambertus Hesselink. Mechanisms for enhancing power throughput from planar nano-apertures for near-field optical data storage. *Japanese journal of applied physics*, 41(3S):1632, 2002.
- [13] Justin S White, Georgios Veronis, Zongfu Yu, Edward S Barnard, Anu Chandran, Shanhui Fan, and Mark L Brongersma. Extraordinary optical absorption through subwavelength slits. *Optics letters*, 34(5):686–688, 2009.

Bibliography

- [14] Harry A. Atwater and Albert Polman. Plasmonics for improved photovoltaic devices. *Nat Mater*, 9(3):205–213, 2010.
- [15] CJ Chen and RM Osgood. Direct observation of the local-field-enhanced surface photochemical reactions. *Physical Review Letters*, 50(21):1705, 1983.
- [16] G Baffou, MP Kreuzer, F Kulzer, and R Quidant. Temperature mapping near plasmonic nanostructures using fluorescence polarization anisotropy. *Optics express*, 17(5):3291–3298, 2009.
- [17] Ajay Nahata, Richard A Linke, T Ishi, and K Ohashi. Enhanced nonlinear optical conversion from a periodically nanostructured metal film. *Optics letters*, 28(6):423–425, 2003.
- [18] A. Kinkhabwala, Z. Yu, S. Fan, Y. Avlasevich, K. Müllen, and WE Moerner. Large single-molecule fluorescence enhancements produced by a bowtie nanoantenna. *Nature Photonics*, 3(11):654–657, 2009.
- [19] Andreas J Huber, Fritz Keilmann, J Wittborn, Javier Aizpurua, and Rainer Hillenbrand. Terahertz near-field nanoscopy of mobile carriers in single semiconductor nanodevices. *Nano letters*, 8(11):3766–3770, 2008.
- [20] Liang Tang, Sukru Ekin Kocabas, Salman Latif, Ali K Okyay, Dany-Sebastien Ly-Gagnon, Krishna C Saraswat, and David AB Miller. Nanometre-scale germanium photodetector enhanced by a near-infrared dipole antenna. *Nature Photonics*, 2(4):226–229, 2008.
- [21] Achim Hartschuh, Erik J Sánchez, X Sunney Xie, and Lukas Novotny. High-resolution near-field raman microscopy of single-walled carbon nanotubes. *Physical Review Letters*, 90(9):095503, 2003.
- [22] Heinrich G Frey, Susanne Witt, Karin Felderer, and Reinhard Guckenberger. High-resolution imaging of single fluorescent molecules with the optical near-field of a metal tip. *Physical review letters*, 93(20):200801, 2004.
- [23] Jiadan Lin, Hai Li, Hua Zhang, and Wei Chen. Plasmonic enhancement of photocurrent in mos₂ field-effect-transistor. *Applied Physics Letters*, 102(20):203109–3, 2013.
- [24] Mark W. Knight, Heidar Sobhani, Peter Nordlander, and Naomi J. Halas. Photodetection with active optical antennas. *Science*, 332(6030):702–704, 2011.
- [25] Carl Hagglund, Michael Zach, Goran Petersson, and Bengt Kasemo. Electromagnetic coupling of light into a silicon solar cell by nanodisk plasmons. *Applied Physics Letters*, 92(5):053110, 2008.
- [26] D Derkacs, SH Lim, P Matheu, W Mar, and ET Yu. Improved performance of amorphous silicon solar cells via scattering from surface plasmon polaritons in nearby metallic nanoparticles. *Applied Physics Letters*, 89(9):093103–093103, 2006.

- [27] Philipp Reineck, George P. Lee, Delia Brick, Matthias Karg, Paul Mulvaney, and Udo Bach. A solid-state plasmonic solar cell via metal nanoparticle self-assembly. *Advanced Materials*, 24(35):4750–4755, 2012.
- [28] Wei Zhang, Michael Saliba, Samuel D. Stranks, Yao Sun, Xian Shi, Ulrich Wiesner, and Henry J. Snaith. Enhancement of perovskite-based solar cells employing core-shell metal nanoparticles. *Nano Letters*, 13(9):4505–4510, 2013.
- [29] D Derkacs, WV Chen, PM Matheu, SH Lim, PKL Yu, and ET Yu. Nanoparticle-induced light scattering for improved performance of quantum-well solar cells. *Applied Physics Letters*, 93(9):091107, 2008.
- [30] Carl Hagglund, Michael Zach, and Bengt Kasemo. Enhanced charge carrier generation in dye sensitized solar cells by nanoparticle plasmons. *Applied Physics Letters*, 92(1):013113–3, 2008.
- [31] EI Wei, Xuanhua Li, and Wallace CH Choy. Breaking the space charge limit in organic solar cells by a novel plasmonic-electrical concept. *Scientific reports*, 4, 2014.
- [32] S. Kim, J. Jin, Y.J. Kim, I.Y. Park, Y. Kim, and S.W. Kim. High-harmonic generation by resonant plasmon field enhancement. *Nature*, 453(7196):757–760, 2008.
- [33] N. Liu, M.L. Tang, M. Hentschel, H. Giessen, and A.P. Alivisatos. Nanoantenna-enhanced gas sensing in a single tailored nanofocus. *Nature materials*, 10(8):631–636, 2011.
- [34] Naomi J. Halas and Martin Moskovits. Surface-enhanced raman spectroscopy: Substrates and materials for research and applications. *MRS Bulletin*, 38(08):607–611, 2013.
- [35] Bhavya Sharma, M. Fernanda Cardinal, Samuel L. Kleinman, Nathan G. Greeneltch, Renee R. Frontiera, Martin G. Blaber, George C. Schatz, and Richard P. Van Duyne. High-performance sers substrates: Advances and challenges. *MRS Bulletin*, 38(08):615–624, 2013.
- [36] Tao Chen, Hong Wang, Gang Chen, Yong Wang, Yuhua Feng, Wei Shan Teo, Tom Wu, and Hongyu Chen. Hotspot-induced transformation of surface-enhanced raman scattering fingerprints. *Acs Nano*, 4(6):3087–3094, 2010.
- [37] Ricardo F. Aroca. Plasmon enhanced spectroscopy. *Physical Chemistry Chemical Physics*, 15(15):5355–5363, 2013.
- [38] Na Liu, Hongcang Guo, Liwei Fu, Stefan Kaiser, Heinz Schweizer, and Harald Giessen. Three-dimensional photonic metamaterials at optical frequencies. *Nature materials*, 7(1):31–37, 2007.
- [39] Jason Valentine, Shuang Zhang, Thomas Zentgraf, Erick Ulin-Avila, Dentcho A Genov, Guy Bartal, and Xiang Zhang. Three-dimensional optical metamaterial with a negative refractive index. *nature*, 455(7211):376–379, 2008.

Bibliography

- [40] Hou-Tong Chen, Willie J Padilla, Joshua MO Zide, Arthur C Gossard, Antoinette J Taylor, and Richard D Averitt. Active terahertz metamaterial devices. *Nature*, 444(7119):597–600, 2006.
- [41] M C K Wiltshire, J B Pendry, and J V Hajnal. Sub-wavelength imaging at radio frequency. *Journal of Physics: Condensed Matter*, 18(22):L315, 2006.
- [42] Wenshan Cai, Uday K Chettiar, Alexander V Kildishev, and Vladimir M Shalaev. Optical cloaking with metamaterials. *Nature photonics*, 1(4):224–227, 2007.
- [43] Gururaj V. Naik, Vladimir M. Shalaev, and Alexandra Boltasseva. Alternative plasmonic materials: Beyond gold and silver. *Advanced Materials*, 25(24):3264–3294, 2013.
- [44] C. Lindquist Nathan, Nagpal Prashant, M. McPeak Kevin, J. Norris David, and Oh Sang-Hyun. Engineering metallic nanostructures for plasmonics and nanophotonics. *Reports on Progress in Physics*, 75(3):036501, 2012.
- [45] Jung Hyeun Kim, Sheryl H Ehrman, and Thomas A Germer. Influence of particle oxide coating on light scattering by submicron metal particles on silicon wafers. *Applied physics letters*, 84(8):1278–1280, 2004.
- [46] Hanwei Gao, Joel Henzie, Min Hyung Lee, and Teri W Odom. Screening plasmonic materials using pyramidal gratings. *Proceedings of the National Academy of Sciences*, 105(51):20146–20151, 2008.
- [47] Krishanu Ray, Mustafa H Chowdhury, and Joseph R Lakowicz. Aluminum nanostructured films as substrates for enhanced fluorescence in the ultraviolet-blue spectral region. *Analytical chemistry*, 79(17):6480–6487, 2007.
- [48] Matthew D Arnold and Martin G Blaber. Optical performance and metallic absorption in nanoplasmonic systems. *Optics express*, 17(5):3835–3847, 2009.
- [49] Martin G Blaber, Matthew D Arnold, and Michael J Ford. A review of the optical properties of alloys and intermetallics for plasmonics. *Journal of Physics: Condensed Matter*, 22(14):143201, 2010.
- [50] Jorge Perez-Juste, Isabel Pastoriza-Santos, Luis M. Liz-Marzan, and Paul Mulvaney. Gold nanorods: Synthesis, characterization and applications. *Coordination Chemistry Reviews*, 249(17-18):1870–1901, 9 2005.
- [51] Babak Nikoobakht and Mostafa A. El-Sayed. Preparation and growth mechanism of gold nanorods (nrs) using seed-mediated growth method. *Chemistry of Materials*, 15(10):1957–1962, 2003.
- [52] Nikhil R. Jana, Latha Gearheart, and Catherine J. Murphy. Wet chemical synthesis of high aspect ratio cylindrical gold nanorods. *The Journal of Physical Chemistry B*, 105(19):4065–4067, 2001.

- [53] Xiaohua Huang, Svetlana Neretina, and Mostafa A. El-Sayed. Gold nanorods: From synthesis and properties to biological and biomedical applications. *Advanced Materials*, 21(48):4880–4910, 2009.
- [54] Yu, Ser-Sing Chang, Chien-Liang Lee, and C. R. Chris Wang. Gold nanorods: electrochemical synthesis and optical properties. *The Journal of Physical Chemistry B*, 101(34):6661–6664, 1997.
- [55] Charles R. Martin. Membrane-based synthesis of nanomaterials. *Chemistry of Materials*, 8(8):1739–1746, 1996.
- [56] Kunio Esumi, Keiichi Matsuhisa, and Kanjiro Torigoe. Preparation of rodlike gold particles by uv irradiation using cationic micelles as a template. *Langmuir*, 11(9):3285–3287, 1995.
- [57] S.A. Maier. *Plasmonics: fundamentals and applications*. Springer Verlag, 2007.
- [58] K. Lance Kelly, Eduardo Coronado, Lin Lin Zhao, and George C. Schatz. The optical properties of metal nanoparticles: The influence of size, shape, and dielectric environment. *The Journal of Physical Chemistry B*, 107(3):668–677, 2003.
- [59] J. Aizpurua, Garnett W. Bryant, Lee J. Richter, Garc, iacute, F. J. a de Abajo, Brian K. Kelley, and T. Mallouk. Optical properties of coupled metallic nanorods for field-enhanced spectroscopy. *Physical Review B*, 71(23):235420, 2005.
- [60] Feng Wang and Y. Ron Shen. General properties of local plasmons in metal nanostructures. *Physical review letters*, 97(20):206806, 2006.
- [61] Weihai Ni, Xiaoshan Kou, Zhi Yang, and Jianfang Wang. Tailoring longitudinal surface plasmon wavelengths, scattering and absorption cross sections of gold nanorods. *ACS Nano*, 2(4):677–686, 2008.
- [62] Garnett W. Bryant, F. Javier Garcia de Abajo, and Javier Aizpurua. Mapping the plasmon resonances of metallic nanoantennas. *Nano Letters*, 8(2):631–636, 2008.
- [63] Alison M. Funston, Carolina Novo, Tim J. Davis, and Paul Mulvaney. Plasmon coupling of gold nanorods at short distances and in different geometries. *Nano Letters*, 9(4):1651–1658, 2009.
- [64] Steven J. Barrow, Alison M. Funston, Daniel E. Gamez, Tim J. Davis, and Paul Mulvaney. Surface plasmon resonances in strongly coupled gold nanosphere chains from monomer to hexamer. *Nano Letters*, 11(10):4180–4187, 2011.
- [65] K. Imura, T. Nagahara, and H. Okamoto. Near-field two-photon-induced photoluminescence from single gold nanorods and imaging of plasmon modes. *The Journal of Physical Chemistry B*, 109(27):13214–13220, 2005.

Bibliography

- [66] Ming-Wen Chu, Viktor Myroshnychenko, Cheng Hsuan Chen, Jing-Pei Deng, Chung-Yuan Mou, and F. Javier Garcia de Abajo. Probing bright and dark surface-plasmon modes in individual and coupled noble metal nanoparticles using an electron beam. *Nano Letters*, 9(1):399–404, 2009. PMID: 19063614.
- [67] Beth S. Guiton, Vighter Iberi, Shuzhou Li, Donovan N. Leonard, Chad M. Parish, Paul G. Kotula, Maria Varela, George C. Schatz, Stephen J. Pennycook, and Jon P. Camden. Correlated optical measurements and plasmon mapping of silver nanorods. *Nano Letters*, 11(8):3482–3488, 2011.
- [68] Boris Luk'yanchuk, Nikolay I. Zheludev, Stefan A. Maier, Naomi J. Halas, Peter Nordlander, Harald Giessen, and Chong Tow Chong. The fano resonance in plasmonic nanostructures and metamaterials. *Nat Mater*, 9(9):707–715, 2010.
- [69] Zhong-Jian Yang, Zong-Suo Zhang, Li-Hui Zhang, Qun-Qing Li, Zhong-Hua Hao, and Qu-Quan Wang. Fano resonances in dipole-quadrupole plasmon coupling nanorod dimers. *Opt. Lett.*, 36(9):1542–1544, 2011.
- [70] Kat Choi Woo, Lei Shao, Huanjun Chen, Yao Liang, Jianfang Wang, and Hai-Qing Lin. Universal scaling and fano resonance in the plasmon coupling between gold nanorods. *ACS Nano*, 5(7):5976–5986, 2011.
- [71] H. Chen, L. Shao, T. Ming, K. C. Woo, Y. C. Man, J. Wang, and H. Q. Lin. Observation of the fano resonance in gold nanorods supported on high-dielectric-constant substrates. *ACS Nano*, 5(8):6754–63, Aug 23 2011.
- [72] Xiaoli Wang, Philippe Gogol, Edmond Cambril, and Bruno Palpant. Near- and far-field effects on the plasmon coupling in gold nanoparticle arrays. *The Journal of Physical Chemistry C*, 116(46):24741–24747, 2012.
- [73] E Prodan, C Radloff, NJ Halas, and P Nordlander. A hybridization model for the plasmon response of complex nanostructures. *Science*, 302(5644):419–422, 2003.
- [74] Peter Nordlander, C Oubre, E Prodan, K Li, and MI Stockman. Plasmon hybridization in nanoparticle dimers. *Nano Letters*, 4(5):899–903, 2004.
- [75] Na Liu, Shaunak Mukherjee, Kui Bao, Lisa V. Brown, Jens Dorfmuller, Peter Nordlander, and Naomi J. Halas. Magnetic plasmon formation and propagation in artificial aromatic molecules. *Nano Letters*, 12(1):364–369, 2011.
- [76] Mario Hentschel, Michael Saliba, Ralf Vogelgesang, Harald Giessen, A. Paul Alivisatos, and Na Liu. Transition from isolated to collective modes in plasmonic oligomers. *Nano Letters*, 10(7):2721–2726, 2010.
- [77] Q. H. Wei, K. H. Su, S. Durant, and X. Zhang. Plasmon resonance of finite one-dimensional au nanoparticle chains. *Nano Letters*, 4(6):1067–1071, 2004/06/01 2004.

- [78] Stefan A Maier, Pieter G Kik, and Harry A Atwater. Observation of coupled plasmon-polariton modes in au nanoparticle chain waveguides of different lengths: Estimation of waveguide loss. *Applied Physics Letters*, 81(9):1714–1716, 2002.
- [79] Andreas M. Kern and Olivier J. F. Martin. Excitation and reemission of molecules near realistic plasmonic nanostructures. *Nano Letters*, 11(2):482–487, 2011.
- [80] Weihai Ni, Tobias Ambjornsson, Sten Peter Apell, Huanjun Chen, and Jianfang Wang. Observing plasmonic-molecular resonance coupling on single gold nanorods. *Nano Letters*, 10(1):77–84, 2009.
- [81] Felicia Tam, Glenn P Goodrich, Bruce R Johnson, and Naomi J Halas. Plasmonic enhancement of molecular fluorescence. *Nano Letters*, 7(2):496–501, 2007.
- [82] Yeechi Chen, Keiko Munechika, and David S. Ginger. Dependence of fluorescence intensity on the spectral overlap between fluorophores and plasmon resonant single silver nanoparticles. *Nano Letters*, 7(3):690–696, 2007.
- [83] Setu Kasera, Frank Biedermann, Jeremy J. Baumberg, Oren A. Scherman, and Sumeet Mahajan. Quantitative sensing using the sequestration of small molecules inside precise plasmonic nanoconstructs. *Nano Letters*, 2012.
- [84] Kristen D Alexander, Kwan Skinner, Shunping Zhang, Hong Wei, and Rene Lopez. Tunable sensing in gold nanorod dimers through strain control on an elastomeric substrate. *Nano letters*, 10(11):4488–4493, 2010.
- [85] Matthew D. Doherty, Antony Murphy, John McPhillips, Robert J. Pollard, and Paul Dawson. Wavelength dependence of raman enhancement from gold nanorod arrays: Quantitative experiment and modeling of a hot spot dominated system. *The Journal of Physical Chemistry C*, 114(47):19913–19919, 2010.
- [86] Prashant K. Jain, Wenyu Huang, and Mostafa A. El-Sayed. On the universal scaling behavior of the distance decay of plasmon coupling in metal nanoparticle pairs: A plasmon ruler equation. *Nano Letters*, 7(7):2080–2088, 2007.
- [87] Ramon A. Alvarez-Puebla, Ashish Agarwal, Pramit Manna, Bishnu P. Khanal, Paula Aldeanueva-Potel, Enrique Carbo-Argibay, Nicolas Pazos-Porez, Leonid Vigderman, Eugene R. Zubarev, Nicholas A. Kotov, and Luis M. Liz-Marzán. Gold nanorods 3d-supercrystals as surface enhanced raman scattering spectroscopy substrates for the rapid detection of scrambled prions. *Proceedings of the National Academy of Sciences*, 108(20):8157–8161, 2011.
- [88] Babak Nikoobakht, Jianping Wang, and Mostafa A. El-Sayed. Surface-enhanced raman scattering of molecules adsorbed on gold nanorods: off-surface plasmon resonance condition. *Chemical Physics Letters*, 366(12):17–23, 2002.

Bibliography

- [89] Alfonso Martin, Andrea Pescaglioni, Carola Schopf, Vittorio Scardaci, Richard Coull, Lorraine Byrne, and Daniela Iacopino. Surface-enhanced raman scattering of 4-aminobenzenethiol on au nanorod ordered arrays. *The Journal of Physical Chemistry C*, 118(24):13260–13267, 2014.
- [90] Bo Peng, Guangyuan Li, Dehui Li, Stephanie Dodson, Qing Zhang, Jun Zhang, Yih Hong Lee, Hilmi Volkan Demir, Xing Yi Ling, and Qihua Xiong. Vertically aligned gold nanorod monolayer on arbitrary substrates: Self-assembly and femtomolar detection of food contaminants. *ACS Nano*, 7(7):5993–6000, 2013.
- [91] Marcos Sanles-Sobrido, Laura Rodriguez-Lorenzo, Silvia Lorenzo-Abalde, Africa Gonzalez-Fernandez, Miguel A Correa-Duarte, Ramon A Alvarez-Puebla, and Luis M Liz-Marzan. Label-free sers detection of relevant bio-analytes on silver-coated carbon nanotubes: the case of cocaine. *Nanoscale*, 1(1):153–158, 2009.
- [92] Yi Cui, Mikael T. Bjark, J. Alexander Liddle, Carsten Sannichsen, Benjamin Boussert, and A. Paul Alivisatos. Integration of colloidal nanocrystals into lithographically patterned devices. *Nano Letters*, 4(6):1093–1098, 2004.
- [93] Cecilia Noguez. Surface plasmons on metal nanoparticles: the influence of shape and physical environment. *The Journal of Physical Chemistry C*, 111(10):3806–3819, 2007.
- [94] Ali A Ashkarran and Alireza Bayat. Surface plasmon resonance of metal nanostructures as a complementary technique for microscopic size measurement. *International Nano Letters*, 3(1):50, 2013.
- [95] Hadas Katz-Boon, Chris J. Rossouw, Matthew Weyland, Alison M. Funston, Paul Mulvaney, and Joanne Etheridge. Three-dimensional morphology and crystallography of gold nanorods. *Nano Letters*, 11(1):273–278, 2010.
- [96] Eric C Le Ru, Johan Grand, Idrissa Sow, Walter RC Somerville, Pablo G Etchegoin, Mona Treguer-Delapierre, Gaëlle Charron, Nordin Félidj, Georges Lévi, and Jean Aubard. A scheme for detecting every single target molecule with surface-enhanced raman spectroscopy. *Nano letters*, 11(11):5013–5019, 2011.
- [97] Carolina Novo, Alison M. Funston, Isabel Pastoriza-Santos, Luis M. Liz-Marzan, and Paul Mulvaney. Influence of the medium refractive index on the optical properties of single gold triangular prisms on a substrate. *The Journal of Physical Chemistry C*, 112(1):3–7, 2008/01/01 2007.
- [98] Xiaohu Xia and Younan Xia. Symmetry breaking during seeded growth of nanocrystals. *Nano Letters*, 12(11):6038–6042, 2012.
- [99] Mikhail Artemyev, Bjarn Maller, and Ulrike Woggon. Unidirectional alignment of cdse nanorods. *Nano Letters*, 3(4):509–512, 2003.
- [100] Franklin Kim, Serena Kwan, Jennifer Akana, and Peidong Yang. Langmuir-blodgett nanorod assembly. *Journal of the American Chemical Society*, 123(18):4360–4361, 2001. PMID: 11457213.

- [101] Ali Ghezelbash, Bonil Koo, and Brian A. Korgel. Self-assembled stripe patterns of cds nanorods. *Nano Letters*, 6(8):1832–1836, 2006.
- [102] Robert D. Deegan, Olgica Bakajin, Todd F. Dupont, Greb Huber, Sidney R. Nagel, and Thomas A. Witten. Capillary flow as the cause of ring stains from dried liquid drops. *Nature*, 389(6653):827–829, 1997.
- [103] Brian C. Gierhart, David G. Howitt, Shiahn J. Chen, Rosemary L. Smith, and Scott D. Collins. Frequency dependence of gold nanoparticle superassembly by dielectrophoresis. *Langmuir*, 23(24):12450–12456, 2007.
- [104] S.M. Marinakos, L.C. Brousseau III, A. Jones, and D.L. Feldheim. Template synthesis of one-dimensional au, au-poly (pyrrole), and poly (pyrrole) nanoparticle arrays. *Chemistry of materials*, 10(5):1214–1219, 1998.
- [105] T. Sawitowski, Y. Miquel, A. Heilmann, and G. Schmid. Optical properties of quasi one-dimensional chains of gold nanoparticles. *Advanced Functional Materials*, 11(6):435–440, 2001.
- [106] Y. Yin, Y. Lu, B. Gates, and Y. Xia. Template-assisted self-assembly: a practical route to complex aggregates of monodispersed colloids with well-defined sizes, shapes, and structures. *Journal of the American Chemical Society*, 123(36):8718–8729, 2001.
- [107] I. Hussain, M. Brust, J. Barauskas, and A.I. Cooper. Controlled step growth of molecularly linked gold nanoparticles: from metallic monomers to dimers to polymeric nanoparticle chains. *Langmuir*, 25(4):1934–1939, 2009.
- [108] Shuzhuo Zhang, Xiaoshan Kou, Zhi Yang, Qihui Shi, Galen D. Stucky, Lingdong Sun, Jianfang Wang, and Chunhua Yan. Nanonecklaces assembled from gold rods, spheres, and bipyramids. *Chemical Communications*, (18):1816–1818, 2007.
- [109] Rajesh Sardar and Jennifer S. Shumaker-Parry. Asymmetrically functionalized gold nanoparticles organized in one-dimensional chains. *Nano Letters*, 8(2):731–736, 2008. PMID: 18269261.
- [110] Kristian Mølhave, Brent A Wacaser, Dirch Hjorth Petersen, Jakob B Wagner, Lars Samuelson, and Peter Bøggild. Epitaxial integration of nanowires in microsystems by local micrometer-scale vapor-phase epitaxy. *small*, 4(10):1741–1746, 2008.
- [111] Carl J Barrelet, Yue Wu, David C Bell, and Charles M Lieber. Synthesis of cds and zns nanowires using single-source molecular precursors. *Journal of the American Chemical Society*, 125(38):11498–11499, 2003.
- [112] Pavle V Radovanovic, Carl J Barrelet, Silvija Gradecak, Fang Qian, and Charles M Lieber. General synthesis of manganese-doped ii-vi and iii-v semiconductor nanowires. *Nano letters*, 5(7):1407–1411, 2005.

- [113] Jonas Johansson, Lisa S Karlsson, C Patrik T Svensson, Thomas Mårtensson, Brent A Wacaser, Knut Deppert, Lars Samuelson, and Werner Seifert. Structural properties of $\langle 111 \rangle$ b-oriented iii-v nanowires. *Nature materials*, 5(7):574–580, 2006.
- [114] Ruoxue Yan, Daniel Gargas, and Peidong Yang. Nanowire photonics. *Nature Photonics*, 3(10):569–576, 2009.
- [115] Linyou Cao, Justin S White, Joon-Shik Park, Jon A Schuller, Bruce M Clemens, and Mark L Brongersma. Engineering light absorption in semiconductor nanowire devices. *Nature materials*, 8(8):643–647, 2009.
- [116] Jean-Pierre Colinge, Chi-Woo Lee, Aryan Afzalian, Nima Dehdashti Akhavan, Ran Yan, Isabelle Ferain, Pedram Razavi, Brendan O’Neill, Alan Blake, Mary White, et al. Nanowire transistors without junctions. *Nature nanotechnology*, 5(3):225–229, 2010.
- [117] Mariano A Zimmler, Daniel Stichtenoth, Carsten Ronning, Wei Yi, Venkatesh Narayanamurti, Tobias Voss, and Federico Capasso. Scalable fabrication of nanowire photonic and electronic circuits using spin-on glass. *Nano letters*, 8(6):1695–1699, 2008.
- [118] Cesare Soci, Arthur Zhang, Bin Xiang, Shadi A Dayeh, DPR Aplin, Jung Park, XY Bao, Yu-Hwa Lo, and Deli Wang. Zno nanowire uv photodetectors with high internal gain. *Nano Letters*, 7(4):1003–1009, 2007.
- [119] Jianfang Wang, Mark S Gudiksen, Xiangfeng Duan, Yi Cui, and Charles M Lieber. Highly polarized photoluminescence and photodetection from single indium phosphide nanowires. *Science*, 293(5534):1455–1457, 2001.
- [120] Cesare Soci, Arthur Zhang, Xin-Yu Bao, Hongkwon Kim, Yuhwa Lo, and Deli Wang. Nanowire photodetectors. *Journal of nanoscience and nanotechnology*, 10(3):1430–1449, 2010.
- [121] Bozhi Tian, Xiaolin Zheng, Thomas J Kempa, Ying Fang, Nanfang Yu, Guihua Yu, Jinlin Huang, and Charles M Lieber. Coaxial silicon nanowires as solar cells and nanoelectronic power sources. *Nature*, 449(7164):885–889, 2007.
- [122] Jesper Wallentin, Nicklas Anttu, Damir Asoli, Maria Huffman, Ingvar Aberg, Martin H. Magnusson, Gerald Siefert, Peter Fuss-Kailuweit, Frank Dimroth, Bernd Witzigmann, H. Q. Xu, Lars Samuelson, Knut Deppert, and Magnus T. Borgstrom. Inp nanowire array solar cells achieving 13.8% efficiency by exceeding the ray optics limit. *science*, 339(6123):1057–1060, March 1, 2013 2013.
- [123] Linyou Cao, Joon-Shik Park, Pengyu Fan, Bruce Clemens, and Mark L. Brongersma. Resonant germanium nanoantenna photodetectors. *Nano Letters*, 10(4):1229–1233, 2010.
- [124] Erik C. Garnett, Mark L. Brongersma, Yi Cui, and Michael D. McGehee. Nanowire solar cells. *Annual Review of Materials Research*, 41(1):269–295, 2011.

- [125] C Colombo, M Hei β , M Gratzel, and A Fontcubertai Morral. Gallium arsenide pin radial structures for photovoltaic applications. *Applied Physics Letters*, 94(17):173108–173108, 2009.
- [126] Martin A. Green, Keith Emery, Yoshihiro Hishikawa, Wilhelm Warta, and Ewan D. Dunlop. Solar cell efficiency tables (version 41). *Progress in Photovoltaics: Research and Applications*, 21(1):1–11, 2013.
- [127] Martin A. Green. Third generation photovoltaics: solar cells for 2020 and beyond. *Physica E: Low-dimensional Systems and Nanostructures*, 14(1-2):65–70, 2002.
- [128] CW Cheng, EJ Sie, B Liu, CHA Huan, TC Sum, HD Sun, and HJ Fan. Surface plasmon enhanced band edge luminescence of zno nanorods by capping au nanoparticles. *Applied Physics Letters*, 96(7):071107, 2010.
- [129] Jerome K Hyun and Lincoln J Lauhon. Spatially resolved plasmonically enhanced photocurrent from au nanoparticles on a si nanowire. *Nano letters*, 11(7):2731–2734, 2011.
- [130] Carlo Colombo, Peter Krogstrup, Jesper Nyg \ddot{a} rd, Mark L Brongersma, and Anna Fontcuberta i Morral. Engineering light absorption in single-nanowire solar cells with metal nanoparticles. *New Journal of Physics*, 13(12):123026, 2011.
- [131] Renjie Chen, Dehui Li, Hailong Hu, Yanyuan Zhao, Ying Wang, Nancy Wong, Shijie Wang, Yi Zhang, Jun Hu, Zexiang Shen, et al. Tailoring optical properties of silicon nanowires by au nanostructure decorations: Enhanced raman scattering and photodetection. *The Journal of Physical Chemistry C*, 116(7):4416–4422, 2012.
- [132] S. A. Maier, M. L. Brongersma, P. G. Kik, S. Meltzer, A. A. G. Requicha, and H. A. Atwater. Plasmonics—a route to nanoscale optical devices. *Advanced Materials*, 13(19):1501–1505, 2001.
- [133] Jerome K. Hyun and Lincoln J. Lauhon. Spatially resolved plasmonically enhanced photocurrent from au nanoparticles on a si nanowire. *Nano Letters*, 11(7):2731–2734, 2011.
- [134] Renjie Chen, Dehui Li, Hailong Hu, Yanyuan Zhao, Ying Wang, Nancy Wong, Shijie Wang, Yi Zhang, Jun Hu, Zexiang Shen, and Qihua Xiong. Tailoring optical properties of silicon nanowires by au nanostructure decorations: Enhanced raman scattering and photodetection. *The Journal of Physical Chemistry C*, 116(7):4416–4422, 2012.
- [135] Ming-Shien Hu, Hsin-Li Chen, Ching-Hsing Shen, Lu-Sheng Hong, Bohr-Ran Huang, Kuei-Hsien Chen, and Li-Chyong Chen. Photosensitive gold-nanoparticle-embedded dielectric nanowires. *Nat Mater*, 5(2):102–106, 2006.
- [136] Jinshui Miao, Weida Hu, Nan Guo, Zhenyu Lu, Xuming Zou, Lei Liao, Suixing Shi, Pingping Chen, Zhiyong Fan, Johnny C Ho, et al. Single inas nanowire

- room-temperature near-infrared photodetectors. *ACS nano*, 8(4):3628–3635, 2014.
- [137] Alberto Casadei, Emanuele F. Pecora, Jacob Trevino, Carlo Forestiere, Daniel Ruffer, Eleonora Russo-Averchi, Federico Matteini, Gozde Tutuncuoglu, Martin Heiss, Anna Fontcuberta i Morral, and Luca Dal Negro. Photonic-plasmonic coupling of gaas single nanowires to optical nanoantennas. *Nano Letters*, 14(5):2271–2278, 2014. PMID: 24742076.
- [138] Jency Pricilla Sundararajan, Pavel Bakharev, Ishwar Niraula, Blaise Alexis Fouetio Kengne, Quinn MacPherson, Meredith Sargent, Brian Hare, and David N. McIlroy. Observation of surface plasmon polariton pumping of optical eigenmodes of gold-decorated gallium nitride nanowires. *Nano Letters*, 12(10):5181–5185, 2012.
- [139] Y. J. Fang, J. Sha, Z. L. Wang, Y. T. Wan, W. W. Xia, and Y. W. Wang. *Behind the change of the photoluminescence property of metal-coated ZnO nanowire arrays*, volume 98. Appl. Phys. Lett, 2011.
- [140] Soumen Dhara and PK Giri. On the origin of enhanced photoconduction and photoluminescence from au and ti nanoparticles decorated aligned zno nanowire heterostructures. *Journal of Applied Physics*, 110(12):124317–9, 2011.
- [141] Ramesh Kattumenu, Chang H. Lee, Limei Tian, Michael E. McConney, and Srikanth Singamaneni. Nanorod decorated nanowires as highly efficient sers-active hybrids. *J. Mater. Chem.*, 21:15218–15223, 2011.
- [142] Xuming Zou, Jingli Wang, Xingqiang Liu, Chunlan Wang, Ying Jiang, Yong Wang, Xiangheng Xiao, Johnny C. Ho, Jinchai Li, Changzhong Jiang, Ying Fang, Wei Liu, and Lei Liao. Rational design of sub-parts per million specific gas sensors array based on metal nanoparticles decorated nanowire enhancement-mode transistors. *Nano Letters*, 13(7):3287–3292, 2013. PMID: 23796312.
- [143] Vivek Pachauri, Klaus Kern, and Kannan Balasubramanian. Field-effect-based chemical sensing using nanowire-nanoparticle hybrids: The ion-sensitive metal-semiconductor field-effect transistor. *Applied Physics Letters*, 102(2):023501–5, 2013.
- [144] Mark W. Knight, Nathaniel K. Grady, Rizia Bardhan, Feng Hao, Peter Nordlander, and Naomi J. Halas. Nanoparticle-mediated coupling of light into a nanowire. *Nano Letters*, 7(8):2346–2350, 2007.
- [145] Sergey V Gaponenko. *Introduction to nanophotonics*. Cambridge University Press, 2010.
- [146] Jonathan A. Scholl, Ai Leen Koh, and Jennifer A. Dionne. Quantum plasmon resonances of individual metallic nanoparticles. *Nature*, 483(7390):421–427, 2012.

- [147] G Grosso and GP Parravicini. *Solid State Physics, 2000*. Academic Press.
- [148] NW Ashcroft and ND Mermin. *Solid State Physics (Brooks Cole, 1976)*.
- [149] P. B. Johnson and R. W. Christy. Optical constants of the noble metals. *Physical Review B*, 6(12):4370–4379, 1972.
- [150] John David Jackson and John D Jackson. *Classical electrodynamics*, volume 3. Wiley New York etc., 1962.
- [151] R. Gans. Äeber die form ultramikroskopischer goldteilchen. *Annalen der Physik*, 342(5):881–900, 1912.
- [152] Craig F. Bohren and Donald R. Huffman. *Absorption and Scattering of Light by Small Particles (Wiley science paperback series)*. Wiley-VCH, April 1998.
- [153] Alfonso MartÅn, Andrea Pescagli, Carola Schopf, Vittorio Scardaci, Richard Coull, Lorraine Byrne, and Daniela Iacopino. Surface-enhanced raman scattering of 4-aminobenzenethiol on au nanorod ordered arrays. *The Journal of Physical Chemistry C*, 118(24):13260–13267, 2014.
- [154] Carlo Forestiere, Alyssa J. Pasquale, Antonio Capretti, Giovanni Miano, Antonello Tamburrino, Sylvanus Y. Lee, Bjorn M. Reinhard, and Luca Dal Negro. Genetically engineered plasmonic nanoarrays. *Nano Letters*, 12(4):2037–2044, 2012.
- [155] Naomi J. Halas, Surbhi Lal, Wei-Shun Chang, Stephan Link, and Peter Nordlander. Plasmons in strongly coupled metallic nanostructures. *Chemical Reviews*, 111(6):3913–3961, 2011.
- [156] Liu and Philippe Guyot-Sionnest. Mechanism of silver(i)-assisted growth of gold nanorods and bipyramids. *The Journal of Physical Chemistry B*, 109(47):22192–22200, 2005.
- [157] Bart Goris, Sara Bals, Wouter Van den Broek, Enrique Carbo-Argibay, Sergio Gomez-Grana, Luis M. Liz-Marzan, and Gustaaf Van Tendeloo. Atomic-scale determination of surface facets in gold nanorods. *Nat Mater*, 11(11):930–935, 2012.
- [158] Khee Chaw Ng and Wenlong Cheng. Fine-tuning longitudinal plasmon resonances of nanorods by thermal reshaping in aqueous media. *Nanotechnology*, 23(10):105602, 2012.
- [159] M. A. Mangold, C. Weiss, M. Calame, and A. W. Holleitner. Surface plasmon enhanced photoconductance of gold nanoparticle arrays with incorporated alkane linkers. *Applied Physics Letters*, 94(16):–, 2009.
- [160] Antje Rey, Guillaume Billardon, Emanuel Lortscher, Kasper Moth-Poulsen, Nicolai Stuhr-Hansen, Heiko Wolf, Thomas Bjornholm, Andreas Stemmer, and Heike Riel. Deterministic assembly of linear gold nanorod chains as a platform for nanoscale applications. *Nanoscale*, 5(18):8680–8688, 2013.

Bibliography

- [161] Amir Zabet-Khosousi and Al-Amin Dhirani. Charge transport in nanoparticle assemblies. *Chemical Reviews*, 108(10):4072–4124, 2008.
- [162] Amy Szuchmacher Blum, James G. Kushmerick, David P. Long, Charles H. Patterson, John C. Yang, Jay C. Henderson, Yuxing Yao, James M. Tour, Ranganathan Shashidhar, and Banahalli R. Ratna. Molecularly inherent voltage-controlled conductance switching. *Nat Mater*, 4(2):167–172, 2005.
- [163] Duygu Kozanoglu, Dogukan Hazar Apaydin, Ali Cirpan, and Emren Nalbant Esenturk. Power conversion efficiency enhancement of organic solar cells by addition of gold nanostars, nanorods, and nanospheres. *Organic Electronics*, 14(7):1720 – 1727, 2013.
- [164] Chenxu Yu and Joseph Irudayaraj. Quantitative evaluation of sensitivity and selectivity of multiplex nanospr biosensor assays. *Biophysical journal*, 93(10):3684–3692, 2007.
- [165] Weibo Cai and Xiaoyuan Chen. Nanoplatforms for targeted molecular imaging in living subjects. *Small*, 3(11):1840–1854, 2007.
- [166] Hironobu Takahashi, Takuro Niidome, Ayuko Nariai, Yasuro Niidome, and Sunao Yamada. Photothermal reshaping of gold nanorods prevents further cell death. *Nanotechnology*, 17(17):4431, 2006.
- [167] Tapan K. Sau and Catherine J. Murphy. Self-assembly patterns formed upon solvent evaporation of aqueous cetyltrimethylammonium bromide-coated gold nanoparticles of various shapes. *Langmuir*, 21(7):2923–2929, 2005.
- [168] Babak Nikoobakht and Mostafa A. El-Sayed. Evidence for bilayer assembly of cationic surfactants on the surface of gold nanorods. *Langmuir*, 17(20):6368–6374, 2001.
- [169] Ramon A Alvarez-Puebla, Ashish Agarwal, Pramit Manna, Bishnu P Khanal, Paula Aldeanueva-Potel, Enrique Carbo-Argibay, Nicolas Pazos-Perez, Leonid Vigdeman, Eugene R Zubarev, and Nicholas A Kotov. Gold nanorods 3d-supercrystals as surface enhanced raman scattering spectroscopy substrates for the rapid detection of scrambled prions. *Proceedings of the National Academy of Sciences*, 108(20):8157–8161, 2011.
- [170] Kristin Weidemaier, H. L. Tavernier, and M. D. Fayer. Photoinduced electron transfer on the surfaces of micelles. *The Journal of Physical Chemistry B*, 101(45):9352–9361, 1997.
- [171] Gustav Mie. Beitrage zur optik truber medien, speziell kolloidaler metallosungen. *Annalen der physik*, 330(3):377–445, 1908.
- [172] R Gans. Uber die form ultramikroskopischer goldteilchen. *Annalen der Physik*, 342(5):881–900, 1912.

- [173] Vivek Sharma, Kyoungweon Park, and Mohan Srinivasarao. Colloidal dispersion of gold nanorods: Historical background, optical properties, seed-mediated synthesis, shape separation and self-assembly. *Materials Science and Engineering: R: Reports*, 65(1-3):1–38, 2009.
- [174] Kane S Yee et al. Numerical solution of initial boundary value problems involving maxwell equations in isotropic media. *IEEE Trans. Antennas Propag*, 14(3):302–307, 1966.
- [175] F. J. Garcia de Abajo and A. Howie. Retarded field calculation of electron energy loss in inhomogeneous dielectrics. *Phys. Rev. B*, 65:115418, Mar 2002.
- [176] Ulrich Hohenester and Andreas Trügler. Mnpbem—a matlab toolbox for the simulation of plasmonic nanoparticles. *Computer Physics Communications*, 183(2):370–381, 2012.
- [177] Chenxu Yu, Leo Varghese, and Joseph Irudayaraj. Surface modification of cetyltrimethylammonium bromide-capped gold nanorods to make molecular probes. *Langmuir*, 23(17):9114–9119, 2007.
- [178] Davood Raoufi, Ahmad Kiasatpour, Hamid Reza Fallah, and Amir Sayid Hassan Rozatian. Surface characterization and microstructure of ito thin films at different annealing temperatures. *Applied Surface Science*, 253(23):9085–9090, 2007.
- [179] Alexander O. Govorov and Hugh H. Richardson. Generating heat with metal nanoparticles. *Nano Today*, 2(1):30 – 38, 2007.
- [180] Mostafa A. El-Sayed. Some interesting properties of metals confined in time and nanometer space of different shapes. *Accounts of Chemical Research*, 34(4):257–264, 2001/04/01 2001.
- [181] Stephan Link and Mostafa A. El-Sayed. Spectral properties and relaxation dynamics of surface plasmon electronic oscillations in gold and silver nanodots and nanorods. *The Journal of Physical Chemistry B*, 103(40):8410–8426, 1999.
- [182] A. L. Gonzalez, J. A. Reyes-Esqueda, and Cecilia Noguez. Optical properties of elongated noble metal nanoparticles. *The Journal of Physical Chemistry C*, 112(19):7356–7362, 2008.
- [183] Yun-Sheng Chen, Wolfgang Frey, Seungsoo Kim, Pieter Kruizinga, Kimberly Homan, and Stanislav Emelianov. Silica-coated gold nanorods as photoacoustic signal nanoamplifiers. *Nano Letters*, 11(2):348–354, Feb 9 2011.
- [184] S. Khatua, W. S. Chang, P. Swanglap, J. Olson, and S. Link. Active modulation of nanorod plasmons. *Nano Lett*, 11(9):3797–802, Sep 14 2011.
- [185] Tang Qingxin, Tong Yanhong, Jain Titoo, Hassenkam Tue, Wan Qing, Moth-Poulsen Kasper, and Björnholm Thomas. Self-assembled nanogaps for molecular electronics. *Nanotechnology*, 20(24):245205, 2009.

Bibliography

- [186] K.D. Hermanson, S.O. Lumsdon, J.P. Williams, E.W. Kaler, and O.D. Velev. Dielectrophoretic assembly of electrically functional microwires from nanoparticle suspensions. *Science*, 294(5544):1082–1086, 2001.
- [187] Carola Schopf, Alfonso Martín, Mícheál Burke, Daniel Jones, Andrea Pescaglino, Alan O’Riordan, Aidan J Quinn, and Daniela Iacopino. Au nanorod plasmonic superstructures obtained by a combined droplet evaporation and stamping method. *Journal of Materials Chemistry C*, 2(18):3536–3541, 2014.
- [188] S. Diefenbach, N. Erhard, J. Schopka, A. Martin, C. Karnetzky, D. Iacopino, and A. W. Holleitner. Polarization dependent, surface plasmon induced photoconductance in gold nanorod arrays. *Physica Status Solidi RRL: Rapid Research Letters*, 8(3):264–268, 2014.
- [189] X. Xiong. Directed assembly of gold nanoparticle nanowires and networks for nanodevices. *Appl. Phys. Lett.*, 91(6):063101, 2007.
- [190] Dirk N. Weiss, Xavier Brokmann, Laurie E. Calvet, Marc A. Kastner, and Mounqi G. Bawendi. Multi-island single-electron devices from self-assembled colloidal nanocrystal chains. *Applied Physics Letters*, 88(14):143507–3, 2006.
- [191] Stefan A. Maier, Pieter G. Kik, Harry A. Atwater, Sheffer Meltzer, Elad Harel, Bruce E. Koel, and Ari A. G. Requicha. Local detection of electromagnetic energy transport below the diffraction limit in metal nanoparticle plasmon waveguides. *Nat Mater*, 2(4):229–232, 2003.
- [192] S. A. Maier. Plasmonics: Metal nanostructures for subwavelength photonic devices. *Selected Topics in Quantum Electronics, IEEE Journal of*, 12(6):1214–1220, 2006.
- [193] Kyle D. Osberg, Abrin L. Schmucker, Andrew J. Senesi, and Chad A. Mirkin. One-dimensional nanorod arrays: Independent control of composition, length, and interparticle spacing with nanometer precision. *Nano Letters*, 11(2):820–824, 2011.
- [194] Hazel Kitching, Matthew J Shiers, Anthony J Kenyon, and Ivan P Parkin. Self-assembly of metallic nanoparticles into one dimensional arrays. *Journal of Materials Chemistry A*, 1(24):6985–6999, 2013.
- [195] Alan O’Riordan, Paul Delaney, and Gareth Redmond. Field configured assembly: Programmed manipulation and self-assembly at the mesoscale. *Nano Letters*, 4(5):761–765, 2004.
- [196] Simon O. Lumsdon and David M. Scott. Assembly of colloidal particles into microwires using an alternating electric field. *Langmuir*, 21(11):4874–4880, 2005.
- [197] A O’Riordan, D Iacopino, P Lovera, L Floyd, K Reynolds, and G Redmond. Dielectrophoretic self-assembly of polarized light emitting poly (9, 9-dioctylfluorene) nanofibre arrays. *Nanotechnology*, 22(10):105602, 2011.

- [198] Birol Ozturk, Charles Blackledge, Bret N. Flanders, and Daniel R. Grischkowsky. Reproducible interconnects assembled from gold nanorods. *Applied Physics Letters*, 88(7):073108, 2006.
- [199] Waqqar Ahmed, E. Stefan Kooij, Arend van Silfhout, and Bene Poelsema. Quantitative analysis of gold nanorod alignment after electric field-assisted deposition. *Nano Letters*, 9(11):3786–3794, 2009. PMID: 19719154.
- [200] T.B. Jones. *Electromechanics of particles*. Cambridge Univ Pr, 2005.
- [201] Yaling Liu, Jae-Hyun Chung, Wing Kam Liu, and Rodney S. Ruoff. Dielectrophoretic assembly of nanowires. *The Journal of Physical Chemistry B*, 110(29):14098–14106, 2006.
- [202] Christoph W. Marquardt, Sabine Blatt, Frank Hennrich, Hilbert v. Lohneysen, and Ralph Krupke. Probing dielectrophoretic force fields with metallic carbon nanotubes. *Applied Physics Letters*, 89(18):183117, 2006.
- [203] R.D. Miller and T.B. Jones. Electro-orientation of ellipsoidal erythrocytes. theory and experiment. *Biophysical journal*, 64(5):1588–1595, 1993.
- [204] A Ramos, H Morgan, N G Green, and A Castellanos. Ac electrokinetics: a review of forces in microelectrode structures. *Journal of Physics D: Applied Physics*, 31(18):2338, 1998.
- [205] N.G. Green, A. Ramos, A. González, A. Castellanos, and H. Morgan. Electrothermally induced fluid flow on microelectrodes. *Journal of Electrostatics*, 53(2):71–87, 2001.
- [206] Q. Hu, R. P. Joshi, and A. Beskok. Model study of electroporation effects on the dielectrophoretic response of spheroidal cells. *Journal of Applied Physics*, 106(2):024701, 2009.
- [207] Wang Xiao-Bo and et al. Relationship of dielectrophoretic and electrorotational behaviour exhibited by polarized particles. *Journal of Physics D: Applied Physics*, 25(6):905, 1992.
- [208] K. H. Muller, G. Wei, B. Raguse, and J. Myers. Three-dimensional percolation effect on electrical conductivity in films of metal nanoparticles linked by organic molecules. *Physical Review B*, 68(15):155407, 2003.
- [209] Raghuv eer Parthasarathy, Xiao-Min Lin, and Heinrich M. Jaeger. Electronic transport in metal nanocrystal arrays: The effect of structural disorder on scaling behavior. *Physical review letters*, 87(18):186807, 2001.
- [210] Cosmin Farcau, Helena Moreira, Benoît Viallet, Jérôme Grisolia, and Laurence Ressier. Tunable conductive nanoparticle wire arrays fabricated by convective self-assembly on nonpatterned substrates. *ACS Nano*, 4(12):7275–7282, 2010.

Bibliography

- [211] Zhong-Qun Tian, Bin Ren, Jian-Feng Li, and Zhi-Lin Yang. Expanding generality of surface-enhanced raman spectroscopy with borrowing sers activity strategy. *Chem. Commun.*, pages 3514–3534, 2007.
- [212] P. Alonso-Gonzalez, P. Albella, M. Schnell, J. Chen, F. Huth, A. Garcia-Etxarri, F. Casanova, F. Golmar, L. Arzubiaga, L. E. Hueso, J. Aizpurua, and R. Hillenbrand. Resolving the electromagnetic mechanism of surface-enhanced light scattering at single hot spots. *Nat Commun*, 3:684, 2012.
- [213] Eric C. Le Ru and Pablo G. Etchegoin. Quantifying sers enhancements. *MRS Bulletin*, 38(08):631–640, 2013.
- [214] Shuming Nie and Steven R. Emory. Probing single molecules and single nanoparticles by surface-enhanced raman scattering. *Science*, 275(5303):1102–1106, 1997.
- [215] Guiye Shan, Lihong Xu, Guorui Wang, and Yichun Liu. Enhanced raman scattering of zno quantum dots on silver colloids. *The Journal of Physical Chemistry C*, 111(8):3290–3293, 2007.
- [216] Jiming Bao, Mariano A Zimmler, Federico Capasso, Xiaowei Wang, and ZF Ren. Broadband zno single-nanowire light-emitting diode. *Nano letters*, 6(8):1719–1722, 2006.
- [217] Mariano A. Zimmler, Tobias Voss, Carsten Ronning, and Federico Capasso. Exciton-related electroluminescence from zno nanowire light-emitting diodes. *Applied Physics Letters*, 94(24):–, 2009.
- [218] Mariano A Zimmler, Federico Capasso, Sven Müller, and Carsten Ronning. Optically pumped nanowire lasers: invited review. *Semiconductor Science and Technology*, 25(2):024001, 2010.
- [219] Ming-Wei Chen, Cheng-Ying Chen, Der-Hsien Lien, Yong Ding, and Jr-Hau He. Photoconductive enhancement of single zno nanowire through localized schottky effects. *Opt. Express*, 18(14):14836–14841, 2010.
- [220] Nishuang Liu, Guojia Fang, Wei Zeng, Hao Long, Longyan Yuan, and Xingzhong Zhao. Novel zno nanorod flexible strain sensor and strain driving transistor with an ultrahigh 10^7 scale on/off ratio fabricated by a single-step hydrothermal reaction. *The Journal of Physical Chemistry C*, 115(2):570–575, 2010.
- [221] Yong Qin, Xudong Wang, and Zhong Lin Wang. Microfibre-nanowire hybrid structure for energy scavenging. *Nature*, 451(7180):809–813, 2008.
- [222] Zhong Lin Wang and Jinhui Song. Piezoelectric nanogenerators based on zinc oxide nanowire arrays. *science*, 312(5771):242–246, April 14, 2006 2006.
- [223] Hsin-Ming Cheng, Kuo-Feng Lin, Hsu-Cheng Hsu, and Wen-Feng Hsieh. Size dependence of photoluminescence and resonant raman scattering from zno quantum dots. *Applied physics letters*, 88(26):261909, 2006.

- [224] A. G. Milekhin, N. A. Yeryukov, L. L. Sveshnikova, T. A. Duda, E. I. Zenkevich, S. S. Kosolobov, A. V. Latyshev, C. Himcinski, N. V. Surovtsev, S. V. Adichtchev, ZheChuan Feng, ChiaCheng Wu, DongSing Wu, and D. R. T. Zahn. Surface enhanced raman scattering of light by zno nanostructures. *Journal of Experimental and Theoretical Physics*, 113(6):983–991, 2011/12/01 2011.
- [225] Xin Wang, Xianggui Kong, Yi Yu, and Hong Zhang. Synthesis and characterization of water-soluble and bifunctional zno-au nanocomposites. *The Journal of Physical Chemistry C*, 111(10):3836–3841, 2007.
- [226] Anna Rumyantseva, Sergey Kostcheev, Pierre-Michel Adam, Sergey V. Gaponenko, Svetlana V. Vaschenko, Olga S. Kulakovich, Andrey A. Ramanenka, Dmitry V. Guzatov, Dmytro Korbutyak, Volodymyr Dzhagan, Alexander Stroyuk, and Vitaliy Shvalagin. Nonresonant surface-enhanced raman scattering of zno quantum dots with au and ag nanoparticles. *ACS Nano*, 7(4):3420–3426, 2013.
- [227] Bruno Pettinger, Gennaro Picardi, Rolf Schuster, and Gerhard Ertl. Surface-enhanced and stm-tip-enhanced raman spectroscopy at metal surfaces. *Single Molecules*, 3(5-6):285–294, 2002.
- [228] M Becker, V Sivakov, G Andrä, R Geiger, J Schreiber, S Hoffmann, J Michler, AP Milenin, P Werner, and SH Christiansen. The sers and ters effects obtained by gold droplets on top of si nanowires. *Nano letters*, 7(1):75–80, 2007.
- [229] Ryota Matsui, Prabhat Verma, Taro Ichimura, Yasushi Inouye, and Satoshi Kawata. Nanoanalysis of crystalline properties of gan thin film using tip-enhanced raman spectroscopy. *Applied physics letters*, 90(6):061906, 2007.
- [230] N Marquestaut, D Talaga, L Servant, P Yang, P Pauzauskie, and F Lagugne-Labarthe. Imaging of single gan nanowires by tip-enhanced raman spectroscopy. *Journal of Raman Spectroscopy*, 40(10):1441–1445, 2009.
- [231] Jian Feng Li, Yi Fan Huang, Yong Ding, Zhi Lin Yang, Song Bo Li, Xiao Shun Zhou, Feng Ru Fan, Wei Zhang, Zhi You Zhou, De Yin Wu, et al. Shell-isolated nanoparticle-enhanced raman spectroscopy. *nature*, 464(7287):392–395, 2010.
- [232] Zeping Peng, Hailong Hu, Muhammad Iqbal Bakti Utama, Lai Mun Wong, Kaushik Ghosh, Renjie Chen, Shijie Wang, Zexiang Shen, and Qihua Xiong. Heteroepitaxial decoration of ag nanoparticles on si nanowires: A case study on raman scattering and mapping. *Nano Letters*, 10(10):3940–3947, 2010.
- [233] Ramesh Kattumenu, Chang H. Lee, Limei Tian, Michael E. McConney, and Srikanth Singamaneni. Nanorod decorated nanowires as highly efficient sers-active hybrids. *Journal of Materials Chemistry*, 21(39):15218–15223, 2011.
- [234] Sayed Y Sayed, Feng Wang, Marek Malac, Al Meldrum, Ray F Egerton, and Jillian M Buriak. Heteroepitaxial growth of gold nanostructures on silicon by galvanic displacement. *ACS nano*, 3(9):2809–2817, 2009.

Bibliography

- [235] S Deng, HM Fan, Xuanjun Zhang, Kian Ping Loh, CL Cheng, CH Sow, and YL Foo. An effective surface-enhanced raman scattering template based on a ag nanocluster–zno nanowire array. *Nanotechnology*, 20(17):175705, 2009.
- [236] Sean T Sivapalan, Brent M DeVetter, Timothy K Yang, Thomas van Dijk, Matthew V Schulmerich, P Scott Carney, Rohit Bhargava, and Catherine J Murphy. Off-resonance surface-enhanced raman spectroscopy from gold nanorod suspensions as a function of aspect ratio: not what we thought. *ACS nano*, 7(3):2099–2105, 2013.
- [237] Peter Y Yu and Manuel Cardona. *Fundamentals of semiconductors: physics and materials properties*. Springer Berlin etc, 1999.
- [238] D. J. Gardiner and P. R. Graves. *Practical Raman Spectroscopy*. Springer-Verlag Derlin Heidelberg, 1989.
- [239] Ramon Cuscó, Esther Alarcón-Lladó, Jordi Ibanez, Luis Artus, Juan Jimenez, Buguo Wang, and Michael J Callahan. Temperature dependence of raman scattering in zno. *Physical Review B*, 75(16):165202, 2007.
- [240] Ser-Sing Chang, Chao-Wen Shih, Cheng-Dah Chen, Wei-Cheng Lai, and C. R. Chris Wang. The shape transition of gold nanorods. *Langmuir*, 15(3):701–709, 1998.
- [241] S. Link, C. Burda, B. Nikoobakht, and M. A. El-Sayed. Laser-induced shape changes of colloidal gold nanorods using femtosecond and nanosecond laser pulses. *The Journal of Physical Chemistry B*, 104(26):6152–6163, 2000.
- [242] Stephan Link and Mostafa A. El-Sayed. Size and temperature dependence of the plasmon absorption of colloidal gold nanoparticles. *The Journal of Physical Chemistry B*, 103(21):4212–4217, 1999.
- [243] Catherine J Murphy, Tapan K Sau, Anand M Gole, Christopher J Orendorff, Jinxin Gao, Linfeng Gou, Simona E Hunyadi, and Tan Li. Anisotropic metal nanoparticles: synthesis, assembly, and optical applications. *The Journal of Physical Chemistry B*, 109(29):13857–13870, 2005.
- [244] Rajeev Gupta, Q. Xiong, G. D. Mahan, and P. C. Eklund. Surface optical phonons in gallium phosphide nanowires. *Nano Letters*, 3(12):1745–1750, 2003.
- [245] S Dhara, Prasana Sahoo, AK Tyagi, and Baldev Raj. *Surface Optical Mode in Semiconductor Nanowires*, volume 2. Intech Open Access Croatia, 2011.
- [246] E. Alarcon-Llado, J. Ibanez, R. Cusco, L. Artus, J. D. Prades, S. Estrade, and J. R. Morante. Ultraviolet raman scattering in zno nanowires: quasimode mixing and temperature effects. *Journal of Raman Spectroscopy*, 42(2):153–159, 2011.
- [247] K. Kalyanasundaram and J. K. Thomas. The conformational state of surfactants in the solid state and in micellar form. a laser-excited raman scattering study. *The Journal of Physical Chemistry*, 80(13):1462–1473, 1976.

- [248] Benedetto Bozzini, Lucia D'Urzo, Marilena Re, and Federica Riccardis. Electrodeposition of cu from acidic sulphate solutions containing cetyltrimethylammonium bromide (ctab). *Journal of Applied Electrochemistry*, 38(11):1561–1569, 2008.
- [249] Kwan Kim, Kyung Lock Kim, and Kuan Soo Shin. Raman spectral characteristics of 4-aminobenzenethiol adsorbed on zno nanorod arrays. *Physical Chemistry Chemical Physics*, 15(23):9288–9294, 2013.
- [250] Masatoshi Osawa, Naoki Matsuda, Katsumasa Yoshii, and Isamu Uchida. Charge transfer resonance raman process in surface-enhanced raman scattering from p-aminothiophenol adsorbed on silver: Herzberg-teller contribution. *The Journal of Physical Chemistry*, 98(48):12702–12707, 1994/12/01 1994.
- [251] Sheng Chu, Guoping Wang, Weihang Zhou, Yuqing Lin, Leonid Chernyak, Jianze Zhao, Jieying Kong, Lin Li, Jingjian Ren, and Jianlin Liu. Electrically pumped waveguide lasing from zno nanowires. *Nat Nano*, 6(8):506–510, 2011.
- [252] Chunfeng Zhang, Fan Zhang, Tian Xia, Nitin Kumar, Jong-in Hahm, Jin Liu, Zhong Lin Wang, and Jian Xu. Low-threshold two-photon pumped znonanowire lasers. *Opt. Express*, 17(10):7893–7900, 2009.
- [253] MH Huang, S Mao, H Feick, H Yan, Y Wu, H Kind, E Weber, R Russo, and P Yang. Room-temperature ultraviolet nanowire nanolasers. *science*, 292(5523):1897, 2001.
- [254] Justin C. Johnson, Haoquan Yan, Peidong Yang, and Richard J. Saykally. Optical cavity effects in zno nanowire lasers and waveguides. *The Journal of Physical Chemistry B*, 107(34):8816–8828, 2003/08/01 2003.
- [255] Tobias Voss, Geoffry T. Svacha, Eric Mazur, Sven Muller, Carsten Ronning, Denan Konjhodzic, and Frank Marlow. High-order waveguide modes in zno nanowires. *Nano Letters*, 7(12):3675–3680, 2007/12/01 2007.
- [256] Alejandro J. Gimenez, J. M. Yanez-Limon, and Jorge M. Seminario. Zno-paper based photoconductive uv sensor. *The Journal of Physical Chemistry C*, 115(1):282–287, 2010.
- [257] H. Kind, H. Yan, B. Messer, M. Law, and P. Yang. Nanowire ultraviolet photodetectors and optical switches. *Advanced Materials*, 14(2):158–160, 2002.
- [258] Josh Goldberger, Donald J. Sirbuly, Matt Law, and Peidong Yang. Zno nanowire transistors. *The Journal of Physical Chemistry B*, 109(1):9–14, 2005.
- [259] Q. H. Li, Q. Wan, Y. X. Liang, and T. H. Wang. Electronic transport through individual zno nanowires. *Applied Physics Letters*, 84(22):4556–4558, 2004.
- [260] M. W. Ahn, K. S. Park, J. H. Heo, J. G. Park, D. W. Kim, K. J. Choi, J. H. Lee, and S. H. Hong. Gas sensing properties of defect-controlled zno-nanowire gas sensor. *Applied Physics Letters*, 93(26):263103–3, 2008.

Bibliography

- [261] L. Liao, H. B. Lu, J. C. Li, C. Liu, D. J. Fu, and Y. L. Liu. The sensitivity of gas sensor based on single zno nanowire modulated by helium ion radiation. *Applied Physics Letters*, 91(17):173110–3, 2007.
- [262] PF Carcia, RS McLean, MH Reilly, and G Nunes Jr. Transparent zno thin-film transistor fabricated by rf magnetron sputtering. *Applied Physics Letters*, 82(7):1117–1119, 2003.
- [263] Michael S Arnold, Phaedon Avouris, Zheng Wei Pan, and Zhong L Wang. Field-effect transistors based on single semiconducting oxide nanobelts. *The Journal of Physical Chemistry B*, 107(3):659–663, 2003.
- [264] J.B.K. Law and J.T.L. Thong. Improving the nh_3 gas sensitivity of zno nanowire sensors by reducing the carrier concentration. *Nanotechnology*, 19(20):205502, 2008.
- [265] AY Polyakov, NB Smirnov, EA Kozhukhova, VI Vdovin, K Ip, YW Heo, DP Norton, and SJ Pearton. Electrical characteristics of au and ag schottky contacts on n-zno. *Applied physics letters*, 83(8):1575–1577, 2003.
- [266] Han-Ki Kim, Sang-Heon Han, Tae-Yeon Seong, and Won-Kook Choi. Low-resistance ti/au ohmic contacts to al-doped zno layers. *Applied Physics Letters*, 77(11):1647–1649, 2000.
- [267] J. H. He, P. H. Chang, C. Y. Chen, and K. T. Tsai. Electrical and optoelectronic characterization of a zno nanowire contacted by focused-ion-beam-deposited pt. *Nanotechnology*, 20(13):135701, 2009.
- [268] Soo Young Kim, Ho Won Jang, Jong Kyu Kim, Chang Min Jeon, Won Il Park, Gyu-Chul Yi, and Jong-Lam Lee. Low-resistance ti/al ohmic contact on undoped zno. *Journal of electronic materials*, 31(8):868–871, 2002.
- [269] Dale L Huber, Ronald P Manginell, Michael A Samara, Byung-Il Kim, and Bruce C Bunker. Programmed adsorption and release of proteins in a microfluidic device. *Science*, 301(5631):352–354, 2003.
- [270] Natalya Privorotskaya, Yi-Shao Liu, Jungchul Lee, Hongjun Zeng, John A Carlisle, Adarsh Radadia, Larry Millet, Rashid Bashir, and William P King. Rapid thermal lysis of cells using silicon–diamond microcantilever heaters. *Lab on a Chip*, 10(9):1135–1141, 2010.
- [271] Patrick Ginet, Kevin Montagne, Sho Akiyama, Ali Rajabpour, Akiyoshi Taniguchi, Teruo Fujii, Yasuyuki Sakai, Beomjoon Kim, Dominique Fourmy, and Sebastian Volz. Towards single cell heat shock response by accurate control on thermal confinement with an on-chip microwire electrode. *Lab on a Chip*, 11(8):1513–1520, 2011.
- [272] C Yan Jin, Zhiyong Li, R Stanley Williams, K-Cheol Lee, and Inkyu Park. Localized temperature and chemical reaction control in nanoscale space by nanowire array. *Nano letters*, 11(11):4818–4825, 2011.

- [273] CC Chen, YS Lin, CH Sang, and J-T Sheu. Localized joule heating as a mask-free technique for the local synthesis of zno nanowires on silicon nanodevices. *Nano letters*, 11(11):4736–4741, 2011.
- [274] Inkyu Park, Zhiyong Li, Albert P Pisano, and R Stanley Williams. Selective surface functionalization of silicon nanowires via nanoscale joule heating. *Nano letters*, 7(10):3106–3111, 2007.
- [275] Soo Young Kim, Ho Won Jang, Jong Kyu Kim, Chang Min Jeon, Won Il Park, Gyu-Chul Yi, and Jong-Lam Lee. Low-resistance ti/al ohmic contact on undoped zno. *Journal of Electronic Materials*, 31(8):868–871, 2002.
- [276] Simon M Sze and Kwok K Ng. *Physics of semiconductor devices*. John Wiley & Sons, 2006.
- [277] Olaf Wunnicke. Gate capacitance of back-gated nanowire field-effect transistors. *Applied Physics Letters*, 89(8):083102, 2006.
- [278] S. E. Mohny, Y. Wang, M. A. Cabassi, K. K. Lew, S. Dey, J. M. Redwing, and T. S. Mayer. Measuring the specific contact resistance of contacts to semiconductor nanowires. *Solid-State Electronics*, 49(2):227–232, 2005.
- [279] C. C. Chen, Y. S. Lin, C. H. Sang, and J.-T. Sheu. Localized joule heating as a mask-free technique for the local synthesis of zno nanowires on silicon nanodevices. *Nano Letters*, 11(11):4736–4741, 2011.
- [280] J. G. Endriz and W. E. Spicer. Surface-plasmon-one-electron decay and its observation in photoemission. *Physical Review Letters*, 24(2):64–68, 01/12/1970.
- [281] Gaoling Zhao, Hiromitsu Kozuka, and Toshinobu Yoko. Sol-gel preparation and photoelectrochemical properties of tio₂ films containing au and ag metal particles. *Thin Solid Films*, 277(1-2):147–154, 1996.
- [282] Yang Tian, Xiu Shi, Chunqiang Lu, Xiting Wang, and Shilong Wang. Charge separation in solid-state gold nanoparticles-sensitized photovoltaic cell. *Electrochemistry Communications*, 11(8):1603–1605, 2009.
- [283] Feng Wu, Xiaoyun Hu, Jun Fan, Enzhou Liu, Tao Sun, Limin Kang, Wenqian Hou, Changjun Zhu, and Hanchen Liu. Photocatalytic activity of ag/tio₂ nanotube arrays enhanced by surface plasmon resonance and application in hydrogen evolution by water splitting. *Plasmonics*, 8(2):501–508, 2013.
- [284] Saji Thomas Kochuveedu, Dong-Pyo Kim, and Dong Ha Kim. Surface-plasmon-induced visible light photocatalytic activity of tio₂ nanospheres decorated by au nanoparticles with controlled configuration. *The Journal of Physical Chemistry C*, 116(3):2500–2506, 2011.
- [285] Mark W. Knight, Yumin Wang, Alexander S. Urban, Ali Sobhani, Bob Y. Zheng, Peter Nordlander, and Naomi J. Halas. Embedding plasmonic nanostructure diodes enhances hot electron emission. *Nano Letters*, 13(4):1687–1692, 2013.

Bibliography

- [286] Zheyu Fang, Zheng Liu, Yumin Wang, Pulickel M Ajayan, Peter Nordlander, and Naomi J Halas. Graphene-antenna sandwich photodetector. *Nano letters*, 12(7):3808–3813, 2012.
- [287] C. Soci, A. Zhang, B. Xiang, S. A. Dayeh, D. P. R. Aplin, J. Park, X. Y. Bao, Y. H. Lo, and D. Wang. Zno nanowire uv photodetectors with high internal gain. *Nano Letters*, 7(4):1003–1009, 2007.
- [288] Zhong Lin Wang. Zinc oxide nanostructures: growth, properties and applications. *J. Phys.: Condens. Matter* 16 (2004), R829-R858, 2004.
- [289] H. Zhang, A. V. Babichev, G. Jacopin, P. Lavenus, F. H. Julien, A. Yu. Egorov, J. Zhang, T. Pauporte, and M. Tchernycheva. Characterization and modeling of a zno nanowire ultraviolet photodetector with graphene transparent contact. *Journal of Applied Physics*, 114(23):234505, 2013.
- [290] Jiming Bao, Mariano A. Zimmler, Federico Capasso, Xiaowei Wang, and Z. F. Ren. Broadband zno single-nanowire light-emitting diode. *Nano Letters*, 6(8):1719–1722, 2006.
- [291] Soumen Dhara and PK Giri. Enhanced uv photosensitivity from rapid thermal annealed vertically aligned zno nanowires. *Nanoscale research letters*, 6(1):1–8, 2011.
- [292] Bing Guo, Zhizhen Ye, and KS Wong. Time-resolved photoluminescence study of a zno thin film grown on a (100) silicon substrate. *Journal of crystal growth*, 253(1):252–257, 2003.
- [293] S. A. Studenikin and Michael Cocivera. Time-resolved luminescence and photoconductivity of polycrystalline zno films. *Journal of Applied Physics*, 91(8):5060–5065, 2002.
- [294] K Moazzami, TE Murphy, JD Phillips, M CK Cheung, and AN Cartwright. Sub-bandgap photoconductivity in zno epilayers and extraction of trap density spectra. *Semiconductor science and technology*, 21(6):717, 2006.
- [295] F. Gonzalez-Posada, R. Songmuang, M. Den Hertog, and E. Monroy. Room-temperature photodetection dynamics of single gan nanowires. *Nano Letters*, 12(1):172–176, 2011.
- [296] Jens Reemts and Achim Kittel. Persistent photoconductivity in highly porous zno films. *Journal of Applied Physics*, 101(1):013709, 2007.
- [297] Stephan Lany and Alex Zunger. Anion vacancies as a source of persistent photoconductivity in ii-vi and chalcopyrite semiconductors. *Physical Review B*, 72(3):035215, 2005.
- [298] Zhi-Min Liao, Hong-Zhou Zhang, Yang-Bo Zhou, Jun Xu, Jing-Min Zhang, and Da-Peng Yu. Surface effects on photoluminescence of single zno nanowires. *Physics Letters A*, 372(24):4505–4509, 2008.

- [299] A. Bera and D. Basak. Role of defects in the anomalous photoconductivity in zno nanowires. *Applied Physics Letters*, 94(16):163119, 2009.
- [300] Bixia Lin, Zhuxi Fu, and Yunbo Jia. Green luminescent center in undoped zinc oxide films deposited on silicon substrates. *Applied Physics Letters*, 79(7):943–945, 2001.
- [301] Arthur Zhang, Sifang You, Cesare Soci, Yisi Liu, Deli Wang, and Yu-Hwa Lo. Silicon nanowire detectors showing phototransistive gain. *Applied Physics Letters*, 93(12):121110, 2008.
- [302] Cesar Clavero. Plasmon-induced hot-electron generation at nanoparticle/metal-oxide interfaces for photovoltaic and photocatalytic devices. *Nat Photon*, 8(2):95–103, 2014.
- [303] Shannon W Boettcher, Nicholas C Strandwitz, Martin Schierhorn, Nina Lock, Mark C Lonergan, and Galen D Stucky. Tunable electronic interfaces between bulk semiconductors and ligand-stabilized nanoparticle assemblies. *Nature materials*, 6(8):592–596, 2007.
- [304] Sriharsha V. Aradhya, Michael Frei, Mark S. Hybertsen, and L. Venkataraman. Van der waals interactions at metal/organic interfaces at the single-molecule level. *Nat Mater*, 11(10):872–876, 2012.
- [305] Andrea Pescaglini, Alan O’Riordan, Aidan J Quinn, and Daniela Iacopino. Controlled assembly of au nanorods into 1d architectures by electric field assisted deposition. *Journal of Materials Chemistry C*, 2(33):6810–6816, 2014.
- [306] Laetitia Bernard, Yavor Kamdzhilov, Michel Calame, Sense Jan van der Molen, Jianhui Liao, and Christian Schonenberger. Spectroscopy of molecular junction networks obtained by place exchange in 2d nanoparticle arrays. *The Journal of Physical Chemistry C*, 111(50):18445–18450, 2007.
- [307] J. Liao, L. Bernard, M. Langer, C. Schonenberger, and M. Calame. Reversible formation of molecular junctions in 2d nanoparticle arrays. *Advanced Materials*, 18(18):2444–2447, 2006.
- [308] Q. H. Li, T. Gao, Y. G. Wang, and T. H. Wang. Adsorption and desorption of oxygen probed from zno nanowire films by photocurrent measurements. *Applied Physics Letters*, 86(12):123117, 2005.
- [309] Ralph H Fowler. The analysis of photoelectric sensitivity curves for clean metals at various temperatures. *Physical Review*, 38(1):45, 1931.
- [310] Yow-Jon Lin and Chia-Lung Tsai. Changes in surface band bending, surface work function, and sheet resistance of undoped zno films due to $(\text{nh}_4)_2\text{S}_x$ treatment. *Journal of applied physics*, 100(11):113721–113721, 2006.
- [311] Alexander O. Govorov, Hui Zhang, Hilmi Volkan Demir, and Yurii K. Gun’ko. Photogeneration of hot plasmonic electrons with metal nanocrystals: Quantum description and potential applications. *Nano Today*, 9(0):85–101, 2014.

Bibliography

- [312] Alexander O. Govorov, Hui Zhang, and Yurii K. Gun'ko. Theory of photoinjection of hot plasmonic carriers from metal nanostructures into semiconductors and surface molecules. *The Journal of Physical Chemistry C*, 117(32):16616–16631, 2013.
- [313] Hui Zhang and Alexander O. Govorov. Optical generation of hot plasmonic carriers in metal nanocrystals: The effects of shape and field enhancement. *The Journal of Physical Chemistry C*, 118(14):7606–7614, 2014.
- [314] Alejandro Manjavacas, Jun G Liu, Vikram Kulkarni, and Peter Nordlander. Plasmon-induced hot carriers in metallic nanoparticles. *ACS nano*, 8(8):7630–7638, 2014.
- [315] A. Apuzzo, M. Fevrier, R. Salas-Montiel, A. Bruyant, A. Chelnokov, G. Leron-del, B. Dagens, and S. Blaize. Observation of near-field dipolar interactions involved in a metal nanoparticle chain waveguide. *Nano Letters*, 13(3):1000–1006, 2013.
- [316] Stefan A. Maier, Pieter G. Kik, and Harry A. Atwater. Optical pulse propagation in metal nanoparticle chain waveguides. *Phys. Rev. B*, 67:205402, May 2003.
- [317] S.A. Maier, P.G. Kik, H.A. Atwater, S. Meltzer, E. Harel, B.E. Koel, A.A.G. Requicha, et al. Local detection of electromagnetic energy transport below the diffraction limit in metal nanoparticle plasmon waveguides. *Nature materials*, 2(4):229–232, 2003.